AD_____

Award Number: W81XWH-07-1-0643

TITLE: Vulnerability of Normal Human Mammary Epithelial Cells to Oncogenic Transformation

PRINCIPAL INVESTIGATOR: James C. Garbe, Ph.D.

CONTRACTING ORGANIZATION: Lawrence Berkeley National Laboratory
Berkeley, CA 94110

REPORT DATE: April 2012

TYPE OF REPORT: Final

PREPARED FOR: U.S. Army Medical Research and Materiel Command
Fort Detrick, Maryland 21702-5012

REPORT DOCUMENTATION PAGE

Form Approved
OMB No. 0704-0188

1. REPORT DATE	2. REPORT TYPE	3. DATES COVERED
Apirl 2012	Final	4 September 2007 - 3March 2012

4. TITLE AND SUBTITLE
Vulnerability of Normal Human Mammary Epithelial Cells to Oncogenic Transformation

5a. CONTRACT NUMBER

5b. GRANT NUMBER
W81XWH-07-1-0643

5c. PROGRAM ELEMENT NUMBER

6. AUTHOR(S)
James Garbe, Ph.D.

E-Mail: jcgarbe@lbl.gov

5d. PROJECT NUMBER

5e. TASK NUMBER

5f. WORK UNIT NUMBER

7. PERFORMING ORGANIZATION NAME(S) AND ADDRESS(ES)

Lawrence Berkeley National Laboratory
Berkeley, CA 94720

8. PERFORMING ORGANIZATION REPORT NUMBER

9. SPONSORING / MONITORING AGENCY NAME(S) AND ADDRESS(ES)
U.S. Army Medical Research and Materiel Command
Fort Detrick, Maryland 21702-5012

10. SPONSOR/MONITOR'S ACRONYM(S)

11. SPONSOR/MONITOR'S REPORT NUMBER(S)

12. DISTRIBUTION / AVAILABILITY STATEMENT
Approved for Public Release; Distribution Unlimited

13. SUPPLEMENTARY NOTES

14. ABSTRACT

Breast tumor cells display great diversity in gene and protein expression, and genomic alterations, associated with striking differences in clinical parameters. Our approach to understanding the molecular pathways that lead to the different types of breast cancer in vivo has been to model this process in vitro. Thus far, almost all in vitro transformed HMEC lines represent a limited subset of in vivo cancer phenotypes. We hypothesized that this could result from restrictive and stressful culture conditions that don't support growth of the target cells. Our proposal has sought to generate lines more reflective of breast cancer phenotypes by using our less stressful HMEC culture methods that support long-term growth of cells of luminal, basal, and progenitor lineages, and to directly examine the effects of stress on vulnerability to oncogenic transformation. We have now shown that unstressed cells are more vulnerable to c-Myc and TERT induced transformation, that different early-stage pathways to transformation are associated with distinct molecular properties, and that normal cells from older women have altered lineage markers that may make their luminal cells more vulnerable to transformation. In the process, we have generated, and continue to characterize, new transformed HMEC lines that exhibit a greater diversity of phenotypes including luminal, progenitor and claudin low as well as basal.

15. SUBJECT TERMS
human mammary epithelial cells, hTERT, c-myc, p16INK4A, oncogenic transformation, epigenetics,

16. SECURITY CLASSIFICATION OF:			17. LIMITATION OF ABSTRACT	18. NUMBER OF PAGES	19a. NAME OF RESPONSIBLE PERSON
a. REPORT	b. ABSTRACT	c. THIS PAGE			USAMRMC
U	U	U	UU	103	19b. TELEPHONE NUMBER *(include area code)*

Table of Contents

INTRODUCTION:

Many studies have shown that cells derived from breast tumors display great diversity in patterns of gene and protein expression, and genomic alterations. Based on these distinctions, multiple breast cancer subtypes have been categorized; importantly, these subtypes show striking differences in clinical parameters. Understanding the pathways of molecular alterations that lead to the different types of breast cancer in vivo could facilitate design of clinical interventions in the carcinogenic progression. One approach to examining human breast carcinogenesis is to model this process in vitro, starting with normal HMEC and using oncogenic agents to transform the normal cells to cancer (see Fig. 1 for a summary of the various conditions we have used to generate transformed lines). However, when this grant started, almost all in vitro transformed HMEC lines represented a limited subset of the phenotypes observed in breast cancer cells in vivo. We hypothesized that these limited phenotypes resulted from culture conditions that restrict proliferation of normal HMEC to mostly cells with a basal phenotype. Normal cultured HMEC proliferate for a variable number of population doublings (PD) before encountering a first senescence barrier, stasis, which is stress-associated, mediated by the retinoblastoma (RB) pathway, correlated with increased levels of $p16^{INK4a}$, and telomere length independent. HMEC may overcome stasis by inactivation of the RB pathway, and continue growth until encountering a second extremely stringent barrier due to telomere attrition (Brenner et al, 1998, Romanov et al. 2001, Garbe et al. 2007, 2009). HMEC grown in the serum-free medium that we first developed and is commonly used (MCDB170/MEGM; Hammond et al. 1984, Stampfer, 1985) reach stasis quickly, and can show "spontaneous" silencing of p16, giving rise to the aberrant p16(-) post-stasis HMEC (called post-selection) that are commercially available and, although significantly abnormal, sold as "normal primaries". Our initial in vitro transformed lines derived from post-stasis HMEC showed a basal phenotype (Stampfer and Bartley, 1985, Perou et al., 2000). This grant proposed to generate HMEC lines more reflective of the in vivo spectrum of breast cancer phenotypes by using improved methods for growing normal pre-stasis HMEC. We previously defined low stress culture conditions that allow pre-stasis HMEC to grow for ~60 PD prior to p16 induction and growth arrest at stasis (Garbe et al., 2009). This medium supports pre-stasis HMEC with phenotypes of luminal, basal, and progenitor lineages, indicating that these cultures represent *in vivo* populations more accurately than previous HMEC culture conditions (Garbe et al., 2009, Chanson et al. 2011, Garbe et al. in revision). These different HMEC lineages can be isolated by flow sorting. We hypothesized that these heterogeneous, or lineage-enriched, unstressed pre-stasis populations would be more vulnerable to transformation when targeted by oncogenic agents, and might yield a greater range of transformed phenotypes. Our objectives included: (1) addressing the basic research questions - are unstressed pre-stasis HMEC more vulnerable to transformation and is a particular normal cell type more vulnerable or more likely to give a specific transformed phenotype, and (2) producing a practical outcome – generation of useful transformed lines. Our initial approach was: (1) Determine whether transduction of unstressed pre-stasis HMEC with oncogenes such as c-myc and Wnt-1, with or without p53 inactivation, will yield transformed lines with phenotypes representative of most human breast cancer cells, and if there are correlations of transformed cell phenotypes with the target cell population and/or agents used for in vitro transformation. (2) Experimentally examine whether cultured HMEC that have not encountered stress are more vulnerable to transformation than those exposed to stress. The generation of diverse transformed HMEC lines with defined genetic alterations may aid the identification of potential therapeutic treatments, including personalized therapeutics.

BODY:

To accomplish our goals, we made collaborations with investigators at LBNL (LaBarge and Bissell labs), Arizona Cancer Center, Tucson (ACC; Futscher and Watts labs), Case Western Reserve U. (Jackson lab); Smurfit Institute, Dublin (Bracken lab). As mentioned in previous reports, due to seismic safety issues beyond the control of anyone at LBNL, we lacked adequate lab space from October 2008 to January 2010. We consequently needed to forego any projects requiring large amounts of ongoing cell culture during that time. Due to this unforeseen delay, work on this project continued into 2012.

Identification of normal HMEC lineages, effects of age, and applications for developing lines with luminal and other phenotypes. One of our initial hypotheses for this grant was that the difficulty in developing in vitro immortalized lines with luminal phenotypes (in our hands as well as others) could be a consequence of the existing culture conditions, which favored growth of myoepithelial cells in culture and generally did not support long-term growth of HMEC with luminal phenotypes. Our new low stress media (Garbe et al. 2009) supports the growth of cells with markers of myoepithelial (e.g., CD10, K(keratin) 14), LEP (e.g., muc1, K18, K19, EpCam, Prom1/CD133), and progenitor cells (e.g., K14 *and* K19, c-Kit), although the luminal decrease with passage (Garbe et al. submitted). Therefore, we chose to use early passage cultures grown in our new low-stress media as starting points for transformation. We also planned on using populations FACS-enriched for specific lineages once we gained more information about possible cells-of-origin of human breast cancer subtypes. Recent publications have suggested BRAC1-associated and basal cancers may arise from luminal progenitors, and multipotent progenitors were implicated in luminal cancer models.

Our collaborative studies with the LaBarge lab on normal HMEC lineages have provided valuable information to guide this work. Additionally, these studies uncovered a novel effect of aging on HMEC lineage representation, which may bear on the observed increased luminal breast cancer subtypes in older women. These data in turn influenced our choice of starting specimens for transformation studies (see below). This work is now in revision for Cancer Research (Garbe, Pelissier, Pepin, Fridriksdottir, Sputova, Guo, Villadsen, Park, Petersen, Borowsky, Stampfer, LaBarge, Aging is associated with increased multipotent progenitors with a basal differentiation bias in human mammary epithelia).

For these studies, we have used the primary organoid material from the Stampfer HMEC Bank (~150 individuals), as well as similar organoid material collected by Dr. Stampfer's former institution after she left (~200 individuals). Pre-stasis HMEC strains from ~18 young (<30) and ~18 older (>55) women have been grown in our new low stress medium M87A+X. As shown in Figures 2-3, the luminal lineage was proportionately over-represented in strains isolated from older compared to younger women (2B). Uncultured organoids showed decreased proportions of myoepithelial and little or no change in the proportion of luminal cells with age (2D). The ability of the luminal cells from older women to proliferate better in culture might be a consequence of their increased expression with age of integrin alpha 6 (2F), thought to be a myoepithelial-expressed ECM-binding protein. Luminal cells from older women were also altered in their increased expression of K14. Thus, a decline of myoepithelial cells, and an increase of luminal cells that exhibited molecular features usually ascribed to myoepithelial cells, were measured with age in cultured pre-stasis strains and in cells from uncultured dissociated organoids. Gene expression profiles also distinguished young vs. older HMEC. Data obtained from 3 young vs. 3 older women's early passage HMEC strains clustered into young and old age groups according to an age-specific gene expression signature derived from RNA in a collection of laser microdissected normal breast epithelia (Dr. Morag Park, McGill University). The receptor tyrosine kinase c-Kit has been postulated to be a marker of luminal progenitors in humans. The proportion of c-Kit-expressing HMEC decreased with passage in pre-stasis strains (3A) but increased as a function of age when measured at passage (p) 4 (3B) and in dissociated reduction mammoplasty samples (3C). FACS-enriched c-Kit+ HMEC at 4p cultured for four additional passages showed self-renewal and multipotent differentiation, including in 3D structures (3D-H), supporting the hypothesis that c-Kit+ cells are progenitors capable of multilineage differentiation.

Altogether, these data suggest the exciting possibility that the observed age-associated increase in luminal breast cancer may have connections to changes that occur normally with aging in the human breast. The significant age-dependent changes to the mammary epithelium that we observed could make older women more vulnerable to malignant progression, and underlay the increased luminal breast cancer incidence in women >55y. Myoepithelial cells are thought to be tumor-suppressive and progenitors are putative etiological roots of some breast cancers. Thus during the aging process, the potential target population of cells is increased and there is simultaneous decrease in the cells thought to suppress tumorigenic activity.

The effect of stress and c-myc overexpression on vulnerability to transformation of pre-stasis, and different types of post-stasis, HMEC. We have hypothesized that exposure to p16-inducing stresses may influence the response of HMEC to agents of transformation, and that a connection may exist between telomerase expression and responses to p16-inducing stresses. We have been able to generate data consistent with these hypotheses, although the underlying molecular mechanisms are still not defined.

In one set of experiments, we assessed whether media stress (how rapidly a medium induced p16 expression) influenced the ability of finite HMEC to be immortalized using hTERT. We (and others) had previously reported (Stampfer et al., 2001) that hTERT can readily immortalize post-stasis HMEC that lack expression of p16, but pre-stasis HMEC, grown in the moderate stress medium MM, or the high stress serum-free MCDB170, were refractile to hTERT immortalization (in MM, one clonal line that gradually lost p16 expression did emerge). Although these results showed that cells that already began the stasis process, and/or expressed p16, were not readily immortalized by hTERT, we postulated that high telomerase activity prior to the onset of the stasis program could allow TERT immortalization and counteract subsequent stress exposures. Pre-stasis 184D HMEC growing in the low stress medium M87A+X were transduced with hTERT at passage 3 and 10. As shown in Figure 4, hTERT readily immortalized these 184D cultures at both passage levels, although the efficiency may have been lower at higher passage, where some cells may have started induction of p16/entering into stasis. This result, in marked contrast to our results with pre-stasis HMEC grown in MM, suggests that the lower stress medium does make these cultures more vulnerable to immortal transformation. We then assessed whether the p16 gene remains functional and inducible in these new TERT-immortalized cultures. In collaboration with the Bracken lab, we tested whether p16 expression could be induced in normal pre-stasis HMEC, the TERT-immortalized lines, and 2 other lines whose p16 status was unknown (4B). Cells were exposed to shRNA to BMI1, an inhibitor of p16 induction in normal human cells. While normal cells show p16 induction in response to BMI1 shRNA (e.g., 184D), the same cultures transduced with hTERT (i.e., 184DTERT) did not. Since immortalization was rapid and efficient there was not time for mutation or selection of subpopulations. These data support the hypothesis that high hTERT levels prior to the onset of stasis can act to prevent subsequent p16 induction and the stasis arrest.

Our second set of experiments examined the effect of overexpressed c-Myc on different types of post-stasis HMEC that had different stress exposures as pre-stasis cultures (see also Figure 1). Our previous work had noted that overexpressed c-Myc had little detectable effect on telomerase expression or immortalization of post-stasis post-selection p16(-) HMEC (i.e., post-stasis cells that had silenced p16, along with many other epigenetic changes, after growth in the high stress MCDB170 medium)(Figure 5A). One early experiment had indicated that a different post-stasis type, Extended Life (EL) 184Aa culture (p16 loss due to mutation) could be immortalized by c-Myc; post-stasis EL cultures were derived following chemical carcinogen exposure of primary 184 HMEC grown in the moderate stress MM medium (Stampfer and Bartley, 1985, 1988). We then examined three independently derived post-stasis EL populations, 184Aa, 184Be, and 184Ce, which were known to lack p16 expression by different mechanisms (mutation in 184Aa, promoter methylation in 184Be and 184Ce). All three EL cultures were readily, and apparently uniformly, immortalized by c-Myc (5B), associated with increased telomerase (TRAP) activity. These results indicate that neither loss of p16 expression, nor specifically loss of p16 due to p16 promoter methylation, was the responsible variable in determining whether post-stasis HMEC are vulnerable to myc-induced immortalization. We then examined a more controlled post-stasis type, i.e., early passage pre-stasis HMEC grown in low stress M87A+X transduced with shRNA to p16. Initially, HMEC from 2 younger women, specimens 184 and 240L were examined (5C). Exposure of the post-stasis p16sh cultures to c-Myc one passage later resulted in rapid and efficient immortalization and increased TRAP activity (these lines will be discussed further below). We conclude that the prior history of HMEC that became post-stasis, but not the loss of p16 per se, influences the cells ability to respond to transduced c-Myc with increased telomerase activity and immortalization. The post-stasis type that had experienced the most stressful culture conditions and undergone extensive epigenetic changes (Novak et al. 2009) was refractile to

immortalization, whereas the other post-stasis types examined could be readily immortalized. The ability of c-Myc to induce rapid efficient immortalization in the post-stasis p16sh populations indicates that this capacity is not dependent upon pre-existing clonal errors in the post-stasis population, as might be possible for the post-stasis carcinogen-exposed EL population.

Our starting hypothesis to explain the different responses to c-Myc by the different post-stasis HMEC types was that differences in the chromatin landscape might make the hTERT gene locus have differential access to the trans-activating potential of c-Myc. We collaborated with the Futscher lab to probe the hTERT locus for possible differences in DNA methylation or histone modifications (permissive H3K4me3 or repressive HeK27me3) that could be correlated with either basal or myc-induced TRAP activity. Figure 6 shows the result using 5-methylcytosine or respective chromatin immunoprecipitation coupled to custom tiling microarray hybridization. We compared normal mammary fibroblasts, pre-stasis HMEC (low or no TRAP activity), the different post-stasis types (post-selection 184B, 48RS: no basal or induced activity; EL 184Aa and 184p16sh: no or low basal but myc-inducible), and TERT expressing immortalized and tumor-derived lines. The TERT region is mostly methylated in all samples analyzed, with no obvious differences based on either the culture's basal or myc-inducible TRAP activity. To increase resolution and sensitivity of the DNA methylation analysis, two regions were analyzed in more detail using MassARRAY technology (6B). No obvious differences in DNA methylation level correlating with TRAP activity were seen not only among the different post-stasis types, but also among all the cell types. All the cultures showed some enrichment of repressive H3K27me3 on the hTERT promoter, with no obvious correlation to TRAP activity. We did not detect any enrichment of permissive H3K4me3 at the hTERT region in all the analyzed samples, including the in vitro immortalized and cancer lines, known to possess sufficient telomerase activity to maintain stable telomeres. Overall, the data show that the DNA methylation state, and the absence of H3K4me3 and the presence H3K27me3 on the hTERT gene promoter, are similar in most of the analyzed HMEC samples (pre-stasis, different post-stasis types, immortal lines) and therefore do not seem to play a role in differential response of post-stasis types to c-Myc overexpression. The overall lack of correlation of these parameters with TRAP activity is consistent with previous reports and highlights the unusual epigenetic landscape of this gene. While these studies did not answer the question about the mechanism underlying the differential response of post-stasis types to c-Myc, we believe these analyses, using isogenic and tumor-derived HMEC with known variability in basal and induced TRAP activity, can provide useful and novel information about the regulation of hTERT expression, which is critically involved in human carcinoma development. We are considering testing other possible explanations for the differential response to c-Myc to examine should funding become available.

We also examined gene expression profiling (Affymetrix) in the post-stasis post-selection vs EL HMEC to see if there were any obvious differences that might correlate with vulnerability to Myc-induced telomerase induction. Three distinct EL cultures were compared with growing post-selection HMEC from 3 different individuals (Figure 7). We performed both unsupervised cluster analysis to determine the top 100 genes differentially expressed (7A), and also specifically examined 70 transcription factors associated with potential binding sites in the hTERT promoter. Cluster analysis showed several transcripts with consistent differences across all post-selection vs EL HMEC, while one transcription factor, LEF1, also differed. Expression of the genes differentially expressed in these two types of post-stasis populations was then examined using the range of our HMEC system samples from normal pre-stasis to immortal and malignant (Fig. 7B). These studies also did not provide an explanation for the differential response of the post-stasis types to c-Myc, but may shed light on errors involved in different pathways of HMEC transformation, adding to our data showing that transformation pathways diverge among the still finite, aberrant post-stasis HMEC types (see also Fig. 12 below). Observation of the data in Fig. 7A led us to realize that we should redo this comparison using both growing and near senescent post-selection HMEC, as some of the genes identified are associated with growth state (the EL cultures examined were less proliferative and nearer to telomere dysfunction than the growing post-selection). Nonetheless, some interesting genes showed up that could be further explored, such as LEF1, a transcription factor with a potential binding site in the hTERT promoter and association with β-catenin

regulation, PHGDH, involved in serine biosynthesis and recently associated with some breast cancer types (Possemato et al, 2011) but shown here to be expressed by normal HMEC, correlated with proliferation state, and TGM1, a transglutaminase.

Immortalization of HMEC following targeting of the tumor-suppressive senescence barriers. Our model of the tumor suppressive senescence barriers to immortalization (Fig. 1) indicates a need to bypass/overcome stasis, and to reactivate sufficient telomerase activity to overcome the telomere dysfunction barrier and gain resistance to OIS. We have also hypothesized that cancer-associated genomic alterations are needed to overcome tumor suppressive barriers and gain malignant properties, but genomic changes per se are not necessary. Further, the inherently genomic instability induced by telomere dysfunction can generate the genomic errors needed for telomerase reactivation, with the ensuing bridge-fusion-breakage cycles maintaining instability even after telomerase reactivation. No specific "mutator gene" is required.

Our studies on immortalization of normal finite lifespan pre-stasis HMEC were designed to address these hypotheses, as well as generate novel HMEC lines. We directly targeted the stasis barrier using p16sh, and more recently, a cyclin D1/CDK2 fusion protein (Chytil et al 2004), and targeted the telomere dysfunction barrier with transduced c-Myc, an hTERT transactivator. In summary, this approach was able to efficiently immortalize large populations (though likely not all) of the HMEC from the 4 women tested, and resulting immortalized lines examined showed no initial gross karyotypic abnormalities. These data support both our senescence barrier model, and our hypothesis about the requirements for genomic instability.

For these experiments, cells were grown in the low stress M87A+X medium. Early passage cultures from two younger women (184, 21 yr; 240L, 19 yr) and two older women (122L, 66 yr; 805P, 91yr) have been used. We added the specimens from older women after our collaborative studies with Mark LaBarge (above) suggested that part of the difficulty in obtaining luminal transformed lines could be a consequence of our using cells from young individuals, whereas the aging-associated changes seen in HMEC from older women might make them more vulnerable to luminal-pathway transformation. Figure 5C contains our latest data showing the growth curves of specimens 184, 240L, 805P, and 122L subjected to this transformation protocol, and the data for TRAP assay from the 184D and 240LB experiments (805P and 122L have yet to be examined for TRAP activity). Cells from all four specimens transduced with c-Myc showed efficient immortalization, accompanied by rapid increases in TRAP activity, once they had been made post-stasis by transduced p16sh or D1/CDK2. We did observe a difference between the younger vs older specimens in response to the p16sh transduction. In the younger women, we did not visually observe selection of cells able to bypass stasis following the transduction, although we would not be able to note if a low percentage of the population did not maintain growth. In the two older women visual observation clearly showed a more patchy growth following p16sh transduction, indicating that not all cells maintained growth. This result implies that many pre-stasis cells from the older women are not ceasing growth due to elevated p16 expression, and opens the possibility that the luminal cells have other mechanisms governing proliferative lifespan. Patchy growth was also seen after 122L was transduced with D1/CDK2, again suggesting that only a subset of the population (possibly distinct from those vulnerable to p16sh) could bypass stasis by this means. Altogether, these studies generated the non-clonal immortalized lines 184Dp16sMY, 184Fp16sMY, 240Lp16sMY, 805Pp16sMY, 122Lp16sMY, and 122LD1MY.

Additional rare clonal immortalizations occurred in HMEC populations grown in the M87A/M85 media that received c-Myc or p16sh alone. No lines have emerged from the control vector cultures. Almost all pre-stasis HMEC receiving c-Myc alone ceased growth at stasis; however rare cells escaped stasis by unknown means and produced clonal immortal lines (184DMY3, 184FMY2, 240LMY, 122LMY) with increased TRAP activity following the passages where most cells stopped at stasis (Fig 5C). For example, 184D-myc initially stopped growth at 10p; however a culture reinitiated at 5p continued growth past stasis, generating 184DMY3. We presume that the overexpressed c-Myc was able to immortalize this population once it became post-stasis by

transactivation of hTERT, similar to the effect of c-Myc on the EL and p16sh post-stasis populations. These results using HMEC grown in our recent low stress media contrast with prior experiments where no immortalization was seen when c-Myc was transduced into pre-stasis HMEC grown in our earlier MM medium (Garbe et al 1999). Similarly, although we have never observed any spontaneous immortalization in unperturbed post-stasis post-selection HMEC at the genomically unstable telomere dysfunction barrier, rare immortalization at this barrier was seen in the post-stasis p16sh cultures, generating the clonal immortal lines 184Fp16s, 240Lp16s and 805Pp16s. The 184Fp16s immortalization-producing error must have occurred after passage 9, since reinitiation of a frozen 9p 184F-p16sh population did not yield an immortal line. The growth curves in Fig. 5C show how the p16shRNA increased the PD potential of the cultured HMEC from what would be expected of a stasis arrest (black curves, control) to what would be expected of post-stasis cultures reaching agonescence (green curves). Unlike the continuous rapid growth seen when c-Myc was introduced into the p16sh populations, the spontaneously immortalized p16sh lines showed slow initial growth following their first, morphologically distinct appearance in the agonescent populations. We presume that the difference in spontaneous immortalization between the post-selection vs p16sh post-stasis HMEC, during the period of genomically instability, is related to the need for multiple errors for telomerase reactivation in the more stress-exposed post-selection cells compared to the ability of one error, such as overexpressed c-Myc, to immortalize the p16sh HMEC. We hypothesize that the initial slow growth of the p53(+) p16sh lines (5C) is due to a need to undergo the conversion process to reactivate sufficient telomerase activity (Stampfer et al. 1995, 2003, Garbe et al. 1999). Collectively, these data are consistent with our initial hypothesis, that unstressed HMEC would be more vulnerable to myc-induced immortalization.

Characterization of new immortally transformed HMEC lines. To understand the molecular alterations responsible for transformation, and to enhance the potential value for further research of our newly developed lines, they have been characterized for a variety of properties. Consistent with our previous observation of p53(+) immortalized HMEC lines, most of these new lines did not display the malignancy-associated property of AIG. The one exception was 184FMY2, which has other properties associated with more aggressive breast cancer cells (see below); we are currently evaluating the p53 status of this line. Our lines that express AIG have been provided to the Bissell lab for examination of tumor formation in vivo in NOD/SCID Il2RGKO mice for use in their DOD Innovator Award studies. 184FMY2 has not made tumors after 12 months. Consistent with our previous studies, non-malignant lines lacking AIG can be readily transformed to AIG by transduction of a single oncogene. Transduction of both 240Lp16sMY and 805Pp16sMY were with mutant HER2 (Neu) conferred AIG (Figure 8HI).

Analysis of lineage and EMT markers: One of our goals has been to develop HMEC lines reflective of the different types of breast tumors in vivo. Molecular characterization of the development of such lines could illuminate the molecular pathways responsible for the diversity of beast cancer subtypes. In collaboration with the LaBarge and Futscher labs, we are examining the phenotypes our newly derived lines for lineage markers and EMT-associated properties. FACS, IHC, and IF have been used to determine expression of mammary lineage markers such as CD10/CALLA, K14 (basal), CD227/Muc1, K19 (luminal), K14+K19+, cKit, (progenitor/stem), and CD44 and CD24. The Futscher lab has been examining markers of EMT such as E-cadherin, miRNA (miR-200c and others in that family), ZEB1 and ZEB2. Each line examined thus far is unique.

Figure 8 illustrates some lineage marker expression in our post-stasis and immortally transformed cells from one younger (240L) and 2 older (805P, 122L) women. 8ABD show that the p16sh/MY lines from 240L and 122L have basal markers, whereas the same exposures in 805P produced a line with mixed luminal/progenitor/basal markers. Most exciting, when D1/CDK2 rather than p16sh was used to bypass stasis in 122L, significantly different results were obtained (8C-F). In vivo, overexpression of cyclin D1 is associated with the luminal breast cancer subtype. While post-stasis 122L-p16sh exhibited a basal phenotype, post-stasis 122L-D1 showed a mixed luminal-progenitor population; immortal 122LD1MY had a luminal phenotype. We

are not aware of any previous studies that have produced luminal HMEC lines starting with reduction mammoplasty-derived cells and using oncogenic agents associated with breast cancer in vivo. Much further work would be needed to understand how these two distinct means of bypassing stasis can lead to such different transformed phenotypes. Fig 8G shows the elaborate organized structures made by the 805Pp16sMY line cultured in Matrigel.

Figures 9-10 show FACS and EMT analysis of some of our new lines. Most still express a predominantly basal phenotype ($CD10^{hi}CD227^{lo}$), and are $CD24^{hi}$. We do not know if the smaller $CD44^{hi}/CD24^{lo}$ profiles in some non-clonal lines (e.g., 240Lp16sMY, 184CeMY) represent a distinct population. For the 805Pp16sMY line, we have been able to isolate a variant subpopulation that exhibits a predominantly $CD44^{hi}/CD24^{lo}$ profile and an altered morphology (Fig. 9C). Analysis of the 184FMY2 line suggests it may belong in the claudin-low breast cancer subtype, and it demonstrates molecular and epigenetic alterations associated with EMT, e.g., in expression of E-cadherin, ZEB1/2, and the miR-200 and miR-141 clusters (10AB). The observed differences in the 184FMY2 line are mirrored in differences between the normal HMEC vs. isogenic fibroblasts, where the phenotype in the normal fibroblasts is similar to 184FMY2 and breast cancer cell lines expressing EMT (Vrba et al. 2010, 2011, and unpublished). The 184BeMY line also shows properties associated with EMT (9B, 10B). Consistent with EMT expression, the 184FMY2 line is $CD44^{hi}/CD24^{lo}$, properties associated with a cancer stem cell phenotype. In contrast, the 184DMY3 line does not have AIG or expression of EMT markers, and is $CD44^{hi}/CD24^{hi}$. Curiously, two major populations are seen in the CD44/CD24 FACS analysis (10E), and these may represent two distinct clonal lines that emerged. IHC analysis of p16 expression showed two cell types: one with strong p16 staining and one with none (10D). In vivo, strong p16 expression is commonly associated with loss of RB function (a pathway to becoming post-stasis distinct from p16 loss or cyclin D1 overexpression).

CGH and karyology: The studies performed under this grant that targeted the tumor suppressive senescence barriers have produced 11 new immortalized HMEC lines (184BeMY, 184CeMY, 184DMY3, 184Dp16sMY, 240Lp16s, 240LMY1, 240Lp16sMY, 805Pp16s, 805Pp16sMY, 122LMY1, 122Lp16sMY, 122LD1MY), and our preliminary studies produced an additional 5 lines (184SMY1, 184AaMY1, 184Fp16s, 184FMY2, 184Fp16sMY). To examine the role of genomic errors in their generation, the lines generated from the younger women have been assayed for karyology profile and/or genome copy number by aCGH (in collaboration with George Watts at the Arizona Cancer Center using the Agilent human genome microarray with 44,000 probes per array; the earlier 184F series was done in collaboration with Koie Chin at UCSF using an array with 2,428 probes). Karyology at early passages following immortalization was determined for the non-clonal lines 184AaMY1 (17p), 184BeMY (11p), 184CeMY (12p), 184Fp16sMY (16p), 184Dp16sMY (16p), and 240Lp16sMY (16p). aCGH was performed on these, and the clonal lines, at higher passages (Figure 11). As expected, the clonally derived lines exhibited numerous copy number changes, consistent with the need to generate genomic errors to overcome stasis in the Myc-alone lines, and to overcome telomere dysfunction in the p16sh-alone lines. While we have suggested that the period of genomic instability during telomere dysfunction can give rise to the errors needed for telomerase reactivation and immortalization, these data suggest that genomic errors may also be involved in the mechanism by which c-Myc allows clonal escape from stasis; myc-induced genomic instability, or insertional mutagenesis are possible causes. Some genomic areas affected, e.g., 1q, 20q, are commonly altered in breast cancer. Of note, the 184Fp16s line, which needed to overcome telomere dysfunction, has amplifications in the 8q22 region harboring c-Myc and the 20q13 region harboring ZNF217. Further investigation of the changes observed in these clonal lines may offer clues on errors that can overcome the senescence barriers.

The karyology of all three p16sh-Myc derived lines examined, and one of the three EL-Myc lines (184CeMY), showed no abnormalities at early passage. At higher passages, 1-2 copy-number alterations were observed in 184Dp16sMY (30p) and 240Lp16sMY (25p). Both also appeared to contain small deletions in the p16 locus on 9p, that would not be obvious by karyology, and 240Lp16sMY had an amplification on 1q. Myc-induced

genomic instability and/or insertional mutagenesis could have conferred a replicative advantage accounting for preferential growth of a clonal 240Lp16sMY cell. We note however, that the possible existence of clonal insertional mutagenesis, while potentially contributing to long-term genomic instability, does not bear upon the basic conclusions of these studies that are examining widespread non-clonal events. The origin of the 9p deletion in lines that had received p16sh is puzzling and currently unexplained; the earlier aCGH performed on 184Fp16MY may have lacked the resolution needed to see if such a deletion also existed in that line. The BaP exposure of the EL-Myc lines may have contributed to the small number of genomic errors seen in 184AaMY1 and 184BeMY.

Most human carcinomas contain many genomic changes, but only a small number of these are thought to play a driving role in carcinogenesis. We have proposed that the inherent genomic instability at telomere dysfunction in vitro (Romanov et al, 2001) and at DCIS in vivo (Chin et al, 2004) may generate driver errors that promote telomerase reactivation and immortalization, as well as many passenger errors (Garbe et al, 2007, 2009). The absence of gross genomic changes in the karyology of the early passage p16sMY lines is consistent with our hypothesis that genomic instability is not inherently necessary for transformation but is a mechanism to generate the errors that allow overcoming senescence barriers. By directly targeting the stasis and telomere dysfunction barriers with p16sh and c-Myc, we were able to transform normal finite pre-stasis HMEC to immortality in the absence of gross genomic changes.

Most of the above studies with the younger women are in a manuscript close to submission: Garbe, Vrba, Pepin, Sputova, Novak, Jackson, Chin, LaBarge, Watts, Futscher, Stampfer, Efficient immortalization of normal human mammary epithelial cells using two pathologically relevant agents does not require gross genomic alterations.

Examining HMEC transformed by different pathways. One of our goals has been to understand the different molecular alterations responsible for the generation of the distinct breast cancer subtypes. Our hypothesis is that the variables of cell of origin, molecular alterations incurred, and stromal-epithelial interactions are most likely key to generating the observed diversity. Under this grant we have been able to vary the molecular alterations incurred, and to some extent the cell of origin, in our effort to develop HMEC lines reflective of the different types of breast tumors in vivo. Molecular characterization of the experimental cell populations, as they transition from normal to malignant in a step-wise fashion, has been performed to ascertain associations between specific molecular pathways to transformation and the resulting cell line phenotype. Such information could illuminate the etiology of early stage cancer progression and assist in development of type-specific therapeutic interventions in this progression.

Our previous and current studies developed HMEC cultures that became post-stasis via different means, e.g., the EL, post-selection, p16sh, and D1 populations. Further perturbations of these post-stasis populations have generated a variety of distinct immortally transformed lines. We have also varied the target cell population along the variable of specimen age. We were unable within the time frame of this grant to use FACS-enriched populations to vary the lineage markers of the initial, normal pre-stasis target cells (e.g., myoepithelial, luminal, progenitor), although we are currently in position to proceed with such studies, should funding become available.

The work discussed above noted important distinctions among post-stasis HMEC that had become post-stasis by different means, in response to c-Myc transduction and gene expression profile; other studies have shown differences in lineage markers. Thus pathways to transformation can diverge in still finite HMEC at the earliest stage, overcoming the stasis barrier. This point was well illustrated by additional studies performed under this grant in collaboration with the Futscher lab. A collection of our finite (pre-and post-stasis) and immortal HMEC cultures was examined for global promoter methylation (μarray with 13,000 human promoters and a methylcytosine antibody)(Figures 12AB; Novak et al. 2009). Little or no differences were seen among pre-

stasis HMEC from different individuals, at different passages, or grown in different media (M85+X vs serum-free MCDB170). There were major difference in the number and location of differentially methylated regions (DMR) among the different types of post-stasis populations. Post-selection post-stasis HMEC showed ~200 DMR, the majority of which are also seen in cancer-derived cells, whereas the EL post-stasis HMEC showed only ~10 DMR. Both of these post-stasis types exhibited changes in the HOXA gene cluster, consistent with the changes seen in breast cancer (12A). The p16sh post-stasis populations had only 5 DMR, which were distinct from the other post-stasis types. Thus epigenetic changes occur very early in the process of transformation, and different pathways of overcoming stasis are associated with different epigenetic changes. All the clonal immortal lines thus far examined showed 400-500 DMR, the majority of which are also seen in breast cancer cells, independent of the pathway taken to immortality. However, the only non-clonal lines thus far examined, the myc-immortalized EL cultures, had many fewer, but still a significant number of DMR (71) compared to their pre-stasis precursors (12B). We are excited by the possibility that epigenetic changes such as DMR may be needed for the immortalization step in carcinogenesis. Our long-term studies have suggested that immortalization (reactivation of sufficient telomerase that maintains short stable telomeres) is a rate-limiting step in human carcinoma progression. This step does not exist in short-lived rodents, which do not possess stringent telomerase repression, and thus cannot serve as accurate models of this key event in human carcinogenesis. We hope to be able to follow up these results to determine if there are epigenetic events crucial for obtaining or maintaining of immortal potential that could serve as therapeutic targets to prevent progression from the pre-malignant to the malignant stage.

We also want to point out that the HMEC currently being sold commercially as "normal primaries" and used as such in numerous publication, are post-selection HMEC derived by the methods described in our Hammond et al. PNAS 1984 publication. This grant's above studies, as well as previous publications (Li et al., 2007, Garbe et al., 2009) have shown that post-selection HMEC have numerous significant changes from normal pre-stasis cells, and a recent publication has suggested they have metaplastic properties (Keller et al. PNAS 2012). Despite repeated efforts, we have thus far been unable to get these companies to change their incorrect characterization of these post-selection HMEC, to the detriment of the accuracy of the scientific enterprise.

In collaboration with the Futscher lab, we have also begun extensive analysis of miRNA expression and epigenetic regulation in the HMEC. Thus far only the normal pre-stasis HMEC and their isogenic fibroblast, and breast cancer cell lines and tissues have been examined (Vrba et al. 2011, and in prep); future studies may examine the HMEC on different pathways from normal to cancer. Cell-type specific miRNAs regulated by epigenetic mechanisms were identified by a global analysis of miRNA expression and epigenetic states in three isogenic pairs of HMEC and mammary fibroblasts; ~10% of miRNAs were cell-type specific with their expression linked to the epigenetic state of their promoter. In breast cancers, more than 25% of miRNA gene promoters analyzed had significant hypermethylated regions. Many of the miRNA gene promoters active in the normal HMEC and fibroblasts contain DMRs in breast cancer cells, with the miRNA promoters targeted by polycomb repression in normal cells significantly more hypermethylated in cancer than other promoters.

KEY RESEARCH ACCOMPLISHMENTS:

• Using our improved methods for long-term growth of normal pre-stasis HMEC populations that express markers of multiple HMEC lineages, demonstrated that these heterogeneous populations can be FACS-enriched into luminal, myoepithelial, and progenitor populations. Such sorted normal pre-stasis HMEC can be analyzed for lineage-associated properties and used as starting material for transformation studies to assess how the cell of origin for transformation can influence the phenotype of the transformed population.

• Showed that the ability of c-myc overexpression to immortalize some, but not all types of post-stasis finite lifespan HMEC, depends upon (still undefined) parameters of the post-stasis type, but not on expression or silencing of p16.

• Showed that the differences among p16(-) post-stasis cells in c-Myc-induced vulnerability to immortalization are not correlated with the DNA methylation or specific histone state of the hTERT gene locus. Further showed that basal expression of telomerase activity by our range of normal to transformed HMEC is not correlated with DNA methylation or specific histone state of the hTERT gene locus (with Futscher lab).

• Showed that the ability of hTERT to immortalize normal pre-stasis finite HMEC varies with the level of stress (rapidity of p16 elevation) of the growth medium; unstressed cells were readily immortalized but not those grown in a stressful medium. Further showed that the hTERT immortalized normal HMEC neither express, nor are inducible for p16 expression (with Bracken lab), consistent with an ability of overexpressed telomerase to affect stress responses.

• Showed that global promoter methylation patterns vary significantly going from normal pre-stasis HMEC to immortal/malignant lines, and that different molecular pathways to transformation (e.g., different post-stasis types) exhibit different patterns of alterations (with Futscher lab). Showed that gene transcript profiling patterns vary between normal pre-stasis and post-stasis HMEC, and between different types of post-stasis HMEC.

• Performed global analysis of miRNA expression and epigenetic states in three isogenic pairs of HMEC and mammary fibroblasts and showed tissue specific miRNA expression; epigenetic regulation of the promoter was shown to control expression of many of these miRNA genes. Many of the epigenetically regulated miRNAs identified are deregulated in breast cancer-derived cells, including EMT-like alterations, such that the cancer cells expressed normal fibroblast-associated miRNAs (with Futscher lab).

• Showed that we can reproducibly obtain non-clonal immortalized HMEC lines from multiple individuals of different ages using normal unstressed HMEC exposed sequentially to shRNA to p16 or activated cyclin D1/CDK2 fusion protein to bypass the stasis senescence barrier, followed by overexpressed c-Myc to overcome the telomere dysfunction barrier through induction of telomerase. These studies help validate our model of the tumor suppressive senescence barriers encountered by cultured HMEC.

• Showed that non-clonal immortalized lines derived by using shRNA to p16 and overexpressed c-myc do not contain karyotypic abnormalities in early passages, indicating that direct targeting of the senescence barriers can produce immortalization without the need for additional gross chromosomal changes. These results further validate our senescence model as well as our hypothesis that genomic instability per se (as occurs prior to telomere dysfunction) is not necessary for transformation, but serves to produce the required genomic changes. CGH results thus far partially support our hypothesis that that genomic instability is not necessary for transformation per se but is a mechanism to generate the errors that allow overcoming barriers.

• Showed that we can obtain clonal immortalized HMEC lines from multiple individuals of different ages using normal unstressed HMEC exposed either to shRNA to p16 or transduced c-Myc. Clonal lines all exhibited gross genomic alterations as hypothesized, since they needed to generate the errors to overcome either stasis (the Myc-alone cultures) or telomere dysfunction (the p16sh-alone cultures).

• Collaborated with Mark Labarge to analyze lineage markers in HMEC from multiple young and old women. Found that aging is associated with changes in the phenotype of HMEC, with reduced myoepithelial cells and increases in luminal cells expressing keratin 14 and integrin $\alpha 6$, traits expressed exclusively in myoepithelial cells in women under 30. The changes to the luminal lineage were associated with age-dependent expansion of multipotent progenitor cells with differentiation defects.

• Applied this observation of aging-associated shifts in luminal/myoepithelial/multipotent progenitor cells to our transformation protocols, and showed that transformation by p16shRNA or D1/CDK2, then overexpressed c-

Myc, could produce transformed cells with luminal/progenitor lineage markers in HMEC derived from 2 older, but not 2 younger women.

• Characterized the many new transformed cultures generated for a variety of cancer-associated properties and lineage markers. These included AIG, tumorigenicity, CGH and karyology, FACS profiles and IHC and IF analysis of lineage markers. Cell lines with diverse properties have been generated, similar to multiple, but still a limited set, of breast cancer phenotypes in vivo.

REPORTABLE OUTCOMES:

Novak, P, Jensen, TJ, Garbe, JC, Stampfer, MR, Futscher, BW (2009), Step-wise DNA methylation changes are linked to escape from defined proliferation barriers and mammary epithelial cell immortalization, Cancer Res 69:5251-58.

Garbe, JC, Bhattacharya, S, Merchant, B, Bassett, E, Swisshelm, K, Feiler, H, Wyrobek, A, and Stampfer, MR, (2009) Long-term culture of normal pre-stasis human mammary epithelial cells demonstrates the molecular distinctions between stasis and telomere attrition senescence barriers, Cancer Res 69:7557-7568.

Vrba, L, Jensen, TJ, Garbe, JC, Heimark, RL, Cress, AE, Dickinson, S, Stampfer, MR, Futscher, BW (2010) Role for DNA Methylation in the Regulation of miR-200c and miR-141 Expression in Normal and Cancer Cells, PloS ONE 5(1): e8697.

Bishop, CL, Bergin, AH, Fessart, D, Borgdorff, V, Hatzimasoura, E, Garbe, JC, Stampfer, MR, Koh, J, Beach, DH (2010). Primary cilium dependent and independent Hedgehog signaling inhibits p16INK4A. Mol Cell 40, 533–547.

Chanson, L, Brownfield, D, Garbe, JC, Kuhn, I, Stampfer, MR, Bissell, MJ, LaBarge, MA (2011). Self-organization is a dynamic and lineage-intrinsic property of mammary epithelial cells. Proc Nat Acad Sci USA 108:3264-69.

Cipriano, R,, Kan, CE, Graham, J, Danielpour, D, Stampfer, M, Jackson, MW (2011). TGF-ß signaling engages an ATM-CHK2-p53–independent RAS-induced senescence and prevents malignant transformation in human mammary epithelial cells. Proc Nat Acad Sci USA 108:8668-73.

Sherman, MY, Meng, L, Stampfer, M, Gabai, VL, Yaglom, JA (2011). Oncogenes induce senescence with incomplete growth arrest and suppress the DNA damage response. Aging Cell 10:949-961.

Vrba, L, Garbe, JC, Stampfer, MR, Futscher, BW (2011). Epigenetic regulation of normal human mammary cell type specific miRNAs. Genome Res 21:2026-2037.

Garbe, JC, Pelissier, F, Pepin, F, Fridriksdottir, AJ, Sputova, K, Guo, DE, Villadsen, R, Park, M, Petersen, OW, Borowsky, AD, Stampfer, MR, LaBarge, MA. Aging is associated with increased multipotent progenitors with a basal differentiation bias in human mammary epithelia. Cancer Res, in revision.

Garbe, JC, Jackson, MW, Stampfer, MR, Vulnerability of Normal Human Mammary Epithelial Cells to Oncogenic Transformation. DOD BCRP Era of Hope Meeting, June 2008, Baltimore, MD.

Garbe J, Wyrobek, A, Futscher, B, Stampfer, M, A Human Mammary Epithelial Cell System to Study the Reactivation of Telomerase Activity during Carcinogenic Progression. Abstract/poster at AACR conference The Role of Telomeres and Telomerase in Cancer Research, February/March 2010, Ft. Worth TX.

Garbe, JC, Vrba, L, Jackson, MW, LaBarge, M, Futscher, BW, Stampfer, MR, Vulnerability of Human Mammary Epithelial Cells to Oncogenic Transformation, poster and talk, DOD Era of Hope Meeting, August 2011, Orlando FL

Stampfer, MR, LaBarge, M, Garbe, JC, An integrated human mammary epithelial cell (HMEC) system for the study of normal HMEC biology and carcinogenesis, poster and talk, DOD Era of Hope Meeting, August 2011, Orlando FL

Immortal cell lines developed: 184DTERT1, 184DTERT2; 184BeMY1, 184CeMY1; 184DMY3, 184Dp16sMY; 240LMY1, 240Lp16s1, 240Lp16sMY, 240Lp16sMY-N/RF (oncogenic Neu or Raf1); 805Pp16s1, 805Pp16sMY, 805Pp16sMY-N/RF (oncogenic Neu or Raf1); 122LMY1, 122Lp16sMY; 122LD1MY.

CONCLUSIONS:

Breast cancers display great phenotypic and molecular diversity, leading to the characterization of distinct subtypes that show striking differences in prognosis and drug responses. A better understanding of the molecular events that give rise to the different subtypes, as well as experimentally tractable human model systems to test potential therapeutics, could facilitate individualized treatment and possibly prevention. The main variables thought to be responsible for generating this diversity are the identity of breast cancer cell of origin, the pattern of molecular alterations during the transition from normal target cell to malignancy, the influence of micro-environmental factors, and the extent to which phenotypes are influenced by cell of origin vs oncogenic lesions. This grant was designed to elucidate factors that influence transformation of normal HMEC to different subtypes, while generating transformed lines more reflective of the in vivo complexity of breast cancer phenotypes; such lines would also provide new cellular reagents for dissemination to the research community.

The approach built upon our previous 30 years work in developing a unique experimentally tractable in vitro model of human breast carcinogenesis. During the course of this project, we have been successful in achieving many of our aims and making many novel and significant discoveries. Using our previously developed low stress medium, we could show that the multiple normal HMEC types (luminal, myoepithelial, progenitor) could be propagated and FACS-enriched, and made novel discoveries about the effects of aging on lineage representation that may help explain the observed age-increased incidence of the luminal breast cancer subtype. This understanding in turn led to our (we believe first) development of in vitro transformed HMEC possessing luminal phenotypes, using in vivo relevant pathological agents and starting with cells from older women. Most exciting, we showed that the use of overexpressed cyclin D1/CDK2 could in vitro, as in vivo, lead to transformed cells with luminal phenotypes. Based on our model of the tumor suppressive senescence barriers, we developed a method that could readily immortally transform HMEC from all women tested by directly targeting the two major senescence barriers – stasis (bypassed by shRNA to p16 or D1/CDK2) and telomere dysfunction (bypassed by overexpressed c-Myc); addition of one oncogene (e.g., Neu) could then confer malignant transformation. From these studies many new transformed lines with varied and unique properties have been generated. These lines were characterized by CGH, karyology, expression of lineage and EMT markers, and other properties. These studies led to the novel finding, confirming our previous hypothesis that genomic instability served to generate cancer causing errors but was not necessary per se, that direct targeting of the senescence barriers could generate lines without gross genomic errors. We confirmed our initial hypothesis that normal HMEC grown in a low stress medium, or prevented from inducing p16, the mediator of the stress response, are more vulnerable to c-Myc and TERT immortalization than stress-exposed HMEC. We were unable to explain the molecular basis of this difference, but did generate novel data examining the epigenetic properties of the hTERT gene locus that showed that differences in basal or induced hTERT expression were

not correlated with the epigenetic state of this gene locus. We have shown that different pathways to transformation are associated with different molecular properties, such as gene expression, epigenetic alterations, and lineage markers, opening the possibility of individualized therapy for these distinct means of becoming malignant. We showed that epigenetic and gene expression changes associated with breast cancer cells can occur very early in the transformation process, and that immortalization is associated with large scale epigenetic reprogramming. We have generated and already provided these new HMEC resources to many other labs worldwide. We are now in a position to test the effects of specific oncogenic perturbations on FACS-enriched different putative HMEC progenitor cell types, to determine if we can identify cells of origin and better model the diverse pathways that lead to the diversity of breast cancer subtypes seen in vivo. However, this grant was not renewed and we currently have no funding to proceed with this work.

REFERENCES:

Brenner, A. J., Stampfer, M. R., and Aldaz, C. M. Increased p16INK4a expression with onset of senescence of human mammary epithelial cells and extended growth capacity with inactivation. Oncogene, 17: 199-205, 1998.

Chanson, L, Brownfield, D, Garbe, JC, Kuhn, I, Stampfer, MR, Bissell, MJ, LaBarge, MA. Self-organization is a dynamic and lineage-intrinsic property of mammary epithelial cells. Proc Nat Acad Sci USA 108:3264-69. 2011

Chin, K, Ortiz de Solorzano, C, Knowles, D, Jones, A, Chou, W, Rodriguez, E, Kuo, W-L, Ljung, B-M, Chew, K, Krig, S, Garbe, J, Stampfer, M, Yaswen, P, Gray, JW, Lockett, SJ. In situ analysis of genome instability in breast cancer. Nature Genetics 36:984-988. 2004

Chytil, A, Waltner-Law, M, West, R, Friedman, D, Aakre, M, Barker, D, Law, B. Construction of a Cyclin D1-Cdk2 Fusion Protein to Model the Biological Functions of Cyclin D1-Cdk2 Complexes, J Biol Chem 279, 47688–47698. 2004

Garbe J, Wong M, Wigington D, Yaswen P, Stampfer MR. Viral oncogenes accelerate conversion to immortality of cultured conditionally immortal human mammary epithelial cells. Oncogene 18:2169-80. 1999

Garbe, J, Holst, CR, Bassett, E, Tlsty, T, Stampfer, MR, Inactivation of p53 Function in Cultured Human Mammary Epithelial Cells Turns the Telomere-Length Dependent Senescence Barrier from Agonescence into Crisis. Cell Cycle 6:1927-1936, 2007.

Garbe, JC, Bhattacharya, S, Merchant, B, Bassett, E, Swisshelm, K, Feiler, H, Wyrobek, A, and Stampfer, MR, Long-term culture of normal pre-stasis human mammary epithelial cells demonstrates the molecular distinctions between stasis and telomere attrition senescence barriers, Cancer Res 69:7557-7568, 2009.

Garbe, JC, Pelissier, F, Pepin, F, Fridriksdottir, AJ, Sputova, K, Guo, DE, Villadsen, R, Park, M, Spellman, P, Barowsky, A, O.W., P, Stampfer, MR, Labarge, MA. Aging associated changes in human mammary gland progenitor fate decisions generate luminal cells with basal characteristics. Cancer Res, in revision.

Hammond, S. L., Ham, R. G., and Stampfer, M. R. Serum-free growth of human mammary epthelial cells: Rapid clonal growth in defined medium and extended serial passage with pituitary extract. Proc. Natl. Acad. Sci. USA, 81: 5435-5439, 1984.

Keller, PJ, Arendt, LM, Skibinski, A, Logvinenko, T, Klebba, I, Dong, S, Smith, AE, Prat, A, Perou, CM, Gilmore, H, Schnitt, S, Naber, SP, Garlick, JA, Kuperwasser, C. Defining the cellular precursors to human breast cancer Proc. Natl. Acad. Sci. USA: 109:2772-77, 2012.

Li Y, Pan J, Li J-L, Lee J-H, Tunkey C, Saraf K, Garbe JC, Whitley MZ, Jelinsky SA, Stampfer MR, Haney SA. Transcriptional changes associated with breast cancer occur as normal human mammary epithelial cells overcome senescence barriers and become immortalized. Mol Cancer 6:7. 2007

Novak, P, Jensen, TJ, Garbe, JC, Stampfer, MR, Futscher, BW, Step-wise DNA methylation changes are linked to escape from defined proliferation barriers and mammary epithelial cell immortalization, Cancer Res 69:5251-58, 2009.

Perou, C. M., Sorlie, T., Eisen, M. B., van de Rijn, M., Jeffrey, S. S., Rees, C. A., Pollack, J. R., Ross, D. T., Johnsen, H., Akslen, L. A., Fluge, O., Pergamenschikov, A., Williams, C., Zhu, S. X., Lonning, P. E., Borresen-

Dale, A. L., Brown, P. O., and Botstein, D. Molecular portraits of human breast tumours. Nature, 406*:* 747-752, 2000.

Possemato, R, Marks, KM, Shaul, YD, et al., Functional genomics reveal that the serine synthesis pathway is essential in breast cancer, Nature 576, 346–350, 2011.

Romanov, SR, Kozakiewicz, K, Holst, CR, Stampfer, MR, Haupt, LM, Tlsty, TD, Normal human mammary epithelial cells spontaneously escape senescence and acquire genomic changes, Nature 409:633-637, 2001.

Stampfer, M.R., Isolation and Growth of Human Mammary Epithelial Cells. J. Tissue Culture Methods 9:107-116, 1985.

Stampfer, MR and Bartley, JC, Induction of transformation and continuous cell lines from normal human mammary epithelial cells after exposure to benzo(a)pyrene. Proc. Natl. Acad. Sci. USA, 82*:* 2394-2398, 1985.

Stampfer, MR and Bartley, JC, Human mammary epithelial cells in culture: Differentiation and transformation. *In:* R. Dickson and M. Lippman (eds.), Breast Cancer: Cellular and Molecular Biology, pp. 1-24. Norwall, MA: Kluwer Academic Publishers, 1988.

Stampfer, MR, Garbe, J, Levine, G, Lichtsteiner, S, Vasserot, AP, Yaswen, P, hTERT expression can induce resistance to TGFß growth inhibition in $p16^{INK4A}$(-) human mammary epithelial cells, Proc Natl Acad Sci (USA) 98:4498-4503, 2001.

Stampfer MR, Garbe J, Nijjar T, Wigington D, Swisshelm K, Yaswen P. Loss of p53 function accelerates acquisition of telomerase activity in indefinite lifespan human mammary epithelial cell lines. Oncogene 22:5238-51. 2003

Vrba, L, Jensen, TJ, Garbe, JC, Heimark, RL, Cress, AE, Dickinson, S, Stampfer, MR, Futscher, BW. DNA Methylation Control of Normal Cell-Type Specific Expression of *miR-200c*, PloS ONE 5(1): e8697. 2010

Vrba, L, Garbe, JC, Stampfer, MR, Futscher, BW. Epigenetic regulation of normal human mammary cell type specific miRNAs. Genome Res 21:2026-2037. 2011

PERSONEL

James Garbe, Ph.D.

Martha Stampfer, Ph.D.

Figure 1. Derivation of our transformed HMEC cultures. Primary cultures derived from reduction mammoplasties (RM), milk (MK) or non-tumor mastectomy tissues (P) were initiated in three different types of medium. Unperturbed cells grown in any of our serum-containing medium (panels A&C below) all ceased proliferation at the stasis barrier. Exposure of pre-stasis cultures to various oncogenic agents (red below) induced cells to overcome or bypass stasis and become post-stasis by different means. Further alterations were required to overcome the telomere dysfunction barrier, gain telomerase expression, and become immortal. Cells grown in low stress media (C) were most vulnerable to transformation following transduction of p16shRNA and/or c-Myc, or hTERT. The differing pathways from normal to immortal/malignant are associated with distinct molecular properties/alterations.

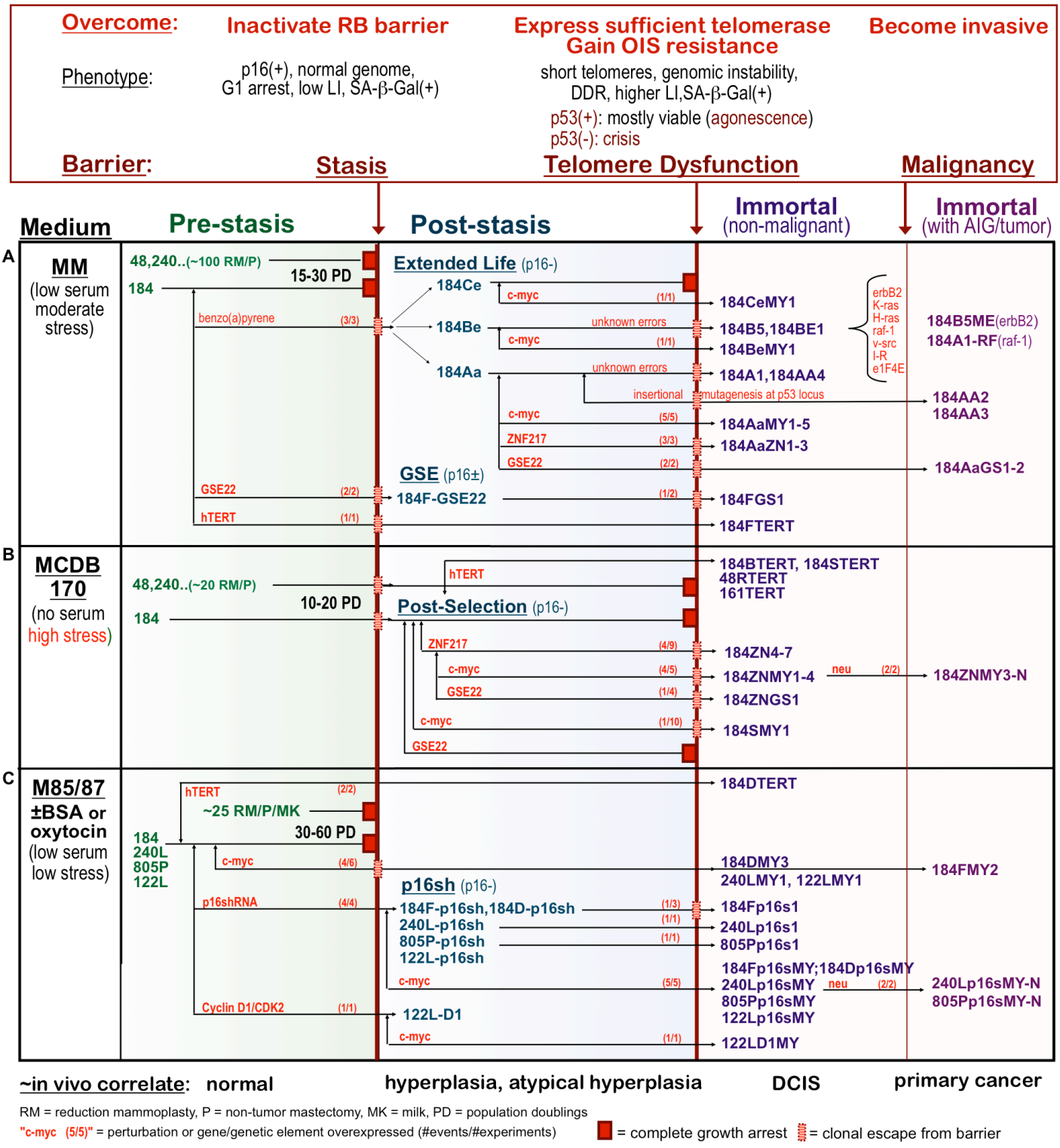

Figure 2. HMEC lineages change as a function of age. (A) FACS analyses of CD227 and CD10 expression in passage 4 strains from one woman <30years (195L) and one >55years (805P). FACS plots are shown as 5% contour plots with outliers identified, at left are isotype antibody controls and at right the CD10 and CD227 stained samples. (B) Linear regression showing changes in proportions of LEP and MEP in HMEC strains at 4p as a function of age (n=36 individuals). RM = reduction mammoplasty-derived, P = non-tumor mastectomy-derived. (C) FACS analyses from the corresponding uncultured dissociated epithelial organoids. (D) Linear regression of proportions of LEP and MEP in dissociated uncultured organoids as a function of age (n=8). (E) Histograms of CD49f (integrin α6) expression by FACS analysis of isotype negative control staining (gray lines), CD227+ LEP (green lines) and CD10+ MEP (red lines) from dissociated organoids. The gray-colored shaded boxes indicate the threshold at which there is little or no CD49f expression. (F) Regression analysis of Log_2 change in mean expression of CD49f in LEP normalized to the levels in MEP from dissociated organoids as a function of age (n=8). (Garbe et al. submitted)

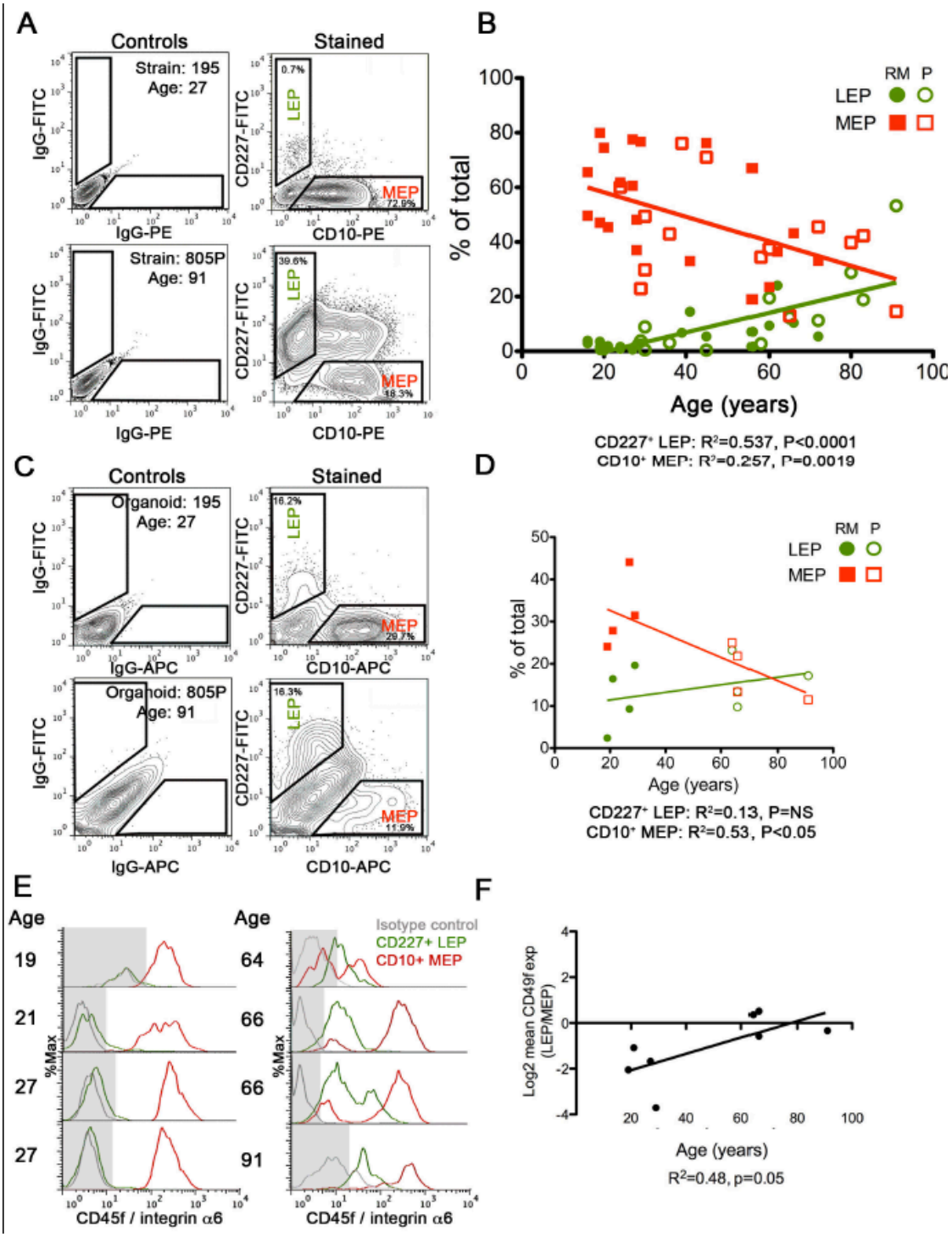

Figure 3. Proportions of cKit+ HMEC, putative multipotent progenitors, increase with age. (A) Changes in proportions of LEP and cKit$^+$ cells in three representative HMEC strains as a function of passage. (B) Linear regression of proportions of cKit$^+$ HMEC in strains at 4p as a function of age (n=36). (C) Linear regression of proportions of cKit$^+$ cells in dissociated uncultured organoids as a function of age (n=29). (D) FACS plot showing the gating logic used for sorting cKit$^+$ HMEC from strain 122L at 4p. Inset shows the LEP and MEP distribution at 4p. (E) FACS analysis of strain 122L at 8p. (F) FACS analysis of cKit-enriched-derived cultures at 8p. (G) Phase images of representative structures derived from cKit$^+$ (left) and cKit$^-$ (right) cells cultured in laminin-rich basement membrane for 14 days. (H) Immunofluorescence on a transverse frozen section that shows K14 (red) and K19 (green) protein expression in a duct of a cKit$^+$-derived structure. Nuclei were stained with DAPI (blue), and the three-color merged image is shown at right. (Garbe et al. submitted)

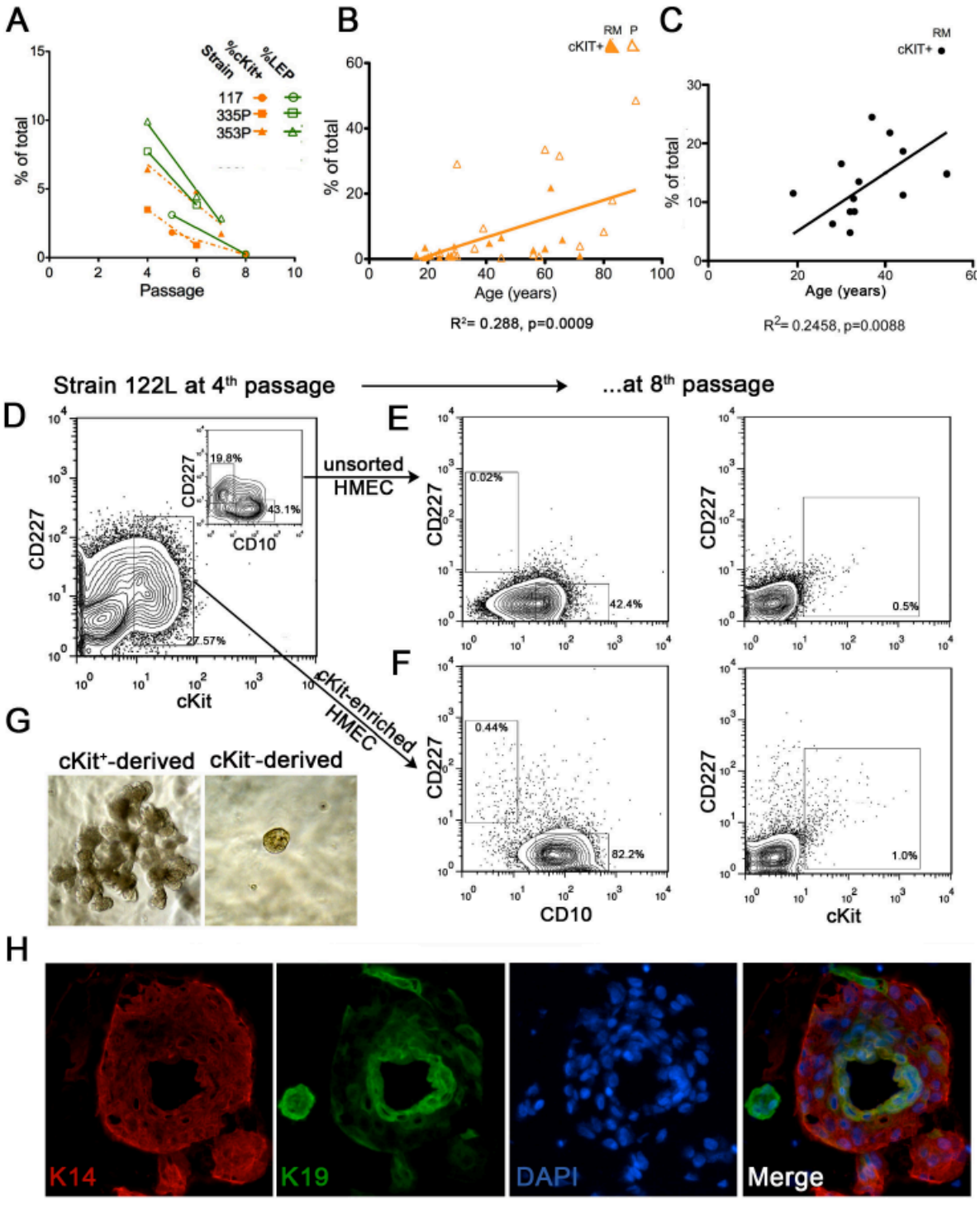

Figure 4A. Growth curve of 184D HMEC transduced with hTERT at 3p or 10p. HMEC were grown in M87A+X medium and transduced with hTERT retrovirus or empty vector and selected with puromycin. Population doublings were calculated for each passage and plotted vs time in culture.

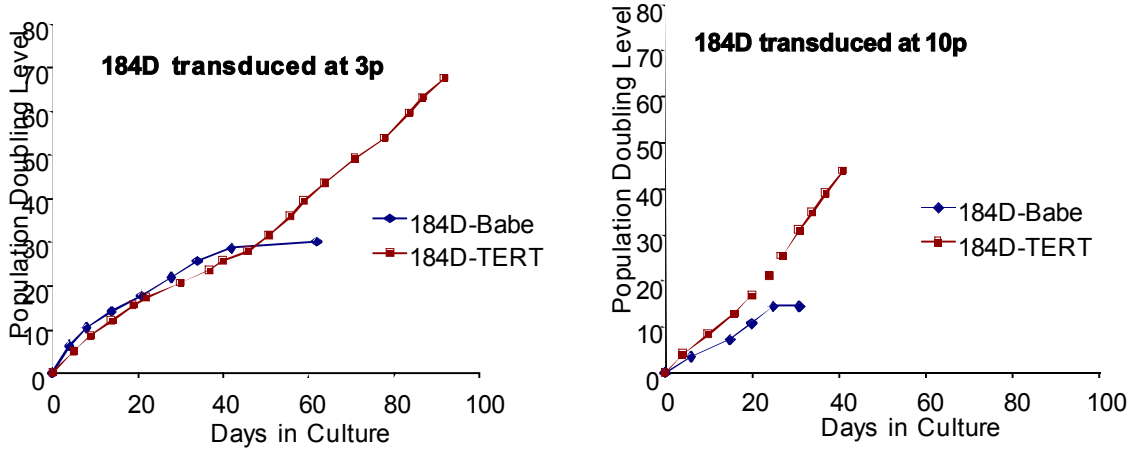

Figure 4B: p16 responsiveness of pre-stasis and immortalized HMEC. qPCR analysis of RNAi mediated knockdown of the negative regulator of p16 expression, BMI1, and resultant changes in p16 mRNA levels in finite pre-stasis (184D, 48RT), hTERT immortalized (184DTERT, 184BTERT, 184FTERT), p53(-) immortal (184FGS1), and myc-immortalized (184FMY2) HMEC. Top panel shows the level of BMI1 knockdown; bottom panel shows resulting effect on p16 expression.

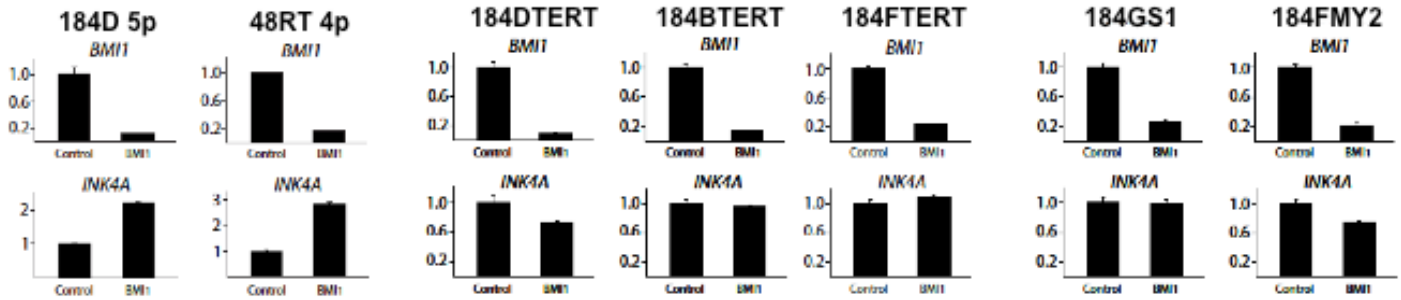

Figure 5. Effect of c-Myc on post-stasis HMEC growth and TRAP activity. A. Post-stasis post-selection 184B HMEC were grown in MCDB 170 and transduced with a c-Myc containing retrovirus (LXSN) or empty vector control at 7p. All cells ceased proliferation at agonescence (15p). Post-selection 184S HMEC were transduced with c-Myc (LXSN) at 15p, and growth ceased at 22p. No significantly increased TRAP activity was seen following c-Myc transduction. Similar results (not shown) were seen with post-stasis post-selection HMEC from specimen 48R. In some TRAP assays, heat-treated controls (+) were run next to unheated (-) samples. Positive TRAP control samples are indicted by "+". (Garbe et al. in prep)

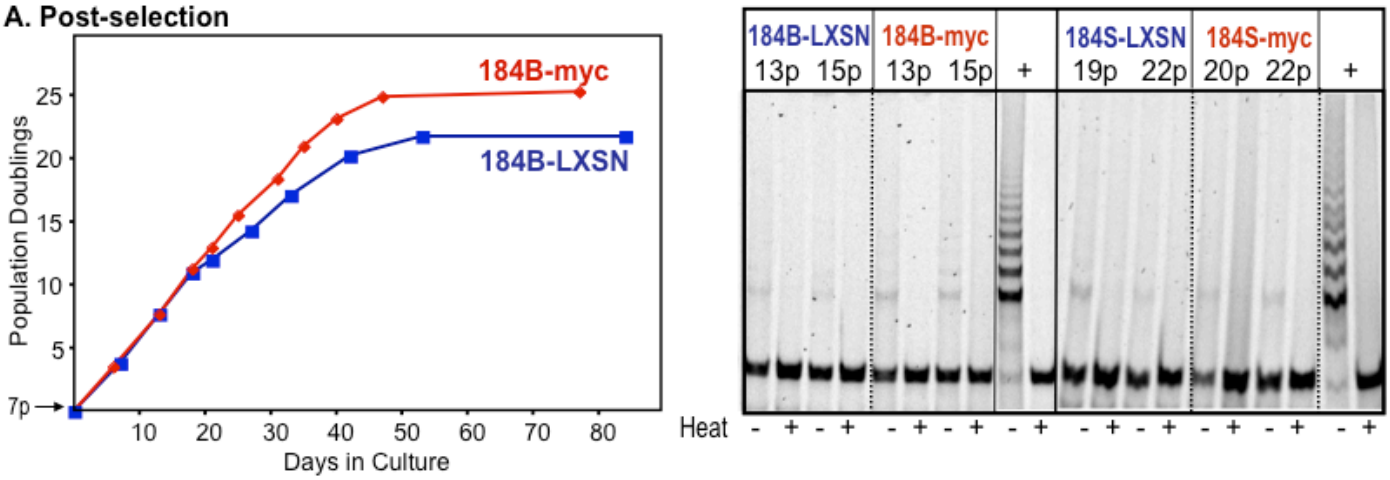

Figure 5B. Post-stasis EL 184Aa, 184Be, and 184Ce HMEC were grown in MCDB 170 and transduced with a c-Myc containing retrovirus (LXSN/pBabe–hygro(BH2)) or empty vector at the indicated passages. All control cells ceased proliferation at agonescence while c-Myc-transduced populations maintained ongoing proliferation indefinitely, associated with increased TRAP activity. Proliferative control 184Ce, but not 184Aa, expressed low TRAP activity.

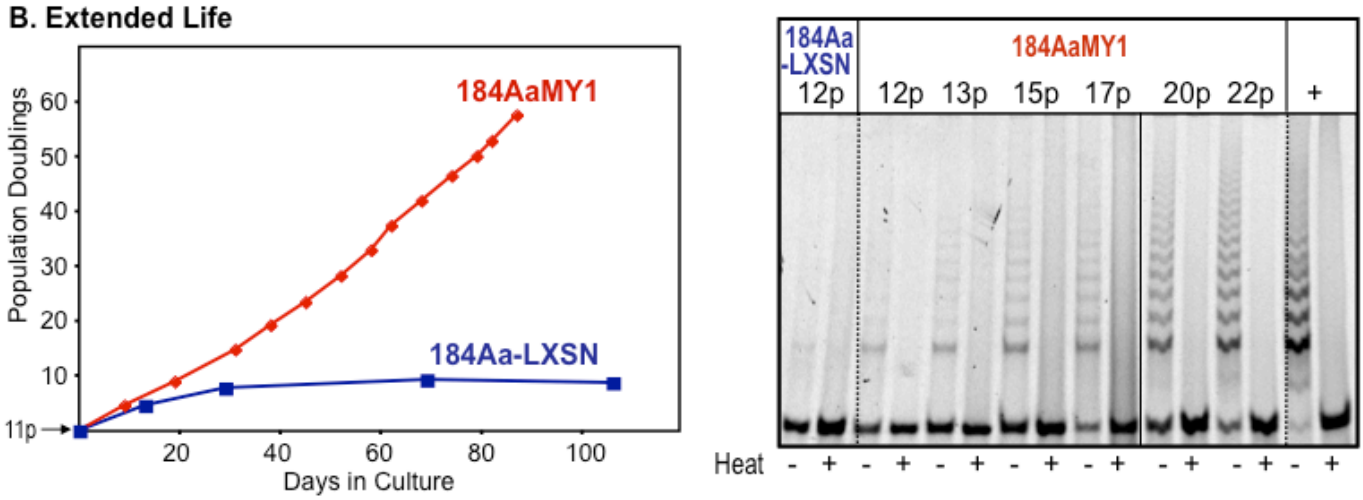

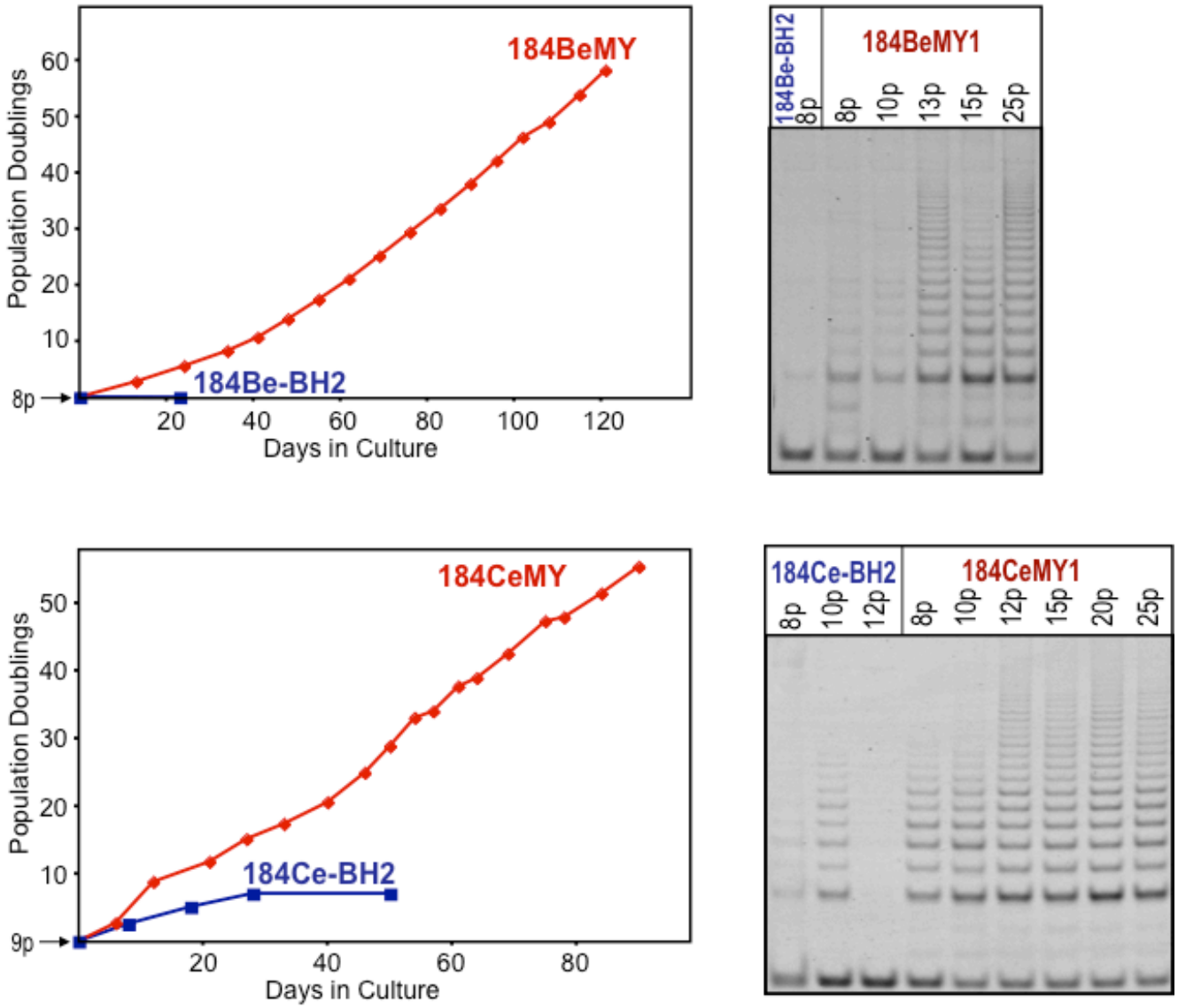

Figure 5C. Growth of HMEC after transduction of p16shRNA/D1/CDK2, followed by c-Myc. Pre-stasis 184D (A), 240L (B), 805P (C), and 122L (D) HMEC were grown in M87A+CT+X and 184F (E) grown in M85 and transduced at 3p or 4p with a p16shRNA expressing retrovirus, or cyclin D1 containing lentivirus, or empty vector. At the next passage, cultures ±p16sh or D1 were transduced with c-Myc or vector control. Cells transduced with p16sh or D1 alone bypassed stasis and ceased growth at agonescence, with rare clonal immortalization at agonescence. Cells transduced with c-Myc alone ceased growth at stasis, with rare clonal escape from stasis leading to immortalized lines. The post-stasis cultures transduced with c-Myc maintained growth indefinitely, associated with increased TRAP activity. Control cultures transduced with empty vectors ceased growth at stasis. Proliferative pre-stasis 184, but not 240L, shows low TRAP activity; p16sh transduction slightly increased TRAP activity. c-Myc alone increased TRAP activity in proliferative pre-stasis populations, while further increased activity was seen in immortalized lines.

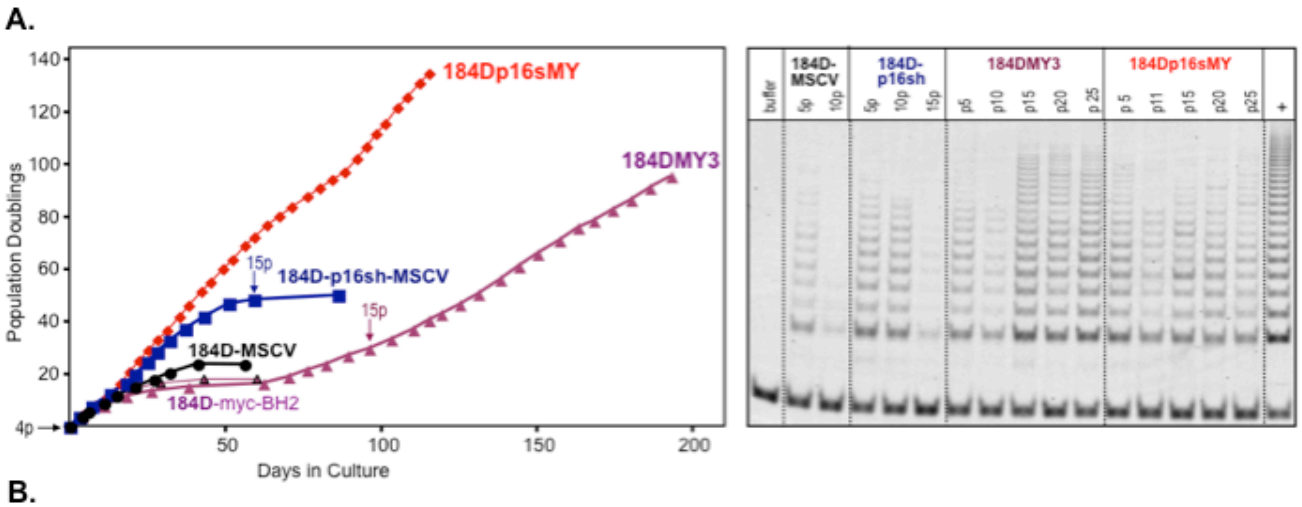
A.
184Dp16sMY
184DMY3
15p
184D-p16sh-MSCV
15p
184D-MSCV
184D-myc-BH2
4p
Population Doublings
Days in Culture
buffer
184D-MSCV
184D-p16sh
184DMY3
184Dp16sMY
5p
10p
15p
p5
p10
p15
p20
p25
+

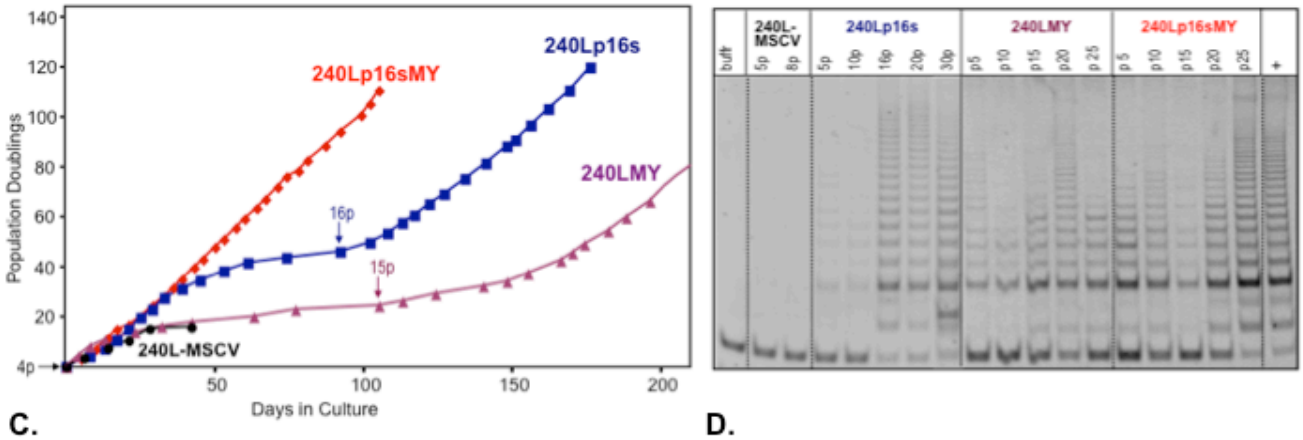
B.
240Lp16sMY
240Lp16s
240LMY
16p
15p
240L-MSCV
4p
Population Doublings
Days in Culture
buffr
240L-MSCV
240Lp16s
240LMY
240Lp16sMY
5p
6p
10p
16p
20p
30p
+

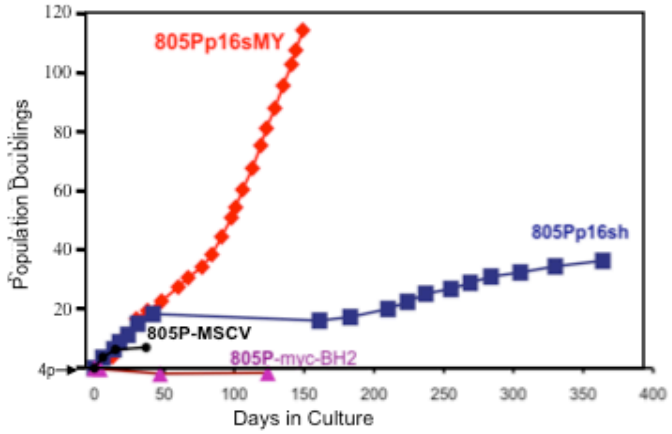
C.
805Pp16sMY
805Pp16sh
805P-MSCV
805P-myc-BH2
Population Doublings
Days in Culture

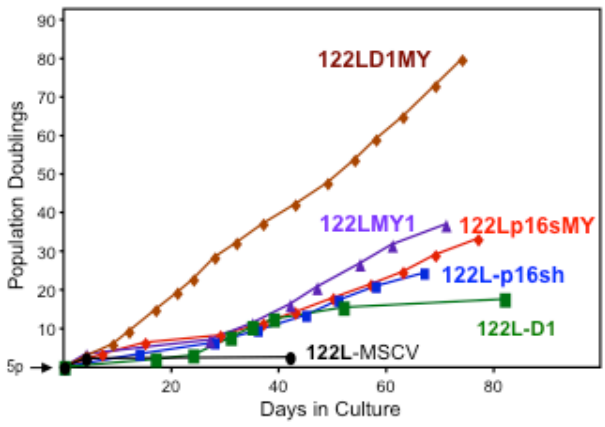
D.
122LD1MY
122LMY1
122Lp16sMY
122L-p16sh
122L-D1
122L-MSCV
5p
Population Doublings
Days in Culture

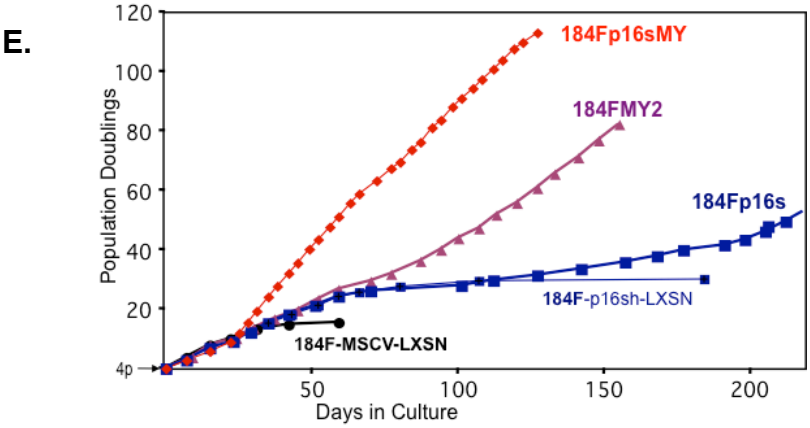
E.
184Fp16sMY
184FMY2
184Fp16s
184F-p16sh-LXSN
184F-MSCV-LXSN
4p
Population Doublings
Days in Culture

Figure 6. DNA methylation and histone modification analysis of hTERT promoter. Upper and middle sections show H3K4me3 and H3K27me3 ChIP-chip data obtained by ChIP linked to tiling microarray hybridization. The permissive H3K4me3 mark is generally absent in all analyzed samples, while the promoter is more or less occupied by polycomb specific repressive H3K27me3 mark in all analyzed samples. The bottom section shows DNA methylation data, analyzed using 5-methylcystosine specific DNA immunnoprecipitation coupled to tiling microarray hybridization. The locus is mostly methylated in all samples. Two short sections (DMR and TSS) indicated by brown rectangles were analyzed at higher resolution by MassARRAY, showing that the transcription start section (TSS) of all but some cancer cell line samples is unmethylated. The small black rectangles above the heatmap indicate positions of individual microarray probes. The line below with the vertical bars on it indicates positions of individual CpG dinucleotides. The CpG island is marked in green. The 5' part of the hTERT gene is in blue. (Garbe et al. in prep)

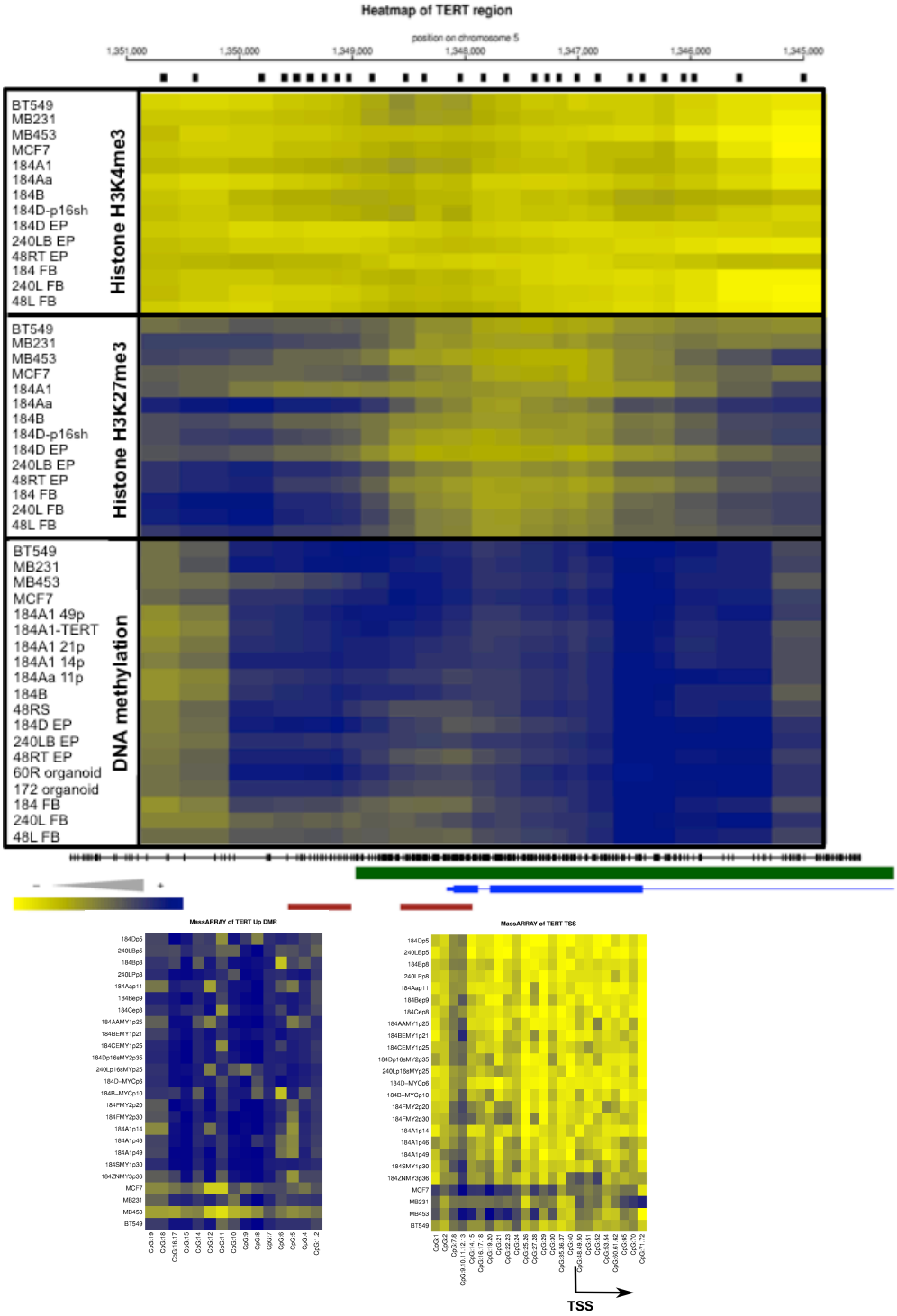

Figure 7. Gene transcript profiles. (A) Heatmap of the top 100 probe-sets (of 11,000) for genes that are differentially expressed between growing post-stasis post-selection vs EL HMEC. (B) Selected probe-sets from the top 100 differentially expressed genes (in A) were examined across pre-stasis, post-stasis EL and post-selection, immortal, and tumor-derived HMEC. (Garbe et al. in prep)

A.

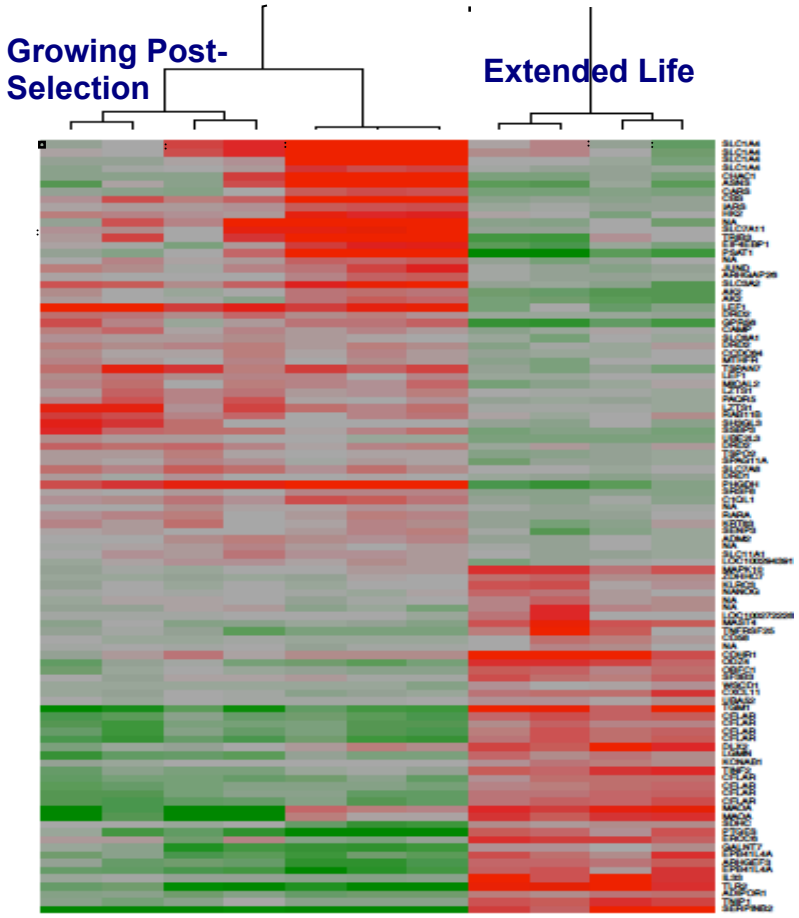

B

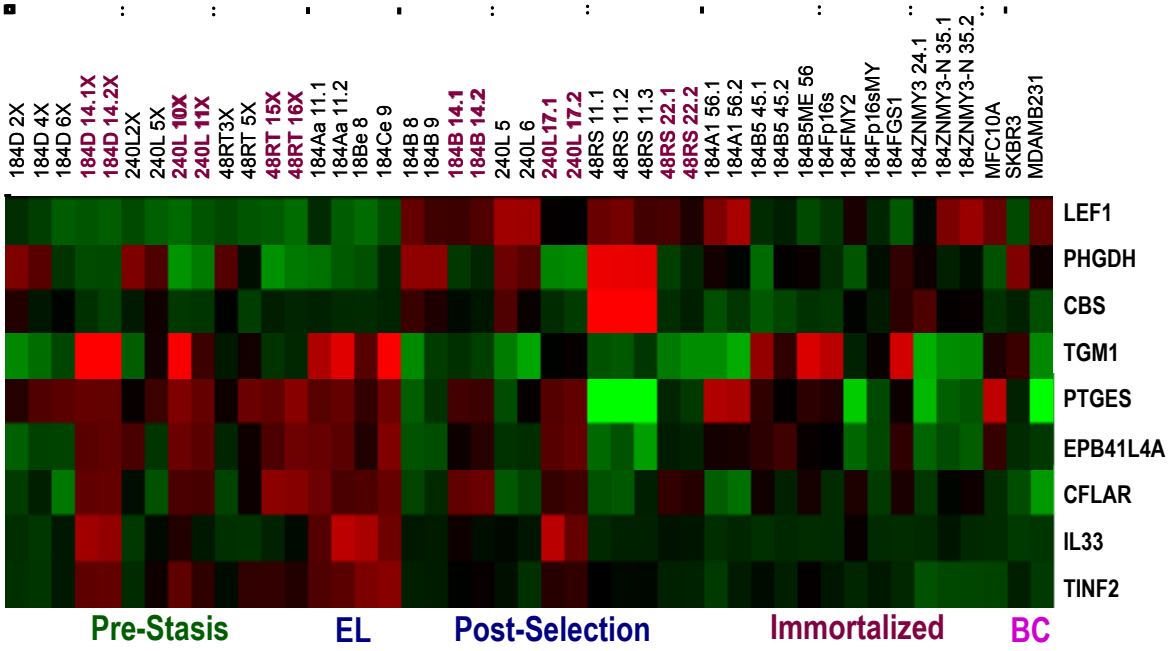

.
Figure 8. Characterization of HMEC following exposure of pre-stasis HMEC to p16shRNA or cyclin D1/CDK2 fusion protein, followed by c-Myc, and further by oncogenic HER2 (neu, to 805Pp16sMY). Note the uniform expression of K19 in the 122L cells exposed to the D1/CDK2 construct. (Garbe et al. in prep, unpublished)

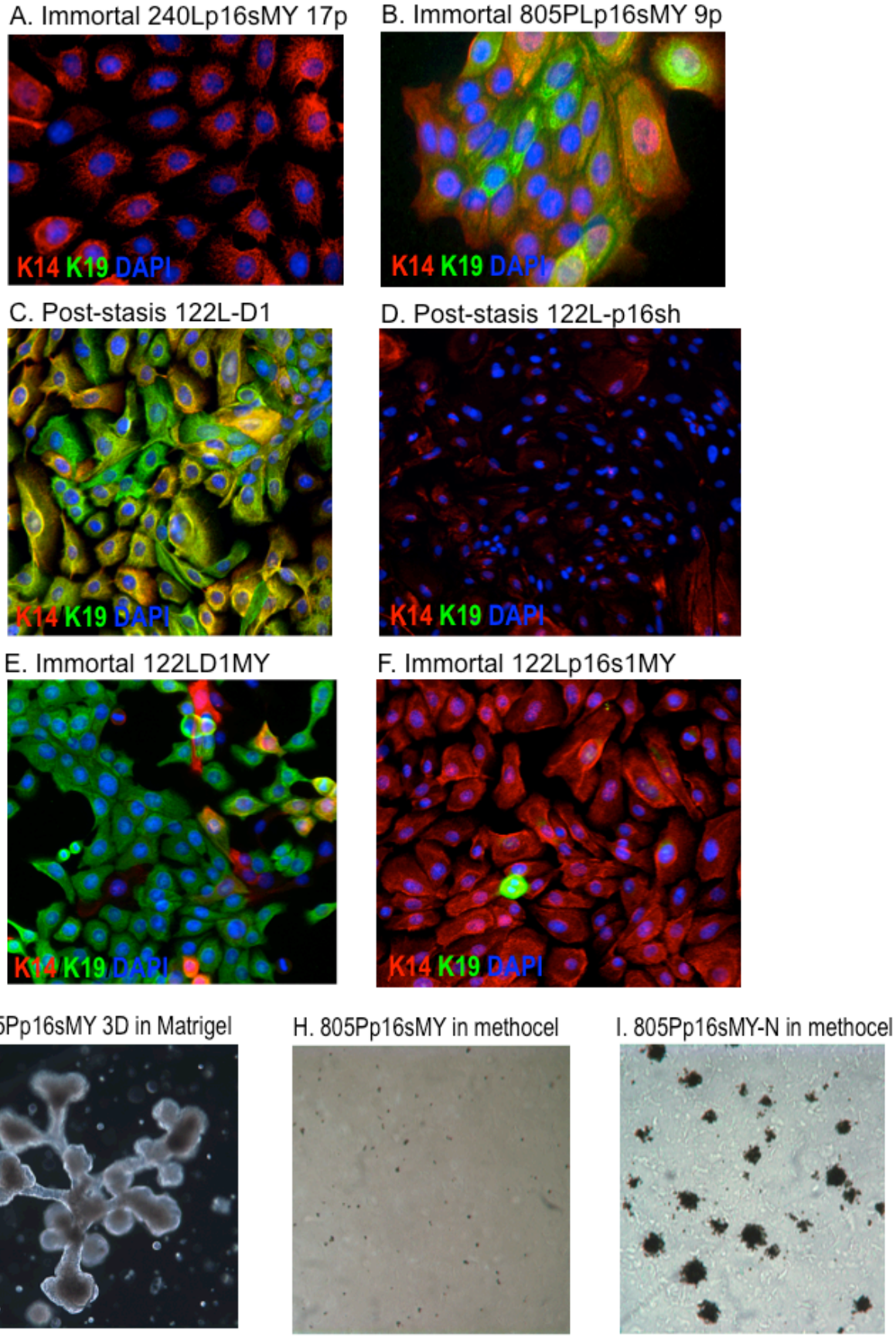

Figure 9. FACS analysis of some of the immortalized lines generated from pre-stasis HMEC grown in low stress media. Cells were analyzed on a FACS-Vantage under sterile conditions. See Fig 1 for derivation of lines. (Garbe et al. in prep)

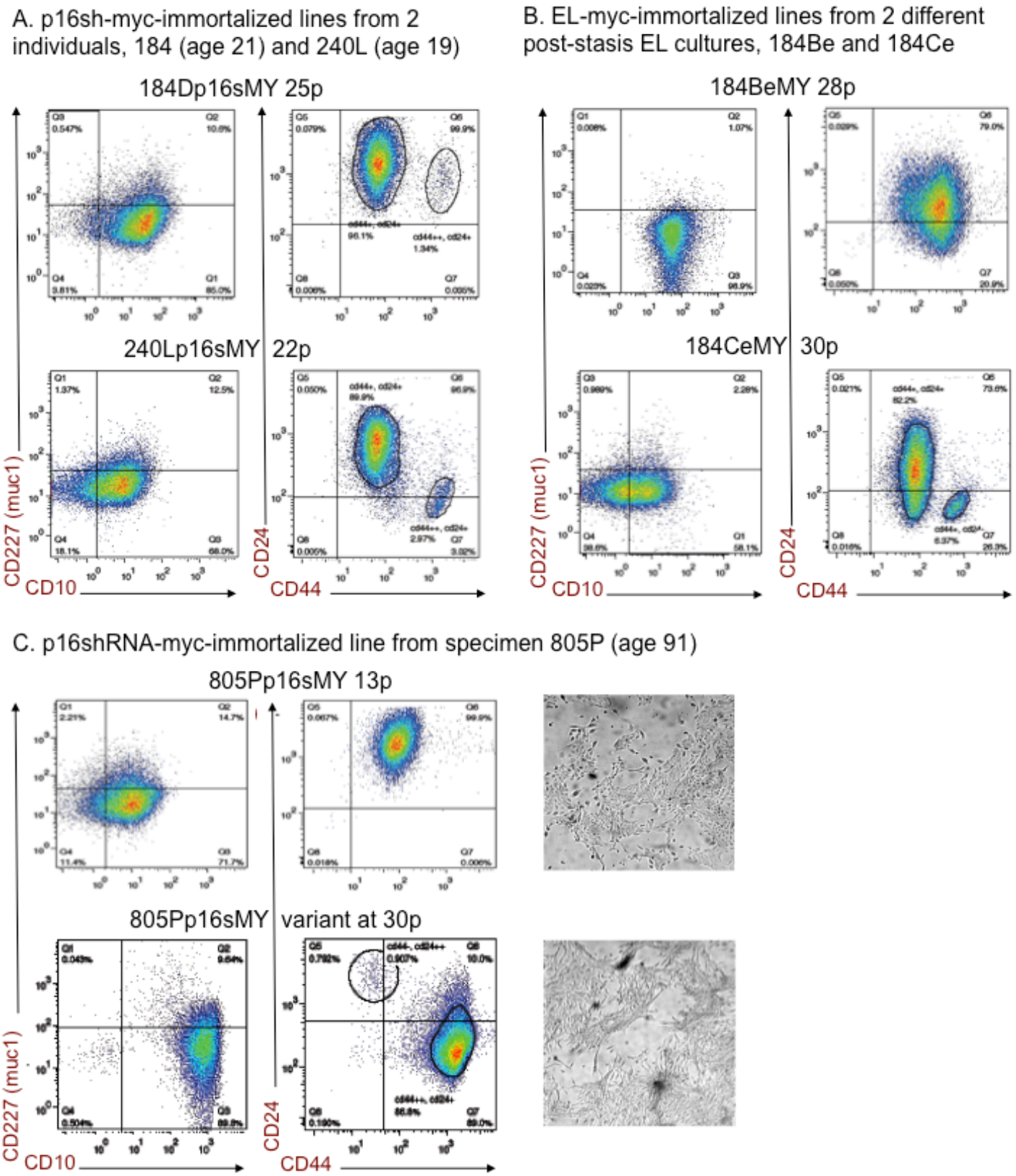

Figure 10. Characterization of two distinct Myc-immortalized lines from pre-stasis HMEC from specimen 184. The 184FMY2 line expresses AIG and markers of EMT, including a $CD44^{hi}/CD24^{lo}$ profile. The 184DMY3 line lacks AIG, but may contain two distinct clones, one of which expresses high p16 levels (possibly is RB-). (Garbe et al. in prep, Vrba et al. 2010, unpublished)

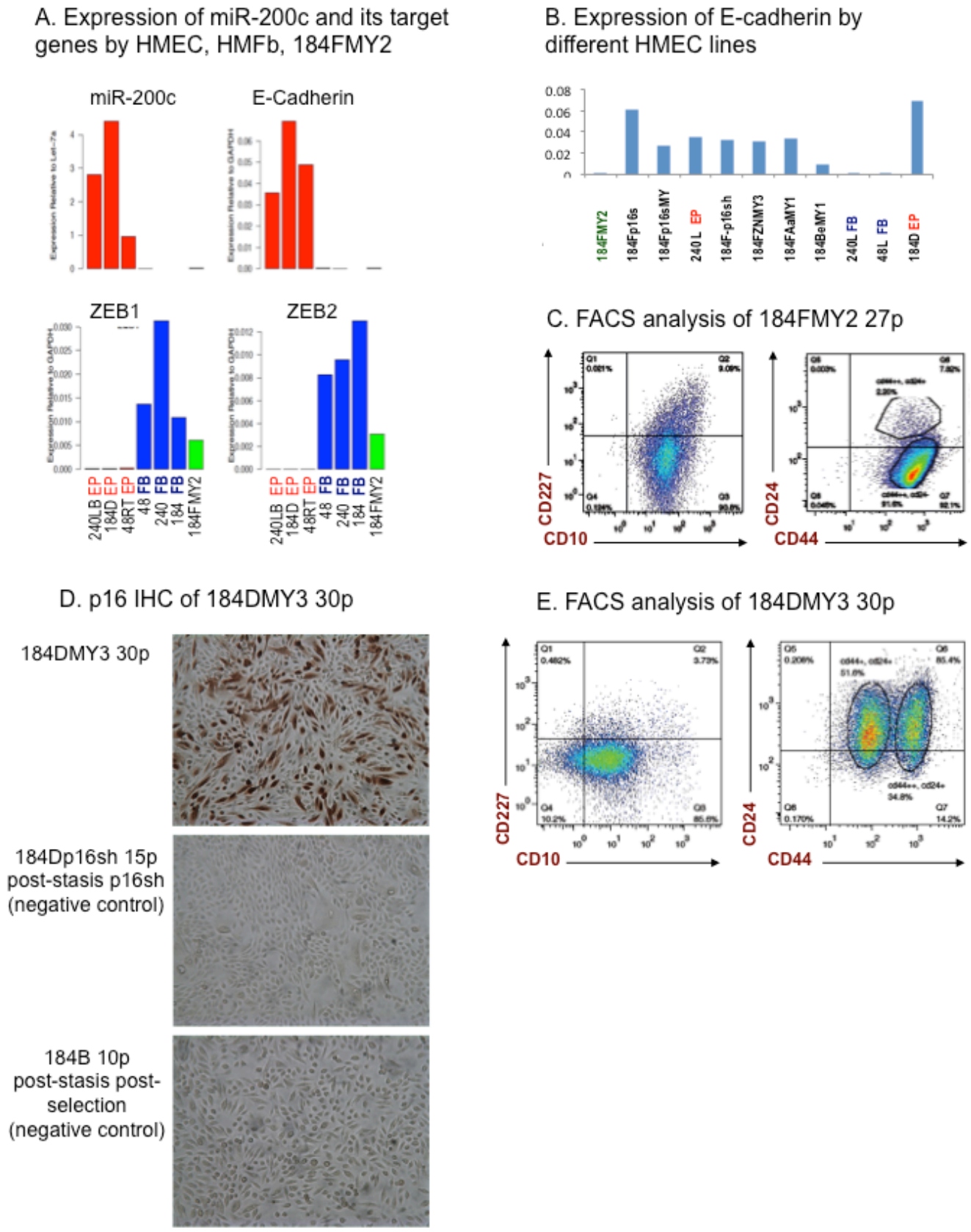

Figure 11. aCGH analysis of clonal and non-clonal HMEC lines. CGH was performed using the Agilent human genome microarray with 44,000 probes/array. The older 184F series were assayed using 2428 probes. (Garbe et al. in prep)

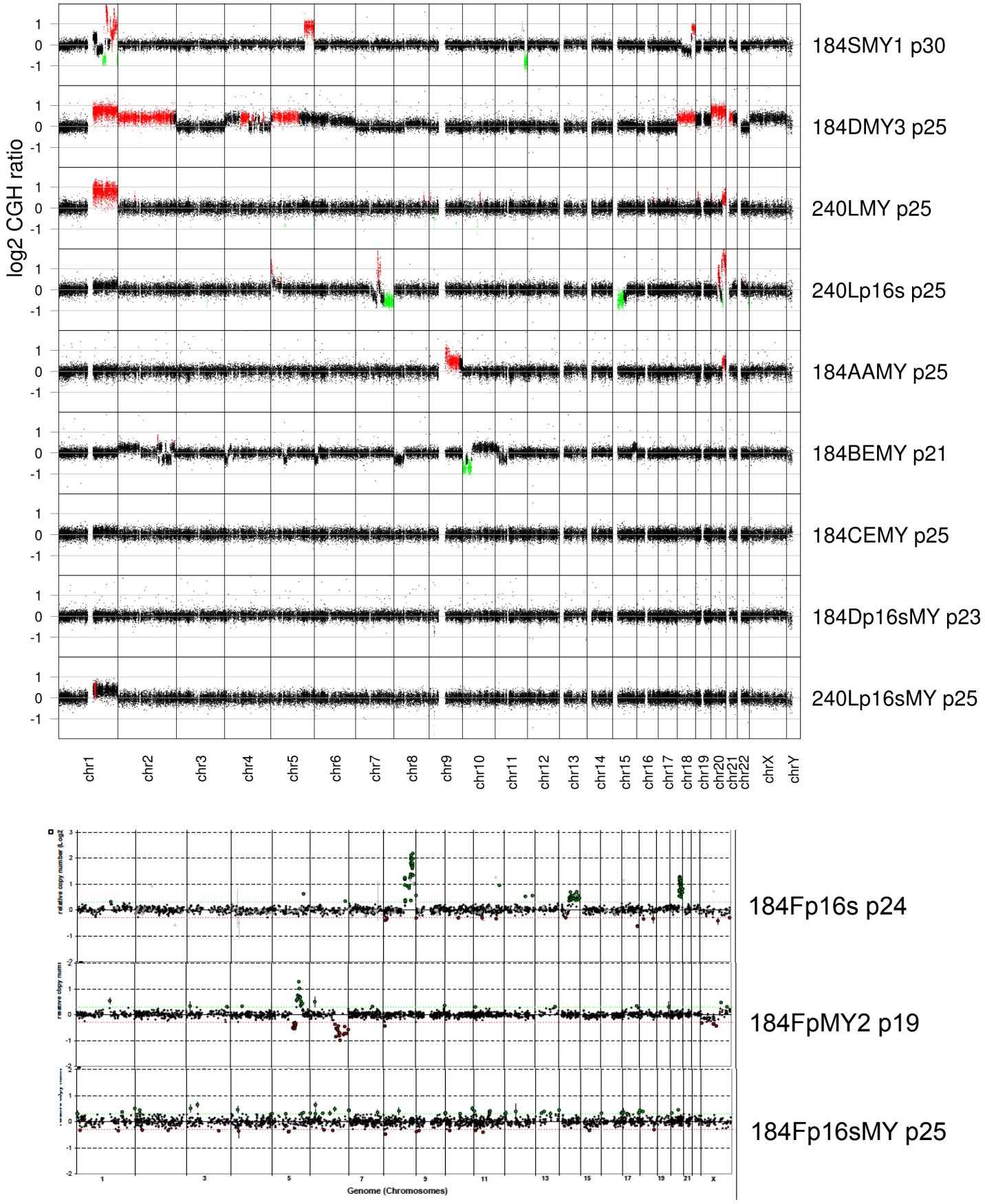

Figure 12. Differentially methylated regions (DMR) in cultured HMEC.
A. HOXA gene cluster shows progressive promoter methylation with transition from normal finite to post-stasis, immortal, and malignant cells. (Novak et al. 2009)

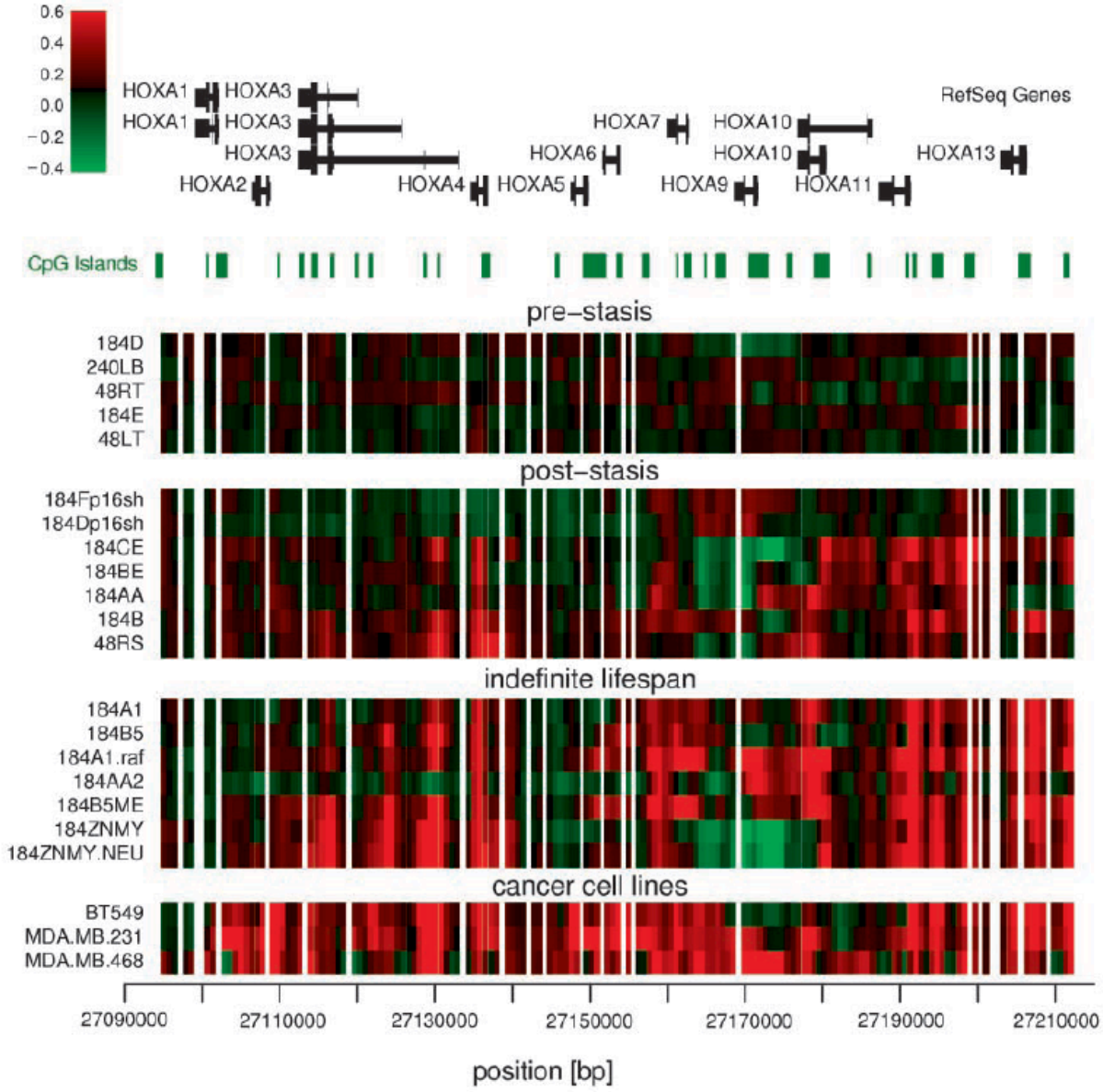

B.Venn diagrams showing common and unique DMR in HMEC at different stages in malignant progression. The different post-stasis types differ in their methylation patterns, with post-selection HMEC exhibiting many DMR, even more than the non-clonal myc-immortalized EL lines.

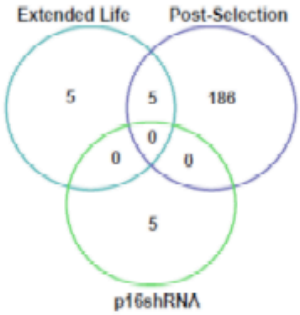

Comparison of DMR in different post-stasis types

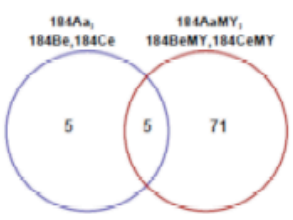

Comparison of DMR in post-stasis EL vs. Myc-immortalized EL cultures

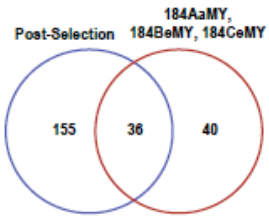

Comparison of DMR in post-stasis post-selection vs. Myc-immortalized EL cultures

Comparison of DMR in post-stasis vs. immortal and malignant lines

Published Online First on June 9, 2009 as 10.1158/0008-5472.CAN-08-4977

Research Article

Stepwise DNA Methylation Changes Are Linked to Escape from Defined Proliferation Barriers and Mammary Epithelial Cell Immortalization

Petr Novak,[1,4] Taylor J. Jensen,[1,2] James C. Garbe,[3] Martha R. Stampfer,[1,3] and Bernard W. Futscher[1,2]

[1]Arizona Cancer Center and [2]Department of Pharmacology and Toxicology, College of Pharmacy, The University of Arizona, Tucson, Arizona; [3]Life Sciences Division, Lawrence Berkeley National Laboratory, Berkeley, California; and [4]Biology Centre ASCR, v.v.i., Institute of Plant Molecular Biology, Ceske Budejovice, Czech Republic

Abstract

The timing and progression of DNA methylation changes during carcinogenesis are not completely understood. To develop a timeline of aberrant DNA methylation events during malignant transformation, we analyzed genome-wide DNA methylation patterns in an isogenic human mammary epithelial cell (HMEC) culture model of transformation. To acquire immortality and malignancy, the cultured finite lifespan HMEC must overcome two distinct proliferation barriers. The first barrier, stasis, is mediated by the retinoblastoma protein and can be overcome by loss of $p16^{INK4A}$ expression. HMEC that escape stasis and continue to proliferate become genomically unstable before encountering a second more stringent proliferation barrier, telomere dysfunction due to telomere attrition. Rare cells that acquire telomerase expression may escape this barrier, become immortal, and develop further malignant properties. Our analysis of HMEC transitioning from finite lifespan to malignantly transformed showed that aberrant DNA methylation changes occur in a stepwise fashion early in the transformation process. The first aberrant DNA methylation step coincides with overcoming stasis, and results in few to hundreds of changes, depending on how stasis was overcome. A second step coincides with immortalization and results in hundreds of additional DNA methylation changes regardless of the immortalization pathway. A majority of these DNA methylation changes are also found in malignant breast cancer cells. These results show that large-scale epigenetic remodeling occurs in the earliest steps of mammary carcinogenesis, temporally links DNA methylation changes and overcoming cellular proliferation barriers, and provides a bank of potential epigenetic biomarkers that may prove useful in breast cancer risk assessment. [Cancer Res 2009;69(12):5251–8]

Introduction

Epigenetic dysfunction is a common and perhaps universal feature of human cancer. One facet of the epigenetic system that shows clear and dramatic differences between normal and cancer cells is DNA methylation. DNA hypermethylation generally occurs in CpG island gene promoters and is linked to transcriptional gene silencing, whereas DNA hypomethylation often occurs in repetitive elements, pericentromeric regions, and within the body of genes and has been linked to gene activation and chromosome instability. Studies into the biological consequences of hypomethylation and hypermethylation indicate that each plays a participative role in carcinogenesis (1, 2). Although significant progress has been made in identifying aberrant methylation events that occur during carcinogenesis, the timing, origins, and consequences of these events remain incompletely understood.

We have used a human mammary epithelial cell (HMEC) model system that allows for assessment of changes in DNA methylation that occur at the earliest stages of multistep human breast carcinogenesis. In this model, the transformation of normal finite lifespan HMEC to malignancy requires overcoming two distinct senescence-associated barriers to immortality (3). The first barrier, termed stasis or stress-induced senescence, is characterized by elevated levels of the cyclin-dependent kinase inhibitor $p16^{INK4A}$ (gene *CDKN2A*), which maintains the retinoblastoma protein in an active state (4). This barrier has been overcome or bypassed in cultured HMEC by various means, such as exposure to the chemical carcinogen benzo(*a*)pyrene, with the resultant post-stasis cells commonly exhibiting inactivation of *CDKN2A* by promoter hypermethylation or by gene mutation (4, 5). Loss of p16 expression due to silencing or mutation is also a frequent event during *in vivo* human breast cell transformation (6, 7). When grown in a serum-free medium, rare HMEC will "spontaneously" silence p16, generating a type of post-stasis HMEC population that has been called post-selection (4, 8). HMECs that have escaped stasis undergo further proliferation before encountering a second more stringent proliferation barrier resulting from critically shortened telomeres (3, 9). When approaching the telomere dysfunction barrier, HMEC exhibit increased chromosomal instability and a DNA damage response. Rare cells that gain telomerase expression may escape this barrier and acquire immortal potential; additional perturbations can confer malignant properties on the immortally transformed cells (5, 10–12).

This HMEC system has proven useful for identifying and reflecting the molecular events involved in early human breast tumorigenesis (3–5, 9, 13–15). For example, the hypermethylation of *CDKN2A* seen in post-stasis HMEC has also been documented in precancerous lesions and histologically normal breast tissue (15, 16). Currently, it is not clear if focal DNA methylation changes, such as in p16, are rare events that accumulate independently and gradually over time or if these are examples of larger sets of DNA methylation changes that occur in groups, concurrently and at distinct points in the immortalization process. Genomic instability and telomere erosion, characteristic of premalignant *in situ*

Note: Supplementary data for this article are available at Cancer Research Online (http://cancerres.aacrjournals.org/).

Requests for reprints: Bernard W. Futscher, Arizona Cancer Center, The University of Arizona, 1515 North Campbell Avenue, Tucson, AZ 85724. Phone: 520-626-4646; Fax: 520-626-4979; E-mail: bfutscher@azcc.arizona.edu.

doi:10.1158/0008-5472.CAN-08-4977

breast lesions, is seen in the cultured HMEC at the telomere dysfunction barrier (3, 9, 13, 17). The potential contribution of epigenetic changes to telomerase reactivation and immortality is currently not known. To begin to address these questions, we examined the DNA methylation profiles of cultured normal finite lifespan HMEC, isogenic derivatives induced to escape the stasis and/or telomere dysfunction barriers, established breast cancer cell lines, and human breast cancer specimens.

Our results show that aberrant DNA methylation patterns emerge at the earliest stages of HMEC transformation *in vitro* in finite lifespan HMEC. Aberrant changes proceeded in a stepwise fashion, with each step temporally linked to escaping one of the two proliferation barriers. The first step of DNA methylation change occurs when stasis is overcome or bypassed, and results in few to hundreds of aberrant hypermethylation and hypomethylation events, depending on the manner by which stasis was overcome. A majority of these events are found in breast cancer cells. The second step occurs in cells that have overcome the telomere dysfunction barrier and become immortal and is associated with hundreds of aberrant methylation events regardless of the manner of immortalization. A majority of these events are also found in breast cancer cells. Further methylation changes occur during malignant progression. These results suggest that groups of DNA methylation changes can arise concurrently and in a stepwise fashion during early breast carcinogenesis.

Materials and Methods

Cell cultures. Organoids were obtained from reduction mammoplasty tissues as described (18). Finite lifespan pre-stasis HMEC from specimens 184 (batches D-F), 48 (batches RT and LT), and 240L (batch B), and post-selection HMEC 184 (batch B, telomere dysfunction arrest at ~passage 15) and 48 (batch RS, telomere dysfunction arrest at ~passage 23) were derived from tissue of women ages 21, 16, and 19 years, respectively. Cells were initiated as organoids in primary culture in either serum-free MCDB 170 medium (MEGM, Clonetics Division of Lonza) plus supplements (8) or serum-containing medium MM (19) or M85 (composed of 50% MM and 50% supplemented MCDB 170 medium).[5] Post-selection HMEC were cultured in MCDB 170 medium as described (8, 18). The post-stasis 184Aa, 184Be, and 184Ce cultures and the nonmalignant immortal lines 184A1 and 184B5 were obtained from primary cultures of specimen 184 grown in MM, which had been exposed to the chemical carcinogen benzo (*a*)pyrene as described (5). 184A1-RF was obtained by retroviral transduction of the 184A1 line with the Raf-1 oncogene and has gained anchorage-independent growth (10). The $p53^{-/-}$ 184AA2 immortal line with anchorage-independent growth was obtained from 184Aa following insertional mutagenesis as described (20). The 184B5ME line with anchorage-independent growth was obtained by transfection of 184B5 with erbB2 and selection for anchorage-independent colonies. The post-stasis 184F-p16sh and 184D-p16sh cultures were obtained by retroviral transduction of pre-stasis HMEC cultures that were grown respectively in M85 and M87A+X [composed of 50% MM4 (19) and 50% supplemented MCDB 170 medium plus 0.1% AlbuMax (Invitrogen) and 0.1 nmol/L oxytocin (Bachem)]. The nonmalignant immortal 184ZNMY3 line was derived from post-selection 184B following retroviral transduction of ZNF217 and c-myc; 184ZNMY3-N with anchorage-independent growth was obtained following retroviral transduction of 184ZNMY3 with the mutated *neu* oncogene. Breast cancer cell lines were cultured as described previously (21).

Breast tumor specimens. Flash-frozen specimens derived from normal or cancerous breast tissue were obtained from patients who underwent surgery for breast cancer, either lumpectomy or mastectomy, at the University Medical Center in Tucson from 2003 to 2005. All patients signed surgical and clinical research consents for tissue collection in accordance with the University of Arizona institutional review board and Health Insurance Portability and Accountability Act regulations. At the time of surgery, a 1 to 3 cm section of the tumor was immediately snap-frozen in liquid nitrogen and stored in our prospective breast tissue bank at −80°C. From each tissue block, a series of 5 μm sections were cut and stained with H&E for pathologic evaluation. All H&E slides were reviewed by two independent pathologists to determine the integrity of the tumor specimen. A partial molecular characterization of these samples have been reported on previously (21, 22). Supplementary Table S1 provides the pathologic assessment of each specimen.

Nucleic acid isolation. RNA and DNA were isolated as described previously (21).

DNA methylation analysis by MassARRAY. Sodium bisulfite-treated genomic DNA was prepared according to the manufacturer's instructions (Zymo Research). Sodium bisulfite-treated DNA (5 ng) was seeded into a region-specific PCR incorporating a T7 RNA polymerase sequence as described by the manufacturer (Sequenom). Resultant PCR product was then subjected to *in vitro* transcription and RNase A cleavage using the MassCLEAVE T-only kit, spotted onto a Spectro CHIP array, and analyzed using the MassARRAY Compact System matrix-assisted laser desorption/ionization-time-of-flight mass spectrometer (Sequenom). Each sodium bisulfite-treated DNA sample was processed in two independent experiments. Data were analyzed using EpiTyper software (Sequenom) as described (22, 23). Primer sequences were designed using EpiDesigner.[6] Primer sequences are available upon request.

The methyl DNA immunoprecipitation microarrays and data analysis. The methylated fraction of DNA was obtained by immunoprecipitation as described (21). Input and immunoprecipitated DNAs were amplified, labeled, and analyzed on Human Promoter arrays as described (24). All microarray data were processed in R programming environment using *Limma* package and differentially methylated elements were identified using statistical approaches as described previously (25). To control for false discovery rate, a multiple testing correction was done according to the methods described (24). A list of differentially methylated elements is provided in Supplementary Table S2. A region was considered differentially methylated if the adjusted $P < 0.05$ and there was at least a 1.25-fold change in methylcytosine immunoprecipitated DNA versus input DNA ratio relative to pre-stasis HMEC. The magnitude of the microarray methylation ratio was directly correlated with the degree of methylation as determined by MassARRAY (Supplementary Fig. S1).

All raw and normalized microarray data with detailed protocols are available in the ArrayExpress database accession E-MEXP-1889.[7] The number of and samples analyzed by DNA methylation microarray are provided in Supplementary Table S3. Gene Ontology terms overrepresentation testing was done using GOstats package (26). Overlapping probabilities of differentially methylated region sets were calculated using a hypergeometric test (27).

Results

DNA methylation changes during transformation. Figure 1 shows the cells analyzed in this study, their relative position with respect to proliferation barriers, the predicted corresponding *in vivo* correlates (3, 9, 13), the timing and accumulation of genetic abnormalities (9, 13, 28–30), and finally the timing and accumulation of DNA methylation changes determined in this study. The DNA methylation state of HMEC at different stages in the transformation from normal finite pre-stasis to immortal with anchorage-independent growth, as well as malignant breast cancer cell lines

[5] Garbe and colleagues, submitted for publication.

[6] www.epidesigner.com

[7] www.ebi.ac.uk/arrayexpress

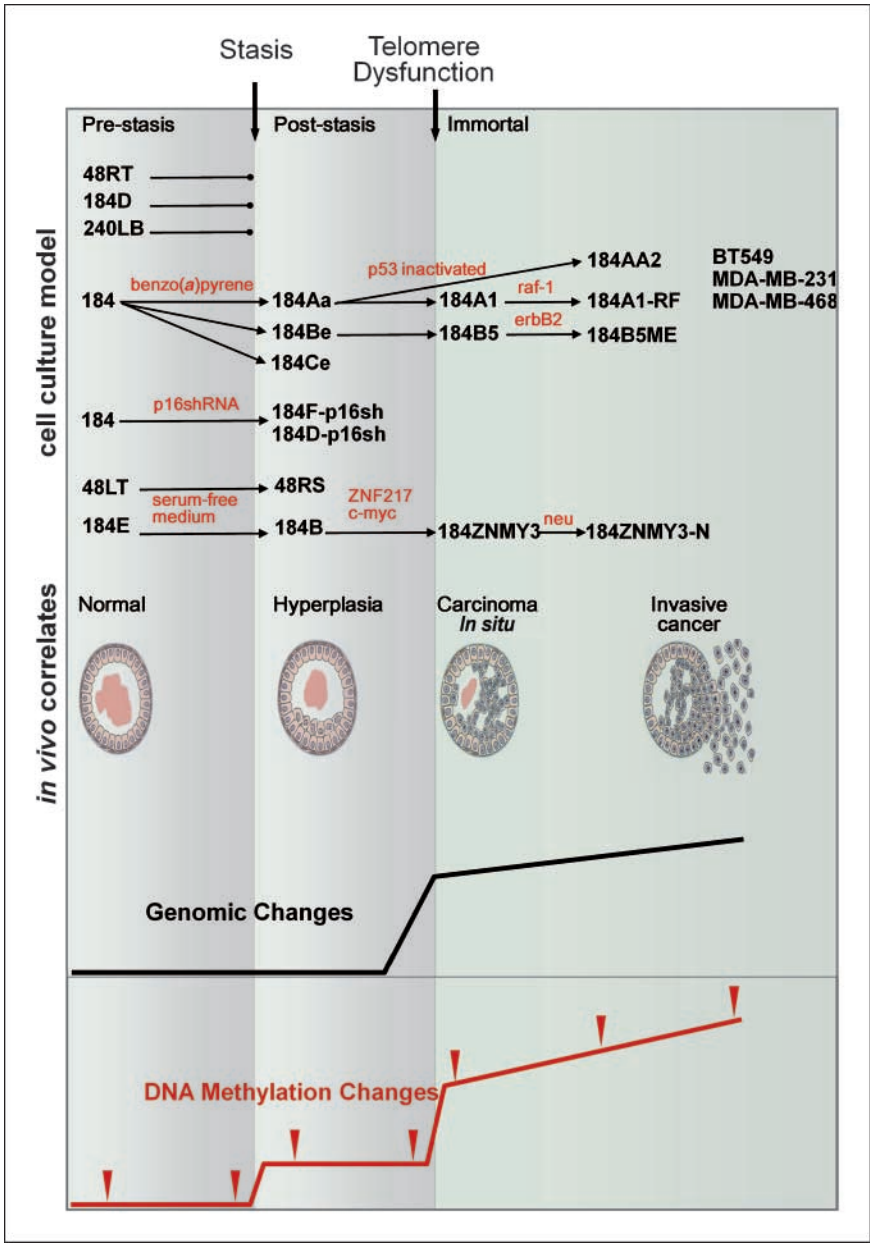

Figure 1. Schematic representation of breast cancer progression and the timing of the underlying genomic and DNA methylation changes. Connection between *in vitro* system and *in vivo* progression is based on the previously published data describing genomic changes (9, 13, 30). *Top,* the temporal position of the two epithelial cell proliferation barriers of stasis and telomere dysfunction that divides the timeline into pre-stasis, post-stasis, and immortal epithelial cells. *Middle,* corresponding cell culture models used in this study. *Red,* treatment or genetic manipulation used. Cell models are described in detail in Materials and Methods. *Bottom, in vivo* correlates of the HMEC system followed by the timeline of previously described genomic dysfunction in HMEC and finally the timeline of DNA methylation changes identified and described in this study. Arrows on the DNA methylation changes curve show the time points analyzed for DNA methylation state.

was analyzed using a 13,500 element human gene promoter microarray (24); arrows in the bottom panel indicate when cells were examined.

The first step of DNA methylation change occurs when stasis is overcome or bypassed and post-stasis HMEC emerge (Fig. 2*A*). When pre-stasis HMEC are compared with post-selection HMEC (48RS and 184B) that overcame stasis associated with silencing of p16 following culture in a stress-inducing serum-free medium (8), 191 differentially methylated regions were identified, in addition to the previously described *CDKN2A* methylation (4). This number represents ~2% of all promoters analyzed on this microarray. In contrast, HMEC that become post-stasis following exposure to the mutagen and complete carcinogen benzo(*a*)pyrene (184Aa, 184Be, and 184Ce; refs. 5, 31) exhibited only 10 differentially methylated regions when compared with pre-stasis HMEC. Although this is a very small number of elements that could represent false discoveries or stochastic events, it appears that at least a few are valid and relevant, such as the *HOXA* gene cluster, because this is a common target among all these post-stasis HMEC samples as well as clinical disease. Supplementary Fig. S2 shows high-resolution methylation analysis that confirms aberrant methylation of the HOXA4 locus in the benzo(*a*)pyrene-treated HMEC. In contrast, HMEC that became post-stasis following transduction with p16 short hairpin RNA (184F-p16sh and 184D-p16sh) accumulated only 5 differentially methylated regions and did not show changes in the HOXA gene cluster. These results suggest that different levels of DNA methylation changes may be associated with HMEC that overcome the stasis proliferation barrier via different genetic or epigenetic mechanisms. Considering that the number of aberrantly methylated genes in cancer has been estimated to be between several hundreds to low thousands (1, 22, 32) and the large number of differentially methylated regions seen in the

post-selection HMEC, the transition through the stasis proliferation barrier may represent a critical epigenetic event in some pathways of carcinogenesis.

The second step of DNA methylation change occurs when telomere dysfunction is overcome and cells become immortal (Fig. 2*A*). This second stepwise increase in DNA methylation changes produced hundreds of new differentially methylated regions regardless of how telomere dysfunction or stasis was overcome. Breast cancer cell lines derived from malignant tumors displayed the greatest number of aberrant DNA methylation changes. Taken together, these results are consistent with progressive, stepwise increases in aberrant DNA methylation during the transformation process.

To further address whether aberrant DNA methylation progresses in a gradual or stepwise fashion in the earliest stages of breast carcinogenesis, we examined multiple early- and late-passage pre-stasis and post-selection HMEC, including cell passages in telomere dysfunction, which are known to have genomic instability (ref. 9; Fig. 2*B*). A comparison of the DNA methylation patterns of early- and late-passage pre-stasis HMEC revealed no differentially methylated regions. Similarly, no additional differentially methylated regions were detected when early passage post-selection HMEC were compared with those at telomere dysfunction. These results showed that there is not a gradual progression or increase in the number of differentially methylated regions between proliferative barriers but rather new differentially methylated regions emerge in cells that overcame stasis or telomere dysfunction. Such stepwise changes are shown on Fig. 2*B*, which shows the methylation status of post-stasis–specific differentially methylated regions and breast cancer cell line-specific differentially methylated regions at various stages of transformation. The abrupt increase in

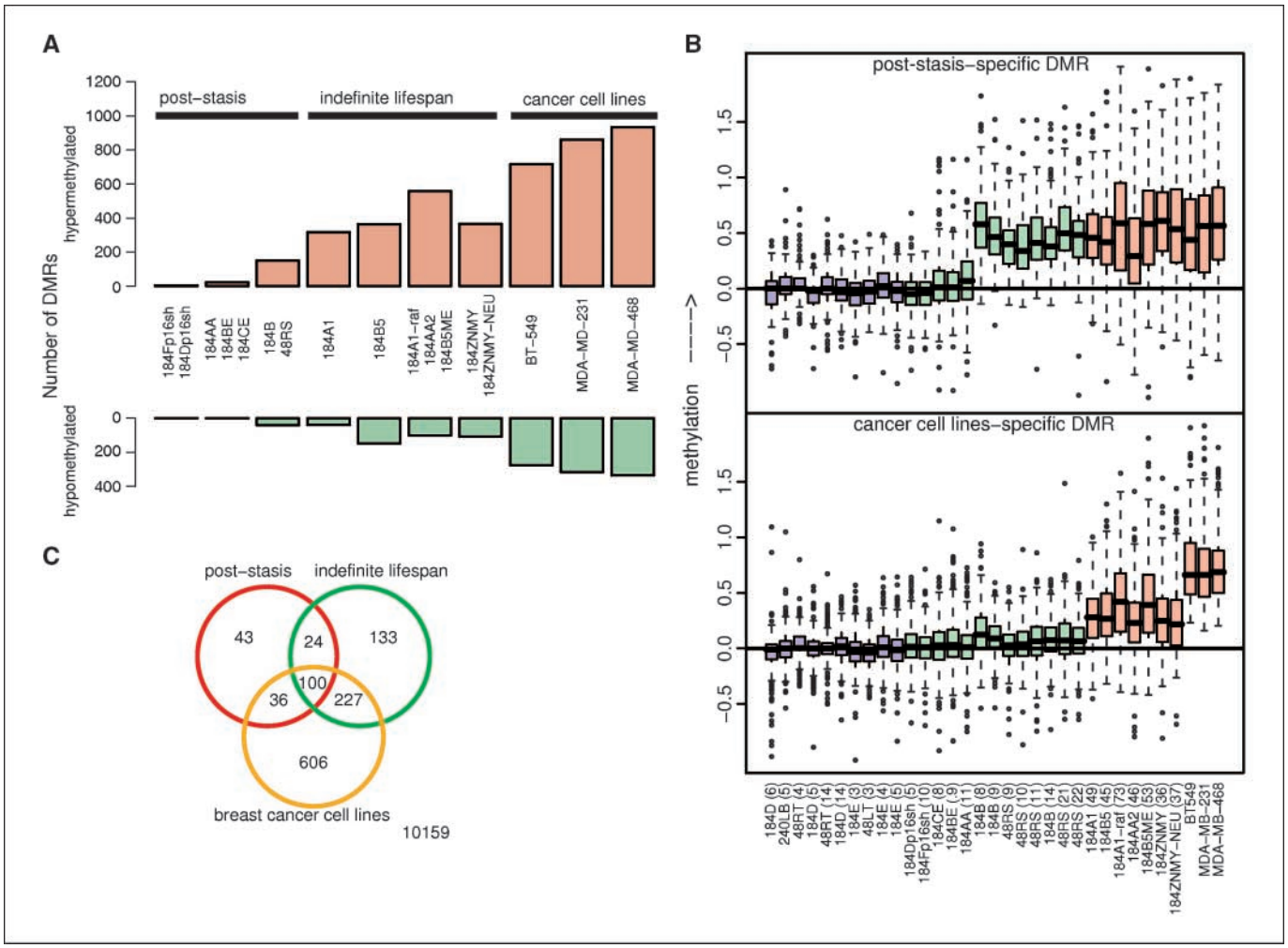

Figure 2. Stepwise progression of DNA methylation changes in an HMEC model of acquired immortality. *A,* total number of DNA hypermethylation and hypomethylation changes in groups of post-stasis HMEC, indefinite lifespan HMEC, and breast cancer cell lines when compared with pre-stasis HMEC. A total of 11,328 of gene promoter regions were analyzed. For purposes of statistical testing, some cell cultures were treated as one group (biological replicate) and each of these groups is represented by one bar. *B,* stepwise progression of DNA methylation in post-stasis–specific differentially methylated regions and cancer cell line-specific differentially methylated regions (*DMR*). DNA methylation on the *Y axis* is based on the normalized microarray data and corresponds to the $\log_2$ ratio of methylcytosine-immunoprecipitated DNA versus input DNA. The passage number of each HMEC culture analyzed is in parenthesis. Only the hypermethylated differentially methylated regions are shown. Samples are color coded with blue boxes corresponding to pre-stasis cells, green to post-stasis cells, and red to immortalized cell lines including breast cancer cell lines. *C,* Venn diagram showing common and unique differentially methylated regions between post stasis HMEC, immortalized HMEC, and breast cancer cell lines. The post-stasis category represents differentially methylated regions detected in any post-stasis HMEC group, the indefinite lifespan category represents differentially methylated regions detected in at least two of the immortal HMEC lines, and the breast cancer cell line category represents differentially methylated regions found in at least two of the three breast cancer cell lines analyzed. The significance of overlap between post-stasis HMEC and breast cancer cell lines and between immortalized HMEC and breast cancer cell lines was calculated using a hypergeometric test.

DNA methylation changes in post-stasis and immortal cells show the breakpoints of epigenetic reprogramming.

DNA methylation changes seen during *in vitro* transformation model the changes seen in *in vivo* carcinogenesis. If the DNA methylation changes found in post-stasis HMEC and immortal HMEC cell lines are relevant to malignant transformation, then the identified methylation changes should resemble those seen in malignant breast cancer cell lines. Figure 2*C* is a Venn diagram relating the differentially methylated region found in post-stasis and immortal HMEC and genetically distinct breast cancer cell lines. Of the 203 differentially methylated regions found in post-stasis HMEC populations, 136 differentially methylated regions (67%) are also aberrantly methylated in breast cancer cell lines (overlapping probability $P < 2.2 \times 10^{-16}$). Furthermore, of the 484 differentially methylated regions identified in the immortalized HMEC lines, 327 (68%) are also found in breast cancer cell lines ($P < 2.2 \times 10^{-16}$). Supplementary Fig. S3 shows the overlap and differences in differentially methylated regions between immortal cell lines that bypassed this proliferation barrier by different mechanisms. These data indicate that a significant overlap exists between the targets of aberrant DNA methylation in breast cancer cells and the targets of aberrant DNA methylation in the premalignant stages represented by the HMEC model.

Stepwise changes in DNA methylation in specific gene clusters at defined proliferation barriers. To further examine the timing of specific methylation events, two gene clusters known to undergo aberrant methylation during breast carcinogenesis were examined in the gene promoter microarrays. Previous studies have shown frequent hypermethylation and silencing of the *HOXA* and *PCDH* gene family clusters in breast cancer (21, 22). Our data indicate that a prevalence of aberrantly methylated *HOXA* genes is also seen in both post-stasis and immortal HMEC. Detailed exploration of the *HOXA* genomic region showed that silencing of the whole cluster can originate early in breast carcinogenesis (Fig. 3). Early DNA methylation changes occur in *HOXA3, HOXA4, HOXA9, HOXA10*, and *HOXA13* genes in the post-selection HMEC. Interestingly, the *HOXA* cluster is also one of the few regions where differentially methylated regions emerged in post-stasis cells that bypassed stasis following exposure to benzo(*a*)pyrene; however, the *HOXA* cluster was not targeted in HMEC that bypassed stasis via silencing of p16 by short hairpin RNA. Further progression in aberrant DNA methylation occurs in the HOXA gene cluster in the immortal HMEC cell lines that overcame the telomere dysfunction barrier. Continued malignant progression is ultimately associated with aberrant DNA hypermethylation of the whole-gene cluster as seen in the breast cancer lines.

A similar progression in aberrant DNA methylation occurs in another genomic region, the *PCDH* gene family cluster. However, detailed exploration of the *PCDH* genomic region showed that, in this cluster, most changes are observed in the transition from post-stasis to immortal HMEC (Supplementary Fig. S4). Whereas almost no changes were seen in the post-stasis HMEC, the nonmalignant immortal cell lines already displayed most of the changes seen in the breast tumor lines. These results clearly illustrate the stepwise nature of the DNA methylation changes in association with overcoming the proliferation barriers to immortality.

High-resolution confirmation of DNA methylation changes. To confirm the methylation microarray data and extend our model, we analyzed the methylation status of post-stasis–specific differentially methylated regions in pre-stasis, post-stasis, and immortalized HMEC, a set of primary breast tumors, and breast epithelial organoids using MassARRAY (Fig. 4; Supplementary Fig. S3). Results obtained confirmed the microarray data and extended them by showing that the DNA methylation changes seen in the *in vitro* model of post-stasis HMEC can also be found in primary breast tumors but are not present in the normal epithelial organoids used to establish the HMEC system (18). In addition to the inappropriate methylation of *CDKN2A* as reported in focal aggregates of histologically normal mammary epithelia (15, 16) and in atypical ductal hyperplasia (33), we also found the promoter region of *PGR* to be inappropriately methylated in post-stasis cells, similar to findings in atypical ductal hyperplasia (34). Overall, these results indicate that post-stasis HMEC are a relevant model of early epigenetic changes in breast carcinogenesis and that the hundreds of differentially methylated regions discovered may serve as potential markers of premalignant breast lesions.

Gene Ontology of DNA methylation–targeted promoters. To evaluate the potential functional importance of the DNA methylation changes, we analyzed the ontology of the genes where the promoters were targeted for changes in DNA methylation, and we found several overrepresented groups of genes (Supplementary Fig. S5). A significant number of genes involved in the extracellular matrix and the extracellular region were hypermethylated in post-stasis cells, consistent with published gene expression data that showed differential expression of extracellular matrix and cell-cell communication genes between pre-stasis and post-stasis HMEC (14). Another noteworthy group of affected genes that are hypermethylated in both post-stasis and breast cancer cell lines is the Gene Ontology group related to adhesion and the plasma membrane. This Gene Ontology analysis revealed groups of genes targeted by aberrant DNA methylation in premalignant mammary epithelial that are also found to be dysregulated in breast cancer, suggesting that epigenetic changes important to the malignant phenotype may occur early in the multistep process of malignant transformation and before immortalization.

Discussion

In this report, we have shown that the transition of cultured HMEC from normal finite lifespan to immortality is associated with a stepwise progression of DNA methylation changes and that these steps are coincident with passage through the defined epithelial cell proliferation barriers of stasis and telomere dysfunction. HMEC that emerged from these proliferation barriers acquired hundreds of DNA methylation changes compared with cells examined just before the proliferation barrier. In contrast, no changes in DNA methylation were observed between early- and late-passage cell populations that preceded the proliferation barriers. These results suggest a direct mechanistic link between epigenetic dysfunction and escape from senescence barriers thought to function as tumor suppressor mechanisms. Importantly, a majority of the two-step DNA methylation changes identified using this HMEC system are also seen in both breast cancer cell lines and tumor specimens. Because these methylation changes occurred at the earliest stages of transformation, in still finite lifespan HMEC populations, our results suggest that numerous aberrant methylation changes may be present in premalignant lesions of breast cancer. Indeed, several genes previously shown to have hypermethylated promoters in histologically normal mammary epithelia and premalignant stages of breast carcinogenesis were also identified in this study, including the *CDKN2A* and *PGR* promoters (15, 16, 33–37).

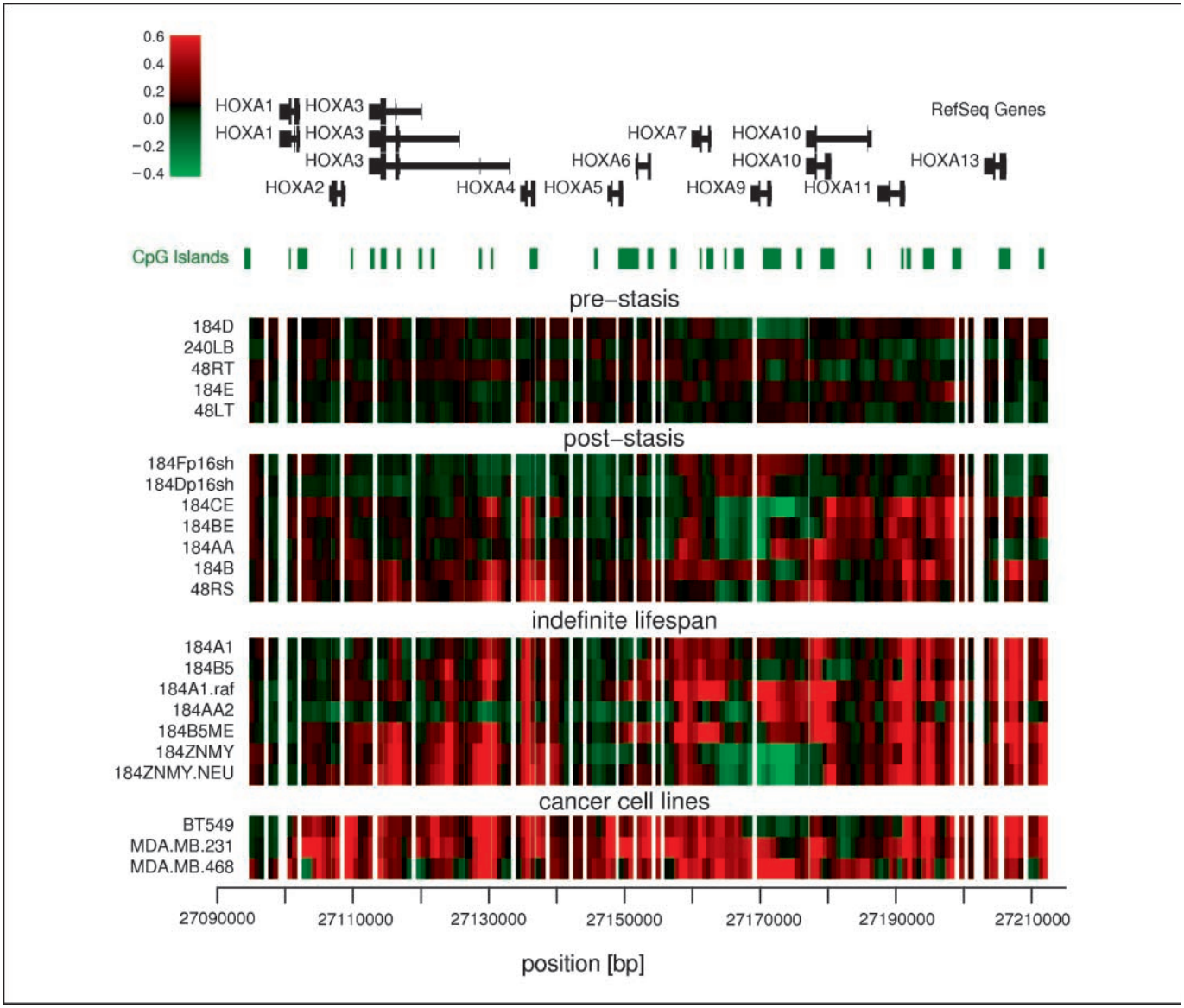

Figure 3. Progression of DNA methylation in the *HOXA* gene family cluster from finite lifespan HMEC to malignantly transformed breast cancer cells. *Top,* map of the RefSeq genes of the *HOXA* cluster taken from University of California at Santa Cruz Genome Browser (http://genome.ucsc.edu) followed by the location of CpG islands. The DNA methylation state of the *HOXA* gene family cluster based on the microarray data obtained from the various HMEC stages and breast cancer cell lines is shown in a heat map format and presented in physical scale along the *HOXA* cluster. *Green,* hypomethylated sites; *red,* hypermethylated sites. Nucleotide position along chromosome 7 is shown below the heat map.

Gene Ontology analysis of the promoters targeted by DNA methylation showed that genes involved in the biological process of multicellular organismal development were overrepresented in both post-stasis cells and cancer cell lines, suggesting that these targets may participate in the initiation and maintenance of the malignant phenotype (Supplementary Fig. S5). *HOXA* genes are prominent in this list and are represented by *HOXA2, HOXA4, HOXA9, HOXA10, HOXA11*, and *HOXA13*. The disruption of these transcriptional regulators, which are involved in control of cell identity, are logical genes to be targeted in the malignant transformation process, and the consequences of their dysregulation are likely manifest through changes in the expression of *HOXA* target genes. The fact that aberrant DNA methylation and transcriptional dysregulation of the *HOXA* gene cluster is seen in a variety of human tumor types suggests that these events play a critical role in human carcinogenesis (21, 38–40). Based on this information, we speculate that *HOXA* genes are critical targets in the epigenetic initiation of malignant transformation.

The *HOXA* genes also represent a gene family cluster that frequently undergoes Long-range epigenetic silencing in invasive breast cancer (21, 22, 41, 42). Interestingly, the *PCDH* gene family clusters (α, β, and γ) on chromosome 5, another known target of long-range epigenetic silencing epigenetic silencing in invasive breast cancer, are also represented in the early steps of our *in vitro* model of transformation (22). The increased DNA methylation observed in these two known long-range epigenetic silencing targets provide evidence that (*a*) long-range epigenetic silencing is initiated early in mammary epithelial cell transformation, (*b*) long-range epigenetic silencing likely initiates in a stepwise fashion, similar to the focal events observed in this study, and (*c*) the *in vitro* HMEC

system is an accurate reflection of the clinical disease. Taken together, these results suggest that the post-stasis–specific and the immortalization-specific differentially methylated regions identified in this study may serve as potential markers of premalignant events in breast carcinogenesis. The specific DNA methylation changes identified in this study can potentially provide a bank of epigenetic biomarkers for assessing breast cancer risk and allow for the analysis of multiple post-stasis and immortalization-specific DNA methylation changes that when combined with additional types of genomic data (e.g., SNPs and gene expression) will help develop increasingly robust risk assessment models.

We examined cells that escaped stasis by three distinct means, exposure to the chemical carcinogen benzo(*a*)pyrene, growth in a stress-inducing serum-free medium, and direct inactivation of p16 by p16 short hairpin RNA; the first two methods generated clonal post-stasis populations. The extent of DNA methylation changes at this step varied greatly depending on the manner by which the HMEC had become post-stasis. Post-selection HMEC displayed DNA methylation changes at hundreds of gene promoters, including *CDKN2A*, whereas HMEC that bypassed stasis following benzo(*a*)pyrene exposure or direct genetic inactivation of p16 showed few changes. These results suggest that different pathways to post-stasis produce different epigenetic signatures. Notably, however, the DNA methylation state of the *HOXA* gene cluster is perturbed in all post-selection and benzo(*a*)pyrene exposed post-stasis cultures regardless of pathway taken. These results suggest that, within the emerging transformation-associated epigenetic signatures, there may be common critical epigenetic targets affected by the distinct paths and etiologies of breast cell transformation. The epigenetic aberrations that are common to the different pathways may play a critical role in driving the transformation process forward; the early deregulation of the *HOX* gene family clusters, which are decisively linked to human carcinogenesis, are one clear example that is consistent with this possibility (21, 39, 40). In contrast, the epigenetic aberrations that are specific to particular pathways to post-stasis and therefore occur at this earliest stage of transformation may allow for the emergence of distinct phenotypes if these cells pass to immortality and malignancy.

Although the stasis proliferation barrier could be bypassed with minimal epigenetic changes, all the immortalized lines examined acquired hundreds of additional DNA methylation changes regardless of how they became post-stasis or immortal. These results suggest that DNA methylation changes may be necessary to achieve immortality. The role of epigenetic control in telomerase reactivation remains controversial and incompletely understood (43, 44). To address the potential role of DNA methylation in the control of *hTERT* in this HMEC model system, future studies will perform high-resolution epigenetic analyses of the *hTERT* region. It is also possible that critical epigenetic changes within the multitude of genes affected during the transition to immortality are important and participate in telomerase reactivation.

Taken together, these results indicate that epigenetic alterations in DNA methylation found in breast cancer cells *in vivo* may arise during the earliest stages of HMEC transformation, prior to and coincident with attainment of immortality. Thus, full understanding of the timing and nature of epigenetic alterations in early breast carcinogenesis will require examination of cells before attaining immortality. Although nonmalignant immortalized lines such as 184A1, 184B5, and MCF10A can be useful starting points for studying epigenetic events involved in the progression to invasive malignancy, they already possess many of the epigenetic aberrations found in breast cancers. Similarly, the post-selection HMEC, although finite, also possess many epigenetic changes found in breast cancer cells. This finding is of particular note because post-selection HMEC are sold commercially as normal primary cells.

Overall, these results support an epigenetic progenitor model whereby genome-wide DNA methylation changes occur early, in a stepwise fashion, may precede genetic mutations and allow for an inappropriate proliferation and expansion of epigenetically comprised progenitor cells (45). The large number of genes affected by

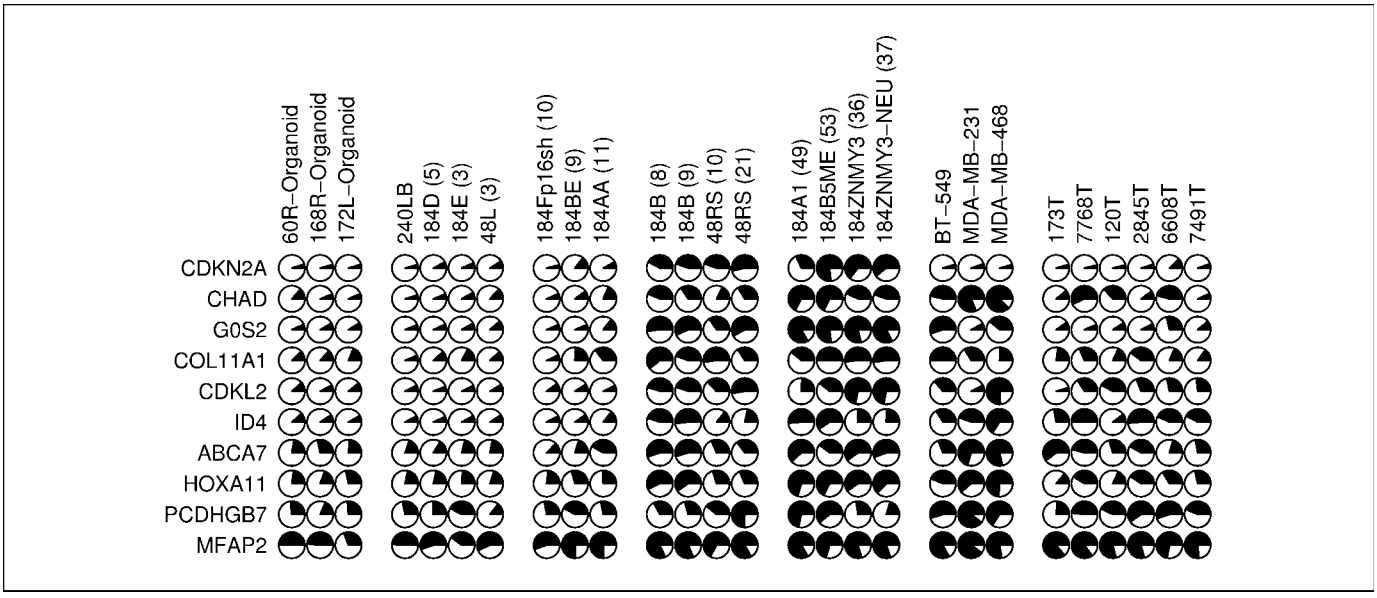

Figure 4. Detailed analysis of DNA methylation levels of selected post-stasis HMEC-specific differentially methylated regions by matrix-assisted laser desorption/ionization–time-of-flight. *Rows,* gene promoters analyzed; *columns,* each sample analyzed; *pie charts,* methylation status of each gene promoter for each HMEC sample (passage number is in parenthesis); *black region,* average percent methylation of the entire region. Percent methylation of individual CpG sites is provided in Supplementary Fig. S6.

aberrant DNA methylation provides a foundation for phenotypic variability in cells that transform to immortality and malignancy and may be an important force that drives the significant biological heterogeneity seen in the clinical disease. The DNA methylation changes identified in this HMEC model system can potentially provide a bank of epigenetic biomarkers for assessing breast cancer risk in premalignant lesions and provide targets for therapeutic interventions.

Disclosure of Potential Conflicts of Interest

The authors declare that no conflicts of interest exist.

Acknowledgments

Received 12/31/08; revised 3/27/09; accepted 4/20/09; published OnlineFirst 6/9/09.

Grant support: Grants R01CA65662 and R33CA091351 (B.W. Futscher); center grants P30ES06694 and P30CA023074 and the BIO5 Interdisciplinary Biotechnology Center at the University of Arizona (Genomics Shared Service); training grants ES007091 and CA09213 (T.J. Jensen); and NIH grant U54 CA112970, Department of Defense grant BCRP BC060444, and Office of Energy Research, Office of Health and Biological Research, U.S. Department of Energy contract DE-AC03-76SF00098 (J.C. Garbe and M.R. Stampfer).

The costs of publication of this article were defrayed in part by the payment of page charges. This article must therefore be hereby marked *advertisement* in accordance with 18 U.S.C. Section 1734 solely to indicate this fact.

We thank Jose Munoz-Rodriguez (University of Arizona) and Batul Merchant (Lawrence Berkeley National Laboratory) for outstanding technical support.

References

1. Jones PA, Baylin SB. The epigenomics of cancer. Cell 2007;128:683–92.

2. Jones PA, Laird PW. Cancer epigenetics comes of age. Nat Genet 1999;21:163–7.

3. Garbe JC, Holst CR, Bassett E, Tlsty T, Stampfer MR. Inactivation of p53 function in cultured human mammary epithelial cells turns the telomere-length dependent senescence barrier from agonescence into crisis. Cell Cycle 2007;6:1927–36.

4. Brenner AJ, Stampfer MR, Aldaz CM. Increased p16 expression with first senescence arrest in human mammary epithelial cells and extended growth capacity with p16 inactivation. Oncogene 1998;17:199–205.

5. Stampfer MR, Bartley JC. Induction of transformation and continuous cell lines from normal human mammary epithelial cells after exposure to benzo[*a*]pyrene. Proc Natl Acad Sci U S A 1985;82:2394–8.

6. Geradts J, Wilson PA. High frequency of aberrant p16 (INK4A) expression in human breast cancer. Am J Pathol 1996;149:15–20.

7. Baylin SB, Herman JG, Graff JR, Vertino PM, Issa JP. Alterations in DNA methylation: a fundamental aspect of neoplasia. Adv Cancer Res 1998;72:141–96.

8. Hammond SL, Ham RG, Stampfer MR. Serum-free growth of human mammary epithelial cells: rapid clonal growth in defined medium and extended serial passage with pituitary extract. Proc Natl Acad Sci U S A 1984;81:5435–9.

9. Romanov SR, Kozakiewicz BK, Holst CR, Stampfer MR, Haupt LM, Tlsty TD. Normal human mammary epithelial cells spontaneously escape senescence and acquire genomic changes. Nature 2001;409:633–7.

10. Olsen CL, Gardie B, Yaswen P, Stampfer MR. Raf-1-induced growth arrest in human mammary epithelial cells is p16-independent and is overcome in immortal cells during conversion. Oncogene 2002;21:6328–39.

11. Stampfer MR, Yaswen P. Human epithelial cell immortalization as a step in carcinogenesis. Cancer Lett 2003;194:199–208.

12. Clark R, Stampfer MR, Milley R, et al. Transformation of human mammary epithelial cells by oncogenic retroviruses. Cancer Res 1988;48:4689–94.

13. Chin K, de Solorzano CO, Knowles D, et al. *In situ* analyses of genome instability in breast cancer. Nat Genet 2004;36:984–8.

14. Li Y, Pan J, Li JL, et al. Transcriptional changes associated with breast cancer occur as normal human mammary epithelial cells overcome senescence barriers and become immortalized. Mol Cancer 2007;6:7.

15. Holst CR, Nuovo GJ, Esteller M, et al. Methylation of p16(INK4a) promoters occurs *in vivo* in histologically normal human mammary epithelia. Cancer Res 2003;63:1596–601.

16. Bean GR, Bryson AD, Pilie PG, et al. Morphologically normal-appearing mammary epithelial cells obtained from high-risk women exhibit methylation silencing of INK4a/ARF. Clin Cancer Res 2007;13:6834–41.

17. Stampfer MR, Bodnar A, Garbe J, et al. Gradual phenotypic conversion associated with immortalization of cultured human mammary epithelial cells. Mol Biol Cell 1997;8:2391–405.

18. Stampfer MR. Isolation and growth of human mammary epithelial cells. J Tissue Culture Methods 1985;9:107–16.

19. Stampfer MR. Cholera toxin stimulation of human mammary epithelial cells in culture. In Vitro 1982;18:531–7.

20. Stampfer MR, Garbe J, Nijjar T, Wigington D, Swisshelm K, Yaswen P. Loss of p53 function accelerates acquisition of telomerase activity in indefinite lifespan human mammary epithelial cell lines. Oncogene 2003;22:5238–51.

21. Novak P, Jensen T, Oshiro MM, et al. Epigenetic inactivation of the HOXA gene cluster in breast cancer. Cancer Res 2006;66:10664–70.

22. Novak P, Jensen T, Oshiro MM, Watts GS, Kim CJ, Futscher BW. Agglomerative epigenetic aberrations are a common event in human breast cancer. Cancer Res 2008;68:8616–25.

23. Coolen MW, Statham AL, Gardiner-Garden M, Clark SJ. Genomic profiling of CpG methylation and allelic specificity using quantitative high-throughput mass spectrometry: critical evaluation and improvements. Nucleic Acids Res 2007;35:e119.

24. Jensen TJ, Novak P, Eblin KE, Gandolfi AJ, Futscher BW. Epigenetic remodeling during arsenical-induced malignant transformation. Carcinogenesis 2008;29:1500–8.

25. Smyth GK. Linear models and empirical Bayes methods for assessing differential expression in microarray experiments. Stat Appl Genet Mol Biol 2004;3:Article3.

26. Falcon S, Gentleman R. Using GOstats to test gene lists for GO term association. Bioinformatics 2007;23:257–8.

27. Fury W, Batliwalla F, Gregersen PK, Li W. Overlapping probabilities of top ranking gene lists, hypergeometric distribution, and stringency of gene selection criterion. Conf Proc IEEE Eng Med Biol Soc 2006;1:5531–4.

28. Kuukasjarvi T, Karhu R, Tanner M, et al. Genetic heterogeneity and clonal evolution underlying development of asynchronous metastasis in human breast cancer. Cancer Res 1997;57:1597–604.

29. Nishizaki T, DeVries S, Chew K, et al. Genetic alterations in primary breast cancers and their metastases: direct comparison using modified comparative genomic hybridization. Genes Chromosomes Cancer 1997;19:267–72.

30. Walen KH, Stampfer MR. Chromosome analyses of human mammary epithelial cells at stages of chemical-induced transformation progression to immortality. Cancer Genet Cytogenet 1989;37:249–61.

31. Stampfer MR, Bartley JC. Human mammary epithelial cells in culture: differentiation and transformation. Cancer Treat Res 1988;40:1–24.

32. Costello JF, Fruhwald MC, Smiraglia DJ, et al. Aberrant CpG-island methylation has non-random and tumour-type-specific patterns. Nat Genet 2000;24:132–8.

33. Liu T, Niu Y, Feng Y, et al. Methylation of CpG islands of p16(INK4a) and cyclinD1 overexpression associated with progression of intraductal proliferative lesions of the breast. Hum Pathol 2008;39:1637–46.

34. Melnikov AA, Scholtens DM, Wiley EL, Khan SA, Levenson VV. Array-based multiplex analysis of DNA methylation in breast cancer tissues. J Mol Diagn 2008;10:93–101.

35. Lee JS. GSTP1 promoter hypermethylation is an early event in breast carcinogenesis. Virchows Arch 2007;450:637–42.

36. Umbricht CB, Evron E, Gabrielson E, Ferguson A, Marks J, Sukumar S. Hypermethylation of 14-3-3σ (stratifin) is an early event in breast cancer. Oncogene 2001;20:3348–53.

37. Futscher BW, O'Meara MM, Kim CJ, et al. Aberrant methylation of the maspin promoter is an early event in human breast cancer. Neoplasia 2004;6:380–9.

38. Ordway JM, Bedell JA, Citek RW, et al. Comprehensive DNA methylation profiling in a human cancer genome identifies novel epigenetic targets. Carcinogenesis 2006;27:2409–23.

39. Rauch T, Wang Z, Zhang X, et al. Homeobox gene methylation in lung cancer studied by genome-wide analysis with a microarray-based methylated CpG island recovery assay. Proc Natl Acad Sci U S A 2007;104:5527–32.

40. Strathdee G, Holyoake TL, Sim A, et al. Inactivation of HOXA genes by hypermethylation in myeloid and lymphoid malignancy is frequent and associated with poor prognosis. Clin Cancer Res 2007;13:5048–55.

41. Frigola J, Song J, Stirzaker C, Hinshelwood RA, Peinado MA, Clark SJ. Epigenetic remodeling in colorectal cancer results in coordinate gene suppression across an entire chromosome band. Nat Genet 2006;38:540–9.

42. Hitchins MP, Lin VA, Buckle A, et al. Epigenetic inactivation of a cluster of genes flanking MLH1 in microsatellite-unstable colorectal cancer. Cancer Res 2007;67:9107–16.

43. Zinn RL, Pruitt K, Eguchi S, Baylin SB, Herman JG. hTERT is expressed in cancer cell lines despite promoter DNA methylation by preservation of unmethylated DNA and active chromatin around the transcription start site. Cancer Res 2007;67:194–201.

44. Renaud S, Loukinov D, Abdullaev Z, et al. Dual role of DNA methylation inside and outside of CTCF-binding regions in the transcriptional regulation of the telomerase hTERT gene. Nucleic Acids Res 2007;35:1245–56.

45. Feinberg AP, Ohlsson R, Henikoff S. The epigenetic progenitor origin of human cancer. Nat Rev Genet 2006;7:21–33.

OPEN ACCESS Freely available online

PLoS one

Role for DNA Methylation in the Regulation of miR-200c and miR-141 Expression in Normal and Cancer Cells

Lukas Vrba[1,4], Taylor J. Jensen[1,2], James C. Garbe[3], Ronald L. Heimark[1], Anne E. Cress[1], Sally Dickinson[1], Martha R. Stampfer[1,3], Bernard W. Futscher[1,2]*

1 Arizona Cancer Center, The University of Arizona, Tucson, Arizona, United States of America, **2** Department of Pharmacology & Toxicology, College of Pharmacy, The University of Arizona, Tucson, Arizona, United States of America, **3** Life Sciences Division, Lawrence Berkeley National Laboratory, Berkeley, California, United States of America, **4** Biology Centre ASCR, v.v.i., Institute of Plant Molecular Biology, Ceske Budejovice, Czech Republic

Abstract

Background: The microRNA-200 family participates in the maintenance of an epithelial phenotype and loss of its expression can result in epithelial to mesenchymal transition (EMT). Furthermore, the loss of expression of miR-200 family members is linked to an aggressive cancer phenotype. Regulation of the miR-200 family expression in normal and cancer cells is not fully understood.

Methodology/Principal Findings: Epigenetic mechanisms participate in the control of miR-200c and miR-141 expression in both normal and cancer cells. A CpG island near the predicted mir-200c/mir-141 transcription start site shows a striking correlation between miR-200c and miR-141 expression and DNA methylation in both normal and cancer cells, as determined by MassARRAY technology. The CpG island is unmethylated in human miR-200/miR-141 expressing epithelial cells and in miR-200c/miR-141 positive tumor cells. The CpG island is heavily methylated in human miR-200c/miR-141 negative fibroblasts and miR-200c/miR-141 negative tumor cells. Mouse cells show a similar inverse correlation between DNA methylation and miR-200c expression. Enrichment of permissive histone modifications, H3 acetylation and H3K4 trimethylation, is seen in normal miR-200c/miR-141-positive epithelial cells, as determined by chromatin immunoprecipitation coupled to real-time PCR. In contrast, repressive H3K9 dimethylation marks are present in normal miR-200c/miR-141-negative fibroblasts and miR-200c/miR-141 negative cancer cells and the permissive histone modifications are absent. The epigenetic modifier drug, 5-aza-2′-deoxycytidine, reactivates miR-200c/miR-141 expression showing that epigenetic mechanisms play a functional role in their transcriptional control.

Conclusions/Significance: We report that DNA methylation plays a role in the normal cell type-specific expression of miR-200c and miR-141 and this role appears evolutionarily conserved, since similar results were obtained in mouse. Aberrant DNA methylation of the miR-200c/141 CpG island is closely linked to their inappropriate silencing in cancer cells. Since the miR-200c cluster plays a significant role in EMT, our results suggest an important role for DNA methylation in the control of phenotypic conversions in normal cells.

Citation: Vrba L, Jensen TJ, Garbe JC, Heimark RL, Cress AE, et al. (2010) Role for DNA Methylation in the Regulation of miR-200c and miR-141 Expression in Normal and Cancer Cells. PLoS ONE 5(1): e8697. doi:10.1371/journal.pone.0008697

Editor: Catherine M. Suter, Victor Chang Cardiac Research Institute, Australia

Received October 13, 2009; **Accepted** December 21, 2009; **Published** January 13, 2010

Funding: Grants R01CA65662 to B.W.F supported this work. Center Grants P30ES06694 and P30CA023074, and the BIO5 interdisciplinary biotechnology center at the UA supported the Genomics Shared Service. J.C.G. and M.R.S. were supported by NIH U54 CA112970, DOD BCRP BC060444, and the Office of Energy Research, Office of Health and Biological Research, U.S. Department of Energy under Contract No. DE-AC03-76SF00098. The funders had no role in study design, data collection and analysis, decision to publish, or preparation of the manuscript.

Competing Interests: The authors have declared that no competing interests exist.

* E-mail: bfutscher@azcc.arizona.edu

Introduction

miRNAs are single-stranded, 20-24 nt long RNAs that regulate gene expression at the posttranscriptional level. miRNAs frequently target 3′ UTRs of mRNA, and since miRNA target motifs do not require complete homology, hundreds of mRNA targets may exist for each miRNA. Current estimates are that there are nearly 900 unique miRNAs encoded in the human genome, and these miRNAs control, in part, the expression of more than one third of human genes [1]. A number of miRNA dysregulated in human cancer have been shown to have oncogenic or tumor suppressive activity [2,3,4]. These include miRNA species that show cell type specific patterns of expression, some of which are important in the maintenance of cell identity [5,6]. These types of miRNA are prime targets for epigenetic control, and early studies of miRNA control support this possibility [7,8].

miR-200c and miR-141 are members of the miR-200 family and are important regulators of the epithelial to mesenchymal transition (EMT) [5,9,10,11]. In addition to the role of miR-200c and miR-141 in the phenotypic conversion of normal cells, dysregulation of normal patterns of miR-200c expression occurs in multiple types of cancer cells and is linked to tumor progression [2,6,12,13,14,15]. The mechanism responsible for the control of miR-200c expression in both normal and cancer cells is not fully understood. In this study, we show that the epigenetic state is closely linked to normal cell type specific expression of miR-200c

and miR-141, and this epigenetic state is dysregulated in carcinoma cells, where loss of miR200c/141 expression is linked to aberrant DNA methylation and histone modifications. Finally, we found that the miR-200c regulation by DNA methylation is evolutionarily conserved between humans and mice. Since miR-200c plays a significant role in EMT, our results suggest that DNA methylation plays an important role in the control of phenotypic conversions of normal and cancer cells.

Results and Discussion

The miR-200 family is comprised of five miRNAs that are encoded within two clusters. Each cluster encodes a polycistronic gene. One cluster resides on human chromosome 1 and encodes miR-200b, miR-200a, and miR-429, while the other cluster is located on human chromosome 12, and encodes miR-200c and miR-141. Our small RNA library sequencing data (Figure 1A) show that the miR-200 family is highly expressed in cultured normal human mammary epithelial cells (HMEC) derived from three different individuals, whereas the isogenic human mammary fibroblast cells (FB) lack miR-200 family expression (Figure 1A). It is apparent from the small RNA library sequencing data (Figure 1A) that the most highly expressed members of the miR-200 family in HMEC are miR-200c and miR-141. We corroborated the expression of miR-200c and miR-141 in the same set of normal mammary samples by real-time PCR, and then expanded these results to pairs of epithelial cells and fibroblasts from prostate and skin, as well (Figure 1B; Figure S1). In all cases, miR-200c and miR-141 were highly expressed in epithelial cells, but were not expressed in fibroblasts.

The mir-200c hairpin coding sequence and approximately 300 bp of upstream genomic sequence is CpG rich. According to our calculations using the program CpG Cluster [16] this region is a highly statistically significant CpG cluster (Figure 2A). This CpG cluster (length 334 bp, GC% 68.56, O/E ratio 0.58, 21CpGs, p-value 8.44×10^{-11}) has the characteristics close to a CpG island definition based on size, GC content and CpG dinucleotide frequency [17], as well as its location with respect to the transcriptional unit [18]. In addition, this region is considered a CpG island based on a recently published probabilistic definition [19]. We analyzed this region as a possible target of epigenetic control.

The epigenetic state of the miR-200c/141 CpG island shows clear and extensive cell type specific differences between normal miR-200c/141-positive and miR-200c/141-negative cells. We used MassARRAY technology to analyze the DNA methylation state of the mir-200c cluster CpG island (Figure 2B). Results show that the CpG sites are unmethylated in three separate strains of miR-200c/miR-141-positive HMEC. In contrast, all the CpG sites are highly methylated in the isogenic miR-200c/miR-141-negative fibroblast strains. The inverse correlation between miRNA expression and DNA methylation extends to other miR-200c/miR-141-positive/negative pairs of normal cells, such as prostate epithelial cells and skin keratinocytes, and their mesenchymal cell type counterparts, prostate and skin fibroblasts. Thus, the miR-200c cluster CpG island is unmethylated in normal miR-200c/miR-141-positive epithelial cells, while being densely methylated in the paired normal miR-200c/miR-141-negative fibroblasts (Figure 1B, Figure 2B, Figure S2).

miR-200c and miR-141 expression is lost in different types of cancer cells [5,11,20,21], and we sought to determine if this loss of expression was linked to epigenetic changes in the miR-200c/miR-141 CpG island. We analyzed 11 breast cancer cell lines, and in each case, miR-200c and miR-141 expression was closely linked to the DNA methylation state of the CpG island (Figure 3A; Figure S3). Seven of the breast cancer cell lines tested express miR-200c and miR-141 and each has an unmethylated mir-200c CpG island. The other four breast cancer cell lines tested do not express miR-200c and miR-141 and exhibit a densely methylated mir-200c CpG island. A similar picture emerges with respect to prostate cancer cells. We show two prostate cancer cell lines (PC3

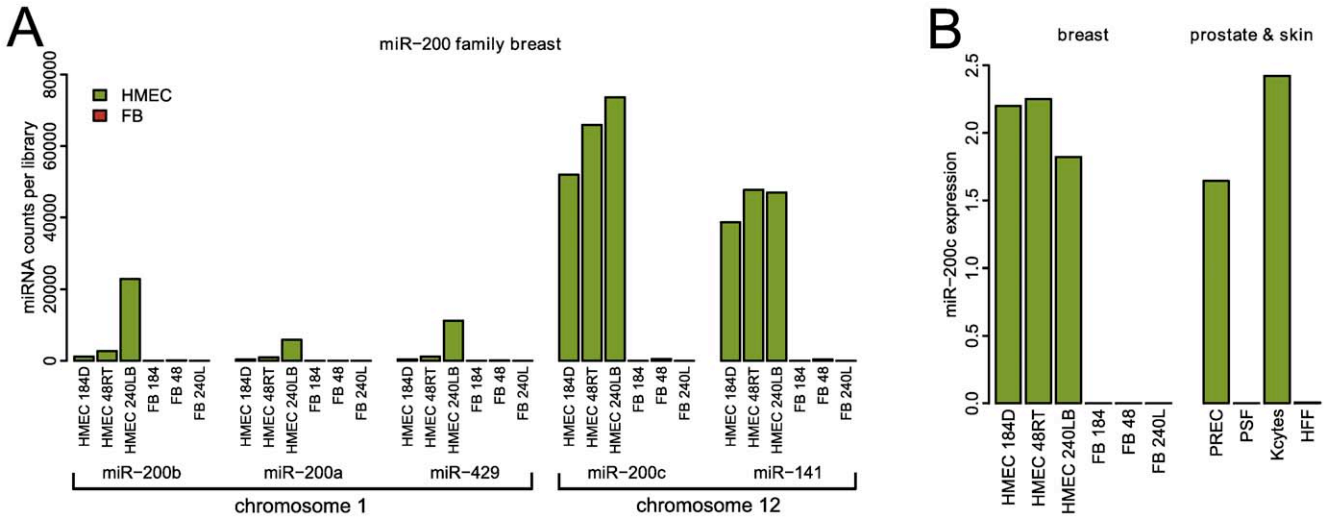

Figure 1. miR-200c is expressed in an epithelial selective fashion. A. miR-200 family expression according to massive parallel sequencing of small RNA libraries from a set of three isogenic pairs of human mammary epithelial cells (HMEC) and fibroblasts (FB). The expression of the mir-200b-200a-429 cluster located on human chromosome 1, and the expression of the mir-200c-141 cluster located on human chromosome 12 are shown. With the average of 63,829 counts out of 3,926,984 per library in HMEC, miR-200c forms 1.625% of all small RNAs in these cells. **B.** Real-time PCR assessment of miR-200c expression in normal cell types. The left panel shows the expression of miR-200c in the same samples as panel A. The right panel shows the expression of miR-200c in human prostate epithelial cells (PREC), prostate stromal fibroblasts (PSF), human skin keratinocytes (Kcytes) and skin fibroblasts (HFF). The data are normalized relative to let-7a, which is expressed at equivalent levels between different samples according to the small RNA sequencing data. Real time PCR analysis of miR-141 expression in these samples is provided in Figure S1.
doi:10.1371/journal.pone.0008697.g001

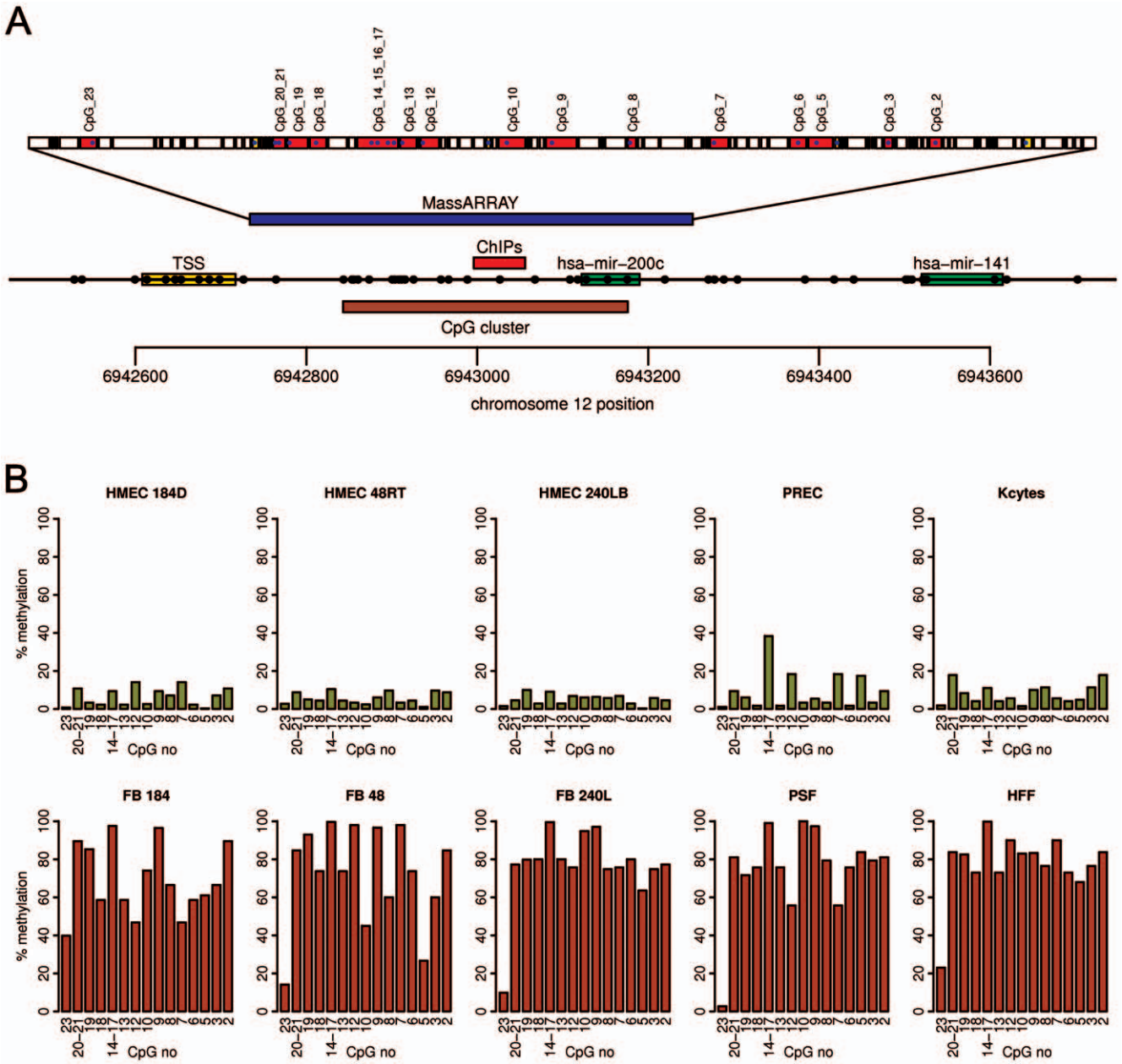

Figure 2. The mir-200c CpG island shows differential cytosine methylation between miR-200c-positive and miR-200c-negative normal human tissues. A. A diagram of the genomic region of hsa-mir-200c. The top bar shows the specific fragments analyzed by MassARRAY. The red fragments named with CpG sites indicate the fragments from which DNA methylation data was obtained. This data is presented panel B. Below this is the region analyzed by MassARRAY in relation to the genomic location (in blue), followed by the region of the real-time PCR amplicon for chromatin immunoprecipitation analysis (ChIP), and the CpG island identified by the program CpGcluster. The regions encoding the mir-200c and mir-141 hairpins and the putative transcription start (TSS) region inferred from the human EST track of the UCSC genome browser are displayed, and each circle on this track represents the position of a CpG dinucleotide. The ruler at the bottom shows the location on human chromosome 12 according to human genome assembly hg18. **B.** Summary of 5-methylcytosine levels obtained by MassARRAY analysis of the hsa-mir-200c CpG island in samples characterized in Figure 1B. The y-axis shows the percent of cytosine methylation within the individual CpG units marked on x-axis. The CpG units within the MassARRAY amplicon are numbered in the reverse direction, with CpG 2 being located within the miR-200c coding sequence.
doi:10.1371/journal.pone.0008697.g002

and PC3 B1) where loss of miR-200c and miR-141 expression is linked with aberrant DNA methylation of the mir-200c/141 CpG island (Figure 3B; Figure S3), and two prostate cancer cell lines (LNCaP and DU145) that retain miR-200c/miR-141 expression and an unmethylated mir-200c/141 CpG island. Together these results indicate that cancer cells derived from normal miR-200c/miR-141-positive epithelial cells can replicate the cell type-specific DNA methylation pattern of the miR-200c/141 CpG island seen in normal miR-200c/miR-141-negative cells, and that the aberrant DNA methylation of the miR200c/141 CpG island in these cancer cells is associated with its transcriptional silencing in carcinoma cells.

To demonstrate the functional significance of the epigenetic state of the miR-200c/mir-141 CpG island in cancer cells, we

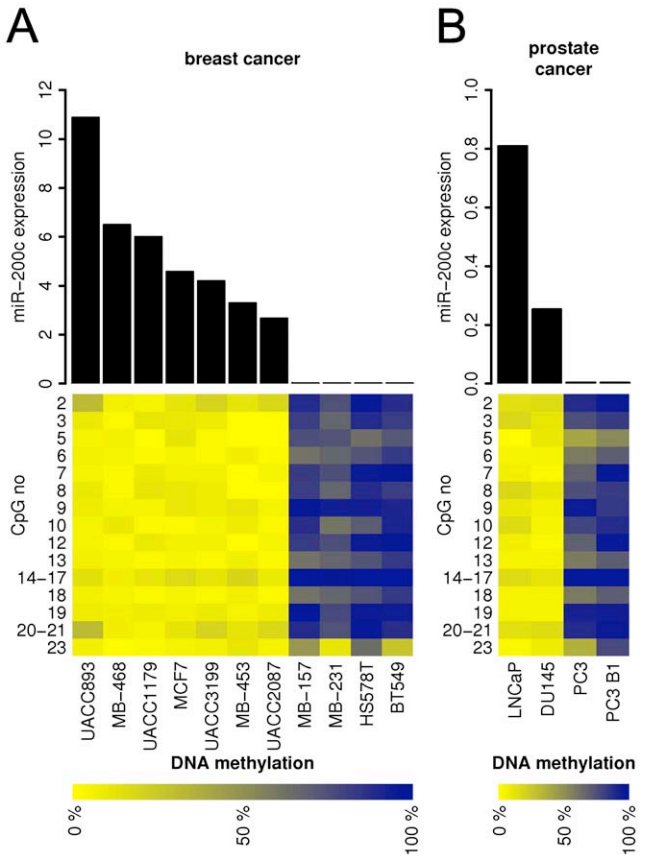

Figure 3. DNA methylation of mir-200c CpG island in breast and prostate cancer cell lines. A. miR-200c expression and mir-200c CpG island methylation in eleven breast cancer cell lines. **B.** miR-200c expression and mir-200c CpG island methylation in four prostate cancer cell lines. The top panel of each figure shows the expression of miR-200c in cancer samples as detected by real-time PCR, normalized to let-7a. The bottom panel shows the methylation level of the mir-200c CpG island region in the same cancer samples. The level of methylation of individual CpG units within the MassARRAY amplicon is displayed as a heatmap with the lowest methylation in yellow and the highest methylation in blue. The y-axis marks the individual CpG units.
doi:10.1371/journal.pone.0008697.g003

exposed cancer cells to the epigenetic modifier and DNA methyltransferase inhibitor 5-aza-2′-deoxycytidine (5-AdC). The miR-200c/miR-141-negative breast cancer cell lines MDA-MB-231 and BT549 and prostate cancer cell line PC3 were treated with 3 μM 5-AdC for 96 h and miR-200c/141 expression was assessed by real-time PCR. Figure 4 shows 5-AdC reactivated miR-200c expression in all three cancer cell lines. The level of miR-200c increased 4.3-fold in MDA-MB-231 (p-value = 0.0004), 6.4-fold in BT549 (p-value = 0.0107) and 4.2-fold in PC3 cells (p-value = 0.0072). A similar reactivation of miR-141 expression (p-value<0.01) was also observed in these cancer cell lines after 5-AdC treatment (Figure S4). These data suggest that epigenetic mechanisms participate in the inappropriate repression of miR-200c/miR-141 expression in cancer cells.

The histone modification state of the mir-200c cluster CpG island also shows cell type-specific differences that are closely linked to the expression state of miR-200c/141 in normal and cancer cells. Figure 5 shows the results of chromatin immunoprecipitations coupled to quantitative real-time PCR analysis that were used to examine the histone modification state of the miR-200c/141 CpG island in normal and cancer cells. The CpG island

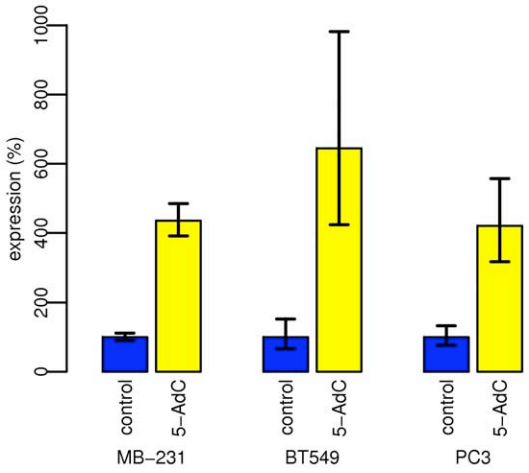

Figure 4. 5-aza-2′-deoxycytidine treatment reactivates miR-200c expression in breast and prostate cancer cell lines. Cells were treated with 3 μM 5-aza-2′-deoxycytidine for 96 h. The level of expression of miR-200c was measured by real-time PCR. The average of 4 independent samples is displayed, the error bars show the standard error of measurement. The values were normalized to untreated controls (100%). Figure S4 shows the 5-aza-2′-deoxycytidine-mediated reactivation of miR-141 in the same samples.
doi:10.1371/journal.pone.0008697.g004

of mir-200c/141 in the three different strains of miR-200c/miR-141-positive HMEC exists in a transcriptionally competent state; it is enriched for the transcriptionally permissive modifications of histone H3 acetylation (H3Ac) and lysine 4 trimethylation (H3TriMeK4), while the transcriptionally repressive histone mark of histone H3 lysine 9 dimethylation (H3DiMeK9) is underrepresented (Figure 5). In contrast, in the isogenic miR-200c/miR-141-negative mammary fibroblasts permissive histone modifications are absent, and the repressive H3 lysine 9 dimethylation mark is present (Figure 5). Similarly, the breast cancer cell lines

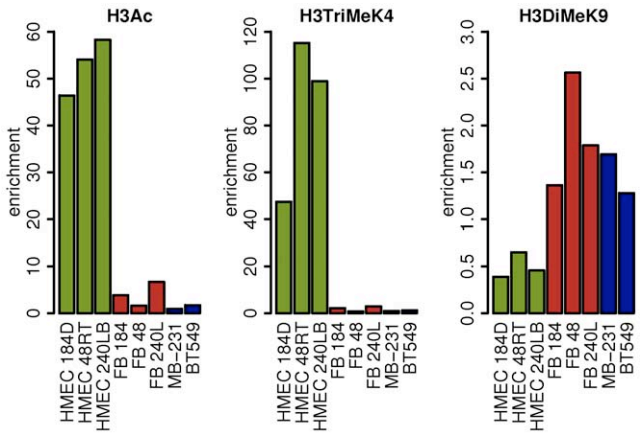

Figure 5. The histone modification state of the mir-200c CpG island. Permissive histone marks represented by acetylation of histone H3 (H3Ac) and trimethylation of lysine 4 of histone H3 (H3TriMeK4) as well as the repressive histone mark dimethylation of lysine 9 of histone H3 (H3diMeK9) were analyzed using chromatin immunoprecipitation coupled to real-time PCR of the region described in Figure 2A. HMEC samples are shown in green, isogenic FB samples are shown in red, and two miR-200-negative breast cancer cell lines are in blue. The y-axis shows fold enrichment of each histone mark over input DNA within the mir-200c CpG island.
doi:10.1371/journal.pone.0008697.g005

that had lost miR-200c/141 expression lost histone H3 acetylation and K4 trimethylation and acquired a repressive histone state, enriched for the H3 lysine 9 dimethylation mark (Figure 5). No enrichment of trimethylation of histone H3 lysine 27 was detected in the miR-200c/141 CpG island in the samples analyzed (Figure S5). Taken together, the results from the analyses of miR-200c/141 expression, DNA methylation, and histone modification states across a variety of normal and cancer cell types demonstrate a close link between the expression of mir-200c/141 and the epigenetic state of their associated CpG island.

Finally, we sought to determine if the epigenetic regulation of miR-200c expression in normal cells is conserved evolutionarily, reasoning that DNA methylation-linked control of miR-200c expression across mammalian species would provide further experimental support for epigenetic control of cell-type specific expression of miR-200c. The whole genomic cluster containing mir-200c and mir-141 is well conserved between the human and mouse genome. Similar to the human mir-200c/141 genomic region, the mouse mir-200c/141 genomic region also contains a CpG island (Figure 6A; length 325 bp, GC% 66.77, O/E ratio 0.58, 19 CpGs, p-value 1.06×10^{-10}). To evaluate a potential role for DNA methylation in the control of miR-200c/141 in mice, CpG methylation and miRNA expression were analyzed in mouse epithelial cells (epidermis of SKH-1 mouse and keratinocyte cell lines 308 and 6R90) and mouse fibroblasts (cell lines NIH 3T3, NIH 3T6, and NR6). A MassARRAY amplicon was designed to analyze the DNA methylation state of the mouse mir-200c/141 region homologous to that analyzed in human (Figure 6A). Strikingly similar results for miR-200c were found between the human cells and mouse cells. Mouse keratinocytes expressed significant levels of miR-200c, while the mouse fibroblasts did not express detectable levels of miR-200c (Figure 6B). DNA methylation analysis by MassARRAY revealed that the miR-200c-positive keratinocytes showed minimal DNA methylation in the mir-200c CpG island, while the miR-200c-negative mouse fibroblasts showed extensive DNA methylation of all CpG sites in the region (Figure 6B). The significant conservation in DNA sequence, patterns of cell type-specific DNA methylation, and the associated miR-200c expression patterns between the human and mouse genomes, which are separated by 75 million years of evolution [22], provides evidence that epigenetic mechanisms play a functional role in the control of miR-200c expression.

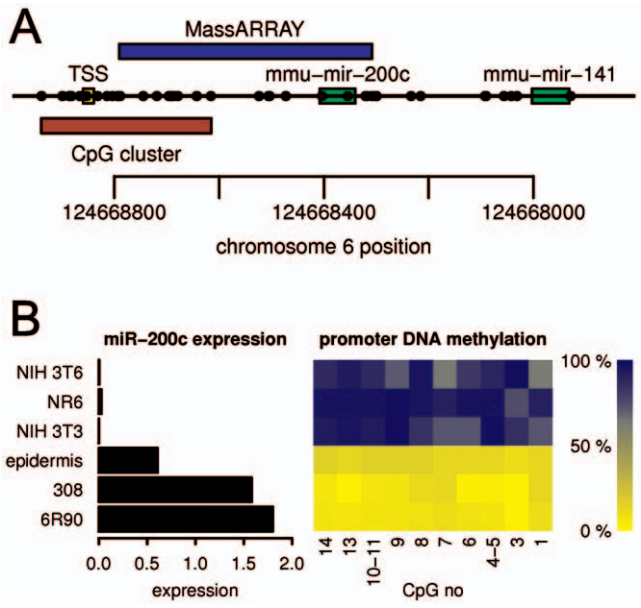

Figure 6. Epigenetic control of miR-200c expression is evolutionarily conserved. A. Diagram of the mouse mmu-mir-200c genomic interval. The top bar shows the area analyzed by MassARRAY. The regions encoding the hairpins of mir-200c and mir-141 and the putative transcription start (TSS) inferred from the mouse EST track displayed on the UCSC genome browser are shown, and each circle on this track represents the location of a CpG dinucleotide. Similar to the human hsa-mir-200c, the mouse mmu-mir-200c contains a CpG island, identified by the program CpG Cluster. The ruler at the bottom shows the location on mouse chromosome 6 according to genome assembly mm9. The genes are encoded on the (-) strand. **B.** Mouse cells show a similar cell type specific pattern in miR-200c expression to human cells and this expression is linked to the DNA methylation state of the CpG island. The left panel shows the expression of miR-200c in mouse epithelial cells (308, 6R90, SKH-1 epidermis) and mouse fibroblast cell lines (NIH 3T3, NR6, NIH 3T6) as detected by real-time PCR. The right panel shows the methylation level of the mir-200c CpG island region in the same mouse samples. The level of methylation of individual CpG units within the MassARRAY amplicon is displayed as a heatmap with the lowest methylation in yellow and the highest methylation in blue. The x-axis marks the individual CpG units. CpG units within MassARRAY amplicon are numbered in reverse direction, with CpG 1 being located within the miR-200c coding sequence.
doi:10.1371/journal.pone.0008697.g006

In summary, our findings provide multiple lines of evidence that epigenetic mechanisms are involved in the regulation of miR-200c/141 expression in both normal and cancer cells. First, there is a consistent inverse correlation between expression and DNA methylation states in normal human and mouse cell types, as well as human breast and prostate cancer cell lines. Second, different histone codes exist between miR-200c/141 expressing and non-expressing cells that accurately mirror the expression and DNA methylation states. Third, the epigenetic modifier 5-aza-2′-deoxycytidine relieves the repression of miR-200c/miR-141 in cancer cell lines. Fourth, the link between DNA methylation and expression states occurs across mammalian species, since it is seen in human and mouse. Taken together, these findings indicate that miR-200c/141 is an evolutionarily conserved epigenetically labile miRNA cluster.

Dysregulation of miR-200c and miR-141 occurs in multiple cancer types [5,11,20,21,23,24,25,26], and this dysregulation involves a compromise of the epigenetic state of the CpG island associated with miR-200c and miR141. Results suggest that these carcinoma cells may co-opt *de novo* DNA methylation pathways involved in the epigenetic control of normal cell type-specific genes, such as those that govern the epigenetic state of miR-200c/miR-141. A similar apparent co-option of cell type specific DNA methylation pathways by cancer cells is also seen in protein-coding genes, such as *maspin* and *14-3-3 sigma* [27,28]. Together these results suggest that pathways responsible for the establishment or maintenance of normal cell type-specific DNA methylation states may be disrupted during carcinogenesis.

Since miR-200c and miR141 play an important role in EMT and therefore cell identity, disruption of mechanisms that govern cell type specific DNA methylation patterns during carcinogenesis could likely effect expression of miR-200c and miR141 and provide phenotypic plasticity to cancer cells. Support of this possibility comes from the phenotypes of the cancer cells analyzed in this study. All four of the breast cancer cell lines that lost miR-200c and miR-141 expression have an aberrantly methylated mir-200c/141 CpG island, and each of these cell lines displays a mesenchymal phenotype [11,29]. In contrast, those breast cancer cell lines that express miR-200c and miR-141 and have an unmethylated CpG island display an epithelial phenotype [11,29]. A similar picture emerges in the prostate cancer cell lines. The

PC3 cells that have lost miR-200c and miR-141 expression, display an aberrantly methylated CpG island and a mesenchymal phenotype, whereas LnCaP and Du145 retain miR-200c and miR-141 expression and an epithelial phenotype [11,30]. These results suggest that DNA methylation may control the phenotypic changes observed in cancer cells.

Materials and Methods

Cell lines and cell culture

Finite lifespan pre-stasis HMEC from specimens 184 (batch D), 48R (batch T), and 240L (batch B), were derived from reduction mammoplasty tissue of women aged 21, 16, and 19 respectively. Cells were initiated as organoids in primary culture in serum-containing M85 medium supplemented with oxytocin (Bachem) at 0.1 nM, and maintained in M87A medium supplemented with oxytocin and cholera toxin at 0.5 ng/ml [31]. Fibroblasts from specimens 184, 48, and 240 L were obtained from the same reduction mammoplasty tissue and were grown in DMEM/F12 with 10% FBS and 10 μg/ml insulin [31] and further propagated in DMEM/F12 with 10% FBS. Prostate epithelial cells were obtained from Clonetics (San Diego, CA), and fetal skin keratinocytes from Cell Applications (San Diego, CA.) and were grown according to the suppliers instructions. Human foreskin fibroblasts (HFFs) were maintained and cultured by the Arizona Cancer Center Cell Culture Shared Service. Human prostate stromal fibroblasts (PSF) were were cultured as previously described [32]. Breast cancer cell lines BT549, HS578T, MCF7, MDA-MB-157, MDA-MB-231, MDA-MB-453, MDA-MB-468, UACC893, UACC1179, UACC2087, and UACC3199 were cultured as previously described [33,34]. Prostate cancer cell lines PC3, PC3 B1, LNCaP, and DU145 [35,36,37] were maintained in RPMI 1640 medium containing 10% fetal bovine serum supplemented with 100 units/ml penicillin and 50 μg/ml streptomycin. Mouse keratinocyte cell lines 308 and 6R90 were cultured as described [38], mouse fibroblast cell lines NIH 3T3, NIH 3T6 and NR6 [39,40,41] were maintained in DMEM medium containing 10% fetal bovine serum. SKH-1 mouse epidermis samples were removed from liquid nitrogen snap frozen dorsal skin by scraping on dry ice.

miRNA library preparation, sequencing and analysis

Total RNA was extracted using Trizol. The small RNA fraction was purified on a 15% polyacrylamide-urea gel. A preadenylated adaptor was ligated to the 3′ end of the small RNA followed by purification of the ligation product on a 15% PAA-urea gel. An Illumina specific 5′ adaptor was ligated and the product was purified on a 10% PAA-urea gel. Small RNA with ligated adaptors was reverse transcribed into DNA using a RT primer with Illumina specific extension. cDNA was then PCR amplified using Illumina specific primers and the PCR product was purified on a 3% agarose gel. Small RNA libraries were submitted for Illumina sequencing to NCGR (Santa Fe, NM). Reads from Illumina GAII were mapped to the hg18 human genome assembly using program Novoalign (www.novocraft.com). Output from Novoalign was further analyzed in R (http://www.r-project.org). The counts of individual miRNAs were normalized for average library size (3,926,984 counts).

Nucleic acid isolation

RNA was isolated using either Trizol (Invitrogen) or the RNeasy Mini kit (Qiagen) and quantified by absorption measurements at 260 nm. Genomic DNA was isolated using the DNeasy Blood and Tissue Kit (Qiagen) and quantified spectrophotometrically.

Real-time PCR detection of miRNA

Real-time PCR detection of microRNAs was performed in principle as described [42]. Reverse transcription was performed using TaqMan Reverse Transcription Reagents (Applied Biosystems, Foster City, CA, USA). Real-time PCR was conducted on an ABI Prism 7500 Sequence Detection System (Applied Biosystems, Foster City, CA, USA) using PerfeCta SYBR Green SuperMix, Low ROX (Quanta Biosciences, Gaithersburg, MD, USA) with a 95°C denaturation for 3 minutes followed by 40 cycles of 95°C for 15 seconds and 60°C for 45 seconds. Differences in expression were determined using the comparative Ct method described in the ABI user manual relative to let-7a. Primer sequences are listed in Table S1.

CpG island prediction

CpG islands were predicted using the program CpGcluster [16]. This program uses a statistical approach to search for regions with significant enrichment of CpG dinucleotides rather than parameters within a sliding window. We set the threshold to 50 (median distance) and p-value cut to 10^{-8}.

DNA methylation analysis by MassARRAY

DNA methylation analysis by MassARRAY was performed as described [43]. Primer sequences are listed in Table S1.

5-aza-2′-deoxycytidine treatment

Cells were treated with 3 μM 5-aza-2′-deoxycytidine (Sigma, St Louis, MO, USA) for 96 h, as previously described [44].

Chromatin immunoprecipitation

Chromatin immoprecipitation (ChIP) analysis was performed as described previously [33,45,46] with antibodies against acetylated histone H3 (#06-599, Millipore), trimethylated histone H3 K4 (#05-745, Upstate), dimethylated histone H3 K9 (CS200587, Millipore), and trimethylated histone H3 K27 (#07-449, Millipore). Equal amounts (1 ng) of ChIP and input DNA were used for real-time PCR analysis. Primers were designed for use with the Human Universal Probe Library Set (Roche Diagnostics, Indianapolis, IN, USA). Real-time PCR was conducted on an ABI Prism 7500 Sequence Detection System (Applied Biosystems, Foster City, CA, USA) using PerfeCta qPCR SuperMix, Low ROX (Quanta Biosciences, Gaithersburg, MD, USA) with a 95°C denaturation for 3 minutes followed by 40 cycles of 95°C for 15 seconds and 60°C for 45 seconds. Primer sequences are listed in Table S1.

Supporting Information

Figure S1 Real-time PCR assessment of miR-141 expression in normal cell types. The left panel shows the expression of miR-141 in three isogenic pairs of mammary epithelial cells (HMEC) and mammary fibroblasts (FB). The right panel shows the expression of miR-141 in human prostate epithelial cells (PREC), prostate stromal fibroblasts (PSF), human skin keratinocytes (Kcytes) and skin fibroblasts (HFF). The data are normalized relative to let-7a, which is expressed at consistent levels between different samples according to the small RNA sequencing data.
Found at: doi:10.1371/journal.pone.0008697.s001 (0.13 MB TIF)

Figure S2 DNA methylation of the mir-200c CpG island inversely correlates with miR-200c expression in normal human samples. This figure summarizes data shown in Figure 1B and 2B. The upper panel shows the expression of miR-200c detected by real-time PCR. The bottom panel shows the methylation level of

mir-200c CpG island region in the same human samples. The level of methylation of individual CpG units within the MassARRAY amplicon is displayed as a heatmap with the lowest methylation in yellow and the highest methylation in blue. The y-axis marks the individual CpG units.
Found at: doi:10.1371/journal.pone.0008697.s002 (0.19 MB TIF)

Figure S3 Real-time PCR assessment of miR-141 expression in breast and prostate cancer cell lines. The left panel shows the expression of miR-141 in eleven human breast cancer cell lines. The right panel shows the expression of miR-141 in four human prostate cancer cell lines.
Found at: doi:10.1371/journal.pone.0008697.s003 (0.14 MB TIF)

Figure S4 miR-141 expression in cancer cell lines is reactivated by 5-aza-2′-deoxycytidine treatment. Cells were treated with 3 μM 5-AdC for 96 h. The level of expression of miR-141 was measured by real-time PCR. The average of 4 measurements is displayed, the error bars show the standard error of measurement. The values were normalized to untreated controls (100%).
Found at: doi:10.1371/journal.pone.0008697.s004 (0.06 MB TIF)

Figure S5 Histone H3 K27 trimethylation state of the mir-200c CpG island. Histone H3 lysine 27 trimethylation levels of the region of the mir-200c CpG island described in Figure 2A were analyzed by chromatin immunoprecipitation coupled to real-time PCR. Epithelial cells (HMEC) are shown in green and their isogenic fibroblasts (FB) are shown in red. The y-axis shows a lack of enrichment of the histone H3 K27 trimethylation mark within the mir-200c CpG island relative to input DNA in all the samples analyzed.
Found at: doi:10.1371/journal.pone.0008697.s005 (0.08 MB TIF)

Table S1 List of primer sequences used in the study
Found at: doi:10.1371/journal.pone.0008697.s006 (0.03 MB PDF)

Acknowledgments

We thank Brenna Rheinheimer (UA) and Batul Merchant (LBNL) for outstanding technical support.

Author Contributions

Conceived and designed the experiments: LV BWF. Performed the experiments: LV TJJ. Analyzed the data: LV TJJ. Contributed reagents/materials/analysis tools: JG RRH AC SD MRS. Wrote the paper: LV MRS BWF.

References

1. Kim VN, Han J, Siomi MC (2009) Biogenesis of small RNAs in animals. Nat Rev Mol Cell Biol 10: 126–139.
2. Ma L, Teruya-Feldstein J, Weinberg RA (2007) Tumour invasion and metastasis initiated by microRNA-10b in breast cancer. Nature 449: 682–688.
3. Negrini M, Nicoloso MS, Calin GA (2009) MicroRNAs and cancer–new paradigms in molecular oncology. Curr Opin Cell Biol 21: 470–479.
4. Bracken CP, Gregory PA, Khew-Goodall Y, Goodall GJ (2009) The role of microRNAs in metastasis and epithelial-mesenchymal transition. Cell Mol Life Sci 66: 1682–1699.
5. Gregory PA, Bert AG, Paterson EL, Barry SC, Tsykin A, et al. (2008) The miR-200 family and miR-205 regulate epithelial to mesenchymal transition by targeting ZEB1 and SIP1. Nat Cell Biol 10: 593–601.
6. Peter ME (2009) Let-7 and miR-200 microRNAs: guardians against pluripotency and cancer progression. Cell Cycle 8: 843–852.
7. Visone R, Croce CM (2009) MiRNAs and cancer. Am J Pathol 174: 1131–1138.
8. Valeri N, Vannini I, Fanini F, Calore F, Adair B, et al. (2009) Epigenetics, miRNAs, and human cancer: a new chapter in human gene regulation. Mamm Genome.
9. Hurteau GJ, Carlson JA, Spivack SD, Brock GJ (2007) Overexpression of the microRNA hsa-miR-200c leads to reduced expression of transcription factor 8 and increased expression of E-cadherin. Cancer Res 67: 7972–7976.
10. Burk U, Schubert J, Wellner U, Schmalhofer O, Vincan E, et al. (2008) A reciprocal repression between ZEB1 and members of the miR-200 family promotes EMT and invasion in cancer cells. EMBO Rep 9: 582–589.
11. Park SM, Gaur AB, Lengyel E, Peter ME (2008) The miR-200 family determines the epithelial phenotype of cancer cells by targeting the E-cadherin repressors ZEB1 and ZEB2. Genes Dev 22: 894–907.
12. Lu J, Getz G, Miska EA, Alvarez-Saavedra E, Lamb J, et al. (2005) MicroRNA expression profiles classify human cancers. Nature 435: 834–838.
13. Volinia S, Calin GA, Liu CG, Ambs S, Cimmino A, et al. (2006) A microRNA expression signature of human solid tumors defines cancer gene targets. Proc Natl Acad Sci U S A 103: 2257–2261.
14. Friedman JM, Liang G, Liu CC, Wolff EM, Tsai YC, et al. (2009) The putative tumor suppressor microRNA-101 modulates the cancer epigenome by repressing the polycomb group protein EZH2. Cancer Res 69: 2623–2629.
15. Varambally S, Cao Q, Mani RS, Shankar S, Wang X, et al. (2008) Genomic loss of microRNA-101 leads to overexpression of histone methyltransferase EZH2 in cancer. Science 322: 1695–1699.
16. Hackenberg M, Previti C, Luque-Escamilla PL, Carpena P, Martinez-Aroza J, et al. (2006) CpGcluster: a distance-based algorithm for CpG-island detection. BMC Bioinformatics 7: 446.
17. Gardiner-Garden M, Frommer M (1987) CpG islands in vertebrate genomes. J Mol Biol 196: 261–282.
18. Ioshikhes IP, Zhang MQ (2000) Large-scale human promoter mapping using CpG islands. Nat Genet 26: 61–63.
19. Irizarry RA, Wu H, Feinberg AP (2009) A species-generalized probabilistic model-based definition of CpG islands. Mamm Genome.
20. Du Y, Xu Y, Ding L, Yao H, Yu H, et al. (2009) Down-regulation of miR-141 in gastric cancer and its involvement in cell growth. J Gastroenterol 44: 556–561.
21. Shimono Y, Zabala M, Cho RW, Lobo N, Dalerba P, et al. (2009) Downregulation of miRNA-200c links breast cancer stem cells with normal stem cells. Cell 138: 592–603.
22. Waterston RH, Lindblad-Toh K, Birney E, Rogers J, Abril JF, et al. (2002) Initial sequencing and comparative analysis of the mouse genome. Nature 420: 520–562.
23. Iorio MV, Visone R, Di Leva G, Donati V, Petrocca F, et al. (2007) MicroRNA signatures in human ovarian cancer. Cancer Res 67: 8699–8707.
24. Ladeiro Y, Couchy G, Balabaud C, Bioulac-Sage P, Pelletier L, et al. (2008) MicroRNA profiling in hepatocellular tumors is associated with clinical features and oncogene/tumor suppressor gene mutations. Hepatology 47: 1955–1963.
25. Nam EJ, Yoon H, Kim SW, Kim H, Kim YT, et al. (2008) MicroRNA expression profiles in serous ovarian carcinoma. Clin Cancer Res 14: 2690–2695.
26. Kong D, Li Y, Wang Z, Banerjee S, Ahmad A, et al. (2009) miR-200 Regulates PDGF-D-Mediated Epithelial-Mesenchymal Transition, Adhesion, and Invasion of Prostate Cancer Cells. Stem Cells 27: 1712–1721.
27. Futscher BW, Oshiro MM, Wozniak RJ, Holtan N, Hanigan CL, et al. (2002) Role for DNA methylation in the control of cell type specific maspin expression. Nat Genet 31: 175–179.
28. Oshiro MM, Futscher BW, Lisberg A, Wozniak RJ, Klimecki WT, et al. (2005) Epigenetic regulation of the cell type-specific gene 14-3-3sigma. Neoplasia 7: 799–808.
29. Blick T, Widodo E, Hugo H, Waltham M, Lenburg ME, et al. (2008) Epithelial mesenchymal transition traits in human breast cancer cell lines. Clin Exp Metastasis 25: 629–642.
30. Hugo H, Ackland ML, Blick T, Lawrence MG, Clements JA, et al. (2007) Epithelial–mesenchymal and mesenchymal–epithelial transitions in carcinoma progression. J Cell Physiol 213: 374–383.
31. Garbe JC, Bhattacharya S, Merchant B, Bassett E, Swisshelm K, et al. (2009) Molecular distinctions between stasis and telomere attrition senescence barriers shown by long-term culture of normal human mammary epithelial cells. Cancer Res 69: 7557–7568.
32. Tran NL, Nagle RB, Cress AE, Heimark RL (1999) N-Cadherin expression in human prostate carcinoma cell lines. An epithelial-mesenchymal transformation mediating adhesion withStromal cells. Am J Pathol 155: 787–798.
33. Oshiro MM, Watts GS, Wozniak RJ, Junk DJ, Munoz-Rodriguez JL, et al. (2003) Mutant p53 and aberrant cytosine methylation cooperate to silence gene expression. Oncogene 22: 3624–3634.
34. Domann FE, Rice JC, Hendrix MJ, Futscher BW (2000) Epigenetic silencing of maspin gene expression in human breast cancers. Int J Cancer 85: 805–810.
35. Kaighn ME, Narayan KS, Ohnuki Y, Lechner JF, Jones LW (1979) Establishment and characterization of a human prostatic carcinoma cell line (PC-3). Invest Urol 17: 16–23.
36. Stone KR, Mickey DD, Wunderli H, Mickey GH, Paulson DF (1978) Isolation of a human prostate carcinoma cell line (DU 145). Int J Cancer 21: 274–281.
37. Horoszewicz JS, Leong SS, Kawinski E, Karr JP, Rosenthal H, et al. (1983) LNCaP model of human prostatic carcinoma. Cancer Res 43: 1809–1818.
38. Gupta A, Rosenberger SF, Bowden GT (1999) Increased ROS levels contribute to elevated transcription factor and MAP kinase activities in malignantly progressed mouse keratinocyte cell lines. Carcinogenesis 20: 2063–2073.

39. Pruss RM, Herschman HR (1977) Variants of 3T3 cells lacking mitogenic response to epidermal growth factor. Proc Natl Acad Sci U S A 74: 3918–3921.
40. Jainchill JL, Aaronson SA, Todaro GJ (1969) Murine sarcoma and leukemia viruses: assay using clonal lines of contact-inhibited mouse cells. J Virol 4: 549–553.
41. Todaro GJ, Green H (1963) Quantitative studies of the growth of mouse embryo cells in culture and their development into established lines. J Cell Biol 17: 299–313.
42. Sharbati-Tehrani S, Kutz-Lohroff B, Bergbauer R, Scholven J, Einspanier R (2008) miR-Q: a novel quantitative RT-PCR approach for the expression profiling of small RNA molecules such as miRNAs in a complex sample. BMC Mol Biol 9: 34.
43. Novak P, Jensen TJ, Garbe JC, Stampfer MR, Futscher BW (2009) Stepwise DNA methylation changes are linked to escape from defined proliferation barriers and mammary epithelial cell immortalization. Cancer Res 69: 5251–5258.
44. Wozniak RJ, Klimecki WT, Lau SS, Feinstein Y, Futscher BW (2007) 5-Aza-2′-deoxycytidine-mediated reductions in G9A histone methyltransferase and histone H3 K9 di-methylation levels are linked to tumor suppressor gene reactivation. Oncogene 26: 77–90.
45. Vrba L, Junk DJ, Novak P, Futscher BW (2008) p53 induces distinct epigenetic states at its direct target promoters. BMC Genomics 9: 486.
46. Jensen TJ, Novak P, Eblin KE, Gandolfi AJ, Futscher BW (2008) Epigenetic remodeling during arsenical-induced malignant transformation. Carcinogenesis 29: 1500–1508.

Molecular Cell
Article

Primary Cilium-Dependent and -Independent Hedgehog Signaling Inhibits p16^{INK4A}

Cleo L. Bishop,[1,*] Ann-Marie H. Bergin,[1,4] Delphine Fessart,[1,4] Viola Borgdorff,[1] Elizabeth Hatzimasoura,[1] James C. Garbe,[2] Martha R. Stampfer,[2] Jim Koh,[3] and David H. Beach[1]
[1]Blizard Institute of Cell and Molecular Science, Barts and The London School of Medicine and Dentistry, 4 Newark Street, London E1 2AT, UK
[2]Life Science Division, Lawrence Berkeley National Laboratory, Berkeley, CA 94720, USA
[3]Division of Surgical Sciences, Department of Surgery, Duke University Medical School, Durham, NC 27710, USA
[4]These authors contributed equally to this work
*Correspondence: c.l.bishop@qmul.ac.uk
DOI 10.1016/j.molcel.2010.10.027

SUMMARY

In a genome-wide siRNA analysis of p16^{INK4a} (p16) modulators, we identify the Hedgehog (Hh) pathway component SUFU and formally demonstrate that Hh signaling promotes mitogenesis by suppression of p16. A fragment of the Hh-responsive GLI2 transcription factor directly binds and inhibits the *p16* promoter and senescence is associated with the loss of nuclear GLI2. Hh components partially reside in the primary cilium (PC), and the small fraction of cells in mass culture that elaborate a PC have the lowest expression of p16. Suppression of p16 is effected by both PC-dependent and -independent routes, and ablation of p16 renders cells insensitive to an Hh inhibitor and increases PC formation. These results directly link a well-established developmental mitogenic pathway with a key tumor suppressor and contribute to the molecular understanding of replicative senescence, Hh-mediated oncogenesis, and potentially the role of p16 in aging.

INTRODUCTION

The mammalian cell-division cycle is primarily regulated at the rate-limiting G1 phase. The CYCLIN D/CDK4 family of protein kinases is a positive effector of G1 transit and is counteracted by p16, a simple ankyrin repeat protein that directly binds and inhibits CDK4/6 (Serrano et al., 1993). p16 is dispensable for development in rodents and man, but becomes progressively expressed in a wide variety of tissues as animals age and is emerging as a useful marker of biological age (Tsygankov et al., 2009). p16 inactivation contributes, as an early step, to an extremely wide spectrum of human cancers, either by mutation or promoter methylation (Kim and Sharpless, 2006), and the gene maps to a complex genetic locus (9p21.3, also known as *INK4/ARF*) that has been repeatedly linked in genome-wide association studies to other prevalent age-associated diseases, including coronary heart disease and type 2 diabetes (Matheu et al., 2009). p16 expression is associated with loss of proliferative capacity in vitro and in animal models of regeneration, such as the rodent immune system (Janzen et al., 2006) and human kidney transplantation (Chkhotua et al., 2003). Alternatively, recovery from chemically induced pancreatic β-cell damage (Krishnamurthy et al., 2006) and reduced (or null) p16 allows improved postoperative function.

Although *p16* mRNA (Wang et al., 2005) and protein (Chen et al., 2007) are unstable and therefore subject to modulation, regulation at the level of gene expression has been more extensively investigated. *p16*, together with the closely linked *Arf* and *p15* genes, are inhibited by two polycomb repressive complexes, the components of which include BMI1, CBX7, CBX8, MEL-18, EZH2, and SUZ12 (Gil and Peters, 2006). Individual transcription factors that directly control p16 expression include ETS1, Id, β-CATENIN (CTNNB1), and recently MEOX2 (GAX) (Irelan et al., 2009). However, with the exception of ETS1-mediated p16 induction by the RAS/RAF/MEK cascade during oncogenic hyperstimulation (resulting in oncogene-induced senescence) (Serrano et al., 1997), there is a conspicuous lack of understanding of the broader physiological pathways that mediate postnatal derepression of p16.

This issue is exemplified by the phenomenon of premature expression of p16 in tissue culture. With the exception of embryonic stem cells, essentially all primary mammalian cells undergo decay of proliferative capacity (replicative senescence) upon repeated passage (Hayflick, 1965). In the great majority of isolates that have not undergone spontaneous genetic changes in vivo or in vitro, cell-cycle arrest is mediated by powerful progressive p16 induction, the physiological inducer(s) of which are essentially unknown. In order to explore this issue and to develop an improved understanding of the repertoire of p16 modulators, we have undertaken a genome-wide siRNA screen in normal finite lifespan human mammary epithelial cells (HMECs) in which p16-mediated senescence is well established (Brenner et al., 1998; Garbe et al., 2009).

RESULTS

Genome-wide siRNA Screen

We have recently developed improved media for the culture of finite life-span HMECs (Garbe et al., 2009) that supports approximately 50 cell doublings. HMECs cultured under these conditions are estrogen independent (tamoxifen resistant) and display

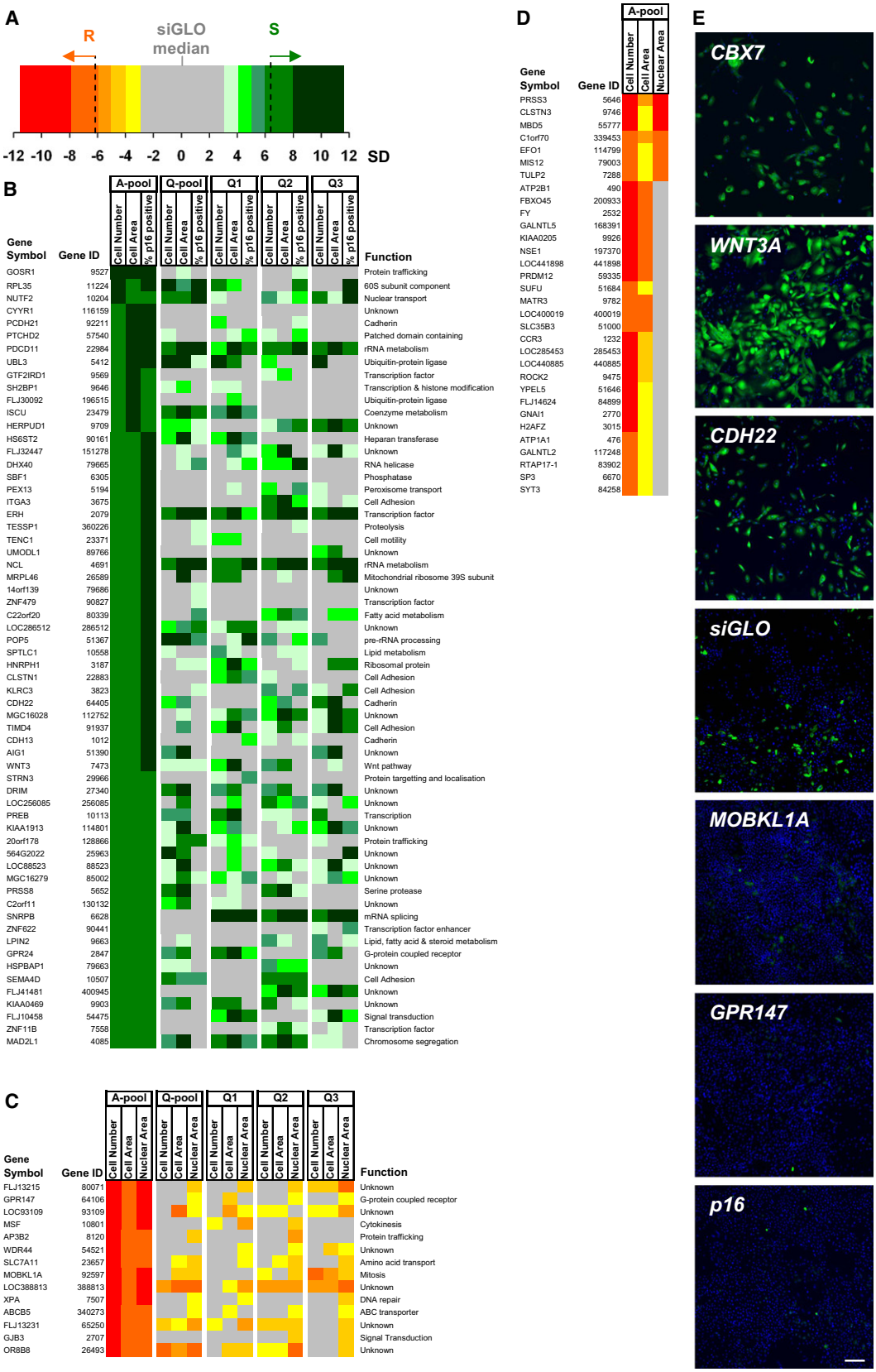
A
R
siGLO median
S
-12 -10 -8 -6 -4 -2 0 2 4 6 8 10 12 SD
B
A-pool
Q-pool
Q1
Q2
Q3
Cell Number
Cell Area
% p16 positive
Gene Symbol
Gene ID
Function
GOSR1 9527 Protein trafficking
RPL35 11224 60S subunit component
NUTF2 10204 Nuclear transport
CYYR1 116159 Unknown
PCDH21 92211 Cadherin
PTCHD2 57540 Patched domain containing
PDCD11 22984 rRNA metabolism
UBL3 5412 Ubiquitin-protein ligase
GTF2IRD1 9569 Transcription factor
SH2BP1 9646 Transcription & histone modification
FLJ30092 196515 Ubiquitin-protein ligase
ISCU 23479 Coenzyme metabolism
HERPUD1 9709 Unknown
HS6ST2 90161 Heparan transferase
FLJ32447 151278 Unknown
DHX40 79665 RNA helicase
SBF1 6305 Phosphatase
PEX13 5194 Peroxisome transport
ITGA3 3675 Cell Adhesion
ERH 2079 Transcription factor
TESSP1 360226 Proteolysis
TENC1 23371 Cell motility
UMODL1 89766 Unknown
NCL 4691 rRNA metabolism
MRPL46 26589 Mitochondrial ribosome 39S subunit
14orf139 79686 Unknown
ZNF479 90827 Transcription factor
C22orf20 80339 Fatty acid metabolism
LOC286512 286512 Unknown
POP5 51367 pre-rRNA processing
SPTLC1 10558 Lipid metabolism
HNRPH1 3187 Ribosomal protein
CLSTN1 22883 Cell Adhesion
KLRC3 3823 Cell Adhesion
CDH22 64405 Cadherin
MGC16028 112752 Unknown
TIMD4 91937 Cell Adhesion
CDH13 1012 Cadherin
AIG1 51390 Unknown
WNT3 7473 Wnt pathway
STRN3 29966 Protein targetting and localisation
DRIM 27340 Unknown
LOC256085 256085 Unknown
PREB 10113 Transcription
KIAA1913 114801 Unknown
20orf178 128866 Protein trafficking
564G2022 25963 Unknown
LOC88523 88523 Unknown
MGC16279 85002 Unknown
PRSS8 5652 Serine protease
C2orf11 130132 Unknown
SNRPB 6628 mRNA splicing
ZNF622 90441 Transcription factor enhancer
LPIN2 9663 Lipid, fatty acid & steroid metabolism
GPR24 2847 G-protein coupled receptor
HSPBAP1 79663 Unknown
SEMA4D 10507 Cell Adhesion
FLJ41481 400945 Unknown
KIAA0469 9903 Unknown
FLJ10458 54475 Signal transduction
ZNF11B 7558 Transcription factor
MAD2L1 4085 Chromosome segregation
C
A-pool
Q-pool
Q1
Q2
Q3
Cell Number
Cell Area
Nuclear Area
Gene Symbol
Gene ID
Function
FLJ13215 80071 Unknown
GPR147 64106 G-protein coupled receptor
LOC93109 93109 Unknown
MSF 10801 Cytokinesis
AP3B2 8120 Protein trafficking
WDR44 54521 Unknown
SLC7A11 23657 Amino acid transport
MOBKL1A 92597 Mitosis
LOC388813 388813 Unknown
XPA 7507 DNA repair
ABCB5 340273 ABC transporter
FLJ13231 65250 Unknown
GJB3 2707 Signal Transduction
OR8B8 26493 Unknown
D
A-pool
Cell Number
Cell Area
Nuclear Area
Gene Symbol
Gene ID
PRSS3 5646
CLSTN3 9746
MBD5 55777
C1orf70 339453
EFO1 114799
MIS12 79003
TULP2 7288
ATP2B1 490
FBXO45 200933
FY 2532
GALNTL5 168391
KIAA0205 9926
NSE1 197370
LOC441898 441898
PRDM12 59335
SUFU 51684
MATR3 9782
LOC400019 400019
SLC35B3 51000
CCR3 1232
LOC285453 285453
LOC440885 440885
ROCK2 9475
YPEL5 51646
FLJ14624 84899
GNAI1 2770
H2AFZ 3015
ATP1A1 476
GALNTL2 117248
RTAP17-1 83902
SP3 6670
SYT3 84258
E
CBX7
WNT3A
CDH22
siGLO
MOBKL1A
GPR147
p16

heterogeneous expression of luminal and myoepithelial lineage markers (Garbe et al., 2009).

To reconstruct a genome-wide siRNA screen for p16 modulators, we transfected HMECs at passage 6 (P6) in 384-well plates with 30 nM siRNA targeting *p16*, *CBX7* (an inhibitor of *p16* expression) (Gil et al., 2004), or *siGLO* (negative control targeting *Cyclophilin B* (*PPIB*); see Experimental Procedures) (Figure 1E). High content analysis was employed to quantitate numerous cellular features (Figure S1), and the most discriminatory measures were selected for hit definition. Based on the frequency distributions generated for each of these phenotypic criteria, we then assigned semi-arbitrary but highly stringent cutoffs for scoring positive hits in the genome-wide screen (Figures S2B–S2E, dashed lines). Using this approach, we found that reduced cell number (6.2 SD), increased cell area (10.2 SD), and an increased percentage of $p16^+$ cells (6.1 SD) best discriminated the *CBX7* siRNA phenotype from the *siGLO* negative control (Figures S2B–S2D, gray versus green). Increased cell number (6.4 SD), reduced cell area (4.8 SD), and reduced nuclear area (6.2 SD) optimally distinguished *p16* siRNA from *siGLO* (Figures S2B–S2E, gray versus orange). The percentage of $p16^+$ cells was naturally reduced following *p16* siRNA transfection and was always scored (Figures 1E and S2D), but for large-scale screening, this parameter was not as discriminatory as nuclear area in distinguishing *p16* siRNA from *siGLO* (Figures S2D versus S2E).

The genome-wide siRNA screen was undertaken under identical conditions (see Experimental Procedures and screen work flow, Figure S2A). A total of 22,010 genes were targeted by a pool of three siRNAs (30 nM; referred to as A-pools, supplied by Ambion), assayed once. Those A-pool siRNAs that caused cell-cycle arrest (mimicking *CBX7* siRNA), were classified as S (p16-associated senescence; green color coding throughout). siRNAs that rescued growth of the culture (mimicking *p16* siRNA) were classified as R (rescue; orange color coding throughout). We added a further designation, SG (super growers), which displayed increased cell number at the assigned cutoff (6.4 SD), without fulfilling all other criteria (Figure S2B). The raw screening data for each phenotypic criterion (Figures S2F–S2J) together with numerical outcomes for each hit classification (Figures S2K–S2L) are shown.

siRNA screening studies are hampered by false negative, false positive, and off-target effects (OTE) (Jackson et al., 2003). To investigate the possibility of false positives, 146 S, 162 R, and selected SG candidates from the primary screen that passed visual inspection were reassessed in triplicate (Figures S2K and S2L, left panels). In the secondary screen, 62 of the original 146 S A-pool siRNAs rescored at the previously required level of stringency for all three phenotypic criteria, while 14 of the original 39 R hits rescored (~40% rescoring in each case; Figures S2K– and S2L, right panels).

To illustrate the phenotype conferred by each siRNA, the same data is presented as heat maps (Figures 1B–1D, A-pool). The color saturation (S, green or R, orange) reflects the number of standard deviations of each of the A-pool median values from the median of the *siGLO* for each indicated phenotypic criterion (a color coded Z-score; Figure 1A). Images of representative S and R hits are shown (Figure 1E). Broadly, the genes identified in this analysis are classified as members of the Wnt pathway (WNT3A), cadherins and related proteins (CDH13, CDH22, PCDH21); transcription factors and other epigenetic regulators (ERH, GTF2IRD1, SH2BP1, ZNF479, ZNF11B, ZNF622, H2AFZ, MBD5); mitotic regulators (MAD2L1, MSF, MOBKL1A); G-protein-coupled receptors (GPR24, GPR147); and many other categories (Figures 1B and 1C).

Finally, genes of no known biological or molecular function that displayed the fully penetrant S or R phenotypes after retesting in triplicate are given the designation *SIF* (p16 Inhibitory Factor) or *SAF* (p16 activating factor), respectively (Figure S3). This nomenclature is based purely on the phenotype observed and makes no further claim as to the nature of the gene function.

To address the issue of OTE, we designed three new siRNAs for each S and R hits that displayed fully penetrant phenotype in the secondary screen. We demanded that each new siRNA sequence did not overlap with any of the A-pool siRNAs or with each other (see Experimental Procedures). Again, pools of three siRNAs were prepared (Q-pools, QIAGEN). Each new siRNA (Q1-Q3) was also assessed individually, at the same concentration (30 nM). Hereafter, each siRNA or pool is always assessed in triplicate.

The majority of Q-series siRNAs rescored, but almost invariably at a lower level of penetrance than the original A-pool (Figures 1B and 1C). However, and crucially, no Q-pool or individual Q-siRNA scored antagonistically to the original phenotype generated by the A-pool, nor were any heterogeneous S/R phenotypes seen (i.e., no siRNA generated a mixture of green and orange scores).

Protein Interaction Map

We further investigated potential relationships between the genes identified above by constructing a "protein interaction map." Briefly, S, R, and SG hits (the Anchor Set, Figures 1B–1D) were probed for protein interactors using the BioGRID and HPRD databases to generate the Set B protein list (see Experimental Procedures). The combined list of Anchor and Set B proteins was then probed for chains of three interacting proteins or more. Only one map emerged from this exercise (Figure 2A). We subjected all newly identified genes that were incorporated into this map to full A/Q siRNA analysis (Figures 2B–2D). A rich array of phenotypes of varying penetrance were apparent, predominantly S. Ten genes whose products have been

Figure 1. High-Content Genome-wide siRNA Screen for Modulators of p16

(A) Color coding used to illustrate the number of SD of the experimental siRNA value from the *siGLO* median. This color-coding system is employed for each phenotypic criterion and is used to define the S (green) and R hits (orange).

(B–D) Heat maps of SD scores as described in (A) for each phenotypic criterion following transfection of HMECs with A-pool, Q-pool, Q1, Q2, or Q3 siRNAs for (B) the S and (C) the R hits and (D) the supergrower (SG) hits. A brief function is assigned to each S and R hit (see Experimental Procedures).

(E) HMECs stained with DAPI (blue) and αp16 (green) following transfection with control siRNAs (*CBX7*, *siGLO*, *p16*) or A-pool siRNAs targeting representative S (*WNT3A*, *CDH22*) and R hits (*MOBKL1A*, *GPR147*). Size bar, 200 μm.

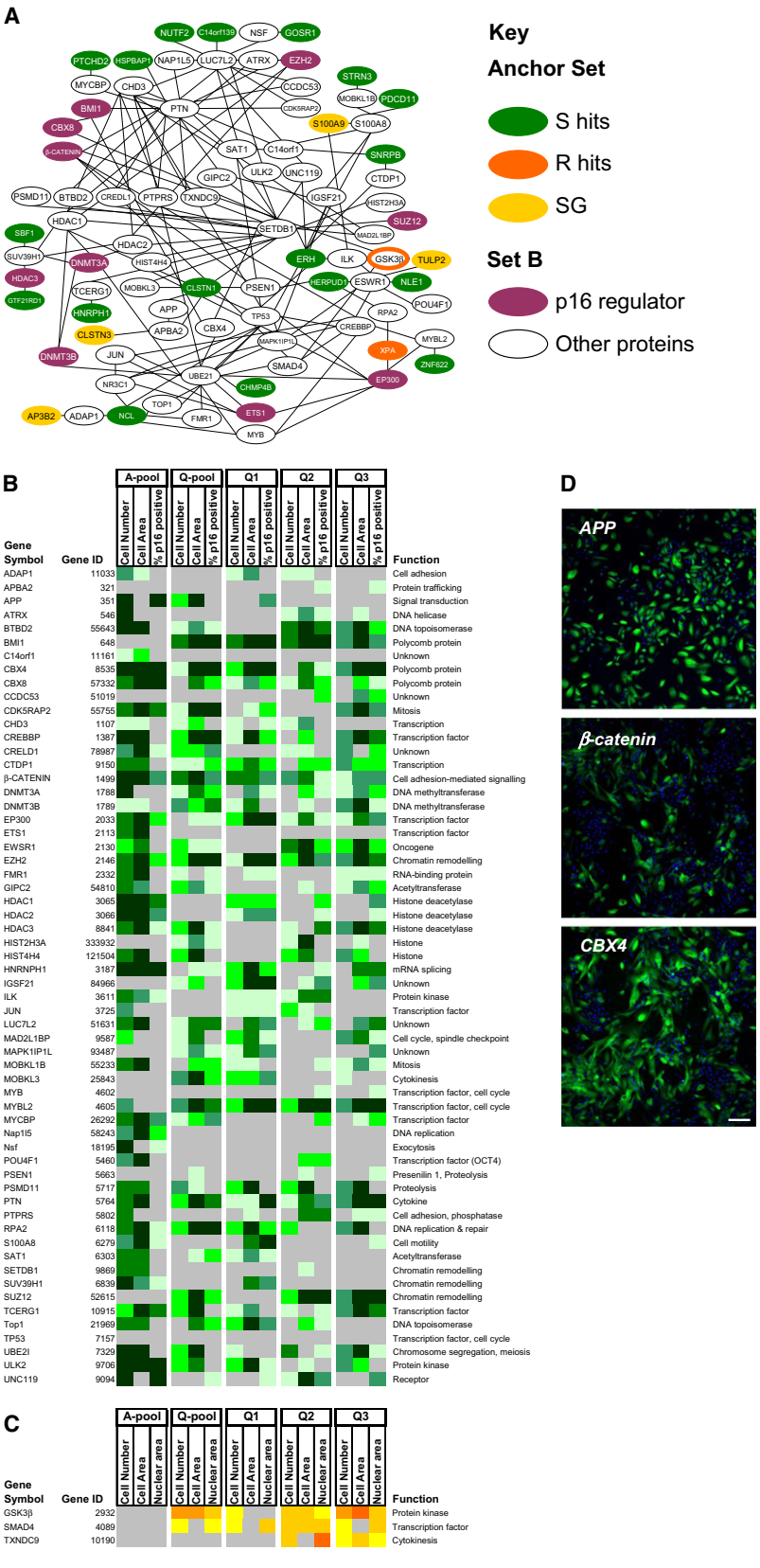

Figure 2. Interaction Map and A/Q Analysis

(A) Interaction map for Anchor Set (green, orange, yellow) and Set B interactors (white, purple). *p16* regulators from Set B are highlighted (purple). Lines represent interactions determined from the BioGrid and HPRD databases.

(B and C) Heat maps of SD scores for each phenotypic criterion following transfection of HMECs with A-pool, Q-pool, Q1, Q2, or Q3 siRNAs targeting Set B interactors. Candidates are divided based on the phenotypic criteria into (B) S or (C) R hits and a brief function is assigned to each candidate.

(D) HMECs stained with DAPI (blue) and αp16 (green) following transfection with A-pool siRNAs targeting *APP*, *β-catenin*, or *CBX4*. Size bar, 200 μm.

previously shown to directly bind *p16* cis-regulatory domains in a variety of cell types were identified (Figure 2A, purple circles). The fully penetrant S phenotype of some of the Set B genes (e.g., *Cbx4*, *Cbx8*, *Cdk5rap2*, *Hdac1*, *Hhrnph1*, and *Ulk2*; Figure 2B, A-pool column) suggests that they represent false negatives from the primary screen.

Among the genes identified in the genome-wide screen and the interaction map (Figures 1 and 2) WNT3A can be directly linked to a known transcriptional regulator of p16, through a well-established pathway. Loss of WNT3A was associated with a highly penetrant S phenotype associated with cell enlargement and high-level p16 expression (Figures 1B and 1E). WNT3A suppression of p16 (also, see below) is consistent with reports that the Wnt effector, β-catenin (identified here in the interaction map; Figures 2A and 2B), directly binds to the *p16* promoter (Delmas et al., 2007; Wassermann et al., 2009) and also the observation that Wnt2 can delay senescence in human fibroblasts (Ye et al., 2007).

Next, the screening data were probed for components of other established pathways that might be involved in p16 regulation. The potential role of Hedgehog (Hh) signaling was highlighted by the inhibitory components SUFU (SG category, Figure 1D) and GSK-3β (Interaction map, Figures 2A and 2C). Hh signaling, initially identified in *Drosophila*, plays a complex role in metazoan developmental patterning, adult stem-cell maintenance, and carcinogenesis (Jiang and Hui, 2008; Kasper et al., 2009). It should be noted that GSK-3β is also a pivotal member of the Wnt signaling pathway and also that SUFU may interact with β-catenin (Meng et al., 2001). However, since no direct relationship between p16 and the Hh pathway has previously been described, this finding was explored in detail.

Hedgehog Acts on p16

First, we genetically probed a set of well-established Hh pathway components in HMECs using A- and Q-pool siRNAs (Figure 3). Inhibition of gene function of each of the SHH and IHH protein ligands caused partial p16 derepression (Figures 3A and 3C) and increased staining with the senescence marker β-galactosidase (not shown). Although the binding partner of SUFU, FU, is not required for mouse development (Wilson et al., 2009), loss of FU in HMEC displayed a senescent phenotype, by contrast with that of SUFU (Figure 3A). Hh signaling is mediated by a still incompletely understood balance between activating and repressive forms of the GLI zinc-finger-containing family of transcription factors (Ruiz i Altaba et al., 2007). The GLI proteins, together with the coreceptor SMO, are subjected to complex regulatory phosphorylation by, among others, CK1 and PKA (Jia et al., 2004; Jiang, 2006; Smelkinson et al., 2007). siRNAs targeting *Ck1* and *Pka* partially elevated p16 levels (Figure 3C). GSK-3β phosphorylation targets the GLI proteins for specific cleavage (Pan et al., 2006; Tempé et al., 2006). The *Gsk-3β* A-pool was ineffective at suppressing p16, whereas Q1-3 siRNAs potently suppressed p16 expression and stimulated growth (Figures 3B and 3C). In each case, the level of *Gsk-3β* mRNA knockdown by siRNA was directly proportional to phenotypic penetrance and suppression of *p16* expression (Figure 3B). We further challenged the siRNA analysis by using a well-established inhibitor of GSK-3β (see Experimental Procedures). This compound inhibited p16 expression and stimulated growth, mimicking the *Gsk-3β* siRNA (Figure 3B). The potency of GSK-3β as a growth inhibitor (Liu et al., 2008, 2009; Zmijewski and Jope, 2004) may also reflect its role in the proteolysis of β-catenin (Figure 2) and CYCLIN D1 (Takahashi-Yanaga and Sasaguri, 2008), the key binding partner of CDK4/6 upon which p16 acts, but *GSK-3β* siRNA increased nuclear GLI2, the key Hh effector in this system (Figure S4I, see Discussion below).

These data demonstrate that Hh signaling is active in HMECs and is required for suppression of p16 expression and cell proliferation. To test whether Hh might be limiting, we exposed HMECs to retrovirally transduced IHH or SHH. In both cases, p16 expression was suppressed (Figure 4A) and cell expansion continued beyond the p16-mediated finite life span characteristic of these HMECs (Figure 4B). However, HMEC.IHH and HMEC.SHH cultures were not immortalized, and eventual cessation of growth was associated with p16 re-expression (not shown). We further explored the role of Hh by direct ligand addition to HMEC cultures. Recombinant SHH-N, a slightly truncated form of the protein, suppressed p16 expression at 6 hr (not shown) and 24 hr post treatment (Figures 4C and 4D). We further took advantage of commercially available recombinant WNT3A protein to challenge cells. As expected, this developmental ligand also suppressed p16. Interestingly cosupplementation with both WNT3A and SHH-N yielded no deeper suppression of p16 than either protein alone. In combination, these studies demonstrate that Hh pathway elements are not only essential for suppression of p16 in HMECs, but also limit expansion of the culture.

GLI2 Transcription Factor

The human genome encodes three GLI transcription factors, each of which can serve as targets of Hh signaling (Ruiz i Altaba et al., 2007). Only siRNAs directed against GLI2 effectively suppressed HMEC growth in association with p16 elevation (Figures 3C and 5A). Western blotting with αGLI2-N antibody in P6 cultures revealed crossreactive bands of approximately 180 kDa and 75 kDa (Figure 5B), both of which were substantially reduced following exposure of cells to a pool of siRNAs directed against *GLI2* (Figure S4F). The lower molecular weight form presumably reflects specific cleavage into the GLI2-R form (see below). The protein is less abundant at P10, compared to P6, whereas HMECs carrying virally encoded Hh proteins (HMEC.IHH or HMEC.SHH) displayed more GLI2 protein than control samples (HMEC.pBabe), in particular the 75 kDa form (Pan et al., 2006). GLI2-C displayed a heterogeneous but diffuse cellular staining pattern, whereas GLI2-N was much more obviously nuclear.

Examination of the p16 promoter region revealed a previously unreported potential GLI binding site, 111 bp 5′ to the *p16* ATG. The sequence, TGGcTGGTC, differs by only one mismatch from the recognized GLI binding site (TGGGTGGTC; Figure 5C) (note: all GLI proteins bind this sequence). Examination of the mouse *p16* gene also uncovered two such sites, one a direct match, within the *p16* protein coding sequence (Figure 5C). Accordingly, we explored the potential action of GLI2 on the relevant site within the human *p16* gene.

Hh signaling is thought to act both by regulation of shuttling of GLI into the nucleus and also by altering the balance between

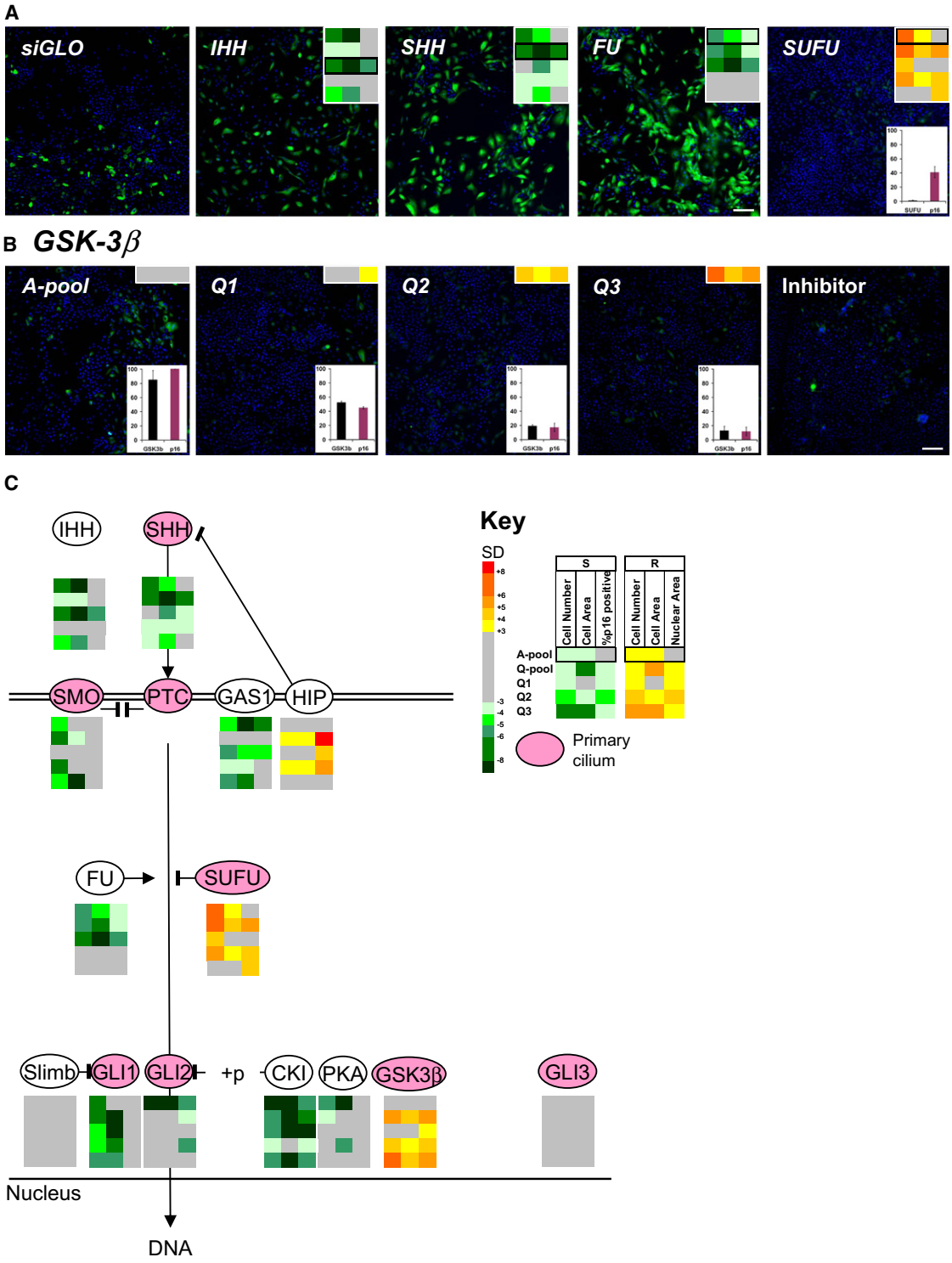

Figure 3. A/Q siRNA Analysis of Selected Hedgehog Pathway Members

(A and B) HMECs stained with DAPI (blue) and αp16 (green) following transfection with (A) A-pool siRNAs targeting *siGLO*, *IHH*, *SHH*, *FU*, or *SUFU* and (B) A-pool, Q1, Q2, or Q3 siRNAs targeting *GSK-3β* or treatment with GSK-3β inhibitor XV. Top inset: Heat map of SD scores for each phenotypic criteria following transfection with A-pool, Q-pool, Q1, Q2, or Q3 siRNAs (see Key). Bottom inset: mean mRNA level for (A) *SUFU* and *p16* following transfection with A-pool siRNAs targeting *SUFU* and (B) *GSK-3β* and *p16* following transfection with A-pool, Q1, Q2 or Q3 siRNAs targeting *GSK-3β*. Values were normalized to the internal *GAPDH* control and expressed relative to *siGLO* control levels (100%). (C) Selected Hh pathway members illustrated with heat maps of SD scores for each phenotypic criteria following transfection with A-pool, Q-pool, Q1, Q2, or Q3 siRNAs. Members of the pathway that localize to the PC are highlighted (pink). Size bar, 200 μm. Error bars = +SD.

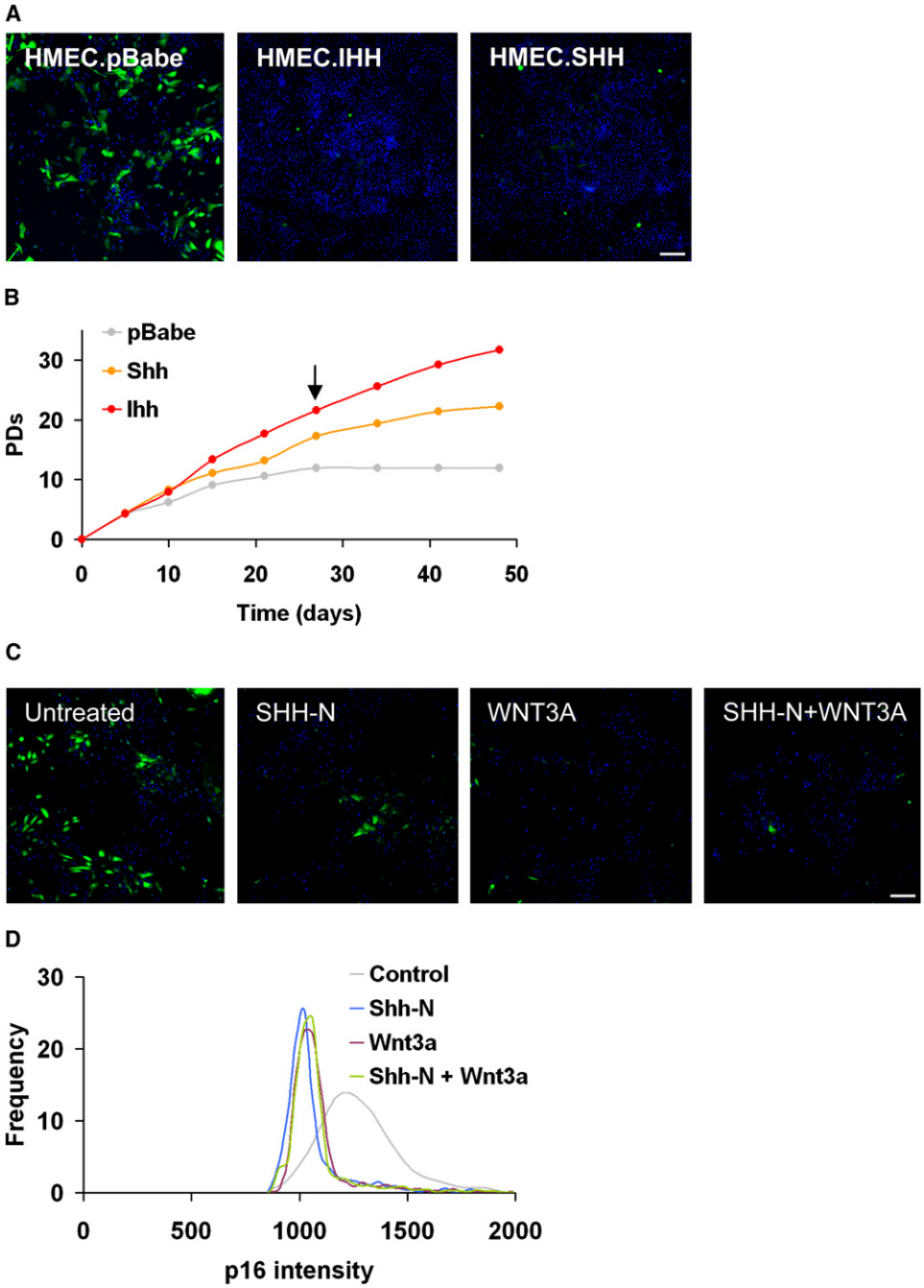

Figure 4. Hedgehog and p16

(A) HMEC.pBabe, HMEC.IHH, and HMEC.SHH cultures stained with DAPI (blue) and αp16 (green) after 27 days of culture.

(B) Cumulative population doublings (PDs) of HMEC cultures stably transduced with HMEC.pBabe (pBabe), HMEC.IHH (IHH), or HMEC.SHH (SHH) constructs, as a function of time. Arrow indicates time point of images shown in (A).

(C) HMECs stained with DAPI (blue) and αp16 (green) either untreated for following treatment with 100 ng/mL SHH-N ligand, 25 ng/mL Wnt3a ligand, or SHH-N and Wnt3a ligand together.

(D) Frequency distributions of p16 intensity in HMECs at P6 (gray) or following 24 hr treatment with 100 ng/mL SHH-N ligand (blue), 25 ng/mL Wnt3a ligand (purple), or SHH-N and Wnt3a ligand together (green). Size bar, 200 μm.

full-length, activator form (GLI-A) and the C-terminally truncated, repressive product (GLI-R) (Pan et al., 2006; Ruiz i Altaba et al., 2007). We generated a reporter construct carrying the single putative GLI-binding site within p16 (see Experimental Procedures). This reagent was transiently cotransfected with full-length GLI2 (pGLI2-FL) or a pGLI2-ΔC construct into HT1080

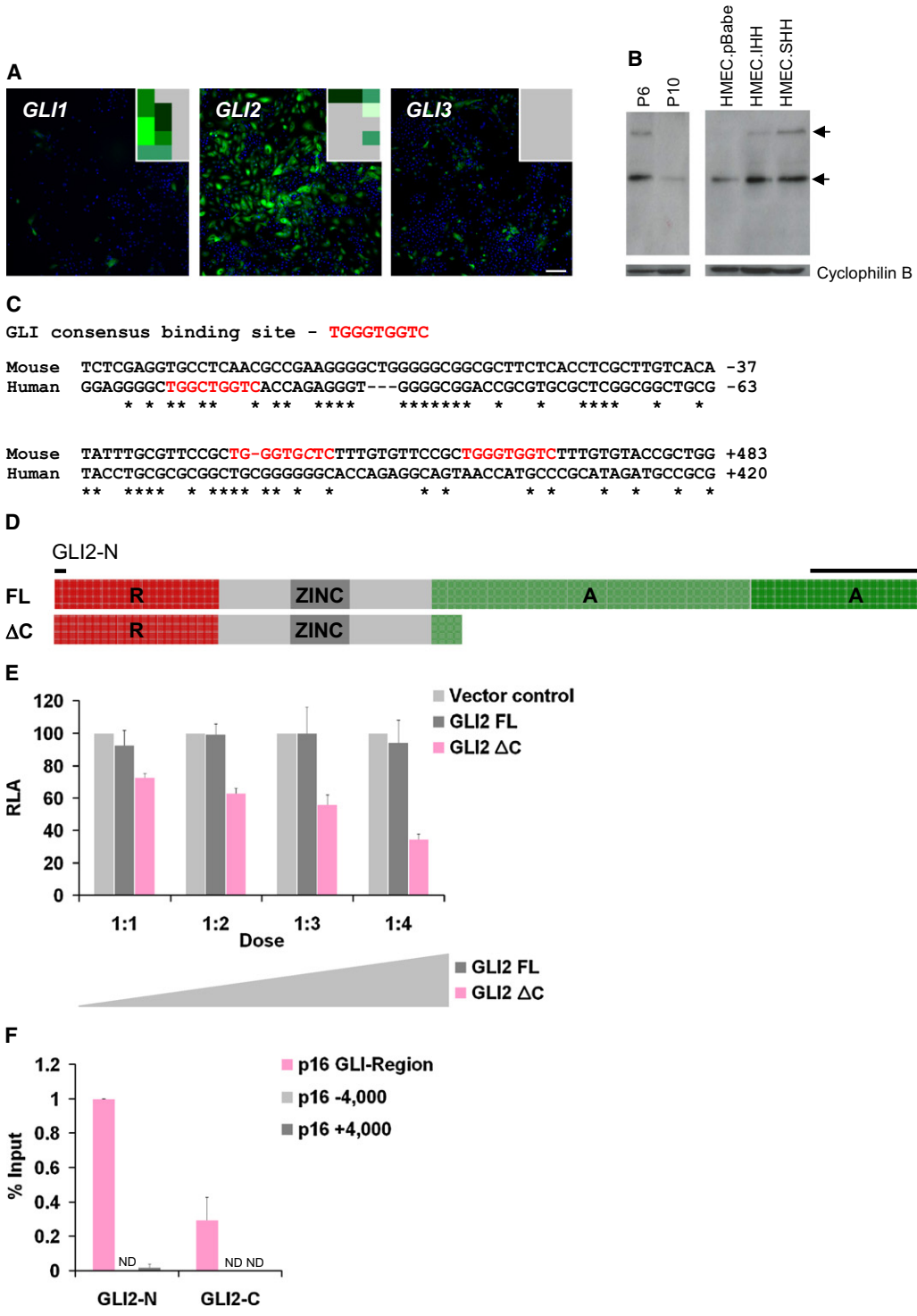

Figure 5. Regulation of p16 by GLI2

(A) HMECs stained with DAPI (blue) and αp16 (green) following transfection with A-pool siRNAs targeting *GLI1, GLI2* or *GLI3*. Inset: Heat map of SD scores for each phenotypic criteria following transfection with A-pool, Q-pool, Q1, Q2, or Q3 siRNAs. Size bar, 200 μm.

(B) Top panel: Western blot analysis using αGLI2-N antibody of protein extracts from HMECs at P6 and P10 (left) and HMEC.pBabe, HMEC.IHH, and HMEC.SHH (right). Full-length and processed forms of GLI2 were detected (arrows). Bottom panel: Loading control.

(C) Sequence alignment of the mouse and human *p16* genomic sequence. The putative GLI-binding sites are highlighted (red).

(D) Full-length GLI2 protein illustrating the N-terminal repressor domain (R), Zinc fingers (Zinc), and C-terminal activator domains (A). The epitopes for the αGLI2-N and αGLI2-C antibodies are shown. GLI2-FL and GLI2-ΔC reporter genes were used in the cotransfection assay shown in (E).

cells (Figures 5D and 5E). Whereas expression of GLI2-FL had no apparent effect on the p16 reporter activity, the expression of GLI2-ΔC inhibited p16 reporter expression in a dose-dependent manner.

Also, we used chromatin immunoprecipitation (ChIP) analysis to probe potential binding of GLI2 to the putative p16 GLI-binding site in HMECs (Figure 5F). Two antibodies were used, αGLI2-N (recognizing both GLI-A and GLI-R) and αGLI2-C (recognizing only the full-length GLI-A; Figures 5D and S4). The established GLI-binding region of the *Ptch* promoter (Hh receptor) was used as a positive control for antibody binding and for normalization (Agren et al., 2004). Using the αGLI2-N antibody, we detected strong binding to the p16 putative GLI-binding region and weaker binding using αGLI2-C. No binding was observed at the two negative control regions flanking the p16 GLI-binding site (−4000 and +4000 bp relative to the *p16* ATG). This experiment directly demonstrates that GLI2 binds the *p16* promoter in vivo and that the predominant binding form carries the N terminus of the protein.

If GLI2 regulates expression of p16, the observed heterogeneity of p16 expression in mass culture might be reflected in the behavior of GLI2. The same αGLI2-N and αGLI2-C antibodies were used for immunofluoresence (IF) analysis of HMECs at P6 (Figures 6A and 6B). A pool of siRNAs directed against *GLI2* essentially ablated the IF signal generated by either antibody, demonstrating specificity of these immunoreagents (Figures S4G and S4H). GLI2-C displayed a heterogeneous but diffuse cellular staining pattern, whereas GLI2-N was much more obviously nuclear. Examination of p16 expression in the same cells suggested exclusion between p16 staining and nuclear GLI2-N. A fraction of the culture appeared to express neither p16 nor GLI2.

If GLI2 suppression of p16 is relaxed during spontaneous senescence, nuclear GLI2 might decay at late passage. We quantitated and plotted total nuclear p16 against total nuclear GLI2-N intensities in cell populations at P6 and at P10, when the culture had virtually reached senescence (Figure 6C). The P6 cell population resolved into two predominant fractions: $p16^{low}/GLI2^{high}$ and $p16^{high}/GLI2^{low}$. A side population of lower p16 and GLI2 was also apparent. At P10 the profile substantially collapsed into $p16^{high}/GLI2^{low}$. This suggests that HMECs, despite considerable culture heterogeneity, exist in one of two proliferative states to which Hh and p16 make a reciprocal contribution.

Finally, we used a well-established SMO inhibitor, cyclopamine (Chen et al., 2002), to explore the relationship between p16 and Hh signaling. HMEC were highly sensitive to the compound, which at 5–10 μM inhibited cell expansion, associated with decreased nuclear GLI2 and increased p16 (Figures 6D and 6E). By contrast, HMEC rendered p16 deficient (HMEC.p16shRNA) were highly resistant to the compound, which inhibited growth and reduced nuclear GLI2 only at much higher concentrations (50–100 μM, Figures 6D and 6F). This observation implies that p16 is the key target of Hh limited cell proliferation.

Primary Cilia and p16

The primary cilium (PC) is a nonmotile 9+0 microtubule-containing cell-surface protrusion nucleated from one of a pair of centrioles. Once formed, a PC can survive centrosome duplication, but regresses at the onset of mitosis (Pan and Snell, 2007). These cellular appendages are found in many cell types in vivo, including breast epithelia (Nickerson, 1989). Hh components, including SHH, SMO, PTCH, SUFU, and GLI, have been localized to the PC and active PC-mediated Hh signaling has been now been described in a wide variety of mammalian cell types in vivo (Eggenschwiler and Anderson, 2007). However, low levels of PC formation are commonly observed in cultured cells. This phenomenon is not well understood.

We investigated PCs in HMECs using antibodies against acetylated tubulin (AcTb) and IHH (similar results were obtained with antibodies against SHH, not shown). All IHH and SHH immunoreagents were validated by knockdown of both Western blot and IF signal following exposure to relevant siRNAs (Figures S4A–S4D). PCs were readily detected in ~1% of cells at P6 (Figures 7A and7B), and active Hh signaling in these cells is suggested by colocalization of SMO in over 60% of PCs (Figure 7C). Culture to stationary phase or serum starvation is widely used to increase PC formation in vitro (Kiprilov et al., 2008). Therefore, we investigated the proliferative status of the PC-carrying cells by costaining with αAcTb and αKi67. Over 90% of PC^+ cells were $Ki67^+$ (Figure 7D). Indeed, cultures at proliferative exhaustion (P10) or after culture to confluence displayed a very low fraction of PC^+ cells (Figure 7B). This issue was further explored by stimulating the culture with *p16* RNA interference. Surprisingly, either transient (siRNA) or virally transduced (shRNA) *p16* suppression yielded cultures displaying a 5-fold increase in PC frequency (Figure 7E). Thus, p16 inhibits PC formation.

Heterogeneous cellular expression of p16, coupled with typical sporadic elaboration of PCs in HMECs, presented the opportunity to explore the relationship between the two. Following quantitative image analysis of >100,000 cells at P6, frequency distributions of p16 intensity were compared in mass culture, PC^+ cells and mass culture exposed to *p16* siRNA. p16 levels were lower in PC^+ cells relative to the whole population, but were not reduced to the levels achieved following p16 knockdown (Figure 7F).

We further probed the relationship between PC formation and p16 in the HMEC.p16shRNA cell line. These cells retain a relatively high fraction of PC^+, with respect to wild-type HMECs, even in the presence of growth-inhibitory levels of cyclopamine (100 μM) and also at confluence (Figures 7G and 7H). Finally, HMEC overexpressing IHH displayed increased PC formation, which was marginally further enhanced by ablation of p16 (Figure 7I). Thus, in each of the experimental conditions investigated there is a reciprocal relationship between p16 expression and PC formation.

(E) Mean relative luciferase activity (RLA) following co-transfection of the GLI2-FL or GLI2-ΔC constructs at the indicated dose with the p16-luciferase construct. (F) αGLI2-N and αGLI2-C ChIP in HMEC cells. The mean relative levels obtained with each antibody for the putative p16 GLI-binding region are indicated (pink). The *Ptch* GLI-binding region and sequences flanking the putative p16 GLI-binding site (gray) were used as positive and negative controls, respectively. PCR signals were normalized to input and are shown relative to the positive *Ptch* control. ND = not detectable, error bars = +SD.

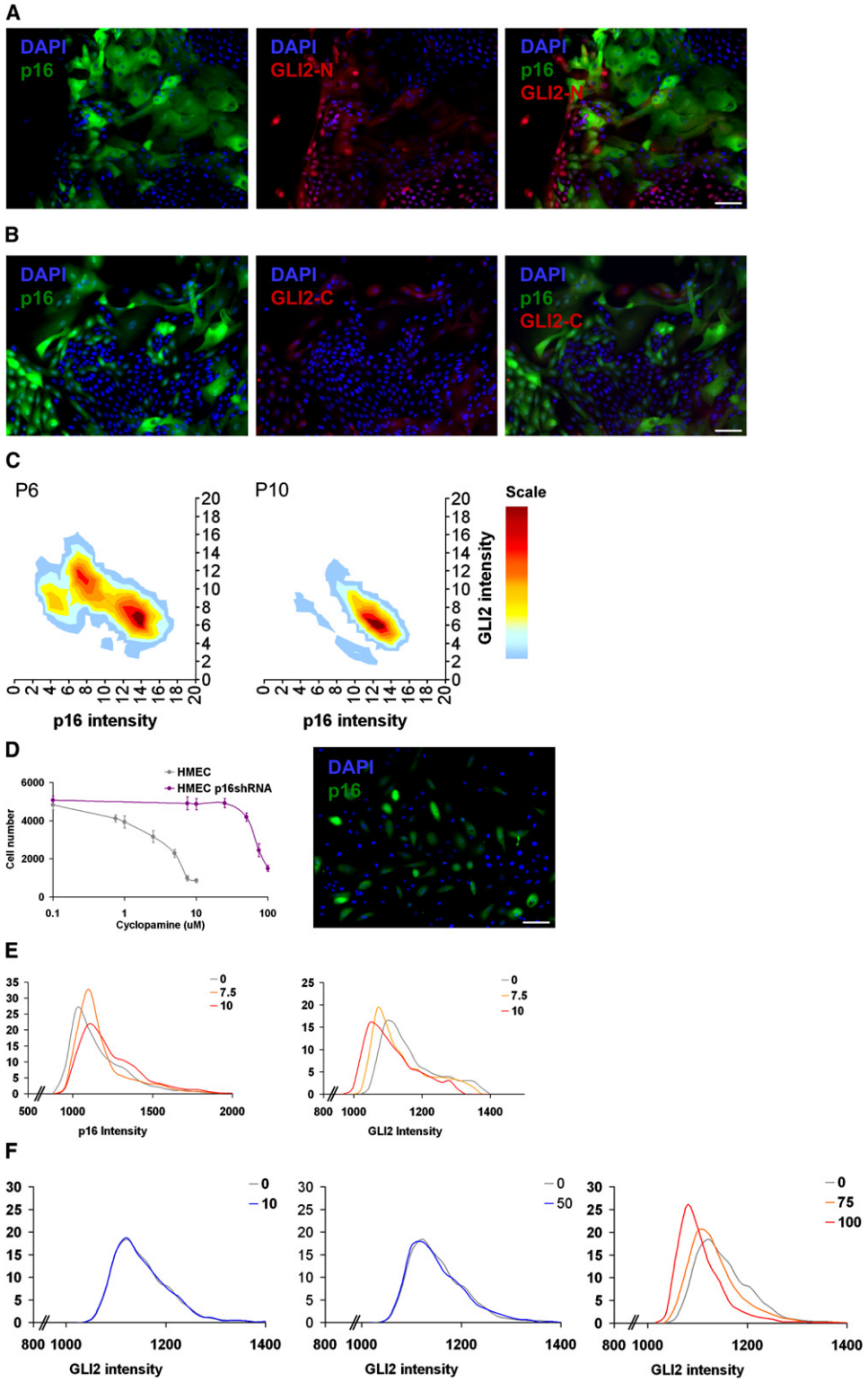

Figure 6. Relationship between GLI2 and p16

(A) HMECs stained with DAPI (blue), αp16 (green), and αGLI2-N (red).

(B) HMECs stained with DAPI (blue), αp16 (green), and αGLI2-C (red).

(C) Contour plots of total p16 nuclear intensity versus total GLI2-N nuclear intensity in individual cells at P6 (left) and P10 (right).

DISCUSSION

Although the majority of known direct transcriptional regulators of p16 were detected in the present siRNA analysis of HMECs, a large number of other participating genes were uncovered for the first time. Among these were Hh pathway components that act to promote mitogenesis by suppression of p16. In *Drosophila* development, Hh acts by altering the balance between GLI-A (full length) and GLI-R (truncated) in favor of the former (Aza-Blanc et al., 2000; Pan et al., 2006). In the present context, however, this situation is apparently reversed. Hh mitogenesis in HMEC is mediated by GLI2-R that accumulates in the nucleus and directly inhibits the promoter of p16. p16 has long been implicated in breast cancer and gene inhibition by promoter methylation is a very early step in this disease (Kim and Sharpless, 2006). The Hh pathway has also been implicated in breast cancer (Kasper et al., 2009). Although many Hh target genes may be relevant to carcinogenesis (Jiang and Hui, 2008), and epithelial/mesenchymal interplay is critical (Jiang and Hui, 2008; Kasper et al., 2009), direct inhibition of p16 by Hh in the epithelial compartment provides immediate insight into one mechanism by which this developmental pathway acts in both normal and pathological mitogenesis.

Progressive p16 expression is the immediate cause of replicative senescence in many types of cultured human cells, with the exception of embryonic stem cells in which the gene is suppressed (Li et al., 2009). This phenomenon has been widely attributed to an ill-defined "culture stress." As studied here, that stress may reflect a progressive decay in signaling by morphogens such as Hh (and possibly Wnt; Figures 1, 2, and 4), presumably consequent to tissue dissociation and disruption of cell-cell contacts upon which they intimately rely in vivo.

The role of the PCs is of particular interest in this regard. In common with the findings of others (Eggenschwiler and Anderson, 2007), PCs form infrequently in cultured HMEC, and since the bulk of the culture responds to very short-term ligand addition, Hh signaling must be active in the PC^- population, as in other described systems (Chen et al., 2009). Indeed, many immortal cancer cells do not have PCs (Seeley et al., 2009), suggesting a potential growth-inhibitory function of PCs. However, in HMECs, p16 expression is lower in PC^+ cells, the majority of which are actively involved in Hh signaling. Although the existence of other p16-supressing pathways in PC^+ cells can certainly not be excluded, the simplest interpretation of our data is that Hh signaling is more potent in this context than in those cells without these structures. Thus, PC^+ cells may act as "germinal centers" in long-lived cultures, and the phenomenon of senescence may reflect not only apparent decay of Hh function in the majority of cells but also relative dilution of PC^+ cells in the absence of sufficient replacement. The regulation of ciliagenesis is therefore of great interest.

The pattern of inheritance of PC has recently been studied in cultured cells (Anderson and Stearns, 2009). After division, the cell inheriting the oldest "grandmother" centriole forms a functional, SHH-sensitive PC earlier than its sister. Thus, the inherent asymmetry of centriolar replication that is deeply implicated in the asymmetry of stem cell division in *Drosophila* neurogenesis (Zhong and Chia, 2008), germ-cell aging (Cheng et al., 2008), and mammalian neural progenitor formation (Chenn and McConnell, 1995; Noctor et al., 2004; Wang et al., 2009) might be reflected in p16 biology. This remains to be studied. Finally, our work adds to the growing list of developmental pathways that inhibit p16 expression. These include polycomb genes (Gil and Peters, 2006), Wnt/β-catenin (Delmas et al., 2007; Wassermann et al., 2009), MEOX2 (Irelan et al., 2009), and now Hh/GLI. Given that p16 is progressively expressed in a wide variety of tissues during aging, these findings may imply that the progressive molecular and cellular damage that clearly contribute to organismal aging could be secondary to deeper defects in pathways that are formative from early embryogenesis. Thus, in vivo aging might reflect "developmental decay," a phenomenon that is apparent in the in vitro context studied here. Our studies suggest avenues by which this possibility might be explored.

EXPERIMENTAL PROCEDURES

Cells and Reagents

Normal finite life-span HMECs were obtained from reduction mammoplasty tissue of a 21-year-old individual, specimen 184, and were cultured as previously described (Garbe et al., 2009). Cells at P6 were used for reconstruction, screening, and follow-up siRNA studies. For compound studies, cells were grown in the presence or absence of 0.1 nM GSK3β-inhibitor XV (CalBiochem),100 ng/mL SHH-N, or 25 ng/mL WNT3A (R&D Systems) or a range of doses for cyclopamine (Sigma).

High-Content Genome-wide siRNA Screening

The screen was performed using the human genome siRNA library from Ambion (RefSeq Version12, pools of three siRNAs targeting 22,010 genes: referred to as A-pools), together with control siRNAs targeting *Cyclophilin B* (Dharmacon), *CBX7* (Ambion), and *p16* (QIAGEN). HMECs at P6 were reverse transfected with 30 nM siRNA in 384-well format using HiperFect (QIAGEN). Plates were incubated for 46 hr, medium changed, and fixed/stained 72 hr later with Moαp16 JC2, GtαMo AlexaFluor488 (Invitrogen), DAPI, and Cell Mask (Invitrogen). High-content images were acquired with the In Cell 1000 automated microscope (GE) at 4× magnification, and analysis was performed using the Developer Analysis software (GE).

Following the screen, the Ambion library was cherry picked and hits retested in triplicate. Next, three siRNAs per target were purchased (Q pool, Q1-3, QIAGEN). Sequences for the A-pool siRNAs were aligned with all available QIAGEN siRNAs (ClustalW, http://www.ebi.ac.uk/clustalw), such that each newly synthesized Q-siRNA had no sequence overlap with any of the A-pool siRNAs or with each other.

Immunofluorescence

Primary antibodies used were Moαp16 JC2; Rbαp16 (sc-468, Santa Cruz); Moαacetylated tubulin (AcTb T7451, Sigma), RbαKi67 (NCL-Ki67p,

(D) Left panel: Mean cell number for HMEC P6 (gray) or HMEC.p16shRNA (purple) following treatment with a range of cyclopamine doses. Error bars = ± SD. Right panel: HMECs stained with DAPI (blue) and αp16 (green) following treatment with 10 μM cyclopamine.
(E) Frequency distributions of p16 intensity (left) or GLI2-N nuclear intensity (right) following treatment of HMEC P6 with 0 μM (gray), 7.5 μM (orange), or 10 μM cyclopamine.
(F) Frequency distribution of GLI2-N nuclear intensity following treatment of HMEC.p16shRNA with 0 μM (gray), 10 μM (blue, left), 50 μM (blue, middle), 75 μM (orange), or 100 μM (red) cyclopamine. Size bar, 100 μm.

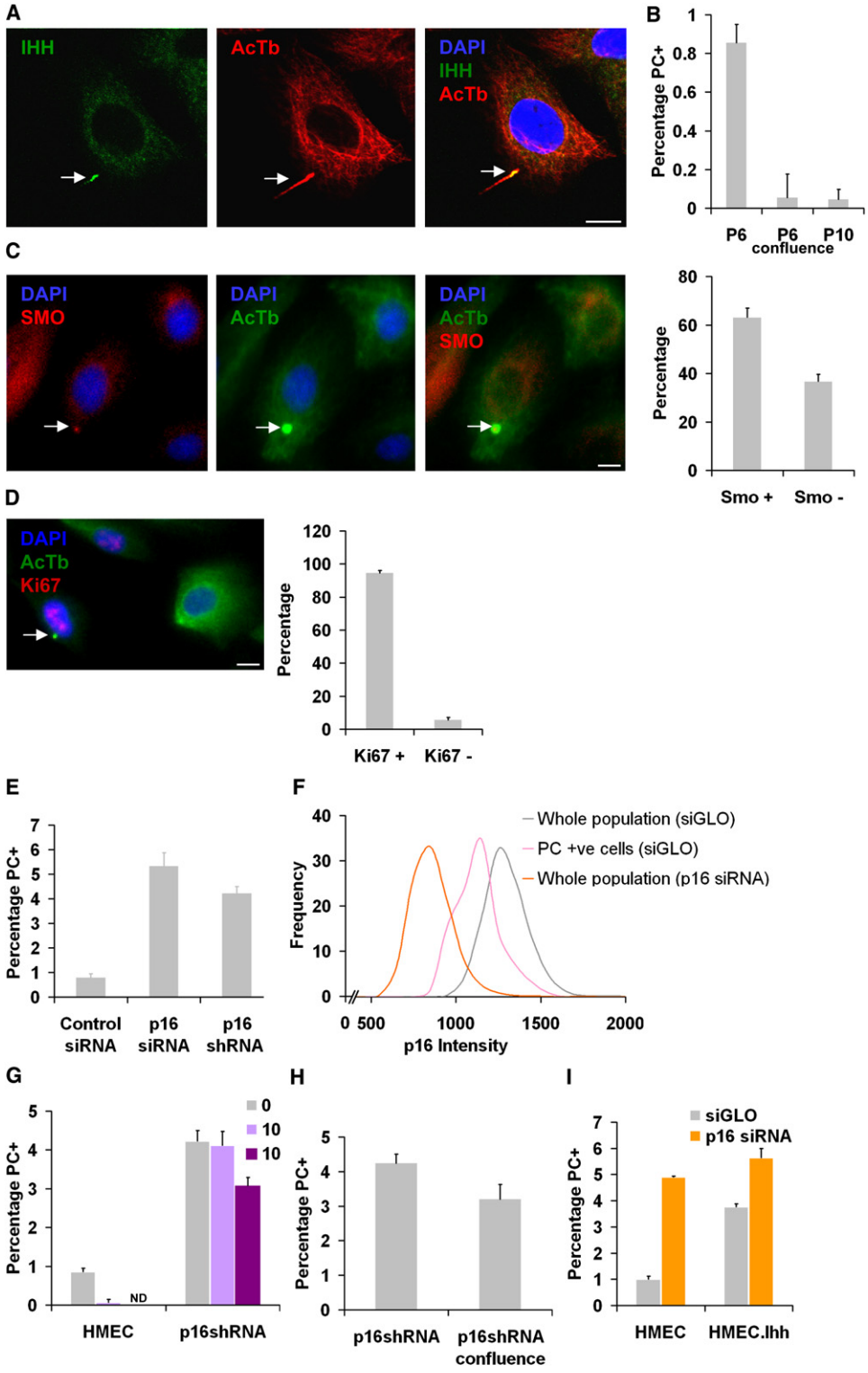

Figure 7. Relationship between Primary Cilium and p16

(A) Confocal images of HMECs stained with αIHH (green), αAcTb (red), and DAPI (blue).

(B) Mean percentage of PC^+ cells +SD in HMECs at P6, P6 cultured to confluence and P10.

(C) Left panels: HMECs stained with αSMO (red), αAcTb (green), and DAPI (blue). Right panel: Mean percentage of SMO+ PCs in HMEC cultures at P6.

(D) Left panel: HMECs stained with αAcTb (green) αKi67 (red) and DAPI (blue). Right panel: Mean percentage of $Ki67^+$ cells in PC^+ population of HMECs at P6.

(E) Mean percentage of PC^+ cells following transfection of HMECs with control siRNA, *p16* siRNA, or in HMEC.p16shRNA stable cell lines.

Novocastra), GtαGLI2 (GLI2-N, sc-20290, Santa Cruz), RbαGLI2 (GLI2-C, sc-28674, Santa Cruz), RbαIHH (sc-13088, Santa Cruz), RbαSHH (sc-9024, Santa Cruz), and RbαSMO (sc-13943, Santa Cruz). Secondary antibodies were the appropriate AlexaFlur-488 or AlexaFlur-546 antibody (Invitrogen). DAPI and CellMask Deep Red (Invitrogen) were also included. Images were collected with the In Cell 1000 microscope (GE) or the Zeiss 510 Meta Confocal microscope (Zeiss) and Developer Software (GE) used for image analysis.

Immunofluorescence for PCs

For PC detection, cells were cultured under normal conditions for 72–96 hr, then imaged by confocal microscopy or with the In Cell. An analysis algorithm based on MoαAcTb signal was designed to specifically detect PCs and to exclude mitotic spindle and midbodies, and cellular or nuclear intensities for proteins of interest determined for PC^+ and PC^- cells. For additional assay robustness, matched samples were costained with RbαSHH or RbαIHH and all images were subjected to visual inspection.

Quantitative RT-PCR (qPCR)

qPCR reactions were performed with SYBR Green Master Mix (ABI) or Quantifast (QIAGEN). For siRNA knockdown experiments, RNA was extracted from 1×10^5 cells 48 hr posttransfection. *GAPDH* levels were quantified for each cDNA sample in separate qPCR reactions and were used as an endogenous control. Target gene-expression levels were quantified using target specific probes. Values were normalized to the internal *GAPDH* control and expressed relative to *siGLO* transfected control levels (100%). All qPCR reactions were run in duplicate for two independent samples.

Database Searches

We searched PUBMED and PANTHER (http://www.pantherdb.org) databases to assign functional annotations to the S and R hits. Protein interactions datasets (Set B) for each S/R hit (Anchor Set) were generated using BioGRID (http://www.thebiogrid.org) and HPRD (http://hprd.beta.ibioinformatics.org). These interactions were then overlaid to generate interaction networks, requiring that an anchor set or Set B target generated a chain with at least two other anchor/Set B proteins (i.e., representation in the map required that an Anchor or Set B protein must form a chain with at least two other anchor or Set B proteins). Accordingly, the map does not contain all members of either set.

Retroviral Stable Cell Lines

cDNA for IHH or SHH (Addgene) were subcloned into the pBabe.puro retroviral expression construct. The previously reported p16 shRNA shRNA expressed from the U6 promoter in MSCV-shp16 was also used (Narita et al., 2003). HMECs at P5 were transduced and the resulting HMEC.pBabe, HMEC.IHH, and HMEC.SHH cultures were passaged as described above for a duration of 50 days, or until the culture reached senescence. The growth curve shown in Figure 4B starts at the equivalent of WT HMEC P7.

p16 Versus GLI2 Nuclear Intensity as a Function of Passage

HMECs at P6 and P10 were cultured for three days and then stained as described above using Moαp16 and GLI2-N (1:50, GtαGLI2-N20 Santa Cruz Biotechnology). The Developer Analysis software was used to define each nucleus and measure the total nuclear pixel intensity for p16 and GLI2-N and contour plots generated.

Luciferase Assays

To generate the p16 GLI-binding site luciferase reporter construct (pGL3.p16) a 221 bp fragment containing the GLI consensus binding site (TGGcTGGTC, 1bp mismatch) was cloned into the *NcoI* site of the pGL3 Luciferase reporter construct (primers: 5′-ATGATCCATGGCTCCTCCGAGC-3′ and 5′-CTACTC CATGGTGCTCCCCGC-3′). Full-length GLI2 cDNA (GLI2-FL) and the first 658AA equivalent of GLI2 were cloned into the BamHI/EcoRI site of pcDNA3.1 to generate pGLI2-FL and pGLI2-ΔC, respectively.

HMECs are not efficiently transiently transfected with plasmid DNA. Therefore, HT1080s cells were seeded in 96-well plates. Twenty-four hours later cells were cotransfected with luciferase expression constructs (pGL3/pGL3.p16), Renilla luciferase, and pcDNA3.1 constructs (pcDNA3.1/pGLI2-FL/pGLI2-ΔC) at a ratio of 1:0.5:1, 1:0.5:2, 1:0.5:3, or 1:0.5:4, respectively, using Lipofectamine 2000 (Invitrogen). Luciferase activity was assayed 48 hr posttransfection using the Dual-Luciferase Reporter Assay System (Promega) according to the manufacturer's instructions. Relative luciferase activity was expressed with respect to the pGL3/Renilla/pcDNA3.1 control (100%) and were generated from at least two independent experiments each performed in triplicate.

Chromatin Immunoprecipitation (ChIP)

Exponentially growing cells were washed with PBS and fixed with 1% paraformaldehyde for 30 min, and the reaction was stopped with 125 mM glycine. Cells were washed twice with PBS and lysed in 50 mM Tris-HCl pH 8.1, 10 mM EDTA pH 8.0, and 1% SDS plus protease inhibitors (Roche). Chromatin was sonicated to an average size of 400–1500 bp, cleared by centrifugation, and diluted in 20 mM Tris-HCl; pH 8.1, 1.1 mM EDTA, pH 8.0; 1.1% Triton X-100, and 167 mM NaCl. Blocked Protein G Dynabeads (Invitrogen) were saturated with GtαGLI2-N, RbαGLI2-C, or Gt/Rb-IgG and incubated with chromatin from 2×10^6 cell equivalents overnight at 4°C. Immune complexes were washed 3× with RIPA (10 mM Tris-HCl, pH 7.5, 1 mM EDTA, 0.5 mM EGTA, 140 mM NaCl, 1% Triton X-100, 0.1% SDS, 0.1% Na deoxycholate, and protease inhibitors), 1× in high-salt buffer (RIPA + 500 mM NaCl), once in LiCl buffer (RIPA + 250 mM LiCl) and 2× in TE pH 8.0. Samples were eluted at 68°C for 5 hr in 20 mM Tris-HCl, pH 7.5; 5 mM EDTA, 50 mM NaCl, 50 μg/ml proteinase K, and 5 μg/ml RNase A. DNA was analyzed by qPCR in triplicate from at least two independent experiments.

SUPPLEMENTAL INFORMATION

Supplemental Information includes four figures and can be found with this article online at doi:10.1016/j.molcel.2010.10.027.

ACKNOWLEDGMENTS

We thank M. Overhoff, M. Philpott, and J. Wang for useful discussion and critical reading of the manuscript. C.L.B. was supported by the Medical Research Council and The Wellcome Trust, D.F. by Cancer Research UK, A.M.H.B. by the MRC, V.B. and E.H. by The Wellcome Trust. J.C.G. and M.R.S. were supported by NIH U54 CA112970 and the Office of Energy Research, Office of Health and Biological Research, U.S. Department of Energy under Contract No. DE-AC02-05CH11231.

Received: January 12, 2010
Revised: June 9, 2010
Accepted: August 27, 2010
Published: November 23, 2010

REFERENCE

Agren, M., Kogerman, P., Kleman, M.I., Wessling, M., and Toftgård, R. (2004). Expression of the PTCH1 tumor suppressor gene is regulated by alternative promoters and a single functional Gli-binding site. Gene *330*, 101–114.

(F) Frequency distribution of p16 intensity in HMECs at P6 for the whole population (gray), PC^+ cells (pink) and cells transfected with *p16* siRNA (orange). Arrows indicate a PC.

(G–I) Mean percentage of PC^+ cells in (G) HMECs or HMEC.p16shRNA cultured with 0 μM, 10 μM, or 100 μM cyclopamine (ND = not done); (H) HMEC.p16shRNA versus HMEC.p16shRNA cultured to confluence; and (I) HMEC or HMEC.IHH following transfection with *siGLO* (gray) or *p16* siRNA (orange). Size bar, 10 μm. Error bars = +SD.

Anderson, C.T., and Stearns, T. (2009). Centriole Age Underlies Asynchronous Primary Cilium Growth in Mammalian Cells. Curr. Biol. *19*, 1498–1502.

Aza-Blanc, P., Lin, H.Y., Ruiz i Altaba, A., and Kornberg, T.B. (2000). Expression of the vertebrate Gli proteins in Drosophila reveals a distribution of activator and repressor activities. Development *127*, 4293–4301.

Brenner, A.J., Stampfer, M.R., and Aldaz, C.M. (1998). Increased p16 expression with first senescence arrest in human mammary epithelial cells and extended growth capacity with p16 inactivation. Oncogene *17*, 199–205.

Chen, J.K., Taipale, J., Cooper, M.K., and Beachy, P.A. (2002). Inhibition of Hedgehog signaling by direct binding of cyclopamine to Smoothened. Genes Dev. *16*, 2743–2748.

Chen, X., Barton, L.F., Chi, Y., Clurman, B.E., and Roberts, J.M. (2007). Ubiquitin-independent degradation of cell-cycle inhibitors by the REGgamma proteasome. Mol. Cell *26*, 843–852.

Chen, M.H., Wilson, C.W., Li, Y.J., Law, K.K., Lu, C.S., Gacayan, R., Zhang, X., Hui, C.C., and Chuang, P.T. (2009). Cilium-independent regulation of Gli protein function by Sufu in Hedgehog signaling is evolutionarily conserved. Genes Dev. *23*, 1910–1928.

Cheng, J., Türkel, N., Hemati, N., Fuller, M.T., Hunt, A.J., and Yamashita, Y.M. (2008). Centrosome misorientation reduces stem cell division during ageing. Nature *456*, 599–604.

Chenn, A., and McConnell, S.K. (1995). Cleavage orientation and the asymmetric inheritance of Notch1 immunoreactivity in mammalian neurogenesis. Cell *82*, 631–641.

Chkhotua, A.B., Gabusi, E., Altimari, A., D'Errico, A., Yakubovich, M., Vienken, J., Stefoni, S., Chieco, P., Yussim, A., and Grigioni, W.F. (2003). Increased expression of p16(INK4a) and p27(Kip1) cyclin-dependent kinase inhibitor genes in aging human kidney and chronic allograft nephropathy. Am. J. Kidney Dis. *41*, 1303–1313.

Delmas, V., Beermann, F., Martinozzi, S., Carreira, S., Ackermann, J., Kumasaka, M., Denat, L., Goodall, J., Luciani, F., Viros, A., et al. (2007). Beta-catenin induces immortalization of melanocytes by suppressing p16INK4a expression and cooperates with N-Ras in melanoma development. Genes Dev. *21*, 2923–2935.

Eggenschwiler, J.T., and Anderson, K.V. (2007). Cilia and developmental signaling. Annu. Rev. Cell Dev. Biol. *23*, 345–373.

Garbe, J.C., Bhattacharya, S., Merchant, B., Bassett, E., Swisshelm, K., Feiler, H.S., Wyrobek, A.J., and Stampfer, M.R. (2009). Molecular distinctions between stasis and telomere attrition senescence barriers shown by long-term culture of normal human mammary epithelial cells. Cancer Res. *69*, 7557–7568.

Gil, J., and Peters, G. (2006). Regulation of the INK4b-ARF-INK4a tumour suppressor locus: all for one or one for all. Nat. Rev. Mol. Cell Biol. *7*, 667–677.

Gil, J., Bernard, D., Martínez, D., and Beach, D. (2004). Polycomb CBX7 has a unifying role in cellular lifespan. Nat. Cell Biol. *6*, 67–72.

Hayflick, L. (1965). The Limited in Vitro Lifetime of Human Diploid Cell Strains. Exp. Cell Res. *37*, 614–636.

Irelan, J.T., Gutierrez Del Arroyo, A., Gutierrez, A., Peters, G., Quon, K.C., Miraglia, L., and Chanda, S.K. (2009). A functional screen for regulators of CKDN2A reveals MEOX2 as a transcriptional activator of INK4a. PLoS ONE *4*, e5067.

Jackson, A.L., Bartz, S.R., Schelter, J., Kobayashi, S.V., Burchard, J., Mao, M., Li, B., Cavet, G., and Linsley, P.S. (2003). Expression profiling reveals off-target gene regulation by RNAi. Nat. Biotechnol. *21*, 635–637.

Janzen, V., Forkert, R., Fleming, H.E., Saito, Y., Waring, M.T., Dombkowski, D.M., Cheng, T., DePinho, R.A., Sharpless, N.E., and Scadden, D.T. (2006). Stem-cell ageing modified by the cyclin-dependent kinase inhibitor p16INK4a. Nature *443*, 421–426.

Jia, J., Tong, C., Wang, B., Luo, L., and Jiang, J. (2004). Hedgehog signalling activity of Smoothened requires phosphorylation by protein kinase A and casein kinase I. Nature *432*, 1045–1050.

Jiang, J. (2006). Regulation of Hh/Gli signaling by dual ubiquitin pathways. Cell Cycle *5*, 2457–2463.

Jiang, J., and Hui, C.C. (2008). Hedgehog signaling in development and cancer. Dev. Cell *15*, 801–812.

Kasper, M., Jaks, V., Fiaschi, M., and Toftgård, R. (2009). Hedgehog signalling in breast cancer. Carcinogenesis *30*, 903–911.

Kim, W.Y., and Sharpless, N.E. (2006). The regulation of INK4/ARF in cancer and aging. Cell *127*, 265–275.

Kiprilov, E.N., Awan, A., Desprat, R., Velho, M., Clement, C.A., Byskov, A.G., Andersen, C.Y., Satir, P., Bouhassira, E.E., Christensen, S.T., and Hirsch, R.E. (2008). Human embryonic stem cells in culture possess primary cilia with hedgehog signaling machinery. J. Cell Biol. *180*, 897–904.

Krishnamurthy, J., Ramsey, M.R., Ligon, K.L., Torrice, C., Koh, A., Bonner-Weir, S., and Sharpless, N.E. (2006). p16INK4a induces an age-dependent decline in islet regenerative potential. Nature *443*, 453–457.

Li, H., Collado, M., Villasante, A., Strati, K., Ortega, S., Cañamero, M., Blasco, M.A., and Serrano, M. (2009). The Ink4/Arf locus is a barrier for iPS cell reprogramming. Nature *460*, 1136–1139.

Liu, S., Fang, X., Hall, H., Yu, S., Smith, D., Lu, Z., Fang, D., Liu, J., Stephens, L.C., Woodgett, J.R., and Mills, G.B. (2008). Homozygous deletion of glycogen synthase kinase 3beta bypasses senescence allowing Ras transformation of primary murine fibroblasts. Proc. Natl. Acad. Sci. USA *105*, 5248–5253.

Liu, H., Remedi, M.S., Pappan, K.L., Kwon, G., Rohatgi, N., Marshall, C.A., and McDaniel, M.L. (2009). Glycogen synthase kinase-3 and mammalian target of rapamycin pathways contribute to DNA synthesis, cell cycle progression, and proliferation in human islets. Diabetes *58*, 663–672.

Matheu, A., Maraver, A., Collado, M., Garcia-Cao, I., Cañamero, M., Borras, C., Flores, J.M., Klatt, P., Viña, J., and Serrano, M. (2009). Anti-aging activity of the Ink4/Arf locus. Aging Cell *8*, 152–161.

Meng, X., Poon, R., Zhang, X., Cheah, A., Ding, Q., Hui, C.C., and Alman, B. (2001). Suppressor of fused negatively regulates beta-catenin signaling. J. Biol. Chem. *276*, 40113–40119.

Narita, M., Nũnez, S., Heard, E., Narita, M., Lin, A.W., Hearn, S.A., Spector, D.L., Hannon, G.J., and Lowe, S.W. (2003). Rb-mediated heterochromatin formation and silencing of E2F target genes during cellular senescence. Cell *113*, 703–716.

Nickerson, S.C. (1989). Cilia on bovine mammary epithelium: ultrastructural observations. Cell Tissue Res. *255*, 675–677.

Noctor, S.C., Martínez-Cerdeño, V., Ivic, L., and Kriegstein, A.R. (2004). Cortical neurons arise in symmetric and asymmetric division zones and migrate through specific phases. Nat. Neurosci. *7*, 136–144.

Pan, J., and Snell, W. (2007). The primary cilium: keeper of the key to cell division. Cell *129*, 1255–1257.

Pan, Y., Bai, C.B., Joyner, A.L., and Wang, B. (2006). Sonic hedgehog signaling regulates Gli2 transcriptional activity by suppressing its processing and degradation. Mol. Cell. Biol. *26*, 3365–3377.

Ruiz i Altaba, A., Mas, C., and Stecca, B. (2007). The Gli code: an information nexus regulating cell fate, stemness and cancer. Trends Cell Biol. *17*, 438–447.

Seeley, E.S., Carrière, C., Goetze, T., Longnecker, D.S., and Korc, M. (2009). Pancreatic cancer and precursor pancreatic intraepithelial neoplasia lesions are devoid of primary cilia. Cancer Res. *69*, 422–430.

Serrano, M., Hannon, G.J., and Beach, D. (1993). A new regulatory motif in cell-cycle control causing specific inhibition of cyclin D/CDK4. Nature *366*, 704–707.

Serrano, M., Lin, A.W., McCurrach, M.E., Beach, D., and Lowe, S.W. (1997). Oncogenic ras provokes premature cell senescence associated with accumulation of p53 and p16INK4a. Cell *88*, 593–602.

Smelkinson, M.G., Zhou, Q., and Kalderon, D. (2007). Regulation of Ci-SCFSlimb binding, Ci proteolysis, and hedgehog pathway activity by Ci phosphorylation. Dev. Cell *13*, 481–495.

Takahashi-Yanaga, F., and Sasaguri, T. (2008). GSK-3beta regulates cyclin D1 expression: a new target for chemotherapy. Cell. Signal. *20*, 581–589.

Tempé, D., Casas, M., Karaz, S., Blanchet-Tournier, M.F., and Concordet, J.P. (2006). Multisite protein kinase A and glycogen synthase kinase 3beta

phosphorylation leads to Gli3 ubiquitination by SCFbetaTrCP. Mol. Cell. Biol. *26*, 4316–4326.

Tsygankov, D., Liu, Y., Sanoff, H.K., Sharpless, N.E., and Elston, T.C. (2009). A quantitative model for age-dependent expression of the p16INK4a tumor suppressor. Proc. Natl. Acad. Sci. USA *106*, 16562–16567.

Wang, W., Martindale, J.L., Yang, X., Chrest, F.J., and Gorospe, M. (2005). Increased stability of the p16 mRNA with replicative senescence. EMBO Rep. *6*, 158–164.

Wang, X., Tsai, J.W., Imai, J.H., Lian, W.N., Vallee, R.B., and Shi, S.H. (2009). Asymmetric centrosome inheritance maintains neural progenitors in the neocortex. Nature *461*, 947–955.

Wassermann, S., Scheel, S.K., Hiendlmeyer, E., Palmqvist, R., Horst, D., Hlubek, F., Haynl, A., Kriegl, L., Reu, S., Merkel, S., et al. (2009). p16INK4a is a beta-catenin target gene and indicates low survival in human colorectal tumors. Gastroenterology *136*, 196–205, e2.

Wilson, C.W., Nguyen, C.T., Chen, M.H., Yang, J.H., Gacayan, R., Huang, J., Chen, J.N., and Chuang, P.T. (2009). Fused has evolved divergent roles in vertebrate Hedgehog signalling and motile ciliogenesis. Nature *459*, 98–102.

Ye, X., Zerlanko, B., Kennedy, A., Banumathy, G., Zhang, R., and Adams, P.D. (2007). Downregulation of Wnt signaling is a trigger for formation of facultative heterochromatin and onset of cell senescence in primary human cells. Mol. Cell *27*, 183–196.

Zhong, W., and Chia, W. (2008). Neurogenesis and asymmetric cell division. Curr. Opin. Neurobiol. *18*, 4–11.

Zmijewski, J.W., and Jope, R.S. (2004). Nuclear accumulation of glycogen synthase kinase-3 during replicative senescence of human fibroblasts. Aging Cell *3*, 309–317.

Self-organization is a dynamic and lineage-intrinsic property of mammary epithelial cells

Lea Chanson[a,1], Douglas Brownfield[b,c,1], James C. Garbe[b], Irene Kuhn[b], Martha R. Stampfer[b], Mina J. Bissell[b,2], and Mark A. LaBarge[b,2]

[a]Institute of Bioengineering, Ecole Polytechnique Fédérale de Lausanne, CH-1015 Lausanne, Switzerland; [b]Life Sciences Division, Lawrence Berkeley National Laboratory, Berkeley, CA 94720; and [c]Department of Bioengineering, University of California, Berkeley, CA 94720

Contributed by Mina J. Bissell, Lawrence Berkeley National Laboratory, December 30, 2010 (sent for review December 6, 2010)

Loss of organization is a principle feature of cancers; therefore it is important to understand how normal adult multilineage tissues, such as bilayered secretory epithelia, establish and maintain their architectures. The self-organization process that drives heterogeneous mixtures of cells to form organized tissues is well studied in embryology and with mammalian cell lines that were abnormal or engineered. Here we used a micropatterning approach that confined cells to a cylindrical geometry combined with an algorithm to quantify changes of cellular distribution over time to measure the ability of different cell types to self-organize relative to each other. Using normal human mammary epithelial cells enriched into pools of the two principal lineages, luminal and myoepithelial cells, we demonstrated that bilayered organization in mammary epithelium was driven mainly by lineage-specific differential E-cadherin expression, but that P-cadherin contributed specifically to organization of the myoepithelial layer. Disruption of the actomyosin network or of adherens junction proteins resulted in either prevention of bilayer formation or loss of preformed bilayers, consistent with continual sampling of the local microenvironment by cadherins. Together these data show that self-organization is an innate and reversible property of communities of normal adult human mammary epithelial cells.

mammary gland | tissue biology

Most mammalian adult tissues are replenished and repaired throughout life by reservoirs of stem cells. As new somatic cells replace old ones or build new tissue, organization and architecture must be maintained. The alternative, loss of organization in adult tissues, is associated with cancer and other diseases. Lineage-specific progenitors or their differentiated progeny must have a means to reach their ultimate site of residence within the adult tissue. The robust ability to organize cells into tissues is marked from conception: Heterogeneous aggregates of dissociated cells from embryonic tissues, suspended in gels or hanging droplets or on agarose-coated plates, self-organize into semblances of the original tissues (1–5). The mechanisms governing self-organization during developmental morphogenesis (6–10) are likely conserved in the maintenance of organization in adult tissues. Here we use normal human mammary epithelial cells (HMEC) as a model to determine how organized states are preserved in normal adult epithelia.

The mammary gland undergoes cycles of proliferation and involution, showing as much as a 10-fold expansion in preparation for lactation followed by return to normal size. During these processes, the precise bilayered branching organization throughout the gland is maintained; secretory luminal epithelial cells (LEPs) line the lumen, surrounded by a layer of contractile myoepithelial cells (MEPs) that are adjacent to the basement membrane. We hypothesized that mammary epithelial cells possessed lineage-specific intrinsic abilities to self-organize into domains of lineage specificity. Such a mechanism would help explain how, for instance, the mammary stem cell-enriched zone in the ducts (11) is maintained separately from the rank-and-file LEPs and MEPs, and how LEPs and MEPs form and maintain bilayers. The phenomenon of self-organization has not been well studied in humans, perhaps because of the challenges of working with primary materials and a paucity of tractable culture systems for maintaining cell types from normal adult tissues. To facilitate a quantitative understanding of those processes in an adult epithelial tissue, we used a robust cell culture system that enables culture of pre-stasis normal HMEC obtained from reduction mammoplasties for 40–60 population doublings while maintaining both the LEP and MEP lineages (12). Flow cytometry-enriched cells from both lineages were placed in arrays of micropatterned microwells, where their distributions were tracked over time to generate a dynamic understanding of lineage-specific self-organizing behavior.

Results and Discussion

Quantification of Self-Organizing Activity in Different Lineages of Normal Human Mammary Epithelial Cells. We first used a classical self-organization assay to determine whether different lineages of cultured HMEC derived from reduction mammoplasty possessed an intrinsic ability to form bilayered structures. Subpopulations of LEPs and MEPs, defined as $CD227^+/CD10^-$/keratin 19 $(K19)^+$/keratin 14 $(K14)^-$ and $CD227^-/CD10^+/K19^-/K14^+$, respectively (11), were enriched by FACS from heterogeneous normal finite-lifespan HMEC (12) at passage 4 or 5 (Fig. 1 *A*, *A′*, and *A″*). The two lineages were labeled with long-lasting fluorescent membrane dyes of different wavelengths, mixed together, and then were suspended in hanging droplets. The formation of cores of LEPs surrounded by MEPs (Fig. 1*B*), similar to their organization in vivo, was observed over 48 h. However, the considerable variation in aggregate size, shape, and focal planes precluded a quantitative understanding of the phenomenon.

Therefore, a microwell culture platform was engineered that confined the HMEC mixtures to a 3D cylindrical geometry, which enabled quantification of lineage distributions over time (Fig. 1*C*). Representative optical sections of mixed LEPs and MEPs in microwells, taken at middepth (~25 μm) at 0 and 48 h, suggest self-organization had occurred, as compared with mixtures of arbitrarily labeled HMEC cultures (Fig. 1*D*). Time-lapse microscopy from one well demonstrates the dynamic nature of the organizing process (Fig. S1 and Movie S1). Heat maps showing the lineage distributions over time suggested that in a majority of microwells MEPs formed a ring surrounding cores of LEPs as early as 24 h, and lasted for at least 48 h (Fig. 1*E*, *Upper*). A 1:1 ratio of LEPs to MEPs was determined empirically to provide the most clearly separable distributions, as compared with ratios of 1:2 or 1:3. Using relatively more LEPs than MEPs (e.g., in a ratio of 2:1 or 3:1) was difficult due to the paucity of LEPs. Arbitrarily labeled HMEC cultures, mixed at a 1:1 ratio, showed overlapping dis-

Author contributions: M.J.B. and M.A.L. designed research; L.C., D.B., J.C.G., and M.A.L. performed research; J.C.G., M.R.S., M.J.B., and M.A.L. contributed new reagents/analytic tools; L.C., I.K., M.R.S., M.J.B., and M.A.L. analyzed data; and I.K., M.J.B., and M.A.L. wrote the paper.

The authors declare no conflict of interest.

[1]L.C. and D.B. contributed equally to this work.

[2]To whom correspondence may be addressed. E-mail: mjbissell@lbl.gov or MALabarge@lbl.gov.

This article contains supporting information online at www.pnas.org/lookup/suppl/doi:10.1073/pnas.1019556108/-/DCSupplemental.

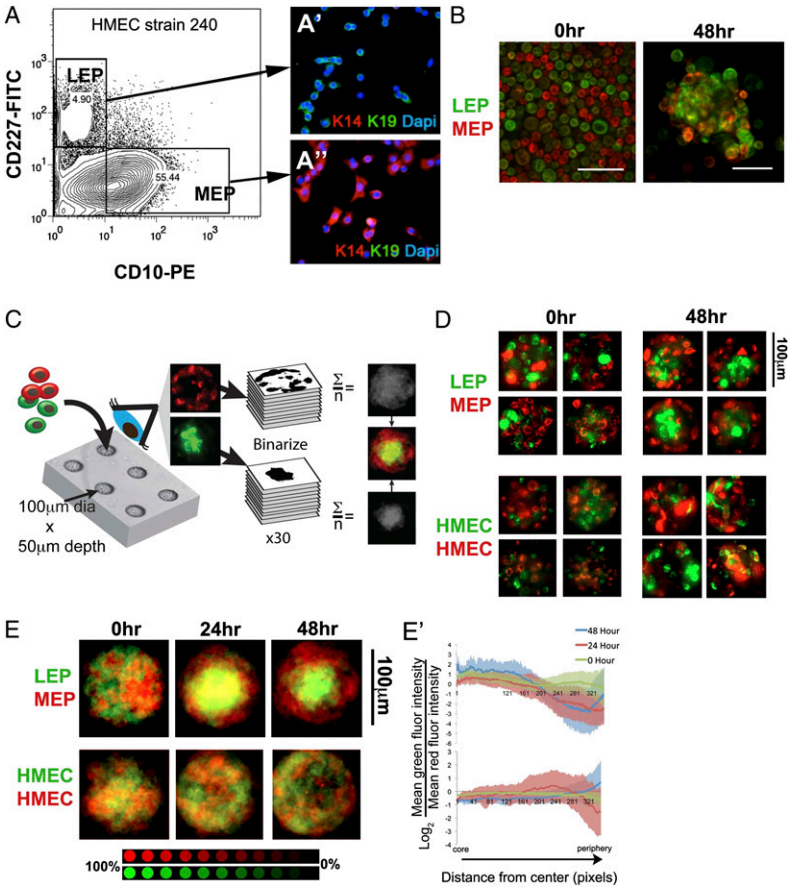

Fig. 1. Heterogeneous mixtures of luminal and myoepithelial cells self-organize into ordered structures. (*A*) Flow cytometry analysis of fourth-passage finite-lifespan HMEC strain 240L reveals distinct populations of the two principal somatic epithelial lineages of mammary gland: MEPs, defined here as $CD227^{-}/CD10^{+}$, and LEPs, defined as $CD227^{+}/CD10^{-}$. (*A′* and *A″*) Immunofluorescence of sorted cells for MEP and LEP markers K14 (red) and K19 (green), respectively, verified that (*A′*) $CD227^{+}$ LEPs were $K14^{-}/K19^{+}$, and (*A″*) $CD10^{+}$ MEPs were $K14^{+}/K19^{-}$. Nuclei were counterstained with DAPI (blue). (*B*) Images of mixtures of fluorescently labeled LEPs (green) and MEPs (red) suspended in hanging droplets and imaged with a confocal microscope just after mixing at 0 h (*Left*) and at 48 h (*Right*). (Scale bars: 20 μm.) (*C*) Cartoon representation of the microwell self-organization assay. Fluorescently labeled LEPs (green) and MEPs (red) were mixed together and placed in arrays of microwells that did not support cell adhesion. Thirty wells were imaged with a confocal microscope just after the addition of cells (0 h) and again at 24 h and 48 h. Fluorescence from both green and red channels in one optical section per well was binarized and then combined and averaged to generate two gray-scale composite images that were overlaid to generate a single two-color composite distribution map for each condition, with LEP distributions in green and MEP distributions in red. (*D*) Representative fluorescence images ofLEP (green) and MEP (red) in four different microwells at 0 h and 48 h (*Upper*) and of controls, which were heterogeneous HMEC arbitrarily labeled with red or green fluorescent labels (*Lower*). (*E*) Distribution maps of LEP (green) and MEP (red) (*Upper*) or control mixtures at the 0-h, 24-h, and 48-h time points (*Lower*). (*E′*) Quantification of heat maps in *E* showing changes in mean distribution of red and green pixels along the radius around 360° of arc at three time points. Green lines show 0 h, red lines show 24 h, and blue lines show 48 h. SD is shown by the lightly shaded regions of colors corresponding to each line.

tributions of cells that did not resolve into distinct populations (Fig. 1*E*, *Lower*). Quantification of the heat maps (Fig S2) confirmed that a core of LEPs surrounded by MEPs was observable as early as 24 h, and showing as much as a fourfold difference in LEP:MEP ratios at the core versus the periphery by 48 h ($P < 0.001$) (Fig. 1*E′*, *Upper*). By contrast there was no difference in ratios at the core and the periphery of the arbitrarily labeled HMEC controls at any time point (Fig. 1*E′*, *Lower*). Inflections in the graphs sometimes were observed toward the peripheral regions because of imperfect registration of the well images. Taken together, these results indicate that self-organizing is an innate property of the LEP and MEP HMEC lineages.

Levels of E-Cadherin Expression Are Lineage Specific. Self-organizing behavior has been ascribed to disparate adhesive properties among the participating cells in embryonic progenitors from the three germ layers, in cancer cell lines, and in fibroblasts engineered to express cell–cell adhesion molecules (the differential adhesion hypothesis, reviewed in ref. 6). Cadherin cell–cell adhesion molecules, particularly E-cadherin, play key roles in tissue morphogenesis during vertebrate gastrulation (13). Quantification of images of fluorescently immunostained tissue sections of normal mammary gland (Fig. 2*A*) from two individuals revealed that more E-cadherin protein was present at the borders between two LEPs than at the borders between a LEP and a MEP ($P < 0.001$) (Fig. 2*B*). Flow cytometry measurements of E-cadherin surface protein levels were made on LEPs and MEPs. In HMEC strains at fourth passage from six individuals, a reproducible pattern was observed, whereby more E-cadherin was detected on LEPs than on MEPs (Fig. 2*C*). The lineage-specific expression levels of E-cadherin made it an attractive candidate for further testing of the differential adhesion hypothesis as it pertains to self-organization among HMEC.

Functional Identification of Adhesion Molecules That Drive Tissue Self-Organization. To determine whether cadherins played a functional role in the self-organization of LEPs and MEPs, inhibitors of E-, P-, and VE-cadherin were added to the medium of the microwell assay to antagonize those specific cell–cell interactions. P-cadherin is expressed by MEPs in vivo but not by LEPs (14). VE-cadherin is expressed by endothelial cells but not by epithelial cells (13) and was used as a control for potential effects of heterotypic cadherin interactions (9). Each of the putative inhibitors was added at the beginning of the experiment and was refreshed every 24 h with medium changes. An antibody that blocked E-cadherin, and recombinant E-cadherin fused to the human IgG-Fc region (recEcad), prevented self-organizing of LEPs and MEPs. Quantification of the heat maps did not reveal differences in LEP:MEP ratios at the core and periphery (Fig. 3 *A* and *A′*). An antibody that blocked P-cadherin did not abolish sorting, because a core enriched for LEPs was surrounded by MEPs ($P < 0.001$) (Fig. 3 *A* and *A′*). However, quantification revealed that there were more MEP at the core [hovering around a ratio of 1:1 (Fig. 3 *A′*)] than in untreated LEPs and MEPs, which usually showed about a twofold enrichment of LEPs at the core (Fig. 1 *E* and *E′*, *Upper*). Those data suggest that LEPs organization at the core is unaffected by P-cadherin antibodies, whereas the MEPs were relatively more challenged in their journey to the periphery. Recombinant VE-cadherin IgG-fusion protein (recVEcad) did not prevent organizing (Fig. 3 *A* and *A′*). These data suggested that differential levels of E-cadherin at the surfaces of LEPs and MEPs were the principle drivers of self-organization and thus were the focus of the majority of subsequent studies. However, these data also show that P-cadherin plays a more lineage-restricted role in MEP self-organizing.

Self-Organization Was Prevented After Negative Modulation of the Actomyosin Network. Previous studies of mammary epithelial morphogenesis have implicated profound roles for the actomy-

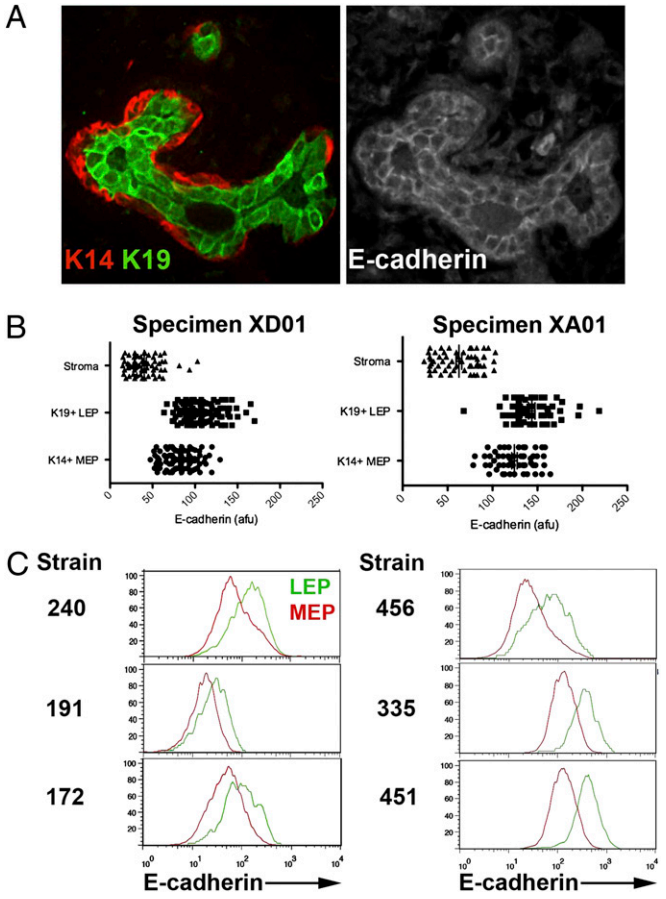

Fig. 2. Epithelial lineages that comprise the mammary gland express E-cadherin differentially. (*A*) A tissue section from a normal mammary gland, specimen XD01, embedded in paraffin and triple-immunostained to show expression of (*Left*) the MEP and LEP markers K14 (red) and K19 (green), respectively, and (*Right*) E-cadherin (gray scale). (*B*) Dot plots show image quantification from two individuals, XD01 and XA01, of E-cadherin protein levels at the border between two LEPs (K19+ LEP) and at the border between an LEP and an MEP cell (K14+ LEP) and background fluorescence as measured on stroma, which does not express E-cadherin (Stroma). Measurements are expressed in arbitrary fluorescence units (afu), n = 100 for each cell type collected from at least three sections. (*C*) Flow cytometry analysis of E-cadherin expression in $CD10^+$ MEPs and $CD227^+$ LEPs in HMEC strains at fourth or fifth passage from six individuals.

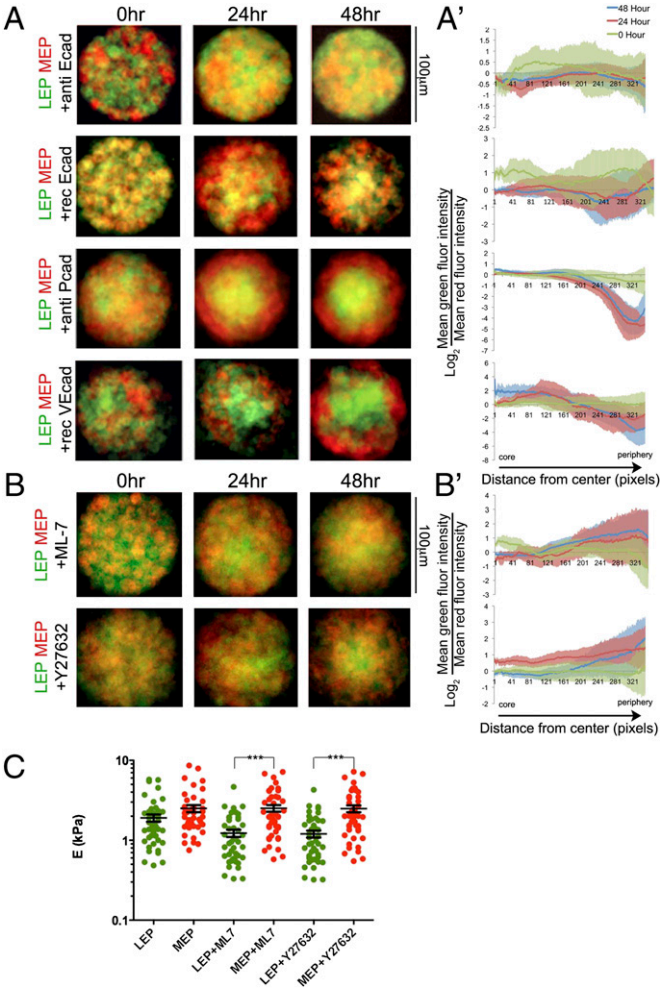

Fig. 3. E-cadherin–containing junctions and the cytoskeleton regulatory molecules ROCK and MLCK are required for self-organizing. (*A*) Maps of HMEC lineage distributions over time in the presence of E-, P-, or VE-cadherin–blocking agents (anti–E-cadherin, recombinant (rec)E-cadherin, anti–P-cadherin, or recVE-cadherin); LEP are green, and MEP are red. (*B*) LEP (green) and MEP (red) distributions in the presence of the MLCK inhibitor ML-7 or the ROCK inhibitor Y27632. (*A′* and *B′*) Quantification of heat maps in *A* and *B*, respectively, showing changes in mean distribution of red (MEP) and green (LEP) pixels along the radius around 360° of arc at three time points. Green lines show 0 h, red lines show 24 h, and blue lines show 48 h. SD is shown by the lightly shaded region of color corresponding to each line. (*C*) Atomic force microscopy measurements of LEP and MEP in the presence of ML-7 and Y27632. The graph represents elasticity (kPa) values for 45 cells per condition; the interior line represents mean elasticity values; error bars show SE. Strain 240L at fourth passage was used for all experiments.

osin regulatory network in normal morphogenesis (15, 16). We therefore examined the impact on HMEC self-organization of the actomyosin network inhibitors ML-7, a myosin light-chain kinase (MLCK) inhibitor (17), and Y27632, a Rho kinase (ROCK) inhibitor that blocks both ROCK1 and ROCK2 (18). Inhibitors were added at the beginning of the experiment and were refreshed every 24 h with medium changes. Analysis of LEPs and MEPs distributions over 48 h revealed that both inhibitors prevented self-organization; there were no differences in lineage distribution between the core and peripheral regions (Fig. 3 *B* and *B′*). Modulation of the actomyosin network also is known to cause changes in the elasticity and cortical tension of cells. Self-organization studies of germline progenitor cells dissociated from zebra fish embryos suggested that differential actomyosin-dependent cell-cortex tension was a crucial component of self-organization in that system (8). Stiffer cells organized to the inside and were surrounded by softer cells, and disruption of the stiffness relationship by actomyosin network inhibitors led to deficits in self-organization (8). Using an atomic force microscope, we measured the elasticity of untreated and inhibitor-treated MEPs and LEPs. Although untreated MEPs tended to be stiffer than LEPs, that difference became significant only in the presence of the inhibitors ($P < 0.001$) (Fig. 3*C*). MEP stiffness was unaffected by ML-7 and by Y27632, but those inhibitors caused softening of LEPs (Fig. 3*C*). In HMEC the actomyosin network inhibitors increased the magnitude of the difference in elasticity between LEPs and MEPs but did not alter their relative elasticity (i.e., LEPs always were softer than MEPs), suggesting that in this system self-organization was not driven by differential elasticity.

Perturbations of the Actomyosin Network in the Microwell Platform Revealed That Self-Organization Is Dynamic and Reversible. How did the actomyosin inhibitors upset the self-organizing mechanism? We investigated whether the actomyosin inhibitors affected expression or binding activities of E-cadherin in HMEC. Addition

of ML-7 or Y27632 to the HMEC culture medium did not change lineage-specific differences in E-cadherin expression as measured via flow cytometry; invariably, LEPs expressed more E-cadherin than did MEPs (Fig. 4*A*). The ability of rec-Ecad simply to bind surfaces of HMEC in suspension also was measured by flow cytometry. Binding of recEcad did not occur in Ca^{2+}-free medium or when HMEC were preincubated with an E-cadherin–blocking antibody (Fig. 4*B*). A 6-h pretreatment with Y27632 or ML-7 did not prevent recEcad binding (Fig. 4*B*). Therefore, neither differential expression levels of E-cadherin nor its ability simply to bind other E-cadherin molecules at the surface was impacted by ML-7 or Y27632.

Because of the central importance of the cytoskeleton in adherens junction regulation, we considered the possibility that the actomyosin inhibitors modulated the ability of E-cadherin junctions to mature or remodel (19), thereby impacting HMEC organization. Disruption of MLCK would prevent proper localization of myosin IIA to the E-cadherin junction, disrupting E-cadherin clustering and decreasing homophilic adhesion (20). Conversely, mature adherens junctions were unable to break down and recycle in the presence of Y27632 in HCT116 and MDCK epithelial cell lines (21). Those reports predicted that ML-7 would ablate already-organized HMEC structures, whereas Y27632 would preserve them. Accordingly, ML-7 or Y27632 was added to mixtures of LEPs and MEPs in the microwell assay, either just after cells were added to wells at the start of the assay (0 h) or after 24 h, when the DMSO controls already started to show signs of organization. In contrast to the experiments shown in Fig. 3*B*, in which the inhibitors were refreshed every 24 h, in these experiments the inhibitors were added a single time, with the expectation, based on empirical findings, that the inhibitor's activity would begin to weaken by 48 h. This protocol tested the reversibility of the system, because in one condition sorting would be prevented from the beginning and then gradually would be unleashed, and in the second condition sorting would be allowed to get underway before perturbation by the inhibitors after 24 h. Both inhibitors, when added at 0 h, prevented self-organization through the 24-h time point, but as the inhibitors' activity diminished significant, differences in LEP:MEP ratios in the core and at the periphery were observed by 48 h ($P < 0.01$) (Fig. 4 *C* and *C′*). The unique phenotypes of each inhibitor were revealed when they were added after the assay had been underway for 24 h. Before addition of the inhibitors, the LEP were enriched at the core and were surrounded by peripheral MEPs ($P < 0.001$) (Fig. 4 *C* and *C′*). When measured at 48 h, addition of ML-7 had obliterated organization, eliminating any difference in the distributions of the lineages (P = ns), whereas Y27632 had preserved the self-organized LEP cores that were encircled by MEPs ($P < 0.001$) (Fig. 4 *C* and *C′*). As a whole, these observations are consistent with the following model: ML-7 prevented adherens junction formation or maturation, and breaking the adherens junctions prevented cells from self-organizing and caused dissolution of already organized structures. Conversely, Y27632 prevented adherens junction recycling, so the cells could not let go of

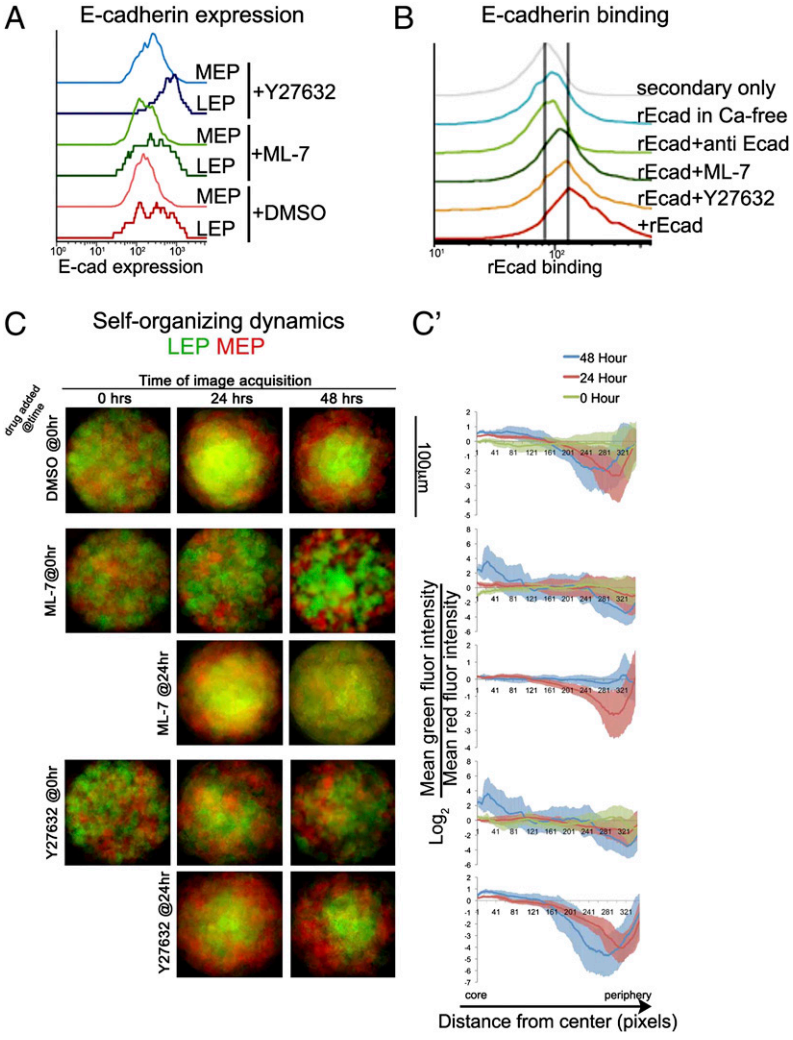

Fig. 4. Self-organization among luminal and myoepithelial cells is driven by E-cadherin activity. (*A*) E-cadherin protein expression at the surface of LEPs and MEPs in the presence of ML-7 or Y27632, as measured by flow cytometry. (*B*) Flow cytometry analysis of recombinant E-cadherin (rEcad) binding to HMEC cell surfaces. (*C*) LEP (green) and MEP (red) distribution maps showing the impact on self-organization over time (time points: 0 h, 24 h, and 48 h) when the inhibitors ML7 and Y27632 were added at 0 h or after 24 h. (*C′*) Quantification of heat maps in *C* showing changes in mean distribution of red (MEP) and green (LEP) pixels along the radius around 360° of arc at three time points: green lines show 0 h, red lines show 24 h, and blue lines show 48 h. SD is shown by the lightly shaded region of color corresponding to each line. Strain 240L at fourth passage was used for all experiments.

one another to sample the surrounding microenvironment. Thus, both establishing and maintaining organized states are dynamic and reversible processes.

Here we demonstrated that self-organization of mammary epithelial cells is a lineage-specific process that is principally E-cadherin driven; however, P-cadherin also may play a role in organizing the MEP layer. Unaltered normal finite-lifespan HMEC and the microwell assay were used together with recombinant proteins and antibodies that blocked specific adherens junction proteins. The elegant proof-of-principal experiments, which that showed differential levels of cell–cell adhesion molecules can drive self-organizing, were performed using fibroblasts and other immortal cell lines that were engineered to express different levels of adherens junction proteins. It is remarkable, given the undoubted complexity of the LEP and MEP cell surfaces, that E-cadherin plays so central a role in the process of self-organization in those cells. It has been hypothesized that self-organizing is not simply the result of differential levels of cadherin expression or of binding affinities, but rather that adhesion energy and the ability to remodel cell–cell junctions are crucial determinants (22). Dynamic analysis of HMEC in the microwell assay platform in the presence of actomyosin inhibitors provided support for that hypothesis in the context of mammary gland (Fig. 4 *C*–*C′*). Elegant time-lapse imaging studies of mouse mammary organoid morphogenesis also revealed that the actomyosin inhibitors Y27632 and ML-7 disrupted the clean bilayered organization (15), but not to the catastrophic extent observed in the HMEC microwell assay. Because the mouse mammary organoids were developed in vivo, a number of additional cellular interconnectivities crucial for tissue stability may have formed that were absent in our recombined system. Although we focused on cell–cell E-cadherin junctions, other adhesive and physical interactions, such as desmosomal interactions between LEPs and MEPs (23), undoubtedly are important in maintaining mammary gland organization and bear further dissection. Cell–extracellular matrix (ECM) interactions also will likely affect sorting in vivo. Because the microwell assay uses a nonfouling coating to prevent cell adhesion, the adherens junction proteins may have had a more pronounced effect on self-organizing than they would have had in the presence of ECM. Atomic force microscopy analysis of LEP and MEP on plastic dishes indicated that LEP tended to be softer than MEP. However, a cultured murine epithelial cell line became less stiff in contact with laminin-111, a principal component of basement membrane, than when in contact with plastic (24). Therefore, MEPs in vivo may be less or equally as stiff as LEPs because of their direct contact with basement membrane. Future iterations of the microwell platform will help elucidate more of the factors involved in making stable and organized tissues.

Studying self-organizing behavior of a human epithelium generally is challenging because results cannot be extrapolated easily to in vivo conditions. However, observations of breast cancer pathogenesis suggest the basic mechanisms described here are important for maintaining mammary gland organization. E-cadherin expression and localization frequently are misregulated in breast cancers (25–27), and loss of E-cadherin is a hallmark of the epithelial-to-mesenchymal transition, which is associated with invasive and aggressive breast cancer (28). The mechanisms governing self-organization also are important in the context of regenerative tissue maintenance. As MEPs and LEPs are produced anew by mammary progenitor cells in vivo, they must adopt their appropriate place within the tissue, or, alternatively, the progenitors must be able to move to receive instructive microenvironments that direct cell-fate decisions (29). Understanding tissue self-organization mechanisms may help explain how stem cell differentiation and maintenance of tissue architecture in adults are coordinated.

Materials and Methods

Cell Culture. HMEC strains were established and maintained according to previously reported methods (12, 30). Cells were maintained in M87A medium and used for assays at fourth and fifth passages; strain 240L was the only strain used for self-organizing and binding assays.

Microwell Self-Organization Assay. Micropatterned substrata were made according to Tan et al. (31). Polydimethylsiloxane (PDMS) microwell arrays were formed by curing prepolymer with base:cure ratio of 10:1 (Sylguard 184) against a prepatterned master. The arrays of wells were peeled away and were cut into 1-cm^2 pieces that were affixed with a few microliters of uncured PDMS to the bottom of a 24-well plate (Mitek). Plates with microwells were UV oxidized for 7 min (UVO-Cleaner 42; Jelight Co.), blocked with 2 mg/mL BSA (Sigma) for 1 h under vacuum, and rinsed with PBS and M87A. All self-organizing experiments were conducted with HMEC strain 240L. Flow cytometry-sorted HMEC were stained with CM-DiI, SP-DiOC18 (3), or DiIC18(5)-DS (Invitrogen), used at 1:1,000 in PBS for 5 min at 37 °C followed by 15 min at 4 °C. Cells were washed extensively with medium after staining. Dye-stained HMEC were mixed at a ratio of 1:1 (LEP:MEP) or 1:1 (randomly stained green:red HMEC cultures) and were resuspended in M87A at 1 million cells/mL. Inhibitors were added to the cell suspensions just before HMEC were introduced into the wells and were allowed to load for 30–60 min. Excess cells were washed away with medium; inhibitors then were added to the medium after excess cells were washed away and at every medium change. anti–E-cadherin (100 μg/mL clone HECD-1; Invitrogen); anti–E-cadherin (100 μg/mL clone HECD-1; Invitrogen); anti–P-cadherin (100 μg/mL clone NCC-CAD-299; Abcam); recombinant human (rh)E-cadherin-Fc (recEcad, 100 μg/mL; R&D Systems); rhVE-cadherin (100 μg/mL; R&D Systems); Y27632 (10^{-5} M; Calbiochem); or ML-7 at 3×10^{-6} M (Calbiochem). HMEC were imaged at 0, 24, or 48 h with a spinning disk confocal microscope (Carl Zeiss). Red and green fluorescence channels in images taken at the ~25-μm *z* axis positions of 30 wells from each condition at each time point were binarized using the Threshold function, merged into a Z-stack, and then averaged using ImageJ software (National Institutes of Health). Gray-scaled average images corresponding to LEP and MEP were merged into a single image with red or green look-up tables applied to each average image.

Heat maps were normalized to the highest intensity value and were used to quantify sorting using the expression $\log_2$(mean green pixel intensity/mean red pixel intensity). A script was written using MATLAB (Mathworks) to plot differential intensity as a function of the distance from the center and to compute the average plot from θ of 0–360° (Fig S2).

Flow Cytometry Sorting and Assays. HMEC at fourth or fifth passage were trypsinized and resuspended in medium. For enrichment of LEP and MEP images, anti–CD227-FITC (clone HMPV; BD) or anti–CD10-PE (clone HI10a; BioLegend) was added to the medium at 1:50 for 25 min on ice. HMEC then were washed in PBS and sorted on a FACS Vantage DIVA (BD) into their own medium.

E-cadherin expression on LEP and MEP was measured by addition of anti–E-cadherin-A647 (clone 67A4; Biolegend) to the above mixture at 1:50.

Atomic Force Microscopy Measurements of Stiffness. Once samples were equilibrated to 25 °C, cell deformity was measured, and stiffness was calculated as previously described (24). The resulting data were plotted using Prism(GraphPad Software) (n = 45).

Statistics. E-cadherin images and atomic force microscopy were analyzed using the Kruskal–Wallis test and Dunn's test for multiple comparisons, using a 95% confidence interval. Differences between first and third thirtiles of $\log_2$ (mean green fluorescence/mean red fluorescence) per pixel plotted as a function of distance from the center were analyzed by one-way ANOVA, using Bartlett's test for equal variance and followed by a Tukey's test for multiple comparison using a 99.9% confidence interval. Statistics were computed with Prism (GraphPad Software, Inc.).

ACKNOWLEDGMENTS. We thank Drs. Matthias Lutolf and Celeste M. Nelson for insightful discussions, Celeste M. Nelson. for providing micropatterned wafers, and Dr. Daniel Fletcher for use of his atomic force microscope. M.A.L is supported by Grant R00AG033176 from the National Institute on Aging, Grant U54CA112970 from the National Cancer Institute, and by Laboratory Directed Research and Development (LDRD) funding from the Lawrence Berkeley National Laboratory, provided by the Director, Office of Science, of the US Department of Energy under Contract DE-AC02-05CH11231. M.J.B. is supported by grants from the US Department of Energy, Office of Biological and Environmental Research, a Distinguished Fellow Award, Low Dose Radiation Program contract DE-AC02-05CH1123; National Cancer Institute Grants R37CA064786, U54CA126552, R01CA057621, U54CA112970, U54CA143836, and U01CA143233; and by US Department of Defense Grant W81XWH0810736. M.R.S. and J.C.G. are supported by US Department of Defense Grants BCRP BC060444 and U54CA112970.

1. Steinberg MS (1962) Mechanism of tissue reconstruction by dissociated cells. II. Time-course of events. *Science* 137:762–763.
2. Steinberg MS (1962) On the mechanism of tissue reconstruction by dissociated cells, Iii. Free energy relations and the reorganization of fused, heteronomic tissue fragments. *Proc Natl Acad Sci USA* 48:1769–1776.
3. Steinberg MS (1962) On the mechanism of tissue reconstruction by dissociated cells. I. Population kinetics, differential adhesiveness, and the absence of directed migration. *Proc Natl Acad Sci USA* 48:1577–1582.
4. Townes PL, Holtfreter J (1955) Directed movements and selective adhesion of embryonic amphibian cells. *J Exp Zool* 128:53–120.
5. Wei C, Larsen M, Hoffman MP, Yamada KM (2007) Self-organization and branching morphogenesis of primary salivary epithelial cells. *Tissue Eng* 13:721–735.
6. Foty RA, Steinberg MS (2004) Cadherin-mediated cell-cell adhesion and tissue segregation in relation to malignancy. *Int J Dev Biol* 48:397–409.
7. Foty RA, Steinberg MS (2005) The differential adhesion hypothesis: A direct evaluation. *Dev Biol* 278:255–263.
8. Krieg M, et al. (2008) Tensile forces govern germ-layer organization in zebrafish. *Nat Cell Biol* 10:429–436.
9. Shi Q, Chien YH, Leckband D (2008) Biophysical properties of cadherin bonds do not predict cell sorting. *J Biol Chem* 283:28454–28463.
10. Manning ML, Foty RA, Steinberg MS, Schoetz EM (2010) Coaction of intercellular adhesion and cortical tension specifies tissue surface tension. *Proc Natl Acad Sci U S A* 107(28):12517–12522.
11. Villadsen R, et al. (2007) Evidence for a stem cell hierarchy in the adult human breast. *J Cell Biol* 177:87–101.
12. Garbe JC, et al. (2009) Molecular distinctions between stasis and telomere attrition senescence barriers shown by long-term culture of normal human mammary epithelial cells. *Cancer Res* 69:7557–7568.
13. Gumbiner BM (2005) Regulation of cadherin-mediated adhesion in morphogenesis. *Nat Rev Mol Cell Biol* 6:622–634.
14. Shimoyama Y, et al. (1989) Cadherin cell-adhesion molecules in human epithelial tissues and carcinomas. *Cancer Res* 49:2128–2133.
15. Ewald AJ, Brenot A, Duong M, Chan BS, Werb Z (2008) Collective epithelial migration and cell rearrangements drive mammary branching morphogenesis. *Dev Cell* 14: 570–581.
16. Vargo-Gogola T, Heckman BM, Gunther EJ, Chodosh LA, Rosen JM (2006) P190-B Rho GTPase-activating protein overexpression disrupts ductal morphogenesis and induces hyperplastic lesions in the developing mammary gland. *Mol Endocrinol* 20: 1391–1405.
17. Makishima M, et al. (1991) Induction of differentiation of human leukemia cells by inhibitors of myosin light chain kinase. *FEBS Lett* 287:175–177.
18. Davies SP, Reddy H, Caivano M, Cohen P (2000) Specificity and mechanism of action of some commonly used protein kinase inhibitors. *Biochem J* 351:95–105.
19. Fukata M, Kaibuchi K (2001) Rho-family GTPases in cadherin-mediated cell-cell adhesion. *Nat Rev Mol Cell Biol* 2:887–897.
20. Smutny M, et al. (2010) Myosin II isoforms identify distinct functional modules that support integrity of the epithelial zonula adherens. *Nat Cell Biol* 12:696–702.
21. Sahai E, Marshall CJ (2002) ROCK and Dia have opposing effects on adherens junctions downstream of Rho. *Nat Cell Biol* 4:408–415.
22. Borghi N, James Nelson W (2009) Intercellular adhesion in morphogenesis: Molecular and biophysical considerations. *Curr Top Dev Biol* 89:1–32.
23. Runswick SK, O'Hare MJ, Jones L, Streuli CH, Garrod DR (2001) Desmosomal adhesion regulates epithelial morphogenesis and cell positioning. *Nat Cell Biol* 3:823–830.
24. Alcaraz J, et al. (2008) Laminin and biomimetic extracellular elasticity enhance functional differentiation in mammary epithelia. *EMBO J* 27:2829–2838.
25. Zhang X, et al. (2009) Atypical E-cadherin expression in cell clusters overlying focally disrupted mammary myoepithelial cell layers: Implications for tumor cell motility and invasion. *Pathol Res Pract* 205:375–385.
26. Korkola JE, et al. (2003) Differentiation of lobular versus ductal breast carcinomas by expression microarray analysis. *Cancer Res* 63:7167–7175.
27. Moll R, Mitze M, Frixen UH, Birchmeier W (1993) Differential loss of E-cadherin expression in infiltrating ductal and lobular breast carcinomas. *Am J Pathol* 143: 1731–1742.
28. Cano A, et al. (2000) The transcription factor snail controls epithelial-mesenchymal transitions by repressing E-cadherin expression. *Nat Cell Biol* 2:76–83.
29. LaBarge MA, et al. (2009) Human mammary progenitor cell fate decisions are products of interactions with combinatorial microenvironments. *Integr Biol* 1:70–79.
30. Stampfer MR, Bartley JC (1985) Induction of transformation and continuous cell lines from normal human mammary epithelial cells after exposure to benzo[a]pyrene. *Proc Natl Acad Sci USA* 82:2394–2398.
31. Tan JL, Liu W, Nelson CM, Raghavan S, Chen CS (2004) Simple approach to micropattern cells on common culture substrates by tuning substrate wettability. *Tissue Eng* 10:865–872.

TGF-β signaling engages an ATM-CHK2-p53–independent RAS-induced senescence and prevents malignant transformation in human mammary epithelial cells

Rocky Cipriano[a], Charlene E. Kan[b], James Graham[a], David Danielpour[c], Martha Stampfer[d], and Mark W. Jackson[a,c,1]

Departments of [a]Pathology and [b]Genetics and [c]Case Comprehensive Cancer Center, Case Western Reserve University, Cleveland, OH 44106; and [d]Life Sciences Divisions, Lawrence Berkeley National Laboratory, Berkeley, CA 94720

Edited* by George R. Stark, Lerner Research Institute NE2, Cleveland, OH, and approved April 14, 2011 (received for review October 7, 2010)

Oncogene-induced senescence (OIS), the proliferative arrest engaged in response to persistent oncogene activation, serves as an important tumor-suppressive barrier. We show here that finite lifespan human mammary epithelial cells (HMEC) undergo a p16/RB- and p53-independent OIS in response to oncogenic RAS that requires TGF-β signaling. Suppression of TGF-β signaling by expression of a dominant-negative TGF-β type II receptor, use of a TGF-β type I receptor inhibitor, or ectopic expression of MYC permitted continued proliferation upon RAS expression. Surprisingly, unlike fibroblasts, shRNA-mediated knockdown of ATM or CHK2 was unable to prevent RAS-mediated OIS, arguing that the DNA damage response is not required for OIS in HMEC. Abrogation of TGF-β signaling not only allowed HMEC lacking p53 to tolerate oncogenic RAS but also conferred the capacity for anchorage-independent growth. Thus, the OIS engaged after dysregulated RAS expression provides an early barrier to malignant progression and is mediated by TGF-β receptor activation in HMEC. Understanding the mechanisms that initiate and maintain OIS in epithelial cells may provide a foundation for future therapies aimed at reengaging this proliferative barrier as a cancer therapy.

breast cancer | tumor suppressor

Cancer cells acquire errors that impart behaviors not present in their normal cells of origin. Such altered capacities include (*i*) loss of sensitivity to antigrowth and/or proapoptotic signals, (*ii*) constitutive growth signaling, (*iii*) unlimited replication potential, and (*iv*) invasive potential (1). Early studies using normal mouse cells indicated that a limited set of genetic manipulations could confer neoplastic potential (2). However, normal human cells have been more difficult to transform to malignancy, indicative of their more stringent tumor-suppressive pathways. Extensive study of cultured human mammary epithelial cells (HMEC) has identified two senescence barriers. One involves the stress-associated induction of the cyclin-dependent kinase inhibitor p16 before attaining critically short telomeres. This stasis barrier can be overcome by inhibiting p16, allowing continued proliferation, which results in agonescence, a proliferative barrier mediated by telomere depletion (3). Additionally, the ability of dysregulated oncogenic signaling to induce senescence in human cells has implicated oncogene-induced senescence (OIS) as an important tumor-suppressive barrier. A number of recent studies have demonstrated the physiological relevance of OIS in human tumorigenesis and in vivo tumor mouse models (4). Additionally, the presence of senescent cells in benign but not advanced tumors argues that OIS serves as an early tumor-suppressive barrier that needs to be dismantled for full oncogenic progression (4). In human fibroblasts, OIS could be bypassed by disabling p16 or molecular components of the DNA damage response (DDR), including ATM, CHK2, or p53, before RAS, MOS, or STAT5 overexpression (5–9). However, OIS in HMEC has been shown to be independent of p53 and the p16-RB pathway after oncogenic RAF-1 expression (10). The contrasting responses between epithelial and fibroblast cells argue that the signaling networks responsible for OIS have tissue specificity. Indeed, fibroblasts and epithelial cells can have markedly different responses to cytokines such as TGF-β, which inhibits HMEC growth while promoting the growth of isogenic fibroblasts (11). Furthermore, there are significant cell-type differences in requirements for RAS effector signaling for malignant transformation (12). Understanding the tumor-suppressive pathways that prevent breast cancer is therefore best performed using HMEC, the cell of origin for the majority of human breast cancers.

We show here that activated RAS expression induces HMEC to undergo a p16- and p53-independent senescence that requires the TGF-β receptor. In contrast to studies performed using fibroblasts, shRNA-mediated knockdown of ATM or CHK2 did not prevent RAS-mediated OIS in HMEC lacking p53. However, suppression of TGF-β signaling by expressing a dominant-negative TGF-β type II receptor, use of a TGF-β type I receptor inhibitor, or ectopic expression of MYC prevented RAS-mediated OIS, and together with loss of p16 and p53 function, permitted the expansion of HMEC with a malignant phenotype. Understanding the unique tumor-suppressive responses that are engaged in human breast epithelial cells can provide a foundation for future therapies aimed at reengaging these suppressive pathways.

Results

Recently identified cell-type–specific requirements for transformation indicate that unique tumor-suppressive mechanisms exist to protect each tissue from cancer development (12). To examine the growth-suppressive mechanisms underlying RAS-mediated OIS in HMEC, we first examined the role of p53. An shRNA targeting p53 and a control shGFP were delivered by lentiviral transduction to postselection HMEC, which lack p16 expression owing to promoter methylation (13, 14). Western analysis confirmed the knockdown of p53 protein levels in the shp53-HMEC and the abrogation of p53-dependent transactivation of target genes HDM2 and p21 in response to Nutlin-3, a p53-stabilizing compound (Fig. S1*A*). Furthermore, treatment of shGFP-HMEC with Nutlin-3 resulted in p53-mediated growth arrest, whereas the shp53-HMEC were unaffected (Fig. S1*B*). The shGFP-HMEC and shp53-HMEC were next examined for their response to activated RAS by infecting them with a retrovirus encoding RAS-G12V or a control vector (V). Both HMEC cultures were strongly growth inhibited, as determined by cell counts 5 d after infection (Fig. 1*A*). The RAS-expressing cells exhibited an increase in cell size, cell spreading, vacuolization, and multinucleated cellular morphology typical of senescence (15) and stained positively for the presence of senescence-associated β-galactosidase activity (Fig. 1*B* and Fig. S2). Western analysis confirmed the expression of RAS-G12V, the induction

Author contributions: R.C. and M.W.J. designed research; R.C., C.E.K., J.G., and M.W.J. performed research; D.D. and M.S. contributed new reagents/analytic tools; R.C. and M.W.J. analyzed data; and R.C. and M.W.J. wrote the paper.

The authors declare no conflict of interest.

*This Direct Submission article had a prearranged editor.

Freely available online through the PNAS open access option.

[1]To whom correspondence should be addressed. E-mail: mwj7@case.edu.

This article contains supporting information online at www.pnas.org/lookup/suppl/doi:10.1073/pnas.1015022108/-/DCSupplemental.

of the cyclin-dependent kinase inhibitor p21, and a consequent decrease in phosphorylated RB protein levels, even in the absence of p53 (Fig. 1*C*). In addition to inactivating p53 using an shRNA, we expressed a dominant-negative p53 [GSE56 (16)] and observed a similar RAS-mediated OIS in both the presence and absence of p53 function (Fig. 1*D* and Fig. S3). We next examined whether various RAS-G12V point mutants capable of activating specific effector pathways also elicited OIS (12). RAS-G12V mutants capable of activating only RAF, PI3K, or RAL-GEF were unable to induce p21 expression or suppress the growth of shp53-HMEC (Fig. S4), confirming that RAS-mediated OIS is dependent on multiple RAS-signaling effectors.

Previous reports using fibroblasts demonstrated a requirement for DDR proteins, including ATM and CHK2, in RAS-G12V–mediated senescence (4, 9, 17). To determine whether the p16/p53-independent senescence in HMEC was dependent on ATM or CHK2, we used shRNAs targeting ATM or CHK2 to knock down their expression in shp53-HMEC (Fig. 1*E*). The shp53/shGFP-HMEC, shp53/shATM-HMEC, and shp53/shCHK2-HMEC were further infected with a control retrovirus or a retrovirus encoding RAS-G12V, and cell number was quantified after 5 d and plotted as relative growth (Fig. 1*F*). The results indicate that ATM and CHK2 are dispensable for the p16/p53-independent senescence induced by RAS-G12V. Furthermore, a negative feedback signaling network responsible for suppressing PI3K/AKT and ERK signaling has been observed after the aberrant activation of RAS (18). In contrast, we observed sustained AKT and ERK activation 4 d after RAS-G12V expression, well after these signals were terminated in fibroblasts (Fig. S5). We conclude that HMEC, in contrast to human fibroblasts, do not require p16, p53, ATM, CHK2, or suppression of RAS effectors to mount a senescence response after aberrant oncogene activation, indicative of cell type specificity in OIS mechanisms.

In murine keratinocytes, expression of v-RAS led to OIS associated with elevated expression of $p19^{ARF}$, p53, p15, and p16 and secretion of TGF-β; abrogation of TGF-β signaling suppressed the OIS phenotype (19). Therefore, we examined the role of TGF-β signaling in the p16/p53-independent HMEC OIS. Shp53-HMEC were infected with RAS-G12V, and the expression of TGF-β was examined over 4 d. TGF-β2 expression was elevated within 24 h of RAS-G12V infection and strongly detected at 96 h (Fig. 2*A*). To determine the importance of TGF-β signaling to the RAS-G12V–mediated OIS, we treated shp53-HMEC with SB431542, a TGF-β type I receptor antagonist, before expressing RAS-G12V (20). Treatment of shp53-HMEC with SB431542 resulted in a significant increase in cell number 5 d after RAS-G12V infection compared with control cells (Fig. 2*B*). However, the protection from OIS was not permanent: removal of the inhibitor led to reduced proliferation and growth arrest (Fig. 2*C*). We next examined whether a dominant-negative TGF-β type II receptor (DN-TGFβRII) could also rescue cells from RAS-mediated OIS. Shp53-HMEC were infected with a retrovirus encoding DN-TGFβRII or an empty vector and subsequently infected with a retrovirus encoding RAS-G12V. Similar to our observation with the TGF-β type I receptor antagonist, the shp53/DN-TGFβRII-HMEC maintained proliferation after RAS-G12V expression (Fig. 2*D*). TGF-β signaling occurs by the ligand-mediated assembly of a receptor complex involving TGF-β type I and II receptor subunits. Therefore, inhibition of either the type I or type II receptor blocks signaling from the TGF-β receptor complex. These data suggest that the p16/p53-independent OIS in HMEC is dependent on functional TGF-β signaling and that abrogating the TGF-β signaling pathway will permit ongoing proliferation in the presence of activated oncogenic RAS.

Canonical TGF-β–mediated arrest involves TGF-β type I/II receptor oligomerization and activation, resulting in a SMAD-mediated induction of CDK inhibitors p15 and p21. Induction of CDK inhibitors results in RB family member hypophosphorylation and RB/E2F-mediated transcriptional repression. To determine whether RAS-mediated OIS requires RB and RB family members p107 and p130, we created HMEC expressing a number of SV40 large T proteins (21). These include wild-type large T, a K1 mutant that specifically inactivates p53, and a Δ434–444 mutant that specifically inactivates RB. Again, each large T mutant capable of inactivating p53 rendered cells resistant to Nutlin-3, yet they remained susceptible to RAS-mediated OIS. Moreover, both large T mutants capable of inactivating RB and RB family members also remained sensitive to RAS-mediated OIS (Fig. S6). Consistent with RAS-mediated OIS being independent of the p16/RB axis, we did not observe senescence-associated heterochromatin foci (SAHF) after RAS expression, despite the strong SA-β-galactosidase staining (Fig. S7). This was not unexpected because SAHF has recently been linked to senescence that is mediated by DNA damage or p16 activation (22, 23). Finally, we examined whether RAS-induced senescence was mediated through p21 by creating shp53-HMEC expressing an shRNA targeting p21. These shp53/shp21-HMEC also remained susceptible to RAS-mediated OIS (Fig. S8). Therefore, our data demonstrate that RAS-mediated OIS in HMEC is independent of p16, p53, ATM, CHK2, p21, RB, p107, and p130.

Previous studies have shown that HMEC no longer sensitive to OIS may acquire malignancy-associated properties when exposed to aberrant oncogenic signaling (10). We therefore tested

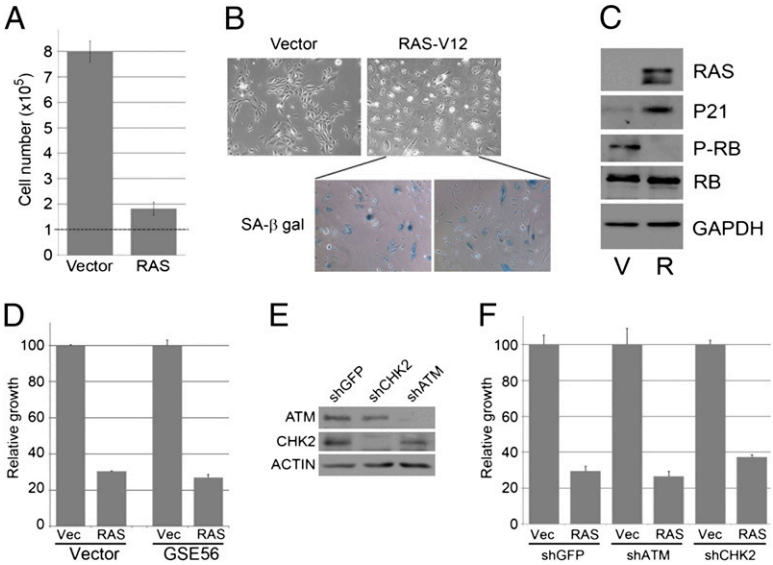

Fig. 1. RAS-mediated OIS is independent of p53, p16, and DDR proteins. (*A*–*C*) Shp53-HMEC were infected with a RAS-G12V–expressing retrovirus or control retrovirus (Vector). Infected cells were plated, grown for 5 d, and counted (*A*), representative images were acquired (*B*, *Upper*) or stained for the presence of senescence-associated β-galactosidase activity (*B*, *Lower*), and Western analysis performed to determine p21 and phosphorylated RB protein levels. (*D*) GSE56-HMEC were infected with a RAS-G12V–expressing retrovirus or control retrovirus (Vector), 1×10^5 cells were plated, grown for 5 d, and counted. (*E* and *F*) Shp53-HMEC were infected with retroviruses encoding shRNAs targeting ATM, CHK2, or GFP. The knockdown of ATM and CHK2 was confirmed by Western analysis (*E*), and the shRNA-expressing cells were infected with a retrovirus encoding RAS-G12V or a control retrovirus (Vec). Infected cells were plated, grown for 5 d, and counted.

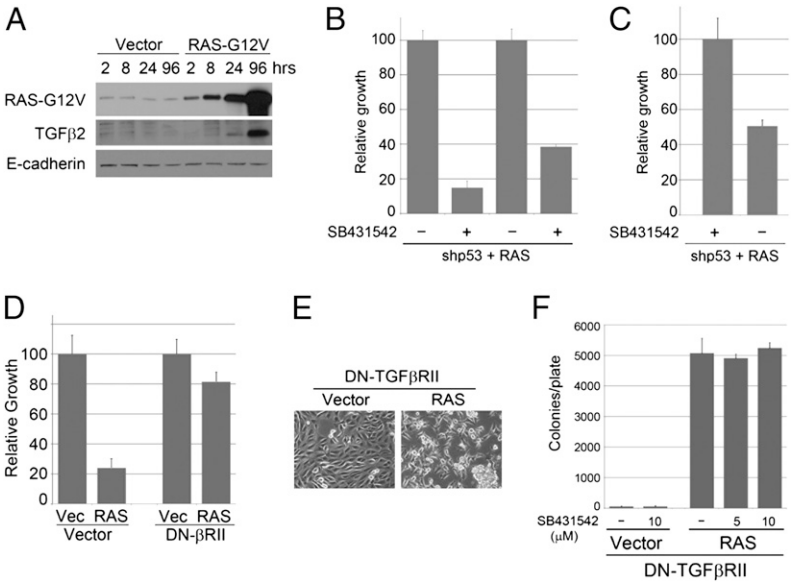

Fig. 2. TGF-β signaling is required for RAS-mediated OIS. (*A*) RAS-G12V–infected Shp53-HMEC were subjected to Western analysis for TGF-β2, RAS, and E-cadherin at the indicated time points. (*B*) Shp53-HMEC were pretreated with SB431542, a TGF-β receptor I antagonist, infected with a retrovirus encoding RAS-G12V, plated, grown for 5 d, and counted. (*C*) Shp53-RAS-G12V-HMEC grown in the presence of SB431542 were plated in the presence (+) or absence (–) of the inhibitor, and relative growth was measured after 5 d. (*D*) Shp53/DN-TGFβRII/-HMEC were infected with a retrovirus encoding RAS-G12V or control retrovirus (Vector) and relative growth determined 5 d after RAS-G12V infection. (*E*) Representative images of Shp53/DN-TGFβRII/RAS-G12V-HMEC and control Shp53/DN-TGFβRII/Vector-HMEC. (*F*) Shp53/DN-TGFβRII/RAS-G12V-HMEC or control Shp53/DN-TGFβRII/Vector-HMEC were examined for AIG in the presence or absence of SB431542.

whether HMEC deficient in three prominent tumor-suppressor pathways (p16, p53, and TGF-β signaling) and resistant to OIS had acquired properties of malignant transformation. Indeed, the shp53/DN-TGFβRII/RAS-HMEC appeared morphologically distinct from control cells, growing as aggregates with diminished attachment to the substratum (Fig. 2*E*). To determine whether the shp53/DN-TGFβRII/RAS-HMEC were malignantly transformed, they were plated into soft agar to assay for anchorage-independent growth (AIG). Shp53/DN-TGFβRII/RAS-HMEC efficiently formed anchorage-independent colonies, whereas control shp53/DN-TGFβRII/Vector-HMEC failed to form colonies (Fig. 2*F*). Addition of the TGF-β type I receptor antagonist SB431542 failed to increase AIG in the control shp53/DN-TGFβRII-HMEC. These results indicate that RAS expression promotes AIG in shp53-HMEC in the absence of functional TGF-β signaling, but inhibition of TGF-β signaling alone is not sufficient for AIG. Further, because SB431542 did not enhance the AIG observed in the shp53/DN-TGFβRII/RAS-HMEC, we conclude that inhibition of either TGFβRI or TFGβRII is sufficient to cooperate with RAS-G12V to induce a malignancy-associated phenotype in the shp53-HMEC.

We also examined a small population of shp53-HMEC that grew out of the senescent cultures after RAS expression (Fig. 3 *A* and *B*). Our hypothesis was that cells capable of tolerating RAS expression would need to first dismantle OIS signaling, which involves TGF-β. However, the RAS-resistant shp53-HMEC (RAS-R cells) that grew out of the senescent cultures for 20 d expressed significantly less RAS-G12V than the senescent cultures examined 4 d after infection (Fig. 3*C*). In addition, the RAS-R cells remained sensitive to growth inhibition in response to exogenous TGF-β and were unable to efficiently form anchorage-independent colonies (Fig. 3*D*). Surprisingly, treatment of these RAS-R cells with SB431542 significantly enhanced AIG, arguing that TGF-β signaling was intact and functioning to suppress AIG. Treatment of control shp53-HMEC lacking RAS expression with SB431542 failed to promote AIG, confirming that combined expression of low levels of RAS-G12V and TGF-β receptor inhibition promotes malignant transformation. We conclude that cells expressing a low level of RAS did not engage a TGF-β–mediated senescence, because they remained sensitive to exogenous TGF-β. Our data suggest that this acquired resistance to the cytostatic effects of TGF-β is required for malignant transformation.

MYC is an oncoprotein frequently overexpressed in breast cancer and is shown to suppress the cytostatic effects of TGF-β (24). Therefore, we examined whether elevated expression of MYC could rescue HMEC from RAS-mediated OIS. Shp53-HMEC were infected with a retrovirus encoding MYC or an empty vector and subsequently infected with a retrovirus encoding RAS-G12V (Fig. 4 *A* and *B*). Control shp53/Vector-HMEC underwent RAS-mediated OIS, whereas shp53/MYC-HMEC continued proliferating in the presence of RAS-G12V (Fig. 4*B*). As expected, HMEC expressing either MYC or DN-TGFβRII were also resistant to the growth-inhibitory properties of exogenous TGF-β treatment (Fig. 4*C*). Our data thus far define a significant role for TGF-β signaling in (*i*) OIS induction and (*ii*) suppressing malignant transformation in the absence of p16/RB and p53 signaling. However, although p53 loss was unable to overcome the OIS barrier, p53 may still have a role in suppressing AIG. To

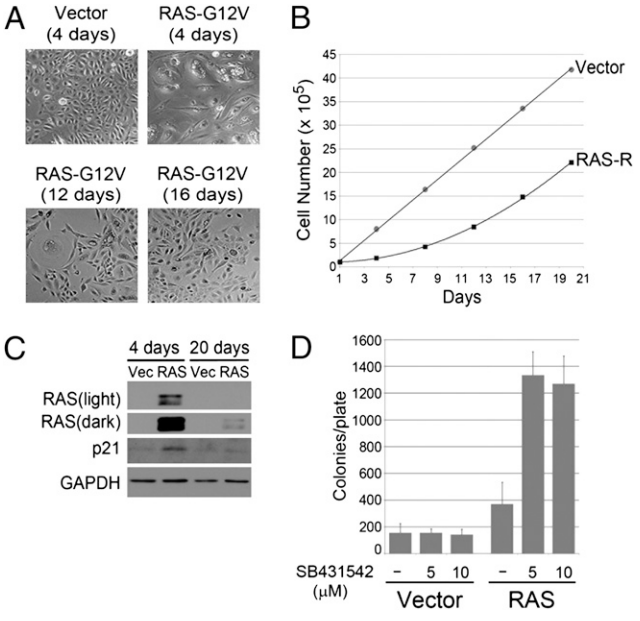

Fig. 3. TGF-β signaling must be inhibited for HMEC transformation. (*A–C*) Representative images (*A*), growth curves (*B*), and Western analysis (*C*) for RAS, p21, and GAPDH of shp53-HMEC infected with a retrovirus encoding RAS-G12V or a control retrovirus at the indicated time points after infection. (*D*) Vector and RAS-R cells were examined for AIG in the absence or presence of SB431542.

test this, HMEC and shp53-HMEC were infected with retroviruses encoding MYC and RAS-G12V, either alone or in combination. Western analysis of each of the HMEC cultures failed to identify known senescence-associated signaling as candidates responsible for the OIS. For example, p53 was phosphorylated and stabilized, CHK2 was phosphorylated, and p14ARF was induced by MYC expression alone but not by RAS-G12V expression alone (Fig. 4*D*) (25). Despite the elevated levels of p14ARF, p53, and DNA damage-responsive signaling, MYC expression in HMEC with or without shp53 does not induce a senescent phenotype (Fig. 4*E*). In contrast, RAS-G12V expression did not induce p14ARF, p53, or DNA damage-responsive signaling, yet induced a senescent phenotype in the both the presence or absence of p53 (Fig. 4*E*).

Each HMEC culture was next assessed for AIG. HMEC and shp53-HMEC expressing MYC or RAS-G12V alone formed colonies inefficiently. In contrast, expression of both MYC and RAS together promoted AIG, with a significant increase in colony number when p53 was abrogated (Fig. 4*F*). We confirmed that p53 remained fully functional in the MYC/RAS-HMEC using Nutlin-3, which induced a potent p53-dependent growth arrest (Fig. S9). Interestingly, these data demonstrate that acquisition of AIG in HMEC can occur independent of human telomerase reverse transcriptase (hTERT) expression or immortality, because the HMEC used in this study were not previously immortalized by exogenous hTERT or reactivation of endogenous hTERT. However, both the MYC/RAS-HMEC and shp53/MYC/RAS-HMEC cultures formed significantly fewer colonies at later passages and, despite their capacity for AIG, eventually stopped proliferating. These data support the contention that telomerase activation is a key rate-limiting step in malignant progression, and further analysis is currently underway (26).

The postselection HMEC used thus far have overcome stasis, the stress-associated senescence barrier, by selecting for p16 promoter methylation (3). In that process, they also acquired additional aberrant properties, including numerous DNA methylation changes (3, 27). We thus extended this work by examining normal, prestasis HMEC transduced with an shRNA targeting p16; this population does not express the aberrant methylation seen with the postselection HMEC (3). Shp16-HMEC were infected with shp53 or control vector, and shp16-HMEC and shp16/shp53-HMEC were further transduced with MYC and RAS-G12V alone or in combination. The results for AIG capacity were similar to what was seen with postselection HMEC (Fig. 4 *G* and *H*). These data indicate that the ability of MYC and RAS to promote AIG in HMEC lacking p16 and p53 does not depend on the particular aberrations present in the postselection cultures.

Prior studies in HMEC have correlated the level of RAS-G12V expression with AIG (28). Therefore, we altered the level of RAS-G12V expression using different retroviral vectors in postselection MYC-HMEC and shp53/MYC-HMEC. Increasing RAS levels increased the AIG of shp53-HMEC until a critical threshold was surpassed, resulting in reduced AIG (Fig. 5*A*). Again, HMEC with wild-type p53 exhibited significantly less AIG in the presence of MYC and RAS than shp53-HMEC (Fig. 5*A*). Thus, we conclude that p53 is not required to suppress OIS but remains a suppressor of malignant transformation. Interestingly, each population of cells recovered from soft agar expressed a level of RAS-G12V that was significantly reduced from that of the initial population (Fig. 5*B*), similar to previous studies using RAF-1 (10). These findings argue that, in tumor-derived cells harboring a RAS mutation, the OIS response may be abrogated by elevating MYC expression. To examine whether MYC depletion in tumor-derived cells harboring activating RAS mutations would reactivate a senescence program, we infected epithelial

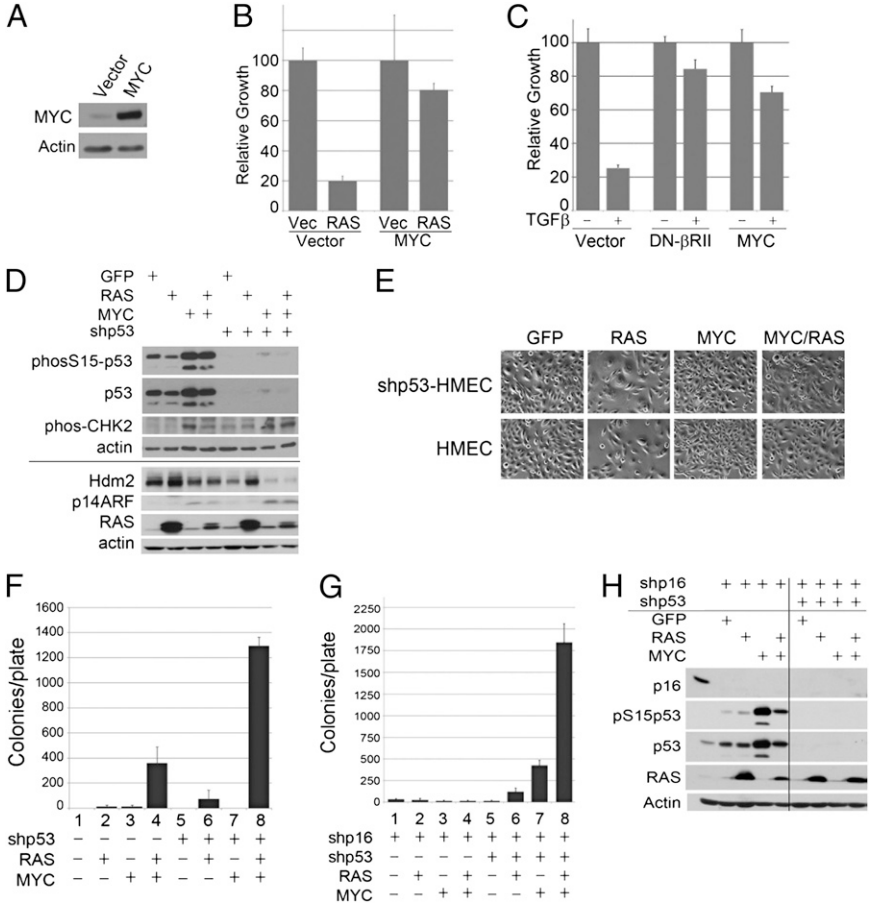

Fig. 4. Neoplastic transformation of HMEC. (*A* and *B*) Shp53-expressing HMEC were infected with a retrovirus encoding MYC or an empty vector (*A*) and subsequently infected with a retrovirus encoding RAS-G12V. Relative growth was determined 5 d after RAS-G12V infection (*B*). (*C*) Shp53-HMEC expressing MYC or DN-TGFβRII, or control cells (vector) were plated in the presence (+) or absence (–) of TGF-β (10 ng/mL) and relative growth determined after 5 d. (*D*) Western analysis of HMEC and shp53-HMEC expressing GFP, RAS-G12V, MYC, or RAS-G12V and MYC together. (*E*) Representative images of shp53-HMEC and shGFP-HMEC infected with a retrovirus encoding GFP, RAS-G12V, MYC, or MYC and RAS together. (*F*) shGFP-HMEC and shp53-HMEC were infected with retroviruses encoding MYC and RAS-G12V, either alone or in combination, and assessed for AIG. (*G*) Shp16-HMEC and shp16/shp53-HMEC were infected with retroviruses encoding MYC and RAS-G12V, either alone or in combination, and assessed for AIG. (*H*) Western analysis of shp16-HMEC and shp16/shp53-HMEC expressing GFP, RAS-G12V, MYC, or RAS-G12V and MYC together.

cancer cell lines containing high levels of MYC expression and RAS mutations with lentiviruses that encode an shRNA targeting GFP or MYC. In two triple-negative breast cancer cell lines, MDA231 (K-RAS-G13D) and Hs578T (H-RAS-G12D), ablation of MYC resulted in a dramatic decrease in relative growth and positive staining for SA-β-galactosidase activity (Fig. 5*C*). In addition, ablation of MYC from lung and colon cancer cell lines harboring RAS mutations, including A549 (K-RAS-G12S), H1299 (*N*-RAS-Q61K), and LoVo (K-RAS-G13D), resulted in a similar senescent phenotype (Fig. S10). We conclude that depletion of MYC from tumor-derived cells harboring activating RAS mutations results in reactivation of a senescence program.

Discussion

It is clear from recent studies that OIS is a critical tumor-suppressive barrier in vivo, because senescent cells are commonly identified in early hyperplastic lesions and naevi (4). A number of genetic and epigenetic events can result in the generation of dysregulated proliferative signals, which trigger OIS in normal cells. Acquiring the errors needed to overcome OIS allows precancerous cells to continue toward neoplastic transformation, because the same oncogenes that previously induced growth arrest now induce malignancy-associated properties such as AIG. To date, much of the work delineating OIS has been performed using rodent and human fibroblasts, identifying p16, RB, DDR proteins, and p53 as important signaling components necessary for OIS. Abrogation of p53, ATM, CHK2, or p19ARF allows these fibroblasts to tolerate activated RAS, MOS, or STAT5 expression and continue dividing, rather than undergoing senescence (5–8, 17). Together with the observation that tumor cells can have persistent DNA damage and often lose DDR signaling responsible for activating p53, the current hypothesis suggests an integral role for DDR signaling in OIS.

We report here that HMEC have an uncharacterized OIS that is dependent on the TGF-β receptor and does not require p16, p53, ATM, CHK2, p21, RB, p107, or p130, as previously described in fibroblasts. In our studies, suppression of TGF-β signaling by expression of a dominant-negative TGF-β type II receptor, use of a TGF-β type I receptor inhibitor, or ectopic expression of MYC prevented RAS-induced senescence and resulted in neoplastic transformation (Fig. 5*D*). Recently, Zhuang et al. (29) reported that activated N-RAS and B-RAF induced a p16/p53-independent OIS in melanocytes and further demonstrated that ectopic MYC expression inhibited senescence, similar to our observations in HMEC. Moreover, abrogation of MYC expression from melanoma cell lines resulted in the reactivation of a senescence program, similar to our observations using breast, lung, and colon cancer cell lines harboring RAS mutations. Like HMEC, normal melanocytes are sensitive to TGF-β–mediated arrest, and melanomas often acquire a resistance to the cytostatic effects of TGF-β. Whether the OIS observed in melanomas results from TGF-β receptor activation, as described here for HMEC, will need additional examination.

Several reports have shown that expression of RAS or its downstream effectors leads to the secretion of several cytokines, including TGF-β (19, 30, 31). However, activation of TGF-β signaling in MCF10A breast epithelial cells after RAS-G12V expression promotes increased invasion rather than senescence. Two independent reports have uncovered *MYC* amplification in MCF10A cells, a genetic alteration that we demonstrate can prevent OIS in response to RAS-G12V (32, 33). TGF-β signaling has been shown to suppress transcription of the *MYC* gene, and defective repression of *MYC* is frequently observed in breast cancer cells that are insensitive to TGF-β (34, 35).

The response of fibroblasts and epithelial cells to TGF-β is markedly different, with fibroblasts increasing proliferation and exhibiting characteristics of morphological transformation, whereas epithelial cells undergo a cell-cycle arrest (11). The use of HMEC in our study has uncovered a role for TGF-β signaling in RAS-mediated OIS, which has not been observed as a tumor-suppressive barrier in studies of OIS that used human fibroblasts. Suppression of TGF-β signaling in HMEC allowed RAS to drive a transformed phenotype rather than senescence. This observation led us toward the identification of a physiologically appropriate set of four genetic events that consistently drive HMEC transformation and are commonly observed in breast cancer. These include the suppression of

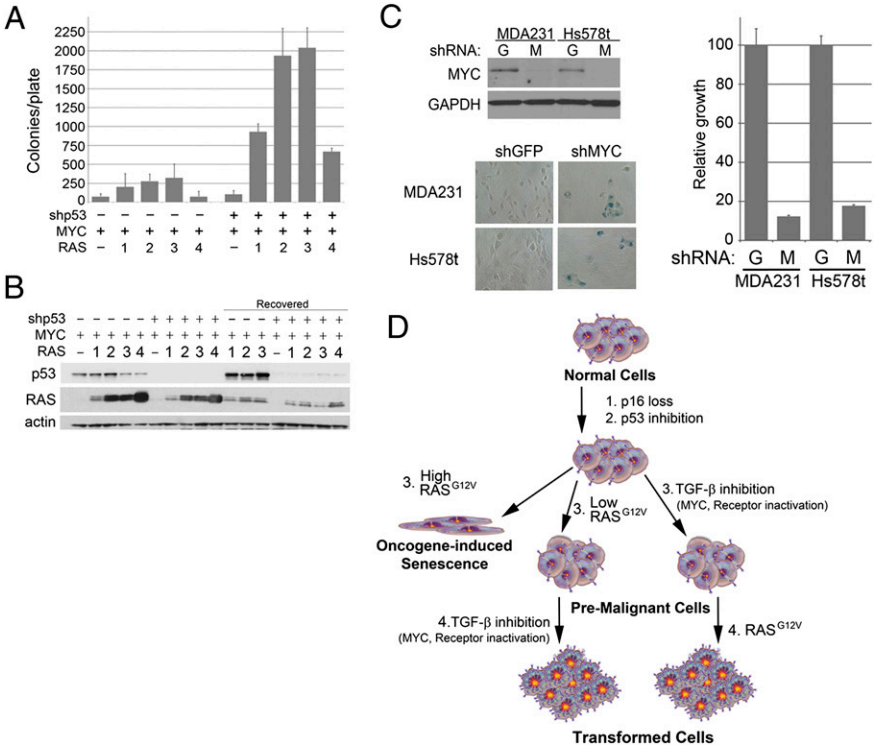

Fig. 5. Model of HMEC transformation. (*A*) Four different retroviral vectors encoding RAS-G12V were used to modulate the level of RAS-G12V expression in shp53/MYC-HMEC and MYC-HMEC retaining wild-type p53 expression. The RAS-expressing HMEC derivatives were examined for AIG. (*B*) Cells that grew anchorage-independently (described in *A*) were recovered from agar and reestablished as monolayer cultures. Western analysis was performed on the cells before plating in agar to compare with the cells recovered from agar growth. (*C*) MDA231 and Hs578T cells were infected with retroviruses encoding shRNAs targeting MYC (M) or GFP (G). Growth assays, Western analysis, and SA-β-galactosidase activity were examined after MYC ablation. (*D*) Model of the progressive transformation of HMEC.

p16 and p53 function, acquired resistance to the cytostatic effects of TGF-β signaling, and acquisition of persistent growth signaling.

On the basis of our study, we propose that a high level of RAS signaling must be accompanied by an acquired resistance to the cytostatic effects of TGF-β, either by TGF-β receptor inhibition or elevated MYC expression (Fig. 5*D*). In contrast, low-level RAS signaling is incapable of engaging OIS but still cooperates with the abrogation of TGF-β signaling to promote malignant transformation. MYC is a well-known suppressor of TGF-β signaling (36) and is amplified in up to 52% of breast cancer specimens, depending on the study. Tumors that do not harbor an MYC amplification often overexpress MYC protein via additional mechanisms (36–39). RAS mutations are surprisingly infrequent in breast cancer (<5%) relative to other cancers (50% of colon and thyroid cancers and 90% of pancreatic cancers). However, the reason for the differences between cancers that tolerate RAS mutations and those that do not remains unclear (40). We speculate that mutant RAS may initiate the tumor-suppressive OIS in HMEC more potently, or more acutely than RAS signaling elevated via overexpression of growth factor receptors or wild-type RAS, which are more frequently observed in breast cancer (41).

The observation that TGF-β signaling suppresses the growth of normal epithelial cells, yet is often required for the maintenance of a transformed phenotype, remains a paradox in the field. However, much like the differences in biological outcomes observed between fibroblasts and epithelial cells exposed to TGF-β, the response of normal, hyperplastic, and transformed epithelial cells may be explained by the diverse signals generated by TGF-β receptor activation. SMAD-dependent and -independent pathways (involving TAK1, NFkB, JNK, MAPK, PI3K/AKT, and mTOR, among others) determine whether cells arrest, continue dividing, or undergo an epithelial-to-mesenchymal transition after exposure to TGF-β (42). In our model, elevated MYC expression suppresses RAS-mediated OIS but maintains the TGF-β receptor in a functional state. We suggest that, in breast cancer, the senescence programs are simply suppressed rather than absent, leaving the option to reengage these hidden limits to proliferation as a cancer therapy.

Materials and Methods

Cell Lines and Culture Conditions. Postselection HMEC [48R batch S (27)] were grown in a humidified atmosphere containing 5% CO_2 in Medium 171 with mammary epithelial growth supplement (Cascade Biologics). Prestasis HMEC (specimen 48R, batch T) were grown in a humidified atmosphere containing 5% CO_2 in M87A media as previously described (27). MDA231, Hs578T, H1299, and LoVo cells were grown in a humidified atmosphere containing 5% CO_2 in DMEM supplemented with 5% FBS; A549 cells were grown in RPMI supplemented with 5% FBS.

Soft Agar and Relative Growth Assays. For AIG assays, HMEC (2×10^5) were suspended in 0.6% type VII agarose (Sigma) and plated onto a bottom layer of 1.2% agar in a 60-mm plate in triplicate. For relative growth assays, HMEC (1×10^5) or MDA231, Hs578T, A549, H1299, and LoVo (5×10^4) cells were plated in triplicate in six-well plates, and cell number was determined on a Beckman Coulter counter after 5 d of growth. Quantification of soft agar colonies and inhibitor treatments are described in detail in *SI Materials and Methods*.

Additional materials and methods are described in *SI Materials and Methods*.

ACKNOWLEDGMENTS. This work was supported by National Institutes of Health Grant T32CA059366 (to R.C.) and Department of Defense Breast Cancer Research Program Grant BC074072 (to M.W.J).

1. Hanahan D, Weinberg RA (2000) The hallmarks of cancer. *Cell* 100:57–70.
2. Parada LF, Land H, Weinberg RA, Wolf D, Rotter V (1984) Cooperation between gene encoding p53 tumour antigen and ras in cellular transformation. *Nature* 312:649–651.
3. Novak P, Jensen TJ, Garbe JC, Stampfer MR, Futscher BW (2009) Stepwise DNA methylation changes are linked to escape from defined proliferation barriers and mammary epithelial cell immortalization. *Cancer Res* 69:5251–5258.
4. Courtois-Cox S, Jones SL, Cichowski K (2008) Many roads lead to oncogene-induced senescence. *Oncogene* 27:2801–2809.
5. Bartkova J, et al. (2005) DNA damage response as a candidate anti-cancer barrier in early human tumorigenesis. *Nature* 434:864–870.
6. Bartkova J, et al. (2006) Oncogene-induced senescence is part of the tumorigenesis barrier imposed by DNA damage checkpoints. *Nature* 444:633–637.
7. Gorgoulis VG, et al. (2005) Activation of the DNA damage checkpoint and genomic instability in human precancerous lesions. *Nature* 434:907–913.
8. Mallette FA, Gaumont-Leclerc MF, Ferbeyre G (2007) The DNA damage signaling pathway is a critical mediator of oncogene-induced senescence. *Genes Dev* 21:43–48.
9. Serrano M, Lin AW, McCurrach ME, Beach D, Lowe SW (1997) Oncogenic ras provokes premature cell senescence associated with accumulation of p53 and p16INK4a. *Cell* 88:593–602.
10. Olsen CL, Gardie B, Yaswen P, Stampfer MR (2002) Raf-1-induced growth arrest in human mammary epithelial cells is p16-independent and is overcome in immortal cells during conversion. *Oncogene* 21:6328–6339.
11. Hosobuchi M, Stampfer MR (1989) Effects of transforming growth factor beta on growth of human mammary epithelial cells in culture. *In Vitro Cell Dev Biol* 25:705–713.
12. Rangarajan A, Hong SJ, Gifford A, Weinberg RA (2004) Species- and cell type-specific requirements for cellular transformation. *Cancer Cell* 6:171–183.
13. Brenner AJ, Aldaz CM (1995) Chromosome 9p allelic loss and p16/CDKN2 in breast cancer and evidence of p16 inactivation in immortal breast epithelial cells. *Cancer Res* 55:2892–2895.
14. Brenner AJ, Stampfer MR, Aldaz CM (1998) Increased p16 expression with first senescence arrest in human mammary epithelial cells and extended growth capacity with p16 inactivation. *Oncogene* 17:199–205.
15. Matsumura T, Zerrudo Z, Hayflick L (1979) Senescent human diploid cells in culture: Survival, DNA synthesis and morphology. *J Gerontol* 34:328–334.
16. Ossovskaya VS, et al. (1996) Use of genetic suppressor elements to dissect distinct biological effects of separate p53 domains. *Proc Natl Acad Sci USA* 93:10309–10314.
17. Di Micco R, et al. (2006) Oncogene-induced senescence is a DNA damage response triggered by DNA hyper-replication. *Nature* 444:638–642.
18. Courtois-Cox S, et al. (2006) A negative feedback signaling network underlies oncogene-induced senescence. *Cancer Cell* 10:459–472.
19. Tremain R, et al. (2000) Defects in TGF-beta signaling overcome senescence of mouse keratinocytes expressing v-Ha-ras. *Oncogene* 19:1698–1709.
20. Halder SK, Beauchamp RD, Datta PK (2005) A specific inhibitor of TGF-beta receptor kinase, SB-431542, as a potent antitumor agent for human cancers. *Neoplasia* 7:509–521.
21. Hahn WC, et al. (2002) Enumeration of the simian virus 40 early region elements necessary for human cell transformation. *Mol Cell Biol* 22:2111–2123.
22. Di Micco R, et al. (2011) Interplay between oncogene-induced DNA damage response and heterochromatin in senescence and cancer. *Nat Cell Biol* 13:292–302.
23. Kosar M, et al. (2011) Senescence-associated heterochromatin foci are dispensable for cellular senescence, occur in a cell type- and insult-dependent manner and follow expression of p16(ink4a). *Cell Cycle* 10:457–468.
24. Alexandrow MG, Kawabata M, Aakre M, Moses HL (1995) Overexpression of the c-Myc oncoprotein blocks the growth-inhibitory response but is required for the mitogenic effects of transforming growth factor beta 1. *Proc Natl Acad Sci USA* 92:3239–3243.
25. Ries S, et al. (2000) Opposing effects of Ras on p53: Transcriptional activation of mdm2 and induction of p19ARF. *Cell* 103:321–330.
26. Garbe JC, Holst CR, Bassett E, Tlsty T, Stampfer MR (2007) Inactivation of p53 function in cultured human mammary epithelial cells turns the telomere-length dependent senescence barrier from agonescence into crisis. *Cell Cycle* 6:1927–1936.
27. Garbe JC, et al. (2009) Molecular distinctions between stasis and telomere attrition senescence barriers shown by long-term culture of normal human mammary epithelial cells. *Cancer Res* 69:7557–7568.
28. Elenbaas B, et al. (2001) Human breast cancer cells generated by oncogenic transformation of primary mammary epithelial cells. *Genes Dev* 15:50–65.
29. Zhuang D, et al. (2008) C-MYC overexpression is required for continuous suppression of oncogene-induced senescence in melanoma cells. *Oncogene* 27:6623–6634.
30. Ancrile BB, O'Hayer KM, Counter CM (2008) Oncogenic ras-induced expression of cytokines: A new target of anti-cancer therapeutics. *Mol Interv* 8:22–27.
31. Wang SE, et al. (2006) HER2 kinase domain mutation results in constitutive phosphorylation and activation of HER2 and EGFR and resistance to EGFR tyrosine kinase inhibitors. *Cancer Cell* 10:25–38.
32. Kadota M, et al. (2010) Delineating genetic alterations for tumor progression in the MCF10A series of breast cancer cell lines. *PLoS ONE* 5:e9201.
33. Worsham MJ, et al. (2006) High-resolution mapping of molecular events associated with immortalization, transformation, and progression to breast cancer in the MCF10 model. *Breast Cancer Res Treat* 96:177–186.
34. Chen CR, Kang Y, Massagué J (2001) Defective repression of c-myc in breast cancer cells: A loss at the core of the transforming growth factor beta growth arrest program. *Proc Natl Acad Sci USA* 98:992–999.
35. Chen CR, Kang Y, Siegel PM, Massagué J (2002) E2F4/5 and p107 as Smad cofactors linking the TGFbeta receptor to c-myc repression. *Cell* 110:19–32.
36. Butt AJ, et al. (2008) Cell cycle machinery: Links with genesis and treatment of breast cancer. *Adv Exp Med Biol* 630:189–205.
37. Deming SL, Nass SJ, Dickson RB, Trock BJ (2000) C-myc amplification in breast cancer: A meta-analysis of its occurrence and prognostic relevance. *Br J Cancer* 83:1688–1695.
38. Escot C, et al. (1986) Genetic alteration of the c-myc protooncogene (MYC) in human primary breast carcinomas. *Proc Natl Acad Sci USA* 83:4834–4838.
39. Jamerson MH, Johnson MD, Dickson RB (2004) Of mice and Myc: c-Myc and mammary tumorigenesis. *J Mammary Gland Biol Neoplasia* 9:27–37.
40. Bos JL (1989) ras oncogenes in human cancer: A review. *Cancer Res* 49:4682–4689.
41. Clark GJ, Der CJ (1995) Aberrant function of the Ras signal transduction pathway in human breast cancer. *Breast Cancer Res Treat* 35:133–144.
42. Moustakas A, Heldin CH (2005) Non-Smad TGF-beta signals. *J Cell Sci* 118:3573–3584.

Aging Cell (2011) **10,** pp949–961 Doi: 10.1111/j.1474-9726.2011.00736.x

Oncogenes induce senescence with incomplete growth arrest and suppress the DNA damage response in immortalized cells

Michael Y. Sherman,[1] Le Meng,[1] Martha Stampfer,[2] Vladimir L. Gabai[1] and Julia A. Yaglom[1]

[1]Department of Biochemistry, Boston University School of Medicine, Boston, MA, USA
[2]Life Sciences Division, Lawrence Berkeley National Lab, Berkeley, CA, USA

Summary

Activation of the Her2 (ErbB2) oncogene is implicated in the development of breast, ovary and other cancers. Here, we show that expression of NeuT, a mutant-activated rodent isoform of Her2, in immortalized breast epithelial cells, while promoting senescence-associated morphological changes, up-regulation of senescence-associated β-galactosidase activity, and accumulation of the cyclin-dependent kinase inhibitor p21, failed to trigger the major senescence end-point, i.e. permanent growth arrest. Similar senescence-associated phenotype with incomplete growth arrest, which we dubbed senescence with incomplete growth arrest (SWING), could also be triggered by the expression of the Ras oncogene. SWING phenotype was stable, and persisted in tumor xenografts established from NeuT-transduced cells. Furthermore, a significant population of cells in SWING state was found in tumors in the MMTV/NeuT transgenic mouse model. SWING cells showed downregulation of histone H2AX, critical for repair of double-stranded DNA breaks, and impaired activation of Chk1 kinase. Overall, SWING cells were characterized by increased DNA instability and hypersensitivity to genotoxic stresses. We propose that the SWING state could be a stage in the process of cancer development.

Key words: DNA damage response; Her2; oncogenes; senescence.

Introduction

Normal human somatic cells have a limited proliferation lifespan and undergo replicative senescence characterized by irreversible growth arrest after a certain number of cell divisions (Hayflick & Moorhead, 1961). This senescence response was shown to be driven by telomere shortening that triggered a DNA damage response (DDR), culminating in irreversible cell cycle arrest (Harley *et al.*, 1990; Bodnar *et al.*, 1998). Alternatively, telomere length-independent senescence could be precipitated in cells that have not yet reached their proliferative limit by exposure to various DNA damaging stresses (Schmitt *et al.*, 2002; Campisi & d'Adda di Fagagna, 2007). For example, oncogene imbalance that can induce DNA damage is a potent inducer of a senescence response (McDuff & Turner, 2010). In fact, various oncogenes such as KRAS, BRAF, Mek, or Mos were shown to stimulate senescence both in fibroblasts and in transformed cell lines (Serrano *et al.*, 1997; Lin *et al.*, 1998; Zhu *et al.*, 1998; Bartkova *et al.*, 2006). Moreover, activation of E2F, Ras, BRaf, or loss of PTEN induced senescence in mouse models (Braig *et al.*, 2005; Chen *et al.*, 2005; Collado *et al.*, 2005; Lazzerini Denchi *et al.*, 2005; Michaloglou *et al.*, 2005). Altogether these observations led to a hypothesis that oncogene-induced senescence (OIS) represents a major barrier toneoplastic transformation (Yaswen & Campisi, 2007). In line with this idea, early preneoplastic lesions like human nevi which carry activating BRafV600E mutation harbor senescent melanocytes and rarely progress to melanomas (Pollock *et al.*, 2003).

On the other hand, once cell have been immortalized with reactivation of endogenous telomerase activity, their response to oncogenes changes. For example, expression of the Raf-1 or Ras oncogene in immortalized human mammary epithelial cells (HMEC) not only fails to produce growth arrest, but confers malignancy associated properties (Olsen *et al.*, 2002; Cipriano *et al.* 2011). *In vivo,* reports show that cells with high level of activated Ras that normally triggers senescence eventually form aggressive tumors (Sarkisian *et al.*, 2007). Furthermore, hyperplastic colorectal polyps with endogenous activated KRAS or BRAF despite showing major signs of senescence, e.g. senescence-associated-β-galactosidase (SA-β-gal) staining, continue to grow (Minoo & Jass, 2006). Similarly, early hyperplastic lesions in the PTEN knockout model of the prostate cancer show extensive SA-β-gal staining. These lesions give rise to slowly growing tumors that stained positively for SA-β-gal, and which upon inactivation of p53 eventually become fast-growing and SA-β-gal-negative (Chen *et al.*, 2005). Also, acute somatic activation of ErbB2 in mammary glands led to the development of precancerous lesions where 75% of cells expressed SA-β-gal. Importantly, these lesions rapidly developed into tumors, where 20–40% of cells were still showing positive staining for SA-β-gal (Reddy *et al.*, 2010). Therefore, at present, the question regarding the role of OIS in preventing tumor development remains open.

One interpretation of the presence of cells with senescent phenotype in hyperplastic lesions and tumors is that there is an ongoing transition to senescence of a fraction of tumor cells, which become SA-β-gal positive, while the rest of the cells remain transformed and proliferative. Alternatively, it is possible that morphological and biochemical signs of senescence are not rigidly linked to permanent growth arrest. In fact, owing to the technical difficulties in many cancer models where senescence was studied, monitoring of SA-β-gal and other senescence-associated biochemical parameters is usually not followed by assessment of cell cycle arrest. Here, we hypothesize that activation of oncogenes in immortalized or cancerous cells, which express endogenous telomerase activity and commonly lack critical regulators of cell cycle progression, may be sufficient to trigger morphological and biochemical manifestations of senescence (e.g. SA-β-gal), but cannot ensure full growth arrest. We call this condition **s**enescence **w**ith **in**complete **g**rowth arrest (SWING). In contrast, activation of oncogenes in finite lifespan cells can cause true senescence resulting in block of tumorigenesis. The latter condition could reflect appearance of senescence markers in nontumorigenic nevi. These different responses of finite and immortalized cells to oncogenes support the concept that cellular senescence represents a set of subprograms with independent end points. Accordingly, in response to activation of oncogenes, immortalized cells may trigger some of the sub-programs (e.g. cell enlargement and SA-β-gal activity), while having impaired capability to

Correspondence
Julia A. Yaglom, Department of Biochemistry, Boston University School of Medicine, 72 East Concord Street K-323, Boston, MA 02118, USA. Tel.: 617 638 5973; fax: 617 638 5339; e-mail: yaglom@bu.edu

Accepted for publication *14 July 2011*

Aging Cell

execute the permanent growth arrest because of the multiple checkpoint deficiencies.

Here, we investigate responses of immortalized HMEC to Her2 and Ras oncogenes. The proto-oncogene Her2 is overexpressed in approximately 30% of aggressive breast carcinomas (Slamon *et al.*, 1989). Furthermore, expression of this oncogene in mammary epithelium in transgenic mice triggers the appearance of breast tumors (Muller *et al.*, 1988). However, as with Ras or Raf-1 oncogenes, expression of the rodent oncogenic form of Her2 (NeuT) in the human breast carcinoma line MCF7 and low-passage murine embryonic fibroblasts failed to stimulate proliferation but instead provoked accumulation of enlarged SA-β-gal-positive cells, which were considered senescent (Trost *et al.*, 2005). Therefore, NeuT oncogene along with Ras represents a relevant disease-related model to investigate OIS in immortalized mammary epithelium cells.

It has been suggested that DNA damage triggered by oncogene imbalance underlies OIS growth arrest. Activated components of the DDR, such as phATM, phChk2, or 53BP1 were detected in various untreated preneoplastic lesions associated with bladder, lung, breast, and colon tumors (Bartkova *et al.*, 2005; Gorgoulis *et al.*, 2005; Campisi, 2010). Furthermore, inhibition or knocking down of the DDR mediators prevented OIS and facilitated transformation of melanocytes (Di Micco *et al.*, 2006; Mallette *et al.*, 2007). Unexpectedly, in the process of this investigation, we uncovered that SWING cells with activated oncogenes, when challenged with various genotoxic stresses, have an impaired ability to activate Chk1 kinase, or carry out phosphorylation of the histone H2A isoform H2AX, which are involved in promoting double-stranded DNA breaks (DSB) repair as part of the DDR. H2AX is a critical factor implicated in early stages of major DSB repair pathways (Thiriet & Hayes, 2005). Phosphorylated H2AX molecules, called γH2AX, form irradiation-induced foci in the vicinity of DSBs, which serve as platform for recruitment of DNA repair factors, thus promoting DSB repair. Through assisting in DNA repair and facilitating chromatin remodeling, γH2AX is involved in the maintenance of DNA stability (Zha *et al.*, 2008; Chanoux *et al.*, 2009). Accordingly, suppression of γH2AX in SWING cells led to the appearance of chromosomal aberrations because of impaired DNA repair. Here, we connect the downregulation of H2AX and Chk1 upon development of SWING state to increased DNA instability in neoplastic transformation.

Results

NeuT oncogene induces true senescence in finite lifespan HMEC and senescence-associated properties without growth arrest in immortalized HMEC

To assess OIS in finite and immortalized HMEC, we compared effects of the oncogenic rodent activated form of Her2 (NeuT) on proliferation of normal finite lifespan 184 HMEC (further marked HMEC) and two distinct immortalized HMEC lines, MCF10A and 184B5, the latter derived from normal 184 HMEC. Finite and immortal HMEC were infected with control or NeuT-expressing retrovirus, and NeuT expression was confirmed by immunoblotting (Fig. 1A). At day 5 postinfection, HMEC/NeuT and MCF10A/NeuT cells acquired typical senescent morphology, where more than 90% of cells became enlarged, flattened, and highly vacuolized (Fig. 1B). 184B5/NeuT cells also acquired senescent morphology but later, on day 12 postinfection (Fig. 1B). Furthermore, approximately 90% of HMEC/NeuT, approximately 50% of MCF10A/NeuT, and approximately 70% of 184B5 cells became SA-β-gal positive (Fig. 1B). In contrast, finite HMEC, the MCF10A, and 184B5 lines expressing control virus retained normal morphology, and fractions of SA-β-gal positive cells were 12%, 3%, and 15% respectively (Fig. 1B). Therefore, by morphological and biochemical criteria, almost all the finite HMEC and the majority of the immortalized MCF10A and 184B5 cells acquired properties associated with senescence upon expression of the NeuT oncogene. Despite these similarities, we observed dramatic difference in growth properties of HMEC/NeuT compared with MCF10A/NeuT and 184B5/NeuT cells. To assess growth status of control and NeuT-expressing cell populations, we monitored expression of the proliferation marker, Ki67. More than 80% of both finite and immortal HMEC populations infected with control virus demonstrated Ki67 positivity (Fig. 1C). In line with the senescent appearance, almost no HMEC/NeuT cells (< 5%) stained positive for Ki67, indicating that NeuT oncogene triggered *bona fide* senescence in these cells. In contrast, the MCF10A/NeuT and 184B5/NeuT populations contained Ki67-positive cells, similar to controls (> 70%), suggesting that these cells were not cell cycle arrested. Noticeably, typically senescent-looking large and flattened cells show strong Ki67 fluorescence (Fig. 1C, bottom panel). In agreement with the Ki67 staining, direct measurement of growth rates demonstrated that HMEC/NeuT cells stopped dividing by day 5 postinfection, while MCF10A/NeuT and 184B5/NeuT cells continued proliferating, albeit slower than cells infected with control virus (Fig. 1D). Thus, in contrast to finite HMEC, expression of NeuT oncogene in immortalized HMEC results in the development of a senescence morphology but not growth arrest.

To further characterize the unusual phenotype of the MCF10A/NeuT and 184B5/NeuT cells, we assessed other senescence-associated properties. Direct measurement of cellular diameters using AuxioVision (Carl Zeiss, Oberkochen, Germany) software (see Experimental Procedures) demonstrated that, on average, diameters of MCF10A/NeuT expressing cells were 60% larger than those in control population (Fig. 1E), which is typical for senescent cells. Importantly, the senescence morphology in MCF10A/NeuT and 184B5/NeuT cells was associated with the accumulation of the CDK inhibitor p21 (Fig. 4A), which is implicated in OIS in various cell lines (Quereda *et al.*, 2007). Of note, we did not detect senescence-associated heterochromatic foci, SAHF, in MCF10A/NeuT cells. On the other hand, SAHF formation is more commonly observed in senescent fibroblast than epithelial cells, where it depends on the CDK inhibitor p16, absent from MCF10A (Narita & Lowe, 2004).

As MCF10A growth was slowed following NeuT expression, there was a possibility that with each round of division, a fraction of the MCF10A/-NeuT becomes truly senescent (i.e., growth arrested and SA-β-gal positive), while in the rest of the population, the senescence program is not activated. To assess growth status of the entire MCF10A/NeuT population, we used FACS analysis. Cell cycle distribution of MCF10A/NeuT cells was almost undistinguishable from that of control MCF10A cells (Fig. 2A), suggesting that the total populations proliferate similarly. To further validate the lack of growth arrest in a subpopulation of NeuT-expressing cells, we employed a method based on staining cells with a fluorescent lipophylic dye PKH67. This dye accumulates in cellular membranes and remains there without defusing into the medium. Therefore, nondividing cells retain PKH67 fluorescence, while PKH67 is diluted in proliferating cells with each round of division. This method allows detecting even a minor population of growth-arrested cells. Control and NeuT-expressing MCF10A cells were loaded with PKH67, the excess of the dye was washed out, and fluorescence was monitored daily for 3 days. We captured images and analyzed fluorescence in three independent fields. As seen in Fig. 2B, upon loading of PKH67 at day 0, control and NeuT-expressing cells showed similar high fluorescence, with the median fluorescence intensity around 2600 relative units. Decrease of average fluorescence over time was 20% slower in MCF10A/NeuT cells as compared to control MCF10A cells (Fig. 2B), which was in agreement

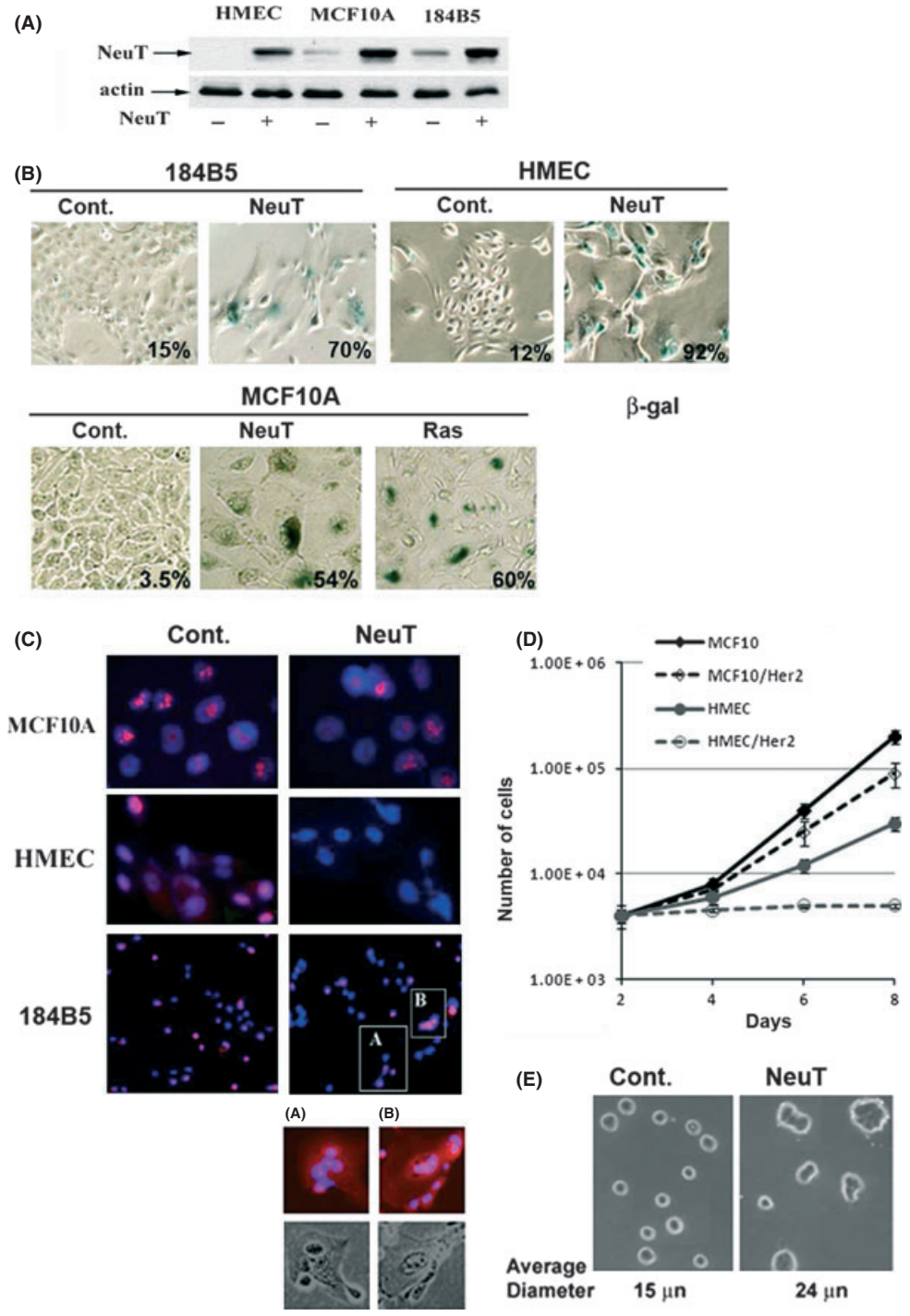

Fig. 1 Effects of oncogenes on senescence and growth properties of MCF10A, finite 184 human mammary epithelial cells (HMEC) and 184B5cells. (A) Retroviral expression of NeuT in MCF10A, HMEC, and 184B5 cells. Samples were collected 5 days postinfection (MCF10A and HMEC) or 12 day postinfection (184B5) and probed by immunoblotting with anti-NeuT antibody. (B) β-Gal staining of cells infected with either NeuT- or Ras-expressing viruses. Tests were performed with cells on same days postinfection, as described earlier. (C) Ki67 immunostaining of cells expressing NeuT oncogene. Nuclei are stained with DAPI. Bottom panels represent enlarged images of the corresponding areas on the figure. (D) NeuT expression blocks growth of HMEC cells but not MCF10A cells. Cells were plated in triplicates at 10% confluence, and growth rate was measured by cell counting over the period of 3 days. (E). NeuT expression leads to increase in sizes of MCF10A cells. Cells were removed from plates with trypsin, dropped onto the slide, and pictures were taken. Image analysis was carried out using AxioVision software.

with a decrease in growth rate of these cells. Importantly, at day 3, median fluorescence of the population of MCF10A/NeuT cells was reduced to < 1000 relative units and no brightly stained cells with fluorescence > 2000 relative units (corresponding to permanently growth arrested cells) were detected. These results indicate that almost every cell in MCF10A/NeuT population underwent divisions during the 3 days period. In contrast, in MCF10A/NeuT cells forced to exit the cell cycle by treatment with a low dose of doxorubicin, median fluorescence after

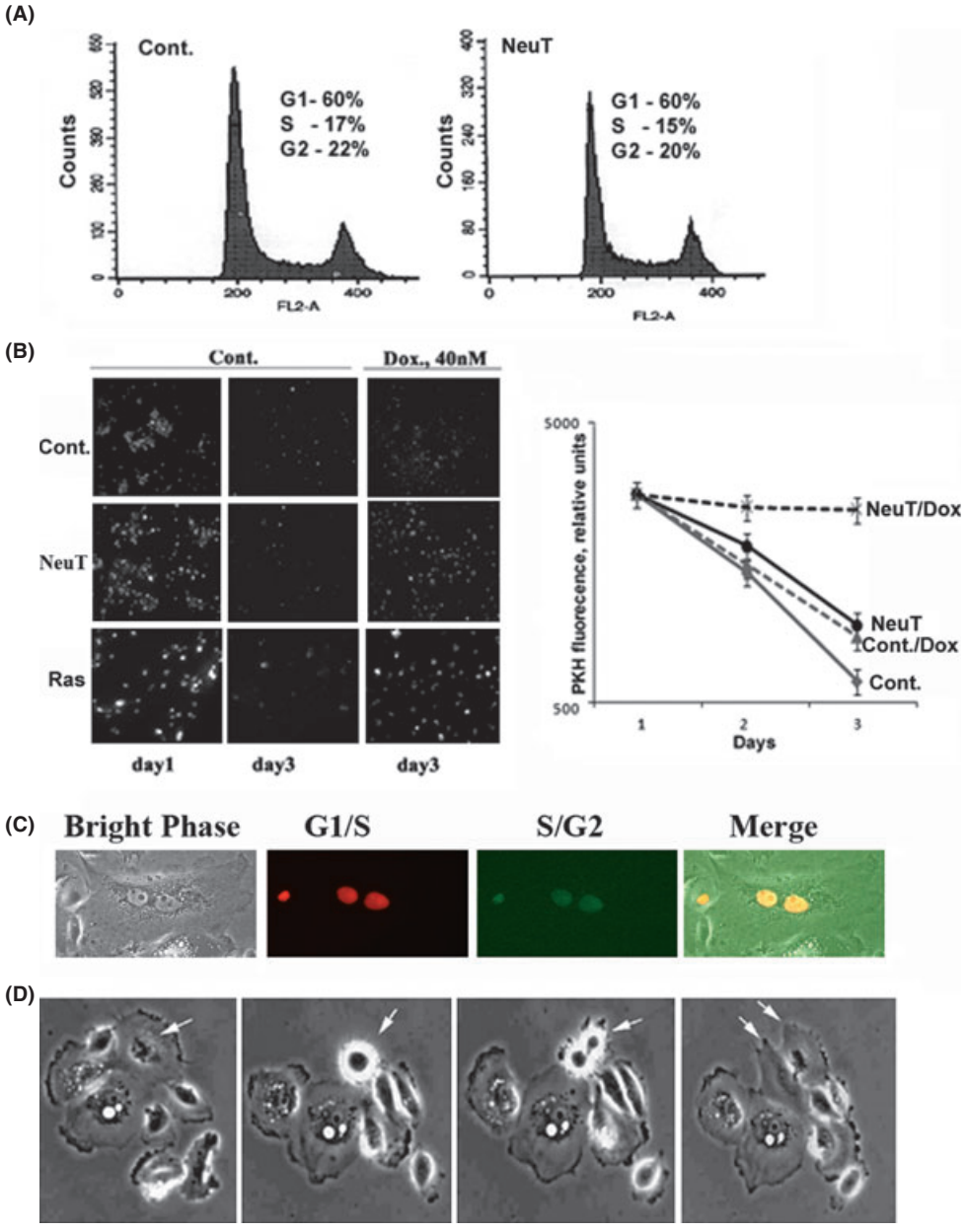

Fig. 2 Effects of NeuT expression on cell cycle progression of MCF10A cells. (A). Cell cycle distribution of control and NeuT-expressing MCF10A cells. FACS analysis of cells harvested on day 6 postinfection. (B) Divisions of cells measured by the PKH67 loading technique. Control, NeuT- and Ras-expressing cells were loaded with PKH67 and then plated at 10% confluency. Pictures were taken for three consecutive days; fluorescence intensity of cells was analyzed in three random fields using AxioVision software. As positive control, we treated cells with 40 nM doxorubicin, which caused minor growth inhibition in control cells and complete growth inhibition in oncogene-expressing cells. (C). S-phase imaging in MCF10A/NeuT cells. MCF10A/NeuT at day 4 postinfection were infected with cell-cycle reporter lentiviruses, i.e., mKO2-hCdt1(30/120) [G1/S; red] and mAG-hGem(1/110) [S/G2; green], and images captured. (D) Time-lapse analyses of division of a senescence-looking flat MCF10A/NeuT cell. (Arrowhead points the cell undergoing mitosis).

3 days was 2400 units, which was not significantly different from that of cells at day 0 (Fig. 2B).

Further, to directly observe that flat, enlarged senescent-looking cells can enter S-phase, we infected MCF10/NeuT cells with lentiviruses expressing the cell-cycle reporters (Sakaue-Sawano *et al.*, 2008). In line with the FACS data, we observed that approximately 15% of the MCF10A/NeuT population expressed both G1/S and S/G2 markers indicative of cells in S-phase (Fig. 2C). Finally, we directly visualized cell division by monitoring MCF10A/NeuT cultures under the microscope for 24 h and capturing images every 30 min. As seen in movie frames in Fig. 2D, a randomly chosen flat enlarged senescent-looking cell underwent a division. Altogether these experiments indicate that in the immortal MCF10A line, NeuT expression precipitated an unusual phenotype, i.e. **S**enescence **W**ith **In**complete **G**rowth arrest, which we called SWING. These results indicate that while NeuT expression promotes OIS in finite lifespan HMEC, in immortal HMEC, its expression triggers the SWING state.

Further we investigated what component of the immortalization process promotes a switch from OIS to the SWING state. Accordingly, we restored expression of p16 in MCF10A/NeuT cells, which lack this cell

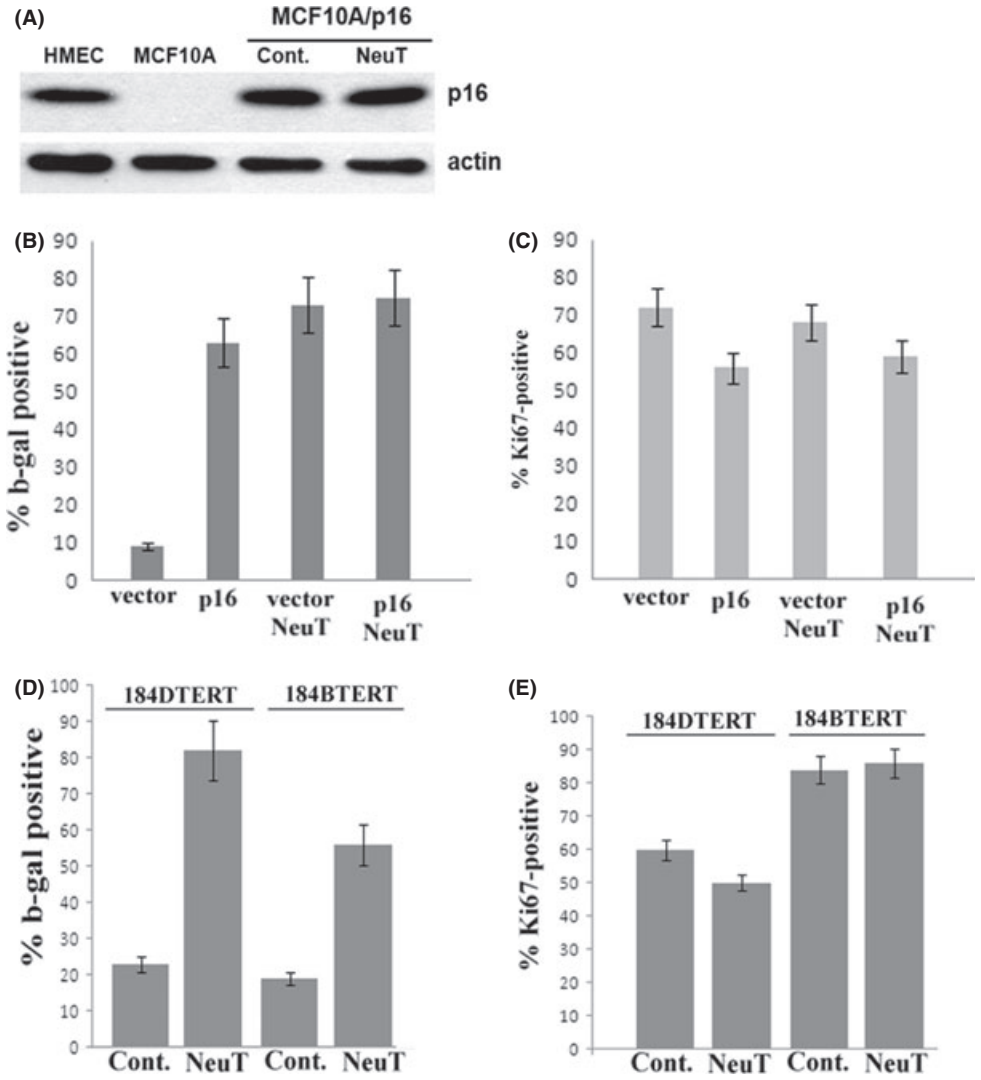

Fig. 3 Effects of p16 and hTERT on the development of the SWING. (A) Retroviral expression of recombinant p16 in MCF10A cells; comparison with p16 levels in finite human mammary epithelial cells. (B) Effects of p16 and NeuT on fractions of SA-β-gal-positive MCF10A cells. Three independent fields were scored. (C) Effects of p16 and NeuT on fractions of Ki67-positive MCF10A cells. Three independent fields were scored. (D) Effects of NeuT on fractions of SA-β-gal-positive 184BTERT and 184DTERT cells. Three independent fields were scored. (E) Effects of NeuT on fractions of Ki67-positive 184BTERT and 184DTERT cells.

cycle inhibitor. The expression level of p16 that we achieved in this system was similar to the endogenous level of p16 in normal HMEC cells passage 4 (Fig. 3A). As MCF10A/NeuT cells, MCF10A/NeuT/p16 cells had SA-β-gal activity in about 70% of the population (Fig. 3B). At the same time, these cells continued proliferating and about 60% displayed Ki67 staining (Fig. 3C). Therefore, reconstitution of p16 did not reverse NeuT-induced SWING state to OIS.

To test for the role of telomerase in establishing the NeuT-induced SWING state, we utilized two derivatives of the finite lifespan 184 HMEC: (i) 184DTERT cells, which were obtained by ectopic expression of hTERT in 184 HMEC, and (ii) 184BTERT cells which were obtained by the expression of recombinant hTERT in 184 HMEC line that spontaneously lost p16 because of promoter methylation (Brenner *et al.*, 1998; Stampfer *et al.*, 2001; Garbe *et al.*, 2009). Both 184DTERT and 184BTERT cells were infected with retrovirus expressing NeuT. By day 8 postinfection, both cell lines acquired typical senescence morphology, including enlargement and flattening, and about 80% of cells became SA-β-gal positive (Fig. 3D), similar to the effect of NeuT on finite lifespan HMEC (Fig. 1B). Importantly, in contrast to finite HMEC, most of NeuT-expressing 184DTERT and 184BTERT cells remained Ki67-positive (Fig. 3E), although certain decrease in the population of Ki67-positive cells upon NeuT expression was seen with 184DTERT (Fig. 3E). These data indicate that expression of telomerase was sufficient to switch the response of epithelial cells to oncogene from OIS to SWING. Surprisingly, this switch was independent on the p16. Next, we investigated whether oncogenes other than NeuT could trigger transition to the SWING state. MCF10A cells were infected with control retrovirus or retrovirus expressing the oncogenic form of Ras, H-RAS V12. Microscopic examination of cells on 5 days postinfection showed that similar to MCF10A/NeuT cells, approximately 70% of MCF10A/Ras cells attained enlarged, flattened, and highly vacuolized morphology and became SA-β-gal positive (Fig. 1B). These data indicate that MCF10A/Ras cells acquired senescent characteristics. To elucidate whether activation of Ras oncogene triggers permanent growth arrest in MCF10A cells, we loaded control and MCF10A/Ras cells with

PKH67 and monitored cell divisions for three consecutive days, as described earlier. We observed that the pace of PKH67 reduction was only slightly diminished in MCF10A/Ras cells compared with control cells, indicating that flat, enlarged, highly vacuolized MCF10A/Ras cells continued dividing (Fig. 2B). Therefore, expression of Ras and NeuT oncogenes in immortal MCF10A cells failed to promote growth arrest but did promote transition into the SWING state, where cells attained some senescence-associated sub-programs (e.g. morphological changes and expression of SA-β-gal).

Acquisition of SWING phenotype depends on p21

CDK inhibitors, p21, p16, and p15, have been reported to be mediators of OIS in some cell types (Quereda *et al.*, 2007). MCF10A, like most *in vitro* immortalized HMEC lines, does not express p16. As noted, expression of p21 increased approximately two-fold in NeuT-exposed MCF10A and 184B5 (Fig. 4A). Therefore, we investigated whether p21 is implicated in the establishment of the SWING state, using a p21 knockout derivative of MCF10A cells (Karakas *et al.*, 2006). Parental and p21KO MCF10A cells were infected with control or NeuT-expressing virus, as described earlier. Microscopic observation of cells for 12 days starting on day 5 postinfection revealed that in contrast to parental cells, NeuT-expressing p21KO cells had minimal senescence-associated changes in morphology. Furthermore, SA-β-gal assay performed on days 5 and 10 postinfection showed that < 10% of MCF10A p21KO/NeuT cells became SA-β-gal positive as compared to approximately 50% SA-β-gal positive parental MCF10A/NeuT cells (Fig. 4B). Next, we demonstrated that p53, which regulates p21 at the level of transcription, is similarly critical in establishing the SWING state. In fact, knockdown of p53 using shRNA almost completely (to < 5%) blocked development of SA-β-gal activity and senescence morphology following NeuT expression (Fig. 4B). Thus, the p53-p21 pathway is required for the NeuT-induced SWING state.

SWING cells could be malignantly transformed

Expression of NeuT in MCF10A cells obtained from ATCC (see Experimental Procedures) established the SWING phenotype, but did not transform them to malignancy as determined by the lack of formation of foci on plates and tumors in nude mice. To address whether the senescence features of NeuT-expressing cells affect tumorigenesis, we assessed malignancy-associated properties of the SWING cells. In these experiments, we used a clone of MCF10A cells obtained from Dr. B. Park that spontaneously acquired the ability to form foci on plates and tumors in nude mice in response to expression of NeuT, suggesting malignant transformation (Fig. 4C). Notably, similar response to NeuT was demonstrated previously in certain MCF10A clones (Giunciuglio *et al.*, 1995). Surprisingly, there was no apparent selection against the senescence properties, and foci formed by MCF10A/NeuT cells stain positive for SA-β-gal (Fig. 4C), indicating that they retain the SWING phenotype. To analyze the stability of the SWING phenotype, we established xenografts in nude mice. Accordingly, 0.5×10^6 control and MCF10A/NeuT cells were injected subcutaneously into front flanks of nude mice, and tumor growth was monitored by caliper. As expected, control MCF10A cells did not form tumors in mice, while MCF10A/NeuT cells readily formed tumors that became palpable 7 days postinjection. Further, we excised tumors and re-established them in cell culture. Cells in these cultures formed foci, indicating that they retain this transformed property. Importantly, these cells stained positively for SA-β-gal, demonstrating that SWING state is stable and persists in tumors (Fig. 4D).

Next, we evaluated whether SWING cells can be detected in a transgenic mouse model of NeuT-induced mammary tumor. Accordingly, tumors that appeared in 6–7-month-old transgenic MMTV/NeuT mice were excised, and processed for immunohistological analysis. Slides were double stained for the senescence marker SA-β-gal and the proliferation marker Ki67. Of note, Ki67 stains nuclei, while SA-β-gal stains cytoplasm,

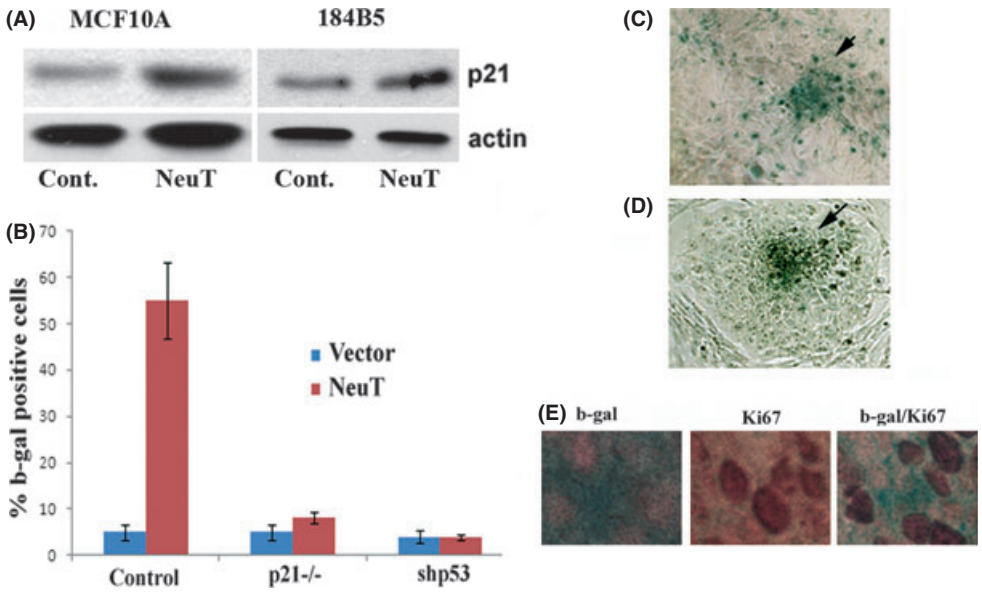

Fig. 4 SWING phenotype depends upon p21 and exists in cancerous cells. (A) NeuT expression causes induction of p21. p21 Levels were measured by immunoblotting in MCF10A cells at day 6 postinfection and in 184B5 at day 12 postinfection. (B) Development of SWING phenotype is p21- and p53-dependent. Fractions of SA-β-gal-positive cells were measured in NeuT-expressing WT, p21KO, and p53 knockdown cells. Three independent fields were scored. (C) SA-β-gal staining of a focus in culture formed by MCF10A cells transformed by NeuT. (D) SA-β-gal staining of a focus formed by MCF10A cells isolated from tumor xenograft. Tumor xenografts were established from NeuT-transformed MCF10A cells, (E) SA-β-gal and Ki67 double staining of NeuT-induced tumor from the MMTVneu transgenic mouse. Newly emerged tumor was excised and stained for β-gal activity; stained tumor was sectioned and processed for immunohistochemical detection of Ki67. Right panel shows section stained for both SA-β-gal and Ki67; sections stained only for SA-β-gal (left panel) or Ki67 (middle panel) are shown for comparison.

and therefore, the presence of the SA-β-gal cytoplasmic staining adjacent to Ki67 nuclear staining indicate the double-stained cell. Tumor sections contained significant cell populations that were positive for both markers (although the percentage of double-stained cells varied significantly between the sections), thus confirming that a population of cells in NeuT-initiated tumors retains SWING phenotype *in vivo* (Fig. 4E). To clarify the appearance of double staining, Fig. 2E shows panels single-stained with either Ki67 or SA-β-gal, and the double-stained panel.

These experiments establish that (i) biochemical properties associated with senescence (SA-β-gal) in immortalized cells and oncogene-expressing tissue may develop independently of growth arrest, (ii) development of the SWING state instead of OIS associates with reactivation of telomerase, (iii) cells in SWING state may be malignantly transformed, and (iv) the SWING state is stable, is not lost after passage of cells through xenografts, and is retained in early tumors.

SWING cells have impaired DNA damage response and increased DNA instability

Recently, we showed that ectopic expression of mediators of the senescence response (e.g. p21 or p16) increases DNA instability and impairs activation of certain branches of the DDR, i.e. accumulation of γH2AX and phosphorylation of Chk1 kinase (Gabai *et al.*, 2008, 2010) in several cancer cell lines. These data were consistent with prior observation that cellular senescence suppresses certain DNA repair pathways (Seluanov *et al.*, 2004). Here, we investigated whether these components of the DDR are also suppressed in SWING cells.

γH2AX serves as an early and critical step in sensing and subsequent repair of DSB. Therefore, we next investigated effects of transition to SWING state on formation of γH2AX foci at the sites of damaged chromosomes. Control and MCF10/NeuT cells were treated with doxorubicin, a potent inducer of DSBs, and γH2AX foci were visualized by immunofluorescence. Incubation of control cells with 200 nM of doxorubicin for 3 h led to the appearance of approximately 30% of cells with more than 10 γH2AX foci per nucleus, and 22% of cells with 1–10 foci per nucleus. Under these conditions, there was 50% reduction in foci formation in NeuT- expressing MCF10A cells, i.e. < 15% of nuclei with more than 10 foci and approximately 10% nuclei with 1–10 foci (Fig. 5A). Thus, activation of NeuT oncogene strongly suppressed γH2AX foci formation.

In parallel, we used immunoblotting to assess levels of γH2AX in oncogene-expressing MCF10A cells exposed to genotoxic stresses. In control cells, both UVC irradiation and doxorubicin treatment led to the rapid appearance of γH2AX (Fig. 5B). Under these conditions, accumulation of γH2AX was significantly reduced in MCF10A/NeuT and MCF10A/Ras cells (Fig. 5B), further indicating that establishment of the SWING state associates with impairment of DDR signaling. At least in part, reduction of γH2AX foci formation and γH2AX levels was associated with the overall downregulation of H2AX expression. We detected two-fold reduction in H2AX levels in both MCF10A/NeuT and MCF10A/Ras cells as compared to control cells; in MCF10A/NeuT cells, the reduction was seen as early as on the second day post-infection (Fig. 5C). Thus, reduction of γH2AX foci formation and γH2AX levels was an early response to oncogene activation and was associated with overall downregulation of H2AX expression.

To investigate effects of NeuT on H2AX *in vivo*, we utilized the MMTV/NeuT transgenic model of the Her2-positive cancer. Expression of NeuT in this model starts at the age of about 2 months because of elevation of estrogen levels. Cancers develop much later in about 12-month-old animals. To assess early effects of NeuT, mammary tissue was collected from the 3-month-old MMTV/NeuT and control mice, and sections were immunostained with anti-p21 and anti-H2AX antibody. As seen on Fig. 5D, NeuT caused induction of p21 and strong downregulation of H2AX, thus replicating effects in cell culture. These biochemical changes coincide with the development of SA-β-gal activity, as reported previously (Reddy *et al.*, 2010).

As establishment of SWING state critically depends upon accumulation of p21, to link H2AX downregulation with the development of SWING phenotype, we utilized the p21KO derivative of MCF10A cells. Control and NeuT-expressing MCF10A p21KO cells were treated with doxorubicin, and levels of γH2AX and total H2AX were assayed by Western blotting with the corresponding antibodies. In contrast to parental MCF10A cells, in p21KO cells, expression of NeuT neither caused suppression of γH2AX following genotoxic treatments (Fig. 5B), nor led to reduction of H2AX levels (Fig. 5C). Similarly, we did not observe NeuT-induced suppression of γH2AX in p53 knockdown cells (Fig. 5B). Thus, downregulation of H2AX following NeuT expression depends on p53 and p21, thus linking the DDR suppression to the development of the SWING state.

Similarly, we observed that expression of either NeuT or Ras oncogenes reduced activation of Chk1. In control cells, UVC irradiation or treatment with doxorubicin led to a strong activation of Chk1; however, in both MCF10A/NeuT and MCF10A/Ras cells activation of Chk1 was strongly suppressed (Fig. 5E). Similar to MCF10A/NeuT, we observed strong suppression of both γH2AX and phChk1 in 184B5/NeuT cells challenged with doxorubicin (Fig. 5F). In these cells, impairment DDR may also be mediated by downregulation of overall levels of H2AX and Chk1. (Figure 5C and data not shown).

Suppression of phChk1 and γH2AX triggered by oncogenes as part of the SWING state could contribute to the increased DNA instability and karyotype abnormalities seen in cancers. Accordingly, we performed micronucleus (MN) assay. Micronucleus arise when extra-nuclear chromosomal fragments induced by DNA damage fail to incorporate into the nucleus, and therefore, MN frequency correlates with genome instability. There was only a minor difference in MN frequencies in MCF10A/NeuT and MCF10A control cells. However, NeuT expression significantly potentiated MN formation in MCF10A cells upon exposure to doxorubicin (Fig. 6A).

Increased DNA instability in cancer is often manifested in aneuploidy. There are numerous reports demonstrating that aneuploidy can be triggered by the centrosome dysfunction (Katsura *et al.*, 2009). To address whether SWING state associates with centrosome dysfunction, we compared the number of centrosomes detected by immunofluorescence with anti-γ-tubulin antibody in control MCF10A and MCF10A/NeuT cells. NeuT expression significantly potentiated centrosome abnormalities. More than 30% of MCF10A/NeuT cells had either more than two centrosomes per cell or broken centrosomes, as compared to 13% in control MCF10A cells (Fig. 6B).

To test whether H2AX downregulation potentiates the centrosome abnormalities in SWING cells, we expressed H2AX protein using the retroviral expression system. (Expression levels of H2AX are shown on Fig. 6C.) Specifically, cells were simultaneously infected with NeuT and H2AX viruses or corresponding control viruses and centrosomes were scored at day 6 postinfection. H2AX expression significantly alleviated centrosome abnormalities seen in SWING cells (Fig. 6B). Taken together, these data indicate that SWING state is characterized by enhanced DNA instability apparently because of suppression of certain branches of the DDR.

SWING cells are sensitive to genotoxic stresses

As SWING cells have reduced activation of Chk1 and H2AX and higher DNA instability, we hypothesized that low-level genotoxic stresses may

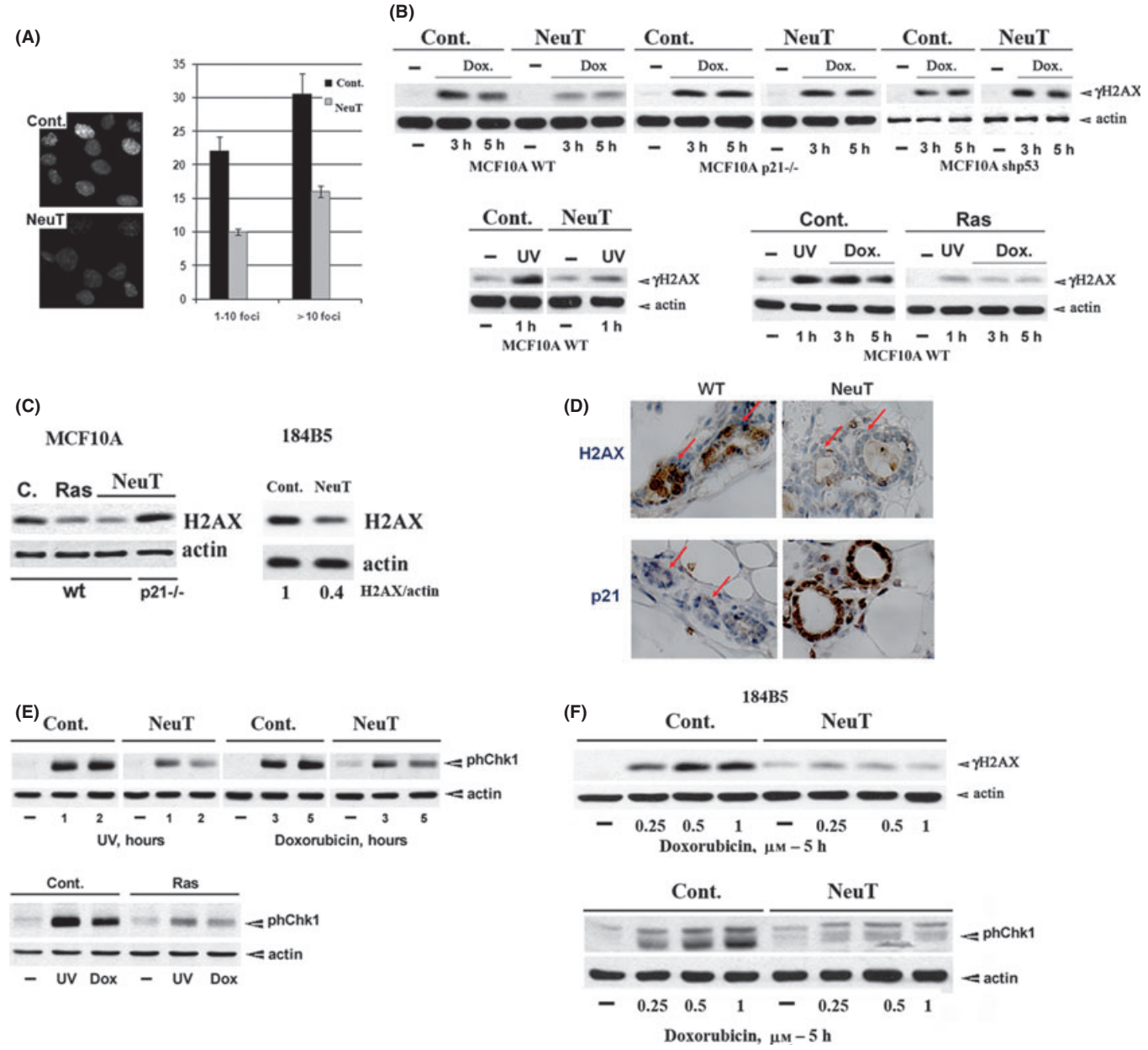

Fig. 5 Downregulation of Chk1 and H2AX in SWING cells. (A) Effect of NeuT oncogene on γH2AX foci formation following doxorubicin treatment. Control and NeuT-expressing cells were treated with 200 nM doxorubicin for 3 h; cells were fixed and immunostained with anti-γH2AX antibody. (B) Effects of Ras and NeuT oncogenes on γH2AX levels following treatments with genotoxic stresses. Treatment conditions were the same as in Fig. 4A. Levels of γH2AX were assessed by immunoblotting. Of note, in p21KO and shp53 cells (upper panel), expression of NeuT did not lead to suppression of γH2AX. (C) Effects of oncogenes on the expression levels of histone H2AX, as assessed by immunoblotting with anti-H2AX antibody. Samples were taken on day 6 postinfection for MCF10A cultures and on day 12 postinfection for 184B5 cultures. (D) Expression of NeuT upregulates p21 and downregulates H2AX in mammary tissue of 3-month-old mice. Mammary glands were collected from control and MMTV/NeuT animals and sections stained for p21 and H2AX with the corresponding antibodies. (E) Oncogene-mediated suppression of Chk1 phosphorylation in response to genotoxic treatments. Cells were infected with control, NeuT- or Ras-expressing retroviruses. At day 6 postinfection, cells were treated with either 100 J/m^{-2} UV or 0.5 μM doxorubicin. Samples were taken at indicated time points after the treatments and levels of phosphorylated Chk1 were assessed by immunoblotting. Bottom panel – samples were taken 1 h after UV irradiation or 5 h treatment with doxorubicin. (F) Effects of NeuT oncogene on γH2AX and phChk1 levels in 184B5 following treatments with indicated doses of doxorubicin.

cause stronger DNA damage in these cells compared with control cells, thus leading to enhanced induction of p21. To test this possibility, we treated control and MCF10A/NeuT cells with doxorubicin and assayed p21 levels by immunoblotting. Following doxorubicin treatment, the levels of p21 were higher in MCF10A/NeuT cells than in control cells (Fig. 6D). To test whether stronger p21 induction was caused by the reduced expression of H2AX, we expressed H2AX in control and MCF10A/NeuT cells using a retroviral expression system, and monitored p21 levels. A buildup of p21 upon exposure to low doses of doxorubicin was suppressed in H2AX-MCF10A/NeuT cells, as compared to MCF10A/NeuT cells (Fig. 6D). Therefore, the H2AX deficiency observed in SWING cells is critical for overinduction of p21.

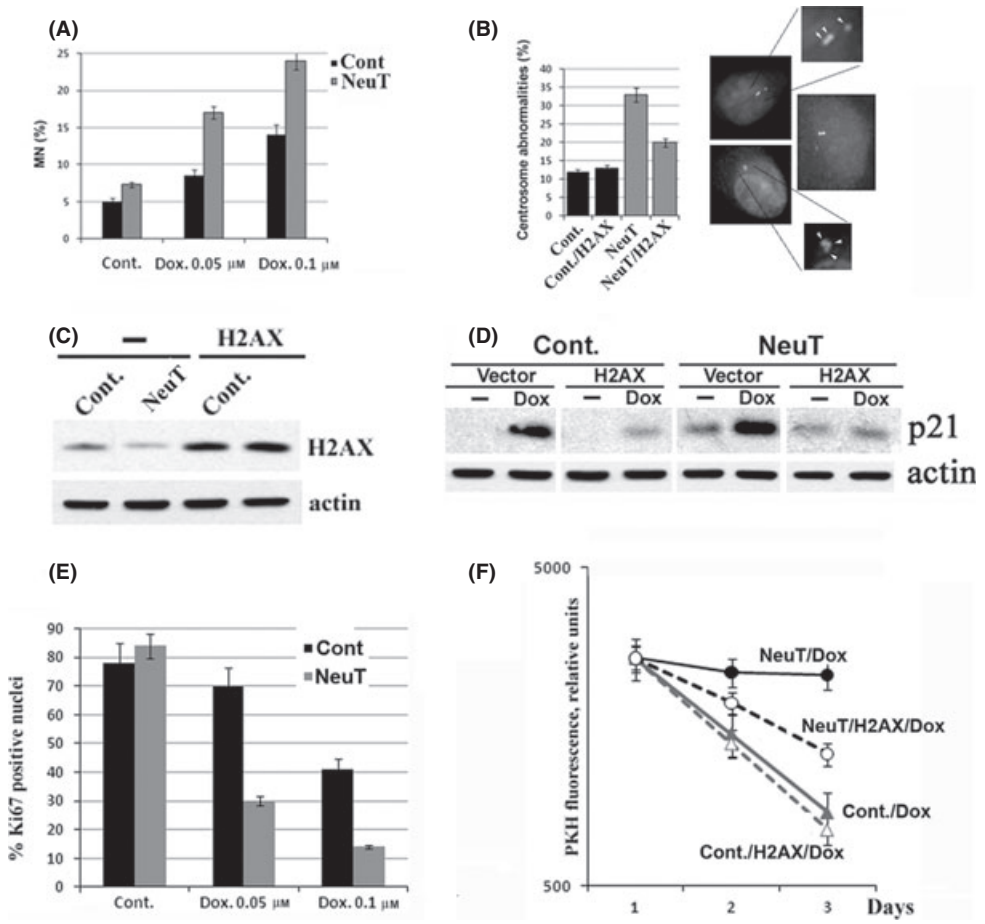

Fig. 6 Chromosome instability and sensitivity toward genotoxic stress in SWING cells. (A) Fractions of micronuclei in control and NeuT-expression cells with or without genotoxic treatments. Cells were treated with indicated doses of doxorubicin for three hours and micronuclei were counted. (B) Centrosome abnormalities in SWING cells. Control and NeuT-expressing cells were fixed on day 6 postinfection and immunostained with γ-tubulin to visualize centrosomes. Fractions of cells with defective centrosomes or increased number of centrosomes were counted. Centrosomes are marked by white arrowheads. Blow up of a section of cells with abnormal centrosomes is shown in two small panels. Nuclei with normal centrosome pair is shown on the right panel, in the middle. Of note, overexpression of H2AX reverses the effect of NeuT expression. (C) Levels of H2AX in cells infected with H2AX-expressing retrovirus. (D) Overexpression of H2AX reverses effects of NeuT on p21 induction by doxorubicin. Conditions were the same as in Fig. 4. (E) SWING cells are more sensitive to genotoxic stress than control cells. Graph shows fractions of Ki67-positive cells in control and NeuT-expressing populations following 3-day treatment with indicated doses of doxorubicin. (F) Effects of H2AX expression on propagation of SWING cells following doxorubicin treatment (50 nM) as measured in PKH67 loading experiment, same as in Fig. 3B.

Increased accumulation of p21 suggests that SWING cells exposed to DNA-damaging stresses may be vulnerable to senescence and permanent growth arrest, and thereby may have increased sensitivity to genotoxic stress. In line with this possibility, there was only minor reduction in the fraction of Ki67 positive cells when control MCF10A cells were treated with 50 nM doxorubicin (from 78% to 70%), while under similar conditions the fraction of Ki67-positive MCF10A/NeuT cells dropped from 84% to 30% (Fig. 6E). Incubation with 100 nM doxorubicin led to about 40% of Ki67-positive control cells and 14% of Ki67-positive MCF10A/-NeuT cells (Fig. 6E).

Further, we monitored growth of control and MCF10A/NeuT cells challenged with low doses of doxorubicin (40 nM) using PKH67. As mentioned earlier, under these conditions, MCF10A/NeuT cells almost completely stopped dividing as manifested by accumulation of significant proportion (about 80%) of brightly stained cells (Fig. 2B). On the other hand, this treatment led to only minor reduction in the rate of dye dilution in control MCF10A cells, indicating that the low dose of doxorubicin did not provoke significant growth inhibitory response in these cells (Fig. 2B right panels and graph). Similarly, PKH67 labeling of MCF10A/Ras cells showed that these cells become highly prone to senescence-inducing stresses and readily stopped dividing upon treatment with 40 nM doxorubicin (Fig. 2B right panels). These experiments indicate that expression of NeuT or Ras oncogenes sensitized MCF10A cells to DNA damage by promoting growth arrest following genotoxic insult.

A plausible explanation for this effect is that SWING cells have a defect in H2AX, which is critical for DNA repair, and thus experience stronger DNA damage when exposed to genotoxic treatments. Hence, we tested whether expression of H2AX can reverse growth inhibition of SWING cells challenged by low doses of genotoxic stress. Growth rates of cells infected simultaneously or separately with NeuT and H2AX viruses as well as control viruses were evaluated using the PKH67 loading experiment, as described earlier (see Fig. 2B). Expression of H2AX significantly potentiated growth of MCF10A/NeuT cells treated with low doses of doxorubicin (Fig. 6F). Of note, growth of untreated or doxorubicin-treated control MCF10A cells was not affected by H2AX overexpression. Altogether

these experiments indicate that (i) downregulation of H2AX is an important property of the SWING cells, (ii) downregulation of H2AX leads to DNA instability and subsequent overinduction of p21, which in turn makes SWING cells sensitive to genotoxic stresses.

Discussion

Oncogene-induced senescence represents one of the major protective responses that guard multicellular organisms from tumor development. However, oncogenes are reported to have opposing effects on cell proliferation and may trigger both senescence and transformation (Braig *et al.*, 2005; Bartkova *et al.*, 2006). These observations make it critical to investigate what specific parameters determine the outcome of oncogene activation on cellular proliferation. Here, we report that expression of either NeuT or Ras oncogene in immortalized HMEC lines MCF10A and 184B triggers the development of the SWING state where cells acquire major characteristics of senescent cells, including enlargement, flattening, vacuolization and SA-β-gal activity, but do not exit the cell cycle. In contrast, expression of NeuT oncogene in finite HMEC triggers all the same morphological changes accompanied with a similar extent of SA-β-gal accumulation, while completely preventing cell proliferation. These unexpected findings indicate that appearance of SA-β-gal, which commonly serves as a major criterion of senescence, may be disconnected from the onset of growth arrest. In line with this idea, there are many reports demonstrating that proliferative hyperplastic tissues and early tumors stain positive for SA-β-gal (Collado *et al.*, 2005; Di Micco *et al.*, 2006; Reddy *et al.*, 2010). Importantly, this work implies that OIS could be viewed as a complex of distinct subprograms, which can be expressed independently of each other, and therefore, are under separate molecular control.

Next, we investigated weather failure of MCF10A cells to achieve the major senescence-associated end point of growth arrest, in response to Ras or NeuT activation, is because of deficiencies in cell cycle regulation that occurred during the process of immortalization. For example, MCF10A cells do not express the CDK inhibitor p16 and have re-activated telomerase. Noteworthy, we have found that reconstitution of p16 levels in MCF10A cells did not restore OIS following expression of NeuT, and did not affect the development of the SWING state. In contrast, expression of hTERT in finite lifespan HMEC was sufficient to switch cellular response to NeuT from OIS to the SWING state. Indeed, these cells, while expressing SA-β-gal at about the same level as control HMEC, continue proliferating and were Ki67-positive. Therefore, telomerase appears to play the major role in development of the SWING state, while p16 seems to be irrelevant. These data indicate that NeuT- or Ras-induced expression of p21 in cells that have reactivated telomerase does not precipitate OIS, but rather triggers transition to the SWING state. Noteworthy, further switching off of cell cycle regulators prevented the development of all signs of senescence. In fact, we have shown that SWING phenotype critically depends upon p21 and did not develop in either MCF10A p21KO cells or p53 knockdown cells.

Interestingly, the SWING state is associated with the suppression of DDR, i.e., is characterized by impaired activation of H2AX and Chk1. Of note, DDR suppression apparently is also mediated by the p21 pathway as it was observed neither in MCF10A cells depleted of p53 nor in MCF10A p21 knockout cells.

Suppression of H2AX and Chk1 causes a number of defects in SWING cells, including, increased sensitivity to genotoxic stress, increased growth arrest in response to low doses of genotoxic stress, and increased chromosome instability. Importantly, all these deficiencies can be reversed upon expression of H2AX. We therefore suggest that reduced H2AX activation leads to DNA damage, especially upon exposure to minor genotoxic stress, which in turn promotes instability. An interesting possibility is that increased DNA instability in cancer, at least in early stages, could be associated with the SWING phenotype of cells and consequently suppression of SWING could reduce DNA instability in cancer. In line with this possibility, we observed that expression of NeuT promotes upregulation of p21 and downregulation of H2AX in mammary tissue of transgenic mice obtained from 3-month-old animals. These effects take place very soon after the beginning of NeuT expression and 9–10 month prior to cancer development. We propose that p21-dependent downregulation of H2AX may be an important factor in DNA instability in early Her2-driven precancerous lesions (Chen *et al.*, 2009).

An important observation is that cells in SWING state remain vulnerable to senescence when challenged by a minor genotoxic stress that did not affect proliferation of non-SWING cells (Fig. 2B). These results raise the possibility that the enhanced sensitivity of SWING cells to genotoxic stresses could be used as an approach toward cancer therapy. In fact, these cells may be especially sensitive to additional suppression of H2AX.

Noteworthy, despite that SWING cells may easily progress to either senescence arrest or malignant transformation, the SWING state is relatively stable and persists while passing cells through xenografts and re-establishing cell culture. Furthermore, we were able to detect a population of SWING cells, expressing both SA-β-gal and Ki67 markers, in mammary tumors from the MMTVneu mouse model. These findings suggest that SWING cells may account for at least some of the previously reported SA-β-gal-positive cells found in tumors.

These data further support the suggestion that cell immortalization is a critical step in tumorigenesis as immortalization favors transition into the SWING upon oncogene activation, which can further evolve to a malignant state. In contrast, as reported previously, activation of oncogenes in normal epithelial and fibroblast cells leads to the onset of OIS (Zhu *et al.*, 1998). The reactivation of telomerase associated with immortalization may be part of the process responsible for this shift in response to oncogene activation from OIS to SWING (Olsen *et al.*, 2002; Stampfer & Yaswen, 2003).

Overall, this work describes new phenomenon associated with oncogene activation and OIS, i.e., the existence of the SWING state, associated with decreased DDR capacity and increased vulnerability to genotoxic stresses. These results suggest a novel contributor to DNA instability in cancer, and the potential for novel clinical interventions in cancer by engaging the intact capacity of cells in the SWING state to growth arrest in response to genotoxic stresses.

Experimental procedures

Cell cultures, treatments, and reagents

HEK293 were from American Type Culture Collection. There were two sources of MCF10A cells, from ATCC and a kind gift of Dr. B. Park. MCF10A p21KO cells were from Dr. B. Park. HEK293 cells were grown in DMEM supplemented with 10% fetal bovine serum; MCF10A and MCF10A p21KO cells were grown in DMEM/F12 (1:1, v:v) containing 5% horse serum and supplemented with 10 mg L^{-1} insulin, 20 μg L^{-1} epidermal growth factor, 50 μg L^{-1} cholera toxin, 50 mg L^{-1} hydrocortisone, 100 units mL^{-1} penicillin, and 0.1 mg mL^{-1} streptomycin in a humidified environment at 37 °C with 5% CO_2. Finite prestasis HMEC from specimen 184, batch D, and their immortalized derivative lines, 184BTERT, 184DTERT, and 184B5, were derived and grown as described (Stampfer & Bartley, 1985; Garbe *et al.*, 2009). UVC irradiation was performed with UV Stratalinker 1800 from Stratagene (Cedar Creek, TX,

USA). Doxorubicin was from BioMol (Plymouth Meeting, PA, USA) (Cat. # GR-319); PKH67 was from Sigma (Sigma-Aldrich Corporation, MO,USA) (Cat. # 0099K0787).

Cell cycle reporters

Lentiviruses expressing G1/S and S/G2 cell-cycle reporters (mKO2-hCdt1(30/120) [red] or mAG-hGem(1/110)[green]) were from RIKEN Bioresource Center (Tsukuba, Ibaraki Prefecture, Japan) (Sakaue-Sawano *et al.*, 2008). Cells were infected with corresponding viruses and observed on day 2 postinfection. Cells in S-phase, expressing both markers can be seen as yellow.

Recombinant retroviral vectors

H2AX-expressing lentivirus and control 'empty' lentivirus were a kind gift of Dr. E. Brown (University of Pennsylvania Medical School); NeuT and control (pBABE) retroviral vectors were a kind gift of Dr. C. Spangenberg (Trost *et al.*, 2005). This version of NeuT carries the activating V664E mutation (NeuT). H-RAS V12 and control (Babe) retroviral vectors were kindly provided by Dr. S. Lowe (Gabai *et al.*, 2009). Retro- and lentiviruses were produced as reported before (Yaglom *et al.*, 2007; Gabai *et al.*, 2009). Briefly, HEK293T cells were co-transfected with plasmids expressing retroviral proteins Gag-Pol, vesicular stomatitis virus glycoprotein pseudotype and enhanced green fluorescent protein or our constructs using Lipofectamine 2000 (Invitrogen, Carlsbad, CA, USA). At 48 h after transfection, supernatants containing the retroviral particles were collected and frozen at −80 °C until use. Cells were infected with diluted supernatant in the presence of 10 μg mL^{-1} Polybrene overnight, and were selected with puromycin (0.75 μg mL^{-1}) 48 h after infection. Retroviral vectors expressing enhanced green fluorescent protein was used as infection efficiency indicator: usually approximately 90% of cells were fluorescent 2 days after infection. Lentiviruses were produced the same except for HEK293T transfections lentivirus-specific packaging plasmids psPAX2 and PMD2.G from Addgene were used.

Immunoblotting

Cells lysates were prepared as described (Yaglom *et al.*, 2007). Antibodies used in the study were β-actin from Sigma; phospho-Chk1 (Ser345), p21 from BD Pharmingen (San Diego, CA, USA); NeuT (Ser 1981) were the kind gift from Dr. T Kowalik (University of Massachusetts Medical Center, Worchester); γH2AX (Ser139) were from Millipore (Billerica, MA, USA) (Cat.# 05-636). Rabbit Polyclonal Ki 67 Antibody was from Thermo Scientific (Barrington, IL, USA) (Cat. #:RB-9043-P), and γ-tubulin was from Santa Cruz (sc-17787; Santa Cruz Biotechnology, Inc., Santa Cruz, CA, USA). Quantification of blots was performed using Quantity One software (Bio-Rad, Waltham, MA, USA).

Cell growth analysis

Growth rate: Cell growth curve was performed by seeding 5000 cells per well in 12-well plate; on three consecutive days, cells were harvested by trypsinization and cell numbers were counted with Scepter Automated Cell Counter (Millipore).

Measurement of cellular diameters was performed using AuxioVision software.

FACS analysis was performed on BD Biosciences (San Jose, CA, USA) FACSCalibur, and data were analyzed with BD Cellquest Pro v5.2 software.

PKH67 assay was carried out according to manufacture protocol. Briefly, PKH67 dye was added to trypsinized single-cell suspension, incubated for 5 min; staining was stopped by adding equal volume of horse serum for 1 min. Cells were washed twice and plated. First images were taken 16 h after plating.

H&E staining was carried out using Mayer's hematoxylin solution (Sigma).

Immunohistochemistry

One-centimeter tumors were excised from animals and fixed in formalin at 4 °C overnight. Next day, tumors were trimmed into thin pieces and stained with β-gal solution for 48 h. Tumor pieces were embedded into paraffin and processed into slides (10 μm in thickness). Ki-67 staining was performed on these slides via standard ABC method (Vector Laboratory, Burlingame, CA, USA). H2AX and p21 staining was performed on paraffin-embedded sections of mammary glands.

Immunofluorescence

After treatments, cells were fixed in 100% ice-cold methanol at −20 °C for 30 min, permeabilized in 0.2% Triton X-100/PBS for 15 min at room temperature (RT), blocked in 3% BSA/PBS for 1 h, and incubated with corresponding primary Ab in the cold room (γH2AX at 1:200; Ki 67 at 1:100; γ-tubulin – 1:200; all dilutions were carried out with 3% BSA/PBS) followed by incubation with secondary Ab for 1 h at RT. Images were analyzed using Zeuss fluorescent microscope (Carl Zeiss, Oberkochen, Germany).

Mouse xenografts and cell-culture re-established from tumor

Animal maintenance and experiments were conducted in compliance with the guidelines of the Institutional Animal Care and Use Committee. Briefly, NeuT-infected MCF-10A cells were trypsinized, mixed at 1:1 ratio with matrigel (BD Scientific, San Jose, CA, USA) and 0.5 million cells were injected subcutaneously into 6-week-old female NCR nude mice (Taconic, Hudson, NY, USA). Tumor growth was monitored weekly.

When developed tumors reached 0.5 cm, they were excised and immediately placed in PBS. Tumor was cut into small fragments that were placed in MCF10A media w/out serum supplemented with 100 u mL^{-1} of collagenase (Sigma) and incubated ON at 37 °C. Next morning cell suspension was passed through cell strainer with 75 μM mesh (BD scientific). Cells were washed twice with media with serum and plated.

β-Galactosidase assay

The β-galactosidase assay was performed using X-Gal (5-bromo-4-chloro-3-indolyl-β-D-galactopyranoside) at pH 6.0, as described earlier (Yaglom *et al.*, 2007). The number of stained cells was counted under a microscope from five different fields, and the proportion of stained cells was calculated. The results were expressed as mean value ± SD on three independent experiments.

MN assay

Cells were incubated with cytochalasin B (3.5 μg mL^{-1}) for 48 h, fixed in Carnoy's fixative (3:1 methanol:acetic acid) three times for 15 min

each, and stored at –20 °C. Micronucleus scoring was carried out after cells were dropped on slides, air dried, and stained with acridine orange (30 μg mL^{-1}). Per each point at least 300 bi-nucleated cells were evaluated. Three independent experiments were performed, and MN frequency was expressed as the number of MN per binucleated cell.

Statistical analysis

The data shown are means ± SE of three independent experiments.

References

Bartkova J, Horejsi Z, Koed K, Kramer A, Tort F, Zieger K, Guldberg P, Sehested M, Nesland JM, Lukas C, Orntoft T, Lukas J, Bartek J (2005) DNA damage response as a candidate anti-cancer barrier in early human tumorigenesis. *Nature* **434**, 864–870.

Bartkova J, Rezaei N, Liontos M, Karakaidos P, Kletsas D, Issaeva N, Vassiliou LV, Kolettas E, Niforou K, Zoumpourlis VC, Takaoka M, Nakagawa H, Tort F, Fugger K, Johansson F, Sehested M, Andersen CL, Dyrskjot L, Orntoft T, Lukas J, Kittas C, Helleday T, Halazonetis TD, Bartek J, Gorgoulis VG (2006) Oncogene-induced senescence is part of the tumorigenesis barrier imposed by DNA damage checkpoints. *Nature* **444**, 633–637.

Bodnar AG, Ouellette M, Frolkis M, Holt SE, Chiu CP, Morin GB, Harley CB, Shay JW, Lichtsteiner S, Wright WE (1998) Extension of life-span by introduction of telomerase into normal human cells. *Science* **279**, 349–352.

Braig M, Lee S, Loddenkemper C, Rudolph C, Peters AH, Schlegelberger B, Stein H, Dorken B, Jenuwein T, Schmitt CA (2005) Oncogene-induced senescence as an initial barrier in lymphoma development. *Nature* **436**, 660–665.

Brenner AJ, Stampfer MR, Aldaz CM (1998) Increased p16 expression with first senescence arrest in human mammary epithelial cells and extended growth capacity with p16 inactivation. *Oncogene* **17**, 199–205.

Campisi J, d'Adda di Fagagna F (2007) Cellular senescence: when bad things happen to good cells. *Nat. Rev. Mol. Cell Biol.* **8**, 729–740.

Campisi J (2011) Cellular senescence: putting the paradoxes in perspective. *Curr. Opin. Genet. Dev.* **21**, 107–112.

Chanoux RA, Yin B, Urtishak KA, Asare A, Bassing CH, Brown EJ (2009) ATR and H2AX cooperate in maintaining genome stability under replication stress. *J. Biol. Chem.* **284**, 5994–6003.

Chen Z, Trotman LC, Shaffer D, Lin HK, Dotan ZA, Niki M, Koutcher JA, Scher HI, Ludwig T, Gerald W, Cordon-Cardo C, Pandolfi PP (2005) Crucial role of p53-dependent cellular senescence in suppression of Pten-deficient tumorigenesis. *Nature* **436**, 725–730.

Chen YY, Hwang ES, Roy R, DeVries S, Anderson J, Wa C, Fitzgibbons PL, Jacobs TW, MacGrogan G, Peterse H, Vincent-Salomon A, Tokuyasu T, Schnitt SJ, Waldman FM (2009) Genetic and phenotypic characteristics of pleomorphic lobular carcinoma in situ of the breast. *Am. J. Surg. Pathol.* **33**, 1683–1694.

Cipriano R, Kan CE, Graham J, Danielpour D, Stampfer M, Jackson MW (2011) TGF-{beta} signaling engages an ATM-CHK2-p53-independent RAS-induced senescence and prevents malignant transformation in human mammary epithelial cells. *Proc. Natl. Acad. Sci. U S A* **108**, 8668–8673.

Collado M, Gil J, Efeyan A, Guerra C, Schuhmacher AJ, Barradas M, Benguria A, Zaballos A, Flores JM, Barbacid M, Beach D, Serrano M (2005) Tumour biology: senescence in premalignant tumours. *Nature* **436**, 642.

Di Micco R, Fumagalli M, Cicalese A, Piccinin S, Gasparini P, Luise C, Schurra C, Garre M, Nuciforo PG, Bensimon A, Maestro R, Pelicci PG, d'Adda di Fagagna F (2006) Oncogene-induced senescence is a DNA damage response triggered by DNA hyper-replication. *Nature* **444**, 638–642.

Gabai VL, O'Callaghan-Sunol C, Meng L, Sherman MY, Yaglom J (2008) Triggering senescence programs suppresses Chk1 kinase and sensitizes cells to genotoxic stresses. *Cancer Res.* **68**, 1834–1842.

Gabai VL, Yaglom JA, Waldman T, Sherman MY (2009) Heat shock protein Hsp72 controls oncogene-induced senescence pathways in cancer cells. *Mol. Cell. Biol.* **29**, 559–569.

Gabai VL, Sherman MY, Yaglom JA (2010) HSP72 depletion suppresses gamma H2AX activation by genotoxic stresses via p53/p21 signaling. *Oncogene* **29**, 1952–1962.

Garbe JC, Bhattacharya S, Merchant B, Bassett E, Swisshelm K, Feiler HS, Wyrobek AJ, Stampfer MR (2009) Molecular distinctions between stasis and telomere attrition senescence barriers shown by long-term culture of normal human mammary epithelial cells. *Cancer Res.* **69**, 7557–7568.

Giunciuglio D, Culty M, Fassina G, Masiello L, Melchiori A, Paglialunga G, Arand G, Ciardiello F, Basolo F, Thompson EW , Albini A (1995) Invasive phenotype of MCF10A cells overexpressing c-Ha-ras and c-erbB-2 oncogenes. *Int. J. Cancer* **63**, 815–822.

Gorgoulis VG, Vassiliou LV, Karakaidos P, Zacharatos P, Kotsinas A, Liloglou T, Venere M, Ditullio RA Jr, Kastrinakis NG, Levy B, Kletsas D, Yoneta A, Herlyn M, Kittas C, Halazonetis TD (2005) Activation of the DNA damage checkpoint and genomic instability in human precancerous lesions. *Nature* **434**, 907–913.

Harley CB, Futcher AB, Greider CW (1990) Telomeres shorten during ageing of human fibroblasts. *Nature* **345**, 458–460.

Hayflick L, Moorhead PS (1961) The serial cultivation of human diploid cell strains. *Exp. Cell Res.* **25**, 585–621.

Karakas B, Weeraratna A, Abukhdeir A, Blair BG, Konishi H, Arena S, Becker K, Wood W III, Argani P, De Marzo AM, Bachman KE, Park BH (2006) Interleukin-1 alpha mediates the growth proliferative effects of transforming growth factor-beta in p21 null MCF-10A human mammary epithelial cells. *Oncogene* **25**, 5561–5569.

Katsura M, Tsuruga T, Date O, Yoshihara T, Ishida M, Tomoda Y, Okajima M, Takaku M, Kurumizaka H, Kinomura A, Mishima HK, Miyagawa K (2009) The ATR-Chk1 pathway plays a role in the generation of centrosome aberrations induced by Rad51C dysfunction. *Nucleic Acids Res.* **37**, 3959–3968.

Lazzerini Denchi E, Attwooll C, Pasini D, Helin K (2005) Deregulated E2F activity induces hyperplasia and senescence-like features in the mouse pituitary gland. *Mol. Cell. Biol.* **25**, 2660–2672.

Lin AW, Barradas M, Stone JC, van Aelst L, Serrano M, Lowe SW (1998) Premature senescence involving p53 and p16 is activated in response to constitutive MEK/MAPK mitogenic signaling. *Genes Dev.* **12**, 3008–3019.

Mallette FA, Gaumont-Leclerc MF, Ferbeyre G (2007) The DNA damage signaling pathway is a critical mediator of oncogene-induced senescence. *Genes Dev.* **21**, 43–48.

McDuff FK, Turner SD (2010) Jailbreak: oncogene-induced senescence and its evasion. *Cell. Signal.* **23**, 6–13.

Michaloglou C, Vredeveld LC, Soengas MS, Denoyelle C, Kuilman T, van der Horst CM, Majoor DM, Shay JW, Mooi WJ, Peeper DS (2005) BRAFE600-associated senescence-like cell cycle arrest of human naevi. *Nature* **436**, 720–724.

Minoo P, Jass JR (2006) Senescence and serration: a new twist to an old tale. *J. Pathol.* **210**, 137–140.

Muller WJ, Sinn E, Pattengale PK, Wallace R, Leder P (1988) Single-step induction of mammary adenocarcinoma in transgenic mice bearing the activated c-neu oncogene. *Cell* **54**, 105–115.

Narita M, Lowe SW (2004) Executing cell senescence. *Cell Cycle* **3**, 244–246.

Olsen CL, Gardie B, Yaswen P, Stampfer MR (2002) Raf-1-induced growth arrest in human mammary epithelial cells is p16-independent and is overcome in immortal cells during conversion. *Oncogene* **21**, 6328–6339.

Pollock PM, Harper UL, Hansen KS, Yudt LM, Stark M, Robbins CM, Moses TY, Hostetter G, Wagner U, Kakareka J, Salem G, Pohida T, Heenan P, Duray P, Kallioniemi O, Hayward NK, Trent JM, Meltzer PS (2003) High frequency of BRAF mutations in nevi. *Nat. Genet.* **33**, 19–20.

Quereda V, Martinalbo J, Dubus P, Carnero A, Malumbres M (2007) Genetic cooperation between p21Cip1 and INK4 inhibitors in cellular senescence and tumor suppression. *Oncogene* **26**, 7665–7674.

Reddy JP, Peddibhotla S, Bu W, Zhao J, Haricharan S, Du YC, Podsypanina K, Rosen JM, Donehower LA, Li Y (2010) Defining the ATM-mediated barrier to tumorigenesis in somatic mammary cells following ErbB2 activation. *Proc. Natl. Acad. Sci. U S A* **107**, 3728–3733.

Sakaue-Sawano A, Kurokawa H, Morimura T, Hanyu A, Hama H, Osawa H, Kashiwagi S, Fukami K, Miyata T, Miyoshi H, Imamura T, Ogawa M, Masai H, Miyawaki A (2008) Visualizing spatiotemporal dynamics of multicellular cell-cycle progression. *Cell* **132**, 487–498.

Sarkisian CJ, Keister BA, Stairs DB, Boxer RB, Moody SE, Chodosh LA (2007) Dose-dependent oncogene-induced senescence in vivo and its evasion during mammary tumorigenesis. *Nat. Cell Biol.* **9**, 493–505.

Schmitt CA, Fridman JS, Yang M, Lee S, Baranov E, Hoffman RM, Lowe SW (2002) A senescence program controlled by p53 and p16INK4a contributes to the outcome of cancer therapy. *Cell* **109**, 335–346.

Seluanov A, Mittelman D, Pereira-Smith OM, Wilson JH, Gorbunova V (2004) DNA end joining becomes less efficient and more error-prone during cellular senescence. *Proc. Natl. Acad. Sci. U S A* **101**, 7624–7629.

Serrano M, Lin AW, McCurrach ME, Beach D, Lowe SW (1997) Oncogenic ras provokes premature cell senescence associated with accumulation of p53 and p16INK4a. *Cell* **88**, 593–602.

Slamon DJ, Godolphin W, Jones LA, Holt JA, Wong SG, Keith DE, Levin WJ, Stuart SG, Udove J, Ullrich A, Press MF (1989) Studies of the HER-2/neu proto-oncogene in human breast and ovarian cancer. *Science* **244**, 707–712.

Stampfer MR, Bartley JC (1985) Induction of transformation and continuous cell lines from normal human mammary epithelial cells after exposure to benzo[a]pyrene. *Proc. Natl. Acad. Sci. U S A* **82**, 2394–2398.

Stampfer MR, Yaswen P (2003) Human epithelial cell immortalization as a step in carcinogenesis. *Cancer Lett.* **194**, 199–208.

Stampfer MR, Garbe J, Levine G, Lichtsteiner S, Vasserot AP, Yaswen P (2001) Expression of the telomerase catalytic subunit, hTERT, induces resistance to transforming growth factor beta growth inhibition in p16INK4A(-) human mammary epithelial cells. *Proc. Natl. Acad. Sci. U S A* **98**, 4498–4503.

Thiriet C, Hayes JJ (2005) Chromatin in need of a fix: phosphorylation of H2AX connects chromatin to DNA repair. *Mol. Cell* **18**, 617–622.

Trost TM, Lausch EU, Fees SA, Schmitt S, Enklaar T, Reutzel D, Brixel LR, Schmidtke P, Maringer M, Schiffer IB, Heimerdinger CK, Hengstler JG, Fritz G, Bockamp EO, Prawitt D, Zabel BU, Spangenberg C (2005) Premature senescence is a primary fail-safe mechanism of ERBB2-driven tumorigenesis in breast carcinoma cells. *Cancer Res.* **65**, 840–849.

Yaglom JA, Gabai VL, Sherman MY (2007) High levels of heat shock protein Hsp72 in cancer cells suppress default senescence pathways. *Cancer Res.* **67**, 2373–2381.

Yaswen P, Campisi J (2007) Oncogene-induced senescence pathways weave an intricate tapestry. *Cell* **128**, 233–234.

Zha S, Sekiguchi J, Brush JW, Bassing CH, Alt FW (2008) Complementary functions of ATM and H2AX in development and suppression of genomic instability. *Proc. Natl. Acad. Sci. U S A* **105**, 9302–9306.

Zhu J, Woods D, McMahon M, Bishop JM (1998) Senescence of human fibroblasts induced by oncogenic Raf. *Genes Dev.* **12**, 2997–3007.

Epigenetic regulation of normal human mammary cell type–specific miRNAs

Lukas Vrba,[1,2] James C. Garbe,[3] Martha R. Stampfer,[1,3] and Bernard W. Futscher[1,4,5]

[1]*Arizona Cancer Center, The University of Arizona, Tucson, Arizona 85724, USA;* [2]*Biology Centre ASCR, v.v.i., Institute of Plant Molecular Biology, Ceske Budejovice 37005, Czech Republic;* [3]*Life Sciences Division, Lawrence Berkeley National Laboratory, Berkeley, California 94720, USA;* [4]*Department of Pharmacology & Toxicology, College of Pharmacy, The University of Arizona, Tucson, Arizona 85724, USA*

Epigenetic mechanisms are important regulators of cell type–specific genes, including miRNAs. In order to identify cell type–specific miRNAs regulated by epigenetic mechanisms, we undertook a global analysis of miRNA expression and epigenetic states in three isogenic pairs of human mammary epithelial cells (HMEC) and human mammary fibroblasts (HMF), which represent two differentiated cell types typically present within a given organ, each with a distinct phenotype and a distinct epigenotype. While miRNA expression and epigenetic states showed strong interindividual concordance within a given cell type, almost 10% of the expressed miRNA showed a cell type–specific pattern of expression that was linked to the epigenetic state of their promoter. The tissue-specific miRNA genes were epigenetically repressed in non-expressing cells by DNA methylation (38%) and H3K27me3 (58%), with only a small set of miRNAs (21%) showing a dual epigenetic repression where both DNA methylation and H3K27me3 were present at their promoters, such as *MIR10A* and *MIR10B*. Individual miRNA clusters of closely related miRNA gene families can each display cell type–specific repression by the same or complementary epigenetic mechanisms, such as the *MIR200* family, and *MIR205*, where fibroblasts repress *MIR200C/141* by DNA methylation, *MIR200A/200B/429* by H3K27me3, and *MIR205* by both DNA methylation and H3K27me3. Since deregulation of many of the epigenetically regulated miRNAs that we identified have been linked to disease processes such as cancer, it is predicted that compromise of the epigenetic control mechanisms is important for this process. Overall, these results highlight the importance of epigenetic regulation in the control of normal cell type–specific miRNA expression.

[Supplemental material is available for this article.]

MicroRNAs (miRNA) are short single-stranded RNA molecules that regulate gene expression at the post-transcriptional level by inhibiting translation of target mRNAs or by stimulating their degradation. Mature miRNAs are processed from hairpin precursors that are either encoded by dedicated miRNA genes that are often found in clusters, or they reside in the introns of protein-coding genes and are processed following transcription of the host gene. According to current estimates, there are >1000 miRNAs expressed from over 500 transcriptional units (miRNA genes) encoded in the human genome. These miRNAs control, in part, the expression of about two-thirds of human genes (Friedman et al. 2009). miRNAs are involved in determination of cell identity and their expression is often deregulated in cancer (Peter 2009); however, relatively little is known about how their expression is regulated. Evidence is emerging that similar to protein-coding genes, epigenetic mechanisms play an important role in this process (Iorio et al. 2010).

Epigenetic mechanisms involve DNA methylation and post-translational modifications of chromatin proteins, including histones. 5-methylcytosine residues are a feature of transcriptionally silent heterochromatin, and this epigenetic mark is indispensable for mammalian development; it participates in X chromosome inactivation, gene imprinting, and control of cell type–specific gene expression patterns (Bird 2002; Lister et al. 2009; Laurent et al. 2010). Methyl groups are deposited on CpG cytosine residues by de novo DNA methyltransferases, DNMT3A and DNMT3B, and then maintained by DNA methyltransferase DNMT1 (Jaenisch and Bird 2003; Miranda and Jones 2007). In addition to DNA methylation, there exist a number of post-translational modifications on histones that act as positive or negative epigenetic regulators of gene expression. Two major repressive histone marks commonly present in euchromatin regions are trimethylation of histone H3 at lysine 27 (H3K27me3) and dimethylation of histone H3 at lysine 9 (H3K9me2). The H3K27me3 modification is deployed by the histone methyltransferase EZH2, a part of the polycomb repressive complex 2 (PRC2) (Simon and Kingston 2009). The H3K9me2 repressive histone modification is deposited by G9a, a member of the H3K9-specific histone methyltransferases (Tachibana et al. 2002). Two major permissive marks are trimethylation of histone H3 at lysine 4 (H3K4me3) and acetylation of histone H3 at multiple lysine residues (H3Ac) (Liang et al. 2004). Recent evidence suggests that epigenetic control is also involved in the regulation of miRNA gene expression in both normal and cancer cells (Bueno et al. 2008; Kozaki et al. 2008; Lujambio et al. 2008; Vrba et al. 2010).

To more fully understand the role of epigenetic mechanisms in the regulation of normal cell type–specific miRNA expression, we studied three different isogenic pairs of human mammary epithelial cells (HMEC) and human mammary fibroblasts (HMF) derived from reduction mammoplasty tissue (Garbe et al. 2009). These normal, previously characterized (Garbe et al. 2009; Novak et al. 2009) finite lifespan cells represent two differentiated cell types typically present within a given organ, each with a distinct phenotype and a distinct epigenotype. The analysis of multiple genotypes allowed us to assess interindividual variability in miRNA

[5]Corresponding author.
E-mail bfutscher@azcc.arizona.edu.
Article published online before print. Article, supplemental material, and publication date are at http://www.genome.org/cgi/doi/10.1101/gr.123935.111.

21:2026–2037 © 2011 by Cold Spring Harbor Laboratory Press; ISSN 1088-9051/11; www.genome.org

expression and epigenetic marks and more precisely identify miRNA genes targeted by epigenetic regulation. To identify cell type–specific miRNAs regulated by epigenetic mechanisms in normal cells, we integrated miRNA expression data obtained by high-throughput sequencing of small RNA libraries with the epigenetic profiles of their miRNA promoter regions obtained using a custom designed miRNA tiling microarray. Results from this analysis showed that miRNA gene expression and epigenetic state display high interindividual concordance within a given cell type; however, intercell-type concordance was lower, with 13% of expressed miRNAs showing >10-fold difference in expression between the two normal mammary cell types. We found that a majority of these cell type–specific miRNAs are regulated by epigenetic mechanisms in normal cells; 38% were subject to DNA methylation-mediated repression of their promoter in the normal nonexpressing cells, while 58% were subject to H3K27me3-mediated repression of their promoter in normal nonexpressing cells. Overall, there is limited overlap of these two repressive marks at individual miRNA promoters, although a few notable exceptions, *MIR10A*, *MIR10B*, and *MIR205* appear to be under dual epigenetic repression by both DNA methylation and H3K27me3 in normal nonexpressing cells. In other cases, DNA methylation and H3K27me3 independently target individual miRNA clusters in order to repress complete miRNA families. These results indicate that a significant fraction of cell type–specific miRNAs are regulated at the epigenetic level and that these miRNAs are likely to be important targets in human diseases caused by epigenetic dysfunction.

Results

We determined miRNA expression in normal human mammary epithelial and fibroblast cells by high-throughput sequencing of small RNA libraries prepared from three isogenic pairs of HMEC, and HMF from specimens 48, 184, and 240. About 3.7 million reads in each library were aligned to annotated miRNA regions. Detailed information about sequencing data quality is provided in Supplemental Figures 1 and 2 and Supplemental Table 1. This miRNA transcriptome sequencing data showed that 392 of 703 (mirbase 13) mature miRNAs were expressed in HMEC and/or HMF at levels that ranged from zero to one million counts per library, demonstrating a large dynamic range of miRNA expression. The expression level of these 392 miRNAs for each of the six samples is provided in Supplemental Data 1. Results also revealed a striking interindividual concordance in miRNA expression within a cell type, with a correlation of 0.94–0.99 for HMEC and 0.97–0.98 for HMF (Supplemental Fig. 3).

Intercell-type concordance was considerably lower than interindividual with correlations between HMEC and HMF ranging from 0.75 to 0.84, indicating a substantial population of miRNAs expressed in a cell type selective fashion. Twenty seven percent (104/392) of the expressed miRNAs showed at least fourfold ($P <$ 0.05) difference in expression, with 68 showing HMEC selective expression, and 36 showing HMF selectivity (Fig. 1). Thirteen percent (50/392) of the expressed mature miRNAs showed at least a 10-fold difference in expression between HMEC and HMF. This fraction was considered cell type–specific, with 32 miRNAs being HMEC specific and 18 being HMF specific. Figure 2 shows quantitative expression results for several representative cell type–specific miRNAs that illustrate the strong interindividual concordance in the cell type–specific expression as well as the magnitudes of difference that can be seen in miRNA expression

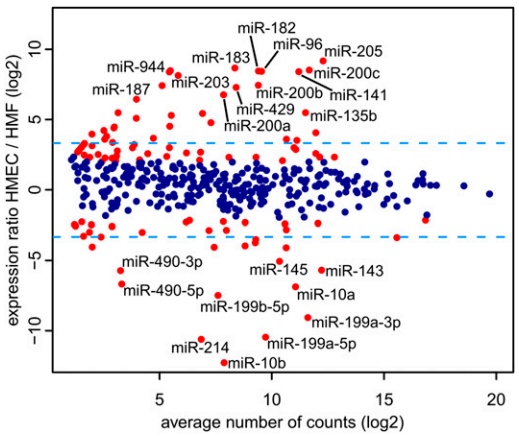

Figure 1. Differential miRNA expression between HMEC and HMF obtained from three independent pairs of samples. The *y*-axis displays the HMEC to HMF expression ratio, the *x*-axis displays the average expression of miRNAs; both axes are in logarithmic scale. (Red) Differentially expressed miRNAs (at least fourfold difference in expression, *P*-value ≤0.05). (Blue dashed horizontal lines) Tenfold differences in expression. Several cell type–specific miRNAs are marked.

between the different cell types (exceeding three orders). Examples of mammary epithelial specific miRNAs include miR-205, the two clusters forming the miR-200 family, and the miR-183/96/182 cluster (Fig. 2, top). The miR-200b/200a/429 cluster of miR-200 family is the only tissue-specific cluster that displays substantial variability between individual HMEC genotypes. Mammary fibroblast–specific miRNAs are represented by the miR-10 family, the miR-199 family (and miR-214), and the miR-143/145 cluster (Fig. 2, bottom). To verify miRNA sequencing data we have analyzed the expression of 10 selected tissue-specific miRNAs by real-time PCR (Supplemental Fig. 4). The real-time PCR data are in high concordance with miRNA sequencing data, including interindividual variability of miR-200b. Overall, these miRNA expression results indicate that normal human mammary cells show strong cell type–specific patterns of a substantial fraction of miRNAs.

Since epigenetic mechanisms play a role in the control of cell type–specific protein-coding genes, we performed a broad epigenomic analysis to identify epigenetically regulated miRNA genes. A custom miRNA gene tiling microarray (described in detail in Methods) was used to probe the epigenetic state of miRNA promoters in each of the three pairs of isogenic HMEC–HMF. 5-methylcytosine or chromatin-immunoprecipitated genomic fractions and their respective inputs were hybridized to the microarrays. Then, miRNA targets of DNA methylation, the repressive histone marks H3K27me3 and H3K9me2, and the permissive histone marks of H3Ac and H3K4me3 were identified. The H3K4me3 mark is present on active promoters (Heintzman et al. 2007), reaching a maximum peak at ~500 bp downstream from the transcription start site (Guenther et al. 2007) and has been extensively used to identify these elements (Marson et al. 2008; Ozsolak et al. 2008). Therefore, we used the results from our H3K4me3 analysis to identify and refine the promoter regions of miRNA genes expressed in normal HMEC and HMF (100 or more reads across the libraries). The positions of the identified promoter regions for 169 miRNA genes and gene clusters including 232 miRNA-coding regions are provided in Supplemental Data 2, and it is these 169 regions that were evaluated for epigenetic state. These 169 regions include promoters of 24 miRNA gene clusters encod-

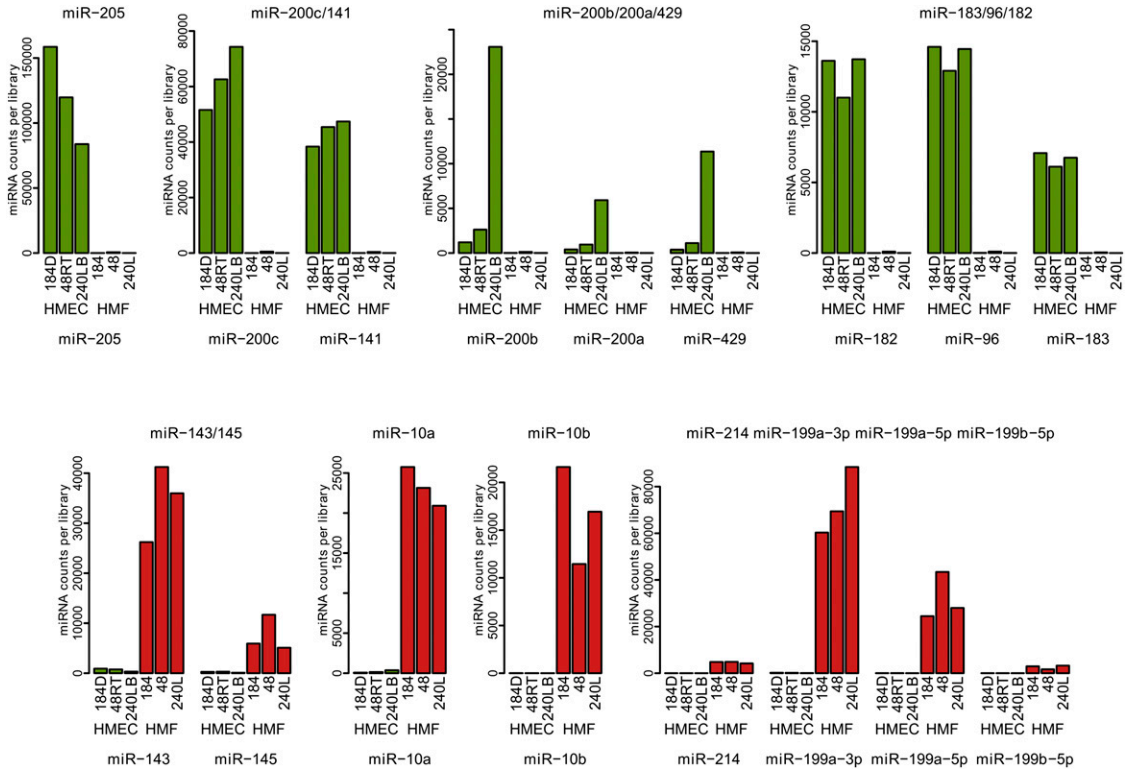

Figure 2. Expression data for selected cell type–specific miRNA genes obtained by sequencing of small RNA libraries from isogenic pairs of human mammary epithelial and fibroblast cells. The normalized counts for each sample are displayed. (Green) Individual HMEC samples; (red) their paired HMF samples. The expression levels of the 392 detected mature miRNAs across all six samples are presented in Supplemental Data 1.

ing 37 out of 50 tissue-specific miRNAs. The remaining 13 tissue-specific miRNAs were either expressed in lower than 100 counts across libraries or there was no significant H3K4me3 enrichment peak in the region covered by microarray, and promoter regions were therefore not predicted for these miRNAs.

Figure 3 shows correlations that exist between miRNA expression and the miRNA promoter's epigenetic state. Specifically, either all expressed miRNA genes, or those 10-fold differentially expressed were compared to discover a correlation to the DNA methylation or histone modification state of their respective promoters. The comparisons show that for cell type–specific miRNAs there is an increase in correlation between miRNA expression and the various epigenetic marks at their promoter regions. As expected, the correlation was much lower when we analyzed only

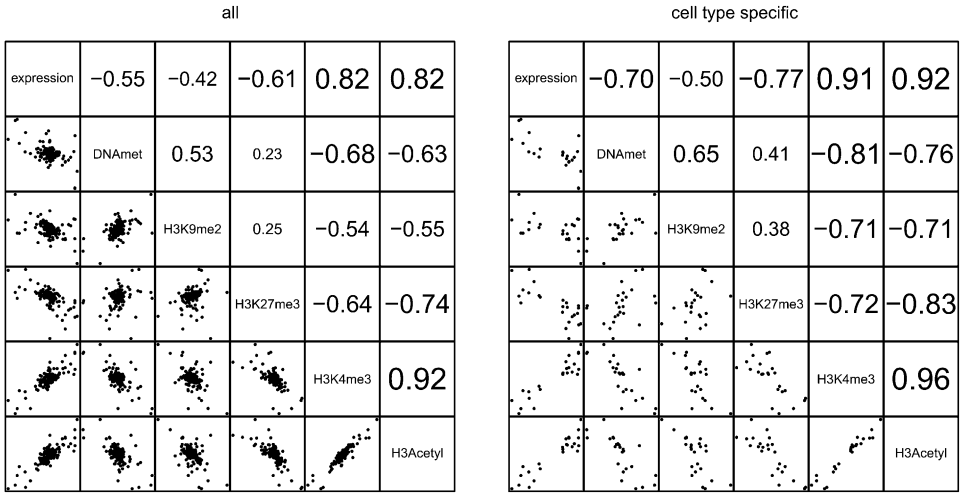

Figure 3. Differences in HMEC/HMF miRNA expression correlated with differences in epigenetic marks at their promoters. We used data from all probes within a 2-kb region centered on the predicted TSS region, and calculated the correlation of difference in enrichment of individual epigenetic marks between the cell types. (*Left*) Correlations for all 169 miRNA genes and gene clusters, where the promoter was predicted; (*right*) 24 cell type–specific miRNA genes only. The numbers show correlation coefficients for individual pairs of epigenetic marks.

promoters of miRNAs not differentially expressed (Supplemental Fig. 5). With respect to permissive histone marks, H3Ac and H3K4me3 display strong positive correlations with miRNA expression (Fig. 3), as well as with each other, consistent with a transcriptionally active state. These permissive histone marks also display strong negative correlations with DNA methylation and the repressive histone modifications, H3K27me3 and H3K9me2.

Repressive epigenetic marks in miRNA promoter regions show increasingly strong negative correlations as the levels of cell type differential expression increases. In miRNAs that show a >10-fold difference in expression, DNA methylation and H3K27me3 show inverse correlations with an miRNA expression of −0.70 and −0.77, respectively, suggesting that a number of these miRNAs are epigenetically regulated (Fig. 3). H3K9me2 shows a weaker negative correlation (−0.50) that is more closely associated with DNA methylation than with H3K27me3, supporting the functional linkage between H3K9me2 and DNA methylation (Epsztejn-Litman et al. 2008). While DNA methylation and H3K27me3 both have strong inverse correlations with permissive histone marks and miRNA expression state, these two marks do not correlate well with each other (0.41), supporting their largely independent mechanisms and distinct targets of epigenetic repression. Taken together, these associations suggest that a subset of cell type–specific miRNA genes are repressed by DNA methylation/H3K9me2 and others by H3K27me3, while only a small fraction of these miRNA genes are likely to be repressed by both epigenetic marks. In addition to promoter regions, we also analyzed the correlation between repressive epigenetic marks and miRNA expression at miRNA hairpin encoding regions downstream from their promoters (Supplemental Fig. 6). In these regions, H3K27me3 correlates negatively with expression at the level similar to that observed in promoter regions. DNA methylation, however, does not correlate with expression in hairpin coding regions. These results indicate that DNA methylation plays a promoter-centric repressive role, in contrast to the polycomb-specific H3K27me3 that spreads over the whole regions of repressed genes.

We further focused on the promoters of 24 miRNA genes and gene clusters expressing 37 cell type–specific miRNAs (Fig. 4). Eighteen of these promoters (75%) show cell type–specific patterns of DNA or H3K27 methylation that are linked to the transcriptional repression of their associated miRNAs in the nonexpressing cell type, while six promoters (25%) show no substantial cell type–specific differences in repressive epigenetic marks. Nine of 24 promoters (38%) are repressed by DNA methylation, 14 of 24 promoters (58%) are differentially occupied by polycomb-specific mark H3K27me3, and interestingly, five of the 18 epigenetically targeted miRNA promoters possess differences in both, DNA methylation and H3K27me3, suggesting a dual epigenetic repression of these miRNAs. Examples of this small fraction of miRNA genes under dual epigenetic repression by DNA methylation and H3K27me3 include the HMEC-specific *MIR*205 and the HMF-specific *MIR10A* and *MIR10B*.

miR-205 is an HMEC-specific miRNA that is functionally related to the miR-200 family. The *MIR205* gene has an increased CpG density at its regulatory region; however, it does not have a CpG island according to the original criteria (Gardiner-Garden and Frommer 1987). H3K4me3 and H3Ac are present in miR-205 expressing HMEC cells, but are absent in nonexpressing HMF (Fig. 5A). In contrast, the repressive epigenetic marks of DNA methylation, H3K9me2 and H3K27me3, are all present in nonexpressing HMF, but are absent in expressing HMEC. To increase the resolution and confirm the DNA methylation data from the microarray analysis, we analyzed certain regions in more detail using MassARRAY technology (Fig. 5A, bottom). The results from MassARRAY are in agreement with the microarray data, showing very low levels of methylation in all HMEC samples and high levels of DNA methylation in HMF. Therefore, in mammary fibroblasts, the *MIR205* gene appears to be under a dual epigenetic repression by both DNA methylation (linked to H3K9me2) and H3K27me3.

cluster ID	expression	DNAmet	H3K9me2	H3K27me3	H3K4me3	H3Acetyl
MIR205	9.17	−1.14	−1.23	−1.68	3.16	3.26
MIR183/96/182	8.52	1.17	0.29	−1.76	0.71	0.84
MIR944	8.46	−2.25	−0.81	−0.50	2.29	2.32
MIR200C/141	8.46	−2.22	−0.38	−0.32	2.40	1.56
MIR203	8.15	0.14	0.31	−0.90	0.21	0.34
MIR200B/200A/429	7.15	−0.23	0.07	−1.02	1.23	1.02
MIR187	6.49	−0.41	0.11	−1.15	0.44	0.74
MIR135B	5.49	−0.51	−0.41	−1.55	2.08	1.54
MIR582	5.46	−0.54	−0.37	−2.79	0.87	1.61
MIR1910	4.98	−0.15	−0.21	−0.44	0.35	0.90
MIR584	4.74	−0.32	−0.40	−0.10	0.79	0.96
MIR577	4.56	−0.74	0.10	−2.04	1.46	1.47
MIR147B	3.63	0.06	−0.10	0.10	0.35	0.25
MIR210	3.59	0.11	−0.21	−0.38	0.21	0.51
MIR378	3.50	−0.09	−0.22	−0.81	0.25	0.69
MIR424~450B	−3.45	0.31	0.12	0.33	−1.28	−1.31
MIR497/195	−3.80	−0.21	0.01	0.45	−0.97	−0.85
MIR143/145	−5.37	0.02	0.50	1.51	−3.17	−2.42
MIR10A	−6.86	1.37	0.19	2.41	−2.15	−3.03
MIR490	−7.00	0.12	−0.06	0.65	−1.51	−1.60
MIR199B	−8.82	0.67	−0.19	0.87	−1.40	−1.10
MIR199A1	−9.47	2.23	−0.19	−0.11	−3.17	−1.93
MIR199A2/214	−10.07	2.15	1.15	0.41	−3.67	−2.82
MIR10B	−12.29	0.94	0.27	2.33	−2.38	−3.15

Figure 4. Cell type–specific miRNA genes (clusters), their difference in expression, and differences in occupation of their promoter regions by five epigenetic marks. The data are presented as $\log_2$ (fold difference HMEC/HMF). The color scale indicates whether the data behave as expected for HMEC-specific miRNAs (green) or HMF-specific miRNAs (red). The *MIR424~450B* is the label for the *MIR424/503/542/450A2/450A1/450B* cluster.

A similar dual epigenetic control is seen in the HMF-specific *MIR10A* and *MIR10B* miRNA genes located within the *HOXB* and *HOXD* gene clusters, respectively. In *MIR10A* and *MIR10B*-expressing fibroblasts, H3K4me3 and H3Ac are present at *MIR10A* and *MIR10B* promoters, but are absent in nonexpressing epithelial cells. In contrast, the repressive H3K27me3 is present throughout the whole region of both the *MIR10A* and *MIR10B* genes in nonexpressing HMEC, but is absent in expressing HMF (Fig. 5B; Supplemental Fig. 7A), consistent with the knowledge that HOX gene clusters are polycomb targets (Simon and Kingston 2009). In addition to the repressive H3K27me3 mark in HMEC, the *MIR10A* and *MIR10B* gene promoters also show HMEC-specific DNA methylation (Fig. 5B; Supplemental Fig. 7A) along with low levels of H3K9me2. These results are similar to those seen for *MIR205*, suggesting that normal cells repress some miRNA genes using multiple epigenetic mechanisms.

Most epigenetically targeted cell type–specific miRNAs are repressed in association with either H3K27Me3 or DNA methylation, and these distinct repressive epigenetic states can even be seen in different members of the same miRNA families. One example is the *MIR200* family, an epithelial-specific miRNA family repressed in mesenchymal cells. In this case, both members of the *MIR200* family have their promoter region occupied by H3K4me3 and H3Ac in expressing epithelial cells. In contrast, nonexpressing

HMF are devoid of these permissive marks and instead, each member of the *MIR200* family is targeted by different repressive epigenetic marks in these cells. The promoter for the *MIR200B/200A/429* cluster is occupied by H3K27me3, (Fig. 5C) indicating that polycomb is responsible for the fibroblast cell type–specific repression of this miRNA gene. DNA methylation of the *MIR200B/200A/429* gene has a complex pattern. MassARRAY analysis revealed that the transcription start region located in the distal part of the CpG island is unmethylated in HMEC and has a low level of methylation in HMF (Fig. 5C). The other analyzed regions downstream from the TSS, however, show that DNA methylation alternates between nonexpressing and expressing cells in this particular H3K27me3 target gene (Fig. 5C). The proximal part of the CpG island shows more DNA methylation in expressing HMEC samples. Then follows the region methylated more in nonexpressing fibroblasts, and finally, the area just upstream of the *MIR200B* hairpin coding region shows an intermediate level of methylation in both cell types. Therefore, DNA methylation does not seem to

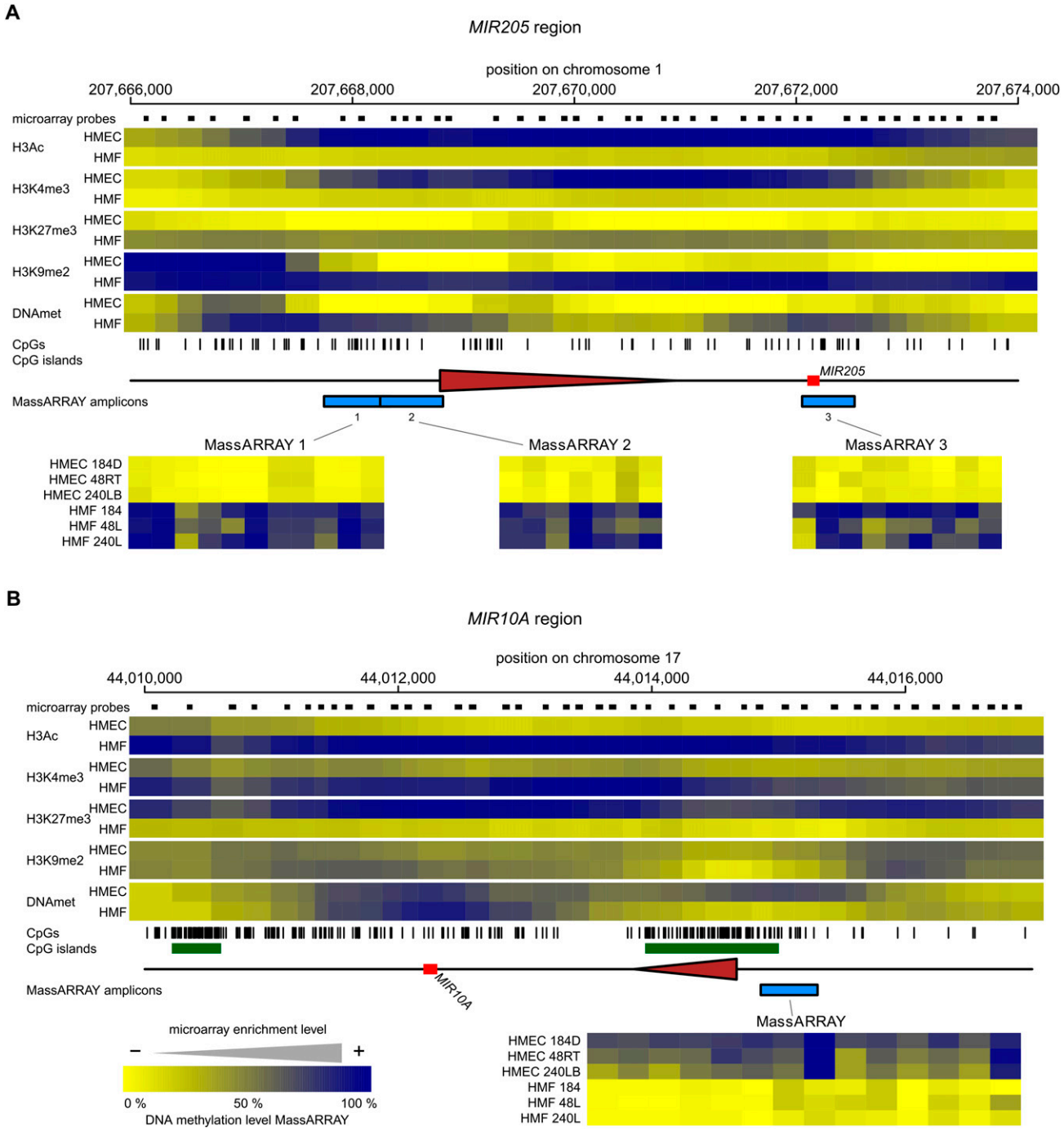

Figure 5. (Continued on next page)

play any conclusive role in normal tissue-specific repression of the *MIR200B/200A/429* cluster. In contrast to the *MIR200B/200A/429* cluster, we have previously shown DNA methylation and H3K9Me2 to be important in the repression of the *MIR200C/141* members of the family (Vrba et al. 2010), and these earlier observations are further confirmed by the microarray analysis in the present studies (Fig. 5D). The DNA of the whole *MIR200C/141* region is unmethylated in expressing HMEC and the microarray data show that DNA methylation in HMF reaches a maximum in the region just downstream from the TSS. The lack of H3K27me3 enrichment in the *MIR200C/141* region in both mammary cell types indicates that this important cell type–specific miRNA cluster is not a polycomb target. Since both clusters of the *MIR200* family share a high level of expression in epithelial cells, but no expres-

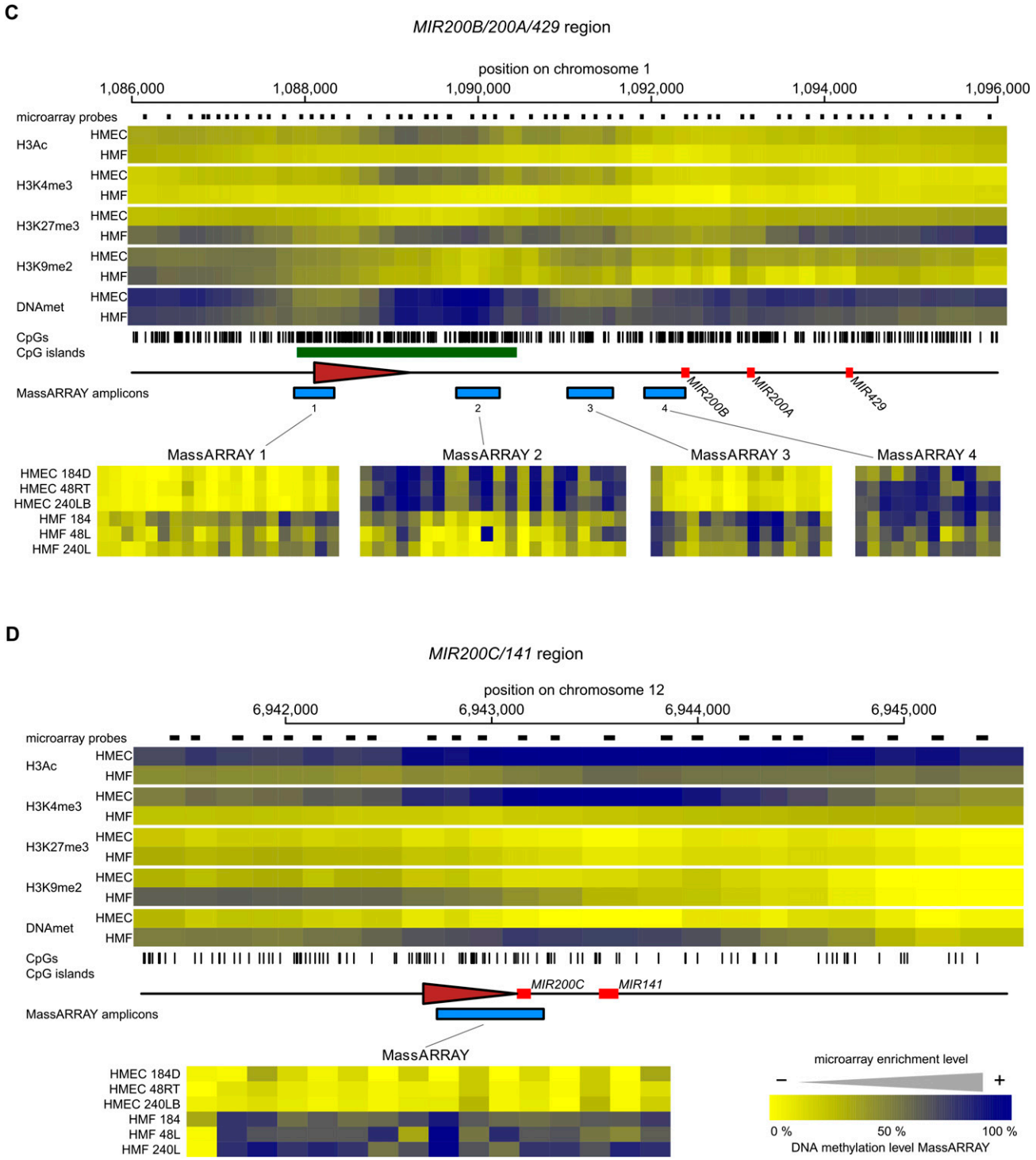

Figure 5. (Continued on next page)

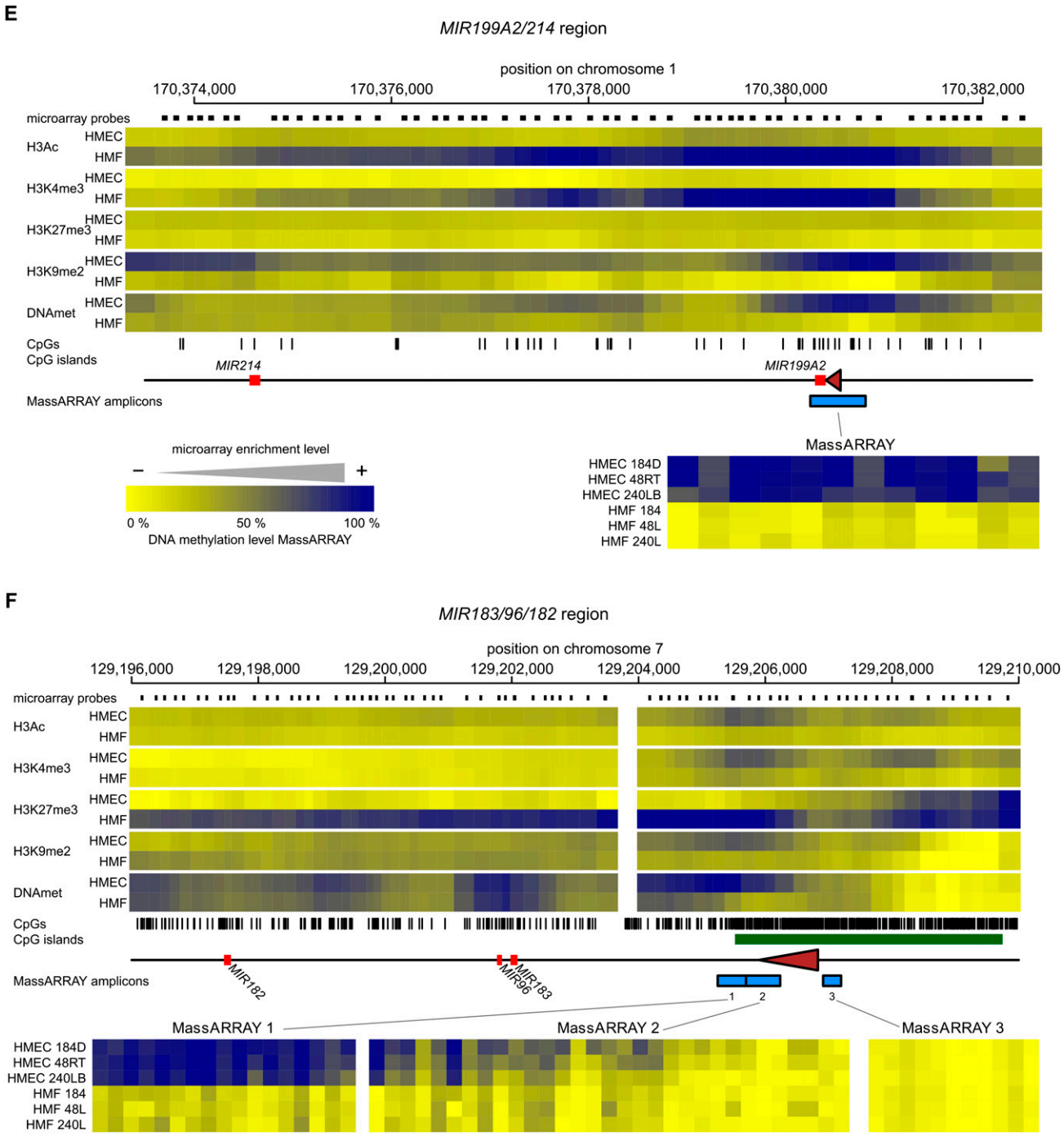

Figure 5. The epigenetic state of cell type–specific miRNA genes in HMEC and HMF. Panels *A–F* show data for *MIR205, MIR10A, MIR200B/200A/429, MIR200C/141, MIR199A2/214*, and *MIR183/96/182* miRNA genes, respectively. (*Top* part of each panel) The enrichment of individual epigenetic marks through the regions in a heatmap form, with yellow indicating no enrichment and blue color indicating high enrichment. The data for HMEC and HMF samples are averages from three genotypes of HMEC and HMF, respectively. The chromosomal positions are according to the hg18 human genome assembly. The miRNA hairpin coding regions are displayed as red rectangles and predicted transcription start site regions as brown triangles. Small black rectangles at the *top* lane indicate positions of individual microarray probes. The tics at the *bottom* indicate positions of individual CpG dinucleotides. CpG islands according to UCSC are displayed as green rectangles when present. The blue rectangles at the *bottom* lane indicate positions of regions analyzed for DNA methylation by MassARRAY technology. Results from MassARRAY for individual regions indicated are shown at the *bottom* part of each panel. The level of methylation of individual CpG units within the MassARRAY amplicon is displayed as a heatmap with the lowest methylation (0%) in yellow and the highest methylation (100%) in blue. The individual samples are labeled on the *left*.

sion in fibroblasts, the distinct repressive epigenetic marks observed for the members of the *MIR200* family suggest that distinct epigenetic mechanisms are involved in their respective repression.

Similar multifaceted forms of epigenetic repression of miRNA families are seen in the fibroblast-specific *MIR199* family, whose members consist of the *MIR199A2/214* cluster, *MIR199A1* and *MIR199B*. These three miRNA genes of the *MIR199* family are located at homologous positions on the antisense strands of introns of the three members of the *DNM* gene family. The *MIR199A2/214* cluster is located in *DNM3*, *MIR199A1* in *DNM2*, and *MIR199B* in *DNM1*, indicating coevolution of the *MIR199* family together with the *DNM* gene family. Similar to HMEC-specific miRNA genes *MIR200C/141* and *MIR205*, there is an increased CpG density in the promoters of the *MIR199* genes; however, it does not meet the original CpG island definition criteria. The miRNA promoters are occupied by H3K4me3 and H3Ac in expressing fibroblasts, but these marks are absent in epithelial cells. Instead, in nonexpressing epithelial cells the *MIR199A2/214* cluster is DNA methylated and H3K9me2 is present, but significant levels of H3K27me3 were not detected, indicating that this region is not a polycomb target (Fig. 5E). In contrast, only DNA methylation-linked repression was detected in the *MIR199A1* regulatory region in epithelial cells, (Supplemental Fig. 7B), while *MIR199B* utilizes a dual epigenetic repression, that of DNA methylation in combination with H3K27me3 (Supplemental Fig. 7C). Overall, these results suggest that expression of the three members of the fibroblast-specific *MIR199* family is repressed predominantly by DNA methylation, and to a lesser extent, by H3K27me3.

A surprising cell type–specific miRNA gene with respect to repressive epigenetic marks is the *MIR183/96/182* gene. The entire *MIR183/96/182* region is heavily occupied by H3K27me3 in nonexpressing HMF, but H3K27me3 is absent in expressing HMEC (Fig. 5F), suggesting that the polycomb repression is the critical repressive epigenetic mechanism regulating the *MIR183/96/182* cluster gene. DNA methylation shows an unexpected phenomenon in this region. Although the TSS region is DNA methylation-free for both cell types, downstream from the TSS at the proximal end of the CpG island there exists a differentially methylated region that is DNA methylation-free in all three nonexpressing HMF samples and heavily methylated in all three expressing HMEC samples (Fig. 5F). MassARRAY analysis confirmed the microarray data for all three genotypes. Thus, the *MIR183/96/182* cluster is a cell type–specific miRNA gene repressed by polycomb, where DNA methylation within the promoter region inversely correlates with H3K27me3 and positively correlates with expression (Fig. 4). Since the DNA hypermethylation in HMEC is located downstream from the TSS, in the area that is most occupied by polycomb-specific mark H3K27me3 in nonexpressing HMF (Fig. 5F), it may represent a case of antagonism between DNA methylation and polycomb repression, as was recently described in a mouse model (Wu et al. 2010).

Taken together, our data show strong tissue-specific expression of a substantial fraction of miRNAs between mammary epithelial cells and mammary fibroblasts, exceeding three orders of magnitude for some miRNAs. Most of the promoters of these tissue-specific miRNA genes are occupied by H3K27me3 or DNA methylation, or both of these marks in nonexpressing cells, indicating that the epigenetic state of miRNA promoters plays an important role in the cell type–specific control of miRNA expression.

Discussion

In this study, we sought to identify cell type–specific miRNAs regulated by epigenetic mechanisms. To this end, we analyzed the expression levels and the epigenetic state of miRNA genes in three isogenic pairs of normal, finite lifespan HMEC and HMF—two predominant differentiated cell types of ectodermal and mesodermal origin, respectively, found in mammary tissue. miRNA expression and epigenetic state showed strong interindividual concordance within a given cell type, but significant expression and epigenetic differences were found between the different cell types. We found 13% of expressed miRNAs to be expressed in a cell type–specific fashion (>10-fold difference between the two cell types), including several known to be important for maintaining cell-specific phenotypes. The differential expression of a majority of these cell type–specific miRNAs was linked to cell type–specific differences in the epigenetic state of their promoters, indicating that epigenetic mechanisms play an important role in the regulation of cell type–specific miRNA genes.

To identify miRNA promoters utilized by HMEC and HMF (Supplemental Data 2), we used H3K4me3 ChIP–chip data that we obtained from these cells, since this mark is exclusively present at promoters (Heintzman et al. 2007). We used the complementary miRNA expression data obtained from these same cells to limit promoter identification to only those miRNA expressed in at least one of the mammary cell types, allowing for precise identification of miRNA promoters relevant to human mammary cells. Our results revealed that the promoters of cell type–specific miRNAs mostly lacked H3K4me3 enrichment in the inactive promoters of the nonexpressing cell type (Fig. 5A,C–E), suggesting that these represent the epigenetically labile miRNAs of normal, nondiseased cells. Similar results were reported previously for tissue-specific protein-coding genes (Guenther et al. 2007). Finally, the H3K4me3 ChIP–chip results further suggest that H3K4me3-directed prediction of promoters for miRNA genes, and likely all genes in general, will be the most accurate if derived from cells known to express the genes of interest.

Of the 24 cell type–specific miRNA genes, three-quarters (75%) were found to be repressed by H3K27me3 or DNA methylation in the nonexpressing cell type, with 58% of the cell type–specific promoters differentially occupied by H3K27me3, 38% differentially occupied by DNA methylation, and 21% differentially occupied by both H3K27me3 and DNA methylation. In miRNAs repressed by H3K27me3, we find this mark extends beyond the promoter and encompasses larger regions that include the miRNA gene body, consistent with recent findings demonstrating a spreading of the H3K27me3 mark from the promoter during differentiation of human embryonic stem cells (Hawkins et al. 2010). Interestingly, when we extend our analysis beyond only miRNA promoters differentially active in mammary cells by integrating our H3K27me3 ChIP–chip data with all of the predicted miRNA promoter data and known miRNA hairpin coding regions, we found that ~27% of all miRNA promoters, as well as miRNA hairpin coding regions, are enriched for H3K27me3 (Supplemental Fig. 8). In contrast, it has been estimated that only 9% of promoters of protein-coding genes are occupied by H3K27me3 (Bracken et al. 2006). Thus, H3K27me3, a polycomb mark responsible for regulating genes involved in cell identity and differentiation, shows an approximately threefold bias toward miRNA compared with protein-coding genes, providing further support for an important role for miRNAs as regulators of cell fate and phenotype and H3K27me3 as an important regulator of cell type–specific miRNA expression.

Cell type–specific DNA methylation of miRNA promoters was correlated with the presence of the H3K9me2 mark and the repression of the associated miRNAs, further supporting the functional linkage between these two repressive epigenetic marks (Epsztejn-Litman et al. 2008). The DNA methylation mark was

found to be centered on the promoter regions of the miRNA and did not extend far upstream or downstream, in contrast to what was observed with the H3K27me3 repressive mark. In addition, a common feature of DNA methylation-repressed miRNA genes was the absence of a CpG island in the promoter region; in the case of cell type–specific miRNA genes with CpG island promoters, the H3K27me3 mark is most often responsible for transcriptional repression (Fig. 5A–F).

The weakest correlation between epigenetic marks was between DNA methylation/H3K9me2 and H3K27me3. The limited overlap between DNA methylation/H3K9me2 and H3K27me3 in miRNA promoters likely reflects the largely independent nature of these two epigenetic repressive pathways in normal cells. Despite this limited overlap there are miRNAs where both marks appear to be involved in their cell type–specific repression. The coincidence of DNA methylation and H3K27me3 on the same miRNA promoters may represent mutual fail-safe mechanisms, so that disruption of one epigenetic mechanism is not sufficient to initiate aberrant activation of the miRNA. If this is the case, then, miRNA targets of this dual epigenetic repression may be critical to maintain cell integrity/identity, and their compromise could be involved in the genesis of human disease states, including cancer. Two examples of miRNAs that support the possible importance of dual epigenetic repression are miR-205, miR-10a, and miR-10b, since their dysregulation has already been linked to a variety of different cancers (Gregory et al. 2008b; Ma and Weinberg 2008; Greene et al. 2010; Lund 2010). For example, the loss of epithelial-specific miR-205 in cancers of epithelial origin has been linked to the acquisition of aggressive tumor phenotypes (Baffa et al. 2009; Iorio et al. 2009; Tellez et al. 2011), while gain of expression of fibroblast-specific miR-10 family members by cancers of epithelial origin have similarly been linked to aggressive tumor phenotypes (Ma et al. 2007; Baffa et al. 2009; Tian et al. 2010).

miR-205 participates in the maintenance of the epithelial phenotype, is expressed in epithelial cells but not in fibroblasts, and is related to the miR-200 family (Gregory et al. 2008a; Park et al. 2008). Expression of miR-205 and the miR-200 family members appears incompatible with a mesenchymal phenotype, and since miR-205 is expressed at much higher levels than the miR-200 family members in HMEC, it is possible that dual epigenetic repression by DNA methylation and H3K27me3 in fibroblasts is necessary to prevent any inappropriate miR-205 expression. miR-205 along with the miR-200 family target the mesenchymal-specific transcriptional repressors *ZEB1* and *ZEB2* (Gregory et al. 2008a). Possibly, the total level of the miR-200 family and miR-205 secures an epithelial phenotype, and complete epigenetic silencing of *MIR205* is necessary to allow *ZEB1* and *ZEB2* to be expressed at levels sufficient to direct the mesenchymal phenotype.

Similar to *MIR205*, we have found that the closely related *MIR200* family members are also epigenetically regulated in a cell type–specific fashion. We and others have previously shown that the *MIR200* family members *MIR200C/141* have a permissive epigenetic state in expressing epithelial cells, while nonexpressing fibroblasts display a repressed epigenetic state driven by DNA methylation and H3K9me2, but not H3K27me3 (Vrba et al. 2010). In contrast, the fibroblast-specific repression of the other *MIR200* family members *MIR200B/200A/429* is linked to the H3K27me3 mark, and DNA methylation and H3K9me2 do not appear to play a decisive role in its repression (Fig. 5C). Therefore, the two genes of the *MIR200* family that likely arose from a single common ancestor have acquired different mechanisms of epigenetic regulation during evolution. Overall, these results suggest that complete epigenetic transcriptional repression of individual miRNAs may require complementary epigenetic mechanisms to prevent spurious transcriptional activity. Similarly, our results also suggest that complementary epigenetic repressive mechanisms may act independently to repress distinct members of the same miRNA family, as is the case with the *MIR200* family.

miR-10a and miR-10b are expressed in a fibroblast-specific fashion and appear to be under dual epigenetic repression in the epithelial cells. Both *MIR10A* and *MIR10B* show significant H3K27me3 and DNA methylation in their promoter regions and both are found in HOX gene clusters, gene families well known for rich and complex epigenetic regulation in normal and cancer cells (Rauch et al. 2007). Interestingly, miR-10b has been reported to be aberrantly expressed in breast cancer cells and this expression is linked to an aggressive cancer phenotype (Ma et al. 2007; Baffa et al. 2009), although this conclusion has been questioned based on the analysis of primary breast cancer specimens that showed no correlation between miR-10b expression levels and clinical progression (Gee et al. 2008). Several molecular, cellular, and organismal facets may contribute to these two different conclusions. The data presented in this study strongly suggest that epigenetic control of cell type–specific expression is one important facet. The experimental biological studies used pure cancer cell line populations to first detect and then verify miR-10b's phenotypic effects. In contrast, it appears that the analysis of breast cancer clinical specimens was performed on heterogeneous tissue samples. Detecting aberrant expression of miR-10b in breast tumor cells from a complex tissue specimen is likely to be difficult, since mammary fibroblasts can constitute a significant portion of stromal cell content typically found in such specimens, and they express more than three orders of magnitude higher levels of miR-10b compared with mammary epithelial cells. This very high expression of miR-10b in the stromal cells of the tissue specimens could obscure any significant changes within the breast cancer cells themselves.

Indeed, this cautionary note extends to all the cell type–specific miRNAs identified in this study. The large magnitude differences seen in the expression levels and epigenetic states of these miRNAs between HMEC and HMF limit the ability to easily determine over- or underexpression or epigenetic status from the analysis of heterogenous tissue samples. Precise analysis of these miRNAs will require approaches that assess the expression or epigenetic state of these miRNAs in specific cell types within a tissue specimen. This is especially important since many of the epigenetically regulated cell type–specific miRNAs identified in this study have already been associated with or functionally linked to human carcinogenesis. The tissue-specific miRNAs that have been found deregulated in cancer are summarized in Supplemental Table 2.

In summary, our study has revealed a significant level of cell type–specific miRNA expression associated with human mammary epithelial and fibroblast cells. We also showed that epigenetic modifications play an important role in this cell type–specific miRNA regulation. The two epigenetic pathways responsible for deployment of repressive epigenetic marks—DNA methylation and H3K27me3—act largely independently. H3K27me3, a hallmark of polycomb repression, appears to play the major role in the normal cell type–specific repression of miRNA genes. Examples of polycomb targets are the *MIR200B/200A/429* and *MIR183/96/182* genes. Some highly cell type–specific miRNA genes like *MIR200C/141* and *MIR199A2/214*, however, are not polycomb targets and their differential expression is determined predominantly by cell type–specific DNA methylation at the promoter region, often in collaboration with the H3K9me2 histone mark in nonexpressing cells. A common feature of these miRNA genes repressed by DNA

methylation is the lack of CpG islands. Different genes forming miRNA families are repressed by different epigenetic marks, indicating that they are targeted by different epigenetic mechanisms. Some miRNA genes, including *MIR205*, *MIR10A*, and *MIR10B*, are under dual epigenetic repression by both DNA methylation and H3K27me3. The miRNAs found to be cell type–specific and repressed by epigenetic marks in nonexpressing cells are often deregulated in cancer, indicating that the disruption of normal epigenetic regulation of cell type–specific miRNA expression can be involved in carcinogenesis. Knowing which epigenetic marks are involved in repression of individual miRNA genes in normal cells and the locations of relevant regulatory regions thus contributes to our better understanding of these processes.

Methods

Cell lines and cell culture

Finite lifespan prestasis HMEC from specimens 184 (batch D), 48 (batch RT), and 240L (batch B), were derived from reduction mammoplasty tissue of women aged 21, 16, and 19, respectively (Garbe et al. 2009). Cells were initiated as organoids in primary culture in serum-containing M85 medium supplemented with oxytocin (Bachem) at 0.1 nM and maintained in M87A medium supplemented with oxytocin and cholera toxin at 0.5 ng/mL (Garbe et al. 2009). Fibroblasts from specimens 184, 48, and 240L were obtained by growing primary reduction mammoplasty cells in DMEM/F12 with 10% FBS and 10 μg/mL insulin, and further propagated in DMEM/F12 with 10% FBS, as previously described (Garbe et al. 2009). The cells used in this study were within cell culture passages 4–9 from primary tissue. Our previous study shows that these cells do not acquire epigenetic changes as late as passage 14. It is only following the emergence from the stasis proliferation barrier (Garbe et al. 2009) that HMEC first show the acquisition of significant epigenetic changes (Novak et al. 2009).

Small RNA library preparation and sequencing

Total RNA from epithelial cells or fibroblasts was extracted using the TRIzol method (Invitrogen). The small RNA fraction (18–35 nt) was purified on a 15% denaturing polyacrylamide gel. A preadenylated adaptor (rAppCTGTAGGCACCATCAAT3ddC) was ligated to the 3′ end of a small RNA using truncated T4 RNA ligase 2 (New England Biolabs), followed by purification of the ligation product on a 15% denaturing polyacrylamide gel. An Illumina-specific 5′ adaptor (GTTCAGAGTTCTACAGTCCGAcgauc; uppercase: DNA, lowercase: RNA) was ligated using T4 RNA ligase 1 (New England Biolabs) and the product was purified on a 10% denaturing polyacrylamide gel. Small RNAs with ligated adaptors were reverse transcribed into DNA using Superscript III reverse transcriptase (Invitrogen) and a primer with a Illumina-specific extension on its 5′ end (GACATCCGTGGTAGTTAGCATACGGC AGAAGACGAAC). The cDNA was then amplified by 15 cycles of PCR using Phusion DNA polymerase (Finnzymes) and Illumina-specific primers (AATGATACGGCGACCACCGACAGGTTCAGAG TTCTACAGTCCGA and GACATCCGTGGTAGTTAGCATACGGCA GAAGACGAAC). The resulting ~110-bp PCR products were separated and purified from a 3% agarose gel, and submitted for Illumina sequencing to NCGR. The data were deposited in SRA archive, accession number SRP001530.

Data analysis

Results from the Illumina Genome Analyzer were received in the fastq format. The reads were mapped to the hg18 human genome assembly using the program Novoalign (www.novocraft.com). Output from Novoalign was further analyzed in R (R_Development_Core_Team 2011). First, data were converted to bed format and peaks of reads were found for pooled data from all samples. The peak regions were used for counts and annotation of reads in individual samples. Counts were normalized for the total number of reads in individual libraries (see Filtered reads in Supplementary Table 1). The miRNAs with at least 10 reads across the libraries represented in at least two libraries were considered expressed and further analyzed. Package edgeR was used for the differential expression calculation.

miRNA gene tiling microarray design

Human miRNA-coding sequence positions were downloaded from miRBase (ver 13) (http://microrna.sanger.ac.uk/sequences/). This data set contains information about the positions of 718 miRNA-coding regions in the human genome. A total of 454 out of 718 miRNA-coding regions have their promoter predicted (Marson et al. 2008). Another 149 of the miRNA-coding regions are part of known protein-coding genes. For these miRNAs the TSS of the host gene was assumed as TSS for miRNA and the position of this region was obtained as the 5′ end of the known gene from the UCSC Genome Browser. The entire region from 10 kb upstream of the predicted promoter (TSS) region down to 5 kb downstream from the miRNA hairpin coding region was tiled for all of these 603 miRNA-coding regions. For the remaining 115 miRNA-coding regions, where there was no prediction of TSS nor do they lie within protein-coding genes, the whole region from 70 kb upstream of the hairpin coding region down to 5 kb downstream was tiled. Additionally, about 100 protein-coding genes, including controls like GAPDH and ACTB, were added. The probes used to tile the specified regions were from the Agilent whole genome tiling microarray set and the Agilent promoter 2 microarray set. The resulting number of probes totals over 99,000, with approximately five probes per kilobase pair. The microarrays were manufactured by Agilent (Agilent Technologies) using their 2 × 105 k platform. Agilent design ID is 024305.

Methyl cytosine DNA and chromatin immunoprecipitation

Methyl cytosine DNA immunoprecipitation (MeDIP) was performed using 5-methylcytosine-specific monoclonal antibody as described (Weber et al. 2005).

Chromatin immoprecipitation (ChIP) was performed as described previously (Oshiro et al. 2003; Vrba et al. 2008) using antibodies specific for histone H3 trimethylated at lysine 4 (#05-745, Upstate), histone H3 trimethylated at lysine 27 (#07-449, Millipore), acetylated histone H3 (#06-599, Millipore), and histone H3 dimethylated at lysine 9 (CS200587, Millipore).

Sample labeling and microarray hybridization

MeDIP DNA or ChIP DNA samples were amplified using the random primed approach and 2 ug of amplified DNA was labeled as described (Vrba et al. 2008). Cy5 was used for input samples, Cy3 for immunoprecipitated samples. After labeling and purification, Cy3 and Cy5 labeled samples were pooled and vacuum concentrated to a volume of 91.5 μL. A total of 12.5 μL of human Cot-1 DNA (1 μg/μL, Invitrogen Cat. No. 15279-011), 26 μL of Agilent blocking agent (10×), and 130 μL of Agilent hybridization buffer (2×) were added. Samples were heated for 3 min at 95°C, transferred to 37°C, incubated for 30 min, and then used for microarray hybridization for 28h at 65°C. After hybridization, slides were washed in Agilent Oligo aCGH/ChIP-on-Chip Wash Buffer 1 for

5 min at room temperature, then in Agilent Oligo aCGH/ChIP-on-Chip Wash Buffer 2 for 5 min at 37°C, washed in acetronitrile for 10 sec at room temperature, and finally in stabilization and drying solution for 30 sec at room temperature. The scanning was performed using an Axon GenePix 4000B microarray scanner (Axon Instruments) and GenePix 6.0 software at 5 μm resolution and PMT settings 750 (635 nm) and 600 (532 nm).

Microarray data analysis

Output from GenePix (*.gpr files) were imported to R using the limma package. Individual channels were first spatially normalized within arrays using ma2D function from the package marray and then loess normalized between arrays using the function normalize.loess from package affy. The RG object was transformed to an MA object and M values were again loess normalized between arrays. M values (log2 ratios of input to immunoprecipitated channel) were used for further analysis as a measure of enrichment of a region centered on individual probes. Differences in histone modification were determined in a 2-kb region centered on a TSS region or miRNA hairpin region. The paired *t*-test was used to analyze data from all probes in each 2-kb region. Differentially enriched regions were defined as regions where the average difference of ratio was at least 1.5-fold and the *P*-value was ≤0.05.

Transcription start regions prediction

We predicted miRNA TSS regions based on the fact that H3K4me3 is present in TSS regions, reaching maximum enrichment at ~0.5 kb downstream from TSS (Guenther et al. 2007). To reduce the amount of false predictions, we used the most proximal major peak of H3K4me3 enrichment, upstream of the miRNA hairpin region, which was at least twofold enriched over input. Further, we limited the predictions only for miRNAs that are expressed (at least 100 reads in libraries). For differentially expressed miRNAs, the pooled H3K4me3 data from expressing samples (either HMEC or HMF) were used, for other miRNAs, the pooled H3K4me3 data from all six samples were used. Once the peak of H3K4me3 enrichment was identified, the area between the peak and nearby Switch gear TSS or EST 5′ end was considered a TSS region. Switch gear TSS and EST positions were downloaded from the UCSC browser. For miRNAs where there was no Switch gear TSS or EST end in the vicinity (2.5 kb upstream, 0.5 kb downstream) of the H3K4me3 peak, the region from H3K4me3 peak 1 kb upstream was considered TSS region.

DNA methylation analysis by MassARRAY

DNA methylation analysis by MassARRAY was performed as described (Novak et al. 2009). Primer sequences are listed in Supplemental Table 3.

All oligonucleotides used in this study were ordered from Integrated DNA Technologies.

Data access

The sequence data from this study have been submitted to the NCBI Sequence Read Archive (SRA) (http://www.ncbi.nlm.nih.gov/sra) under accession no. SRP001530. The microarray data have been submitted to the NCBI Gene Expression Omnibus (GEO) (http://www.ncbi.nlm.nih.gov/geo/) under accession no. GSE28380.

Acknowledgments

This work was supported by grants CA-65662 and 1U01CA153086-01, and by the Margaret E. and Fenton L. Maynard Endowment for Breast Cancer Research. J.C.G. and M.R.S. were supported by Department of Defense grant BCRP BC060444 carried out at Lawrence Berkeley National Laboratory under Contract No. DE-AC02-05CH11231.

References

Baffa R, Fassan M, Volinia S, O'Hara B, Liu CG, Palazzo JP, Gardiman M, Rugge M, Gomella LG, Croce CM, et al. 2009. MicroRNA expression profiling of human metastatic cancers identifies cancer gene targets. *J Pathol* **219:** 214–221.

Bird A. 2002. DNA methylation patterns and epigenetic memory. *Genes Dev* **16:** 6–21.

Bracken AP, Dietrich N, Pasini D, Hansen KH, Helin K. 2006. Genome-wide mapping of Polycomb target genes unravels their roles in cell fate transitions. *Genes Dev* **20:** 1123–1136.

Bueno MJ, Perez de Castro I, Gomez de Cedron M, Santos J, Calin GA, Cigudosa JC, Croce CM, Fernandez-Piqueras J, Malumbres M. 2008. Genetic and epigenetic silencing of microRNA-203 enhances ABL1 and BCR-ABL1 oncogene expression. *Cancer Cell* **13:** 496–506.

Epsztejn-Litman S, Feldman N, Abu-Remaileh M, Shufaro Y, Gerson A, Ueda J, Deplus R, Fuks F, Shinkai Y, Cedar H, et al. 2008. De novo DNA methylation promoted by G9a prevents reprogramming of embryonically silenced genes. *Nat Struct Mol Biol* **15:** 1176–1183.

Friedman RC, Farh KK, Burge CB, Bartel DP. 2009. Most mammalian mRNAs are conserved targets of microRNAs. *Genome Res* **19:** 92–105.

Garbe JC, Bhattacharya S, Merchant B, Bassett E, Swisshelm K, Feiler HS, Wyrobek AJ, Stampfer MR. 2009. Molecular distinctions between stasis and telomere attrition senescence barriers shown by long-term culture of normal human mammary epithelial cells. *Cancer Res* **69:** 7557–7568.

Gardiner-Garden M, Frommer M. 1987. CpG islands in vertebrate genomes. *J Mol Biol* **196:** 261–282.

Gee HE, Camps C, Buffa FM, Colella S, Sheldon H, Gleadle JM, Ragoussis J, Harris AL. 2008. MicroRNA-10b and breast cancer metastasis. *Nature* **455:** E8–E9.

Greene SB, Herschkowitz JI, Rosen JM. 2010. The ups and downs of miR-205: identifying the roles of miR-205 in mammary gland development and breast cancer. *RNA Biol* **7:** 300–304.

Gregory PA, Bert AG, Paterson EL, Barry SC, Tsykin A, Farshid G, Vadas MA, Khew-Goodall Y, Goodall GJ. 2008a. The miR-200 family and miR-205 regulate epithelial to mesenchymal transition by targeting ZEB1 and SIP1. *Nat Cell Biol* **10:** 593–601.

Gregory PA, Bracken CP, Bert AG, Goodall GJ. 2008b. MicroRNAs as regulators of epithelial-mesenchymal transition. *Cell Cycle* **7:** 3112–3118.

Guenther MG, Levine SS, Boyer LA, Jaenisch R, Young RA. 2007. A chromatin landmark and transcription initiation at most promoters in human cells. *Cell* **130:** 77–88.

Hawkins RD, Hon GC, Lee LK, Ngo Q, Lister R, Pelizzola M, Edsall LE, Kuan S, Luu Y, Klugman S, et al. 2010. Distinct epigenomic landscapes of pluripotent and lineage-committed human cells. *Cell Stem Cell* **6:** 479–491.

Heintzman ND, Stuart RK, Hon G, Fu Y, Ching CW, Hawkins RD, Barrera LO, Van Calcar S, Qu C, Ching KA, et al. 2007. Distinct and predictive chromatin signatures of transcriptional promoters and enhancers in the human genome. *Nat Genet* **39:** 311–318.

Iorio MV, Casalini P, Piovan C, Di Leva G, Merlo A, Triulzi T, Menard S, Croce CM, Tagliabue E. 2009. microRNA-205 regulates HER3 in human breast cancer. *Cancer Res* **69:** 2195–2200.

Iorio MV, Piovan C, Croce CM. 2010. Interplay between microRNAs and the epigenetic machinery: an intricate network. *Biochim Biophys Acta* **1799:** 694–701.

Jaenisch R, Bird A. 2003. Epigenetic regulation of gene expression: how the genome integrates intrinsic and environmental signals. *Nat Genet* **33:** 245–254.

Kozaki K, Imoto I, Mogi S, Omura K, Inazawa J. 2008. Exploration of tumor-suppressive microRNAs silenced by DNA hypermethylation in oral cancer. *Cancer Res* **68:** 2094–2105.

Laurent L, Wong E, Li G, Huynh T, Tsirigos A, Ong CT, Low HM, Kin Sung KW, Rigoutsos I, Loring J, et al. 2010. Dynamic changes in the human methylome during differentiation. *Genome Res* **20:** 320–331.

Liang G, Lin JC, Wei V, Yoo C, Cheng JC, Nguyen CT, Weisenberger DJ, Egger G, Takai D, Gonzales FA, et al. 2004. Distinct localization of histone H3 acetylation and H3-K4 methylation to the transcription start sites in the human genome. *Proc Natl Acad Sci* **101:** 7357–7362.

Lister R, Pelizzola M, Dowen RH, Hawkins RD, Hon G, Tonti-Filippini J, Nery JR, Lee L, Ye Z, Ngo QM, et al. 2009. Human DNA methylomes at base resolution show widespread epigenomic differences. *Nature* **462:** 315–322.

Lujambio A, Calin GA, Villanueva A, Ropero S, Sanchez-Cespedes M, Blanco D, Montuenga LM, Rossi S, Nicoloso MS, Faller WJ, et al. 2008. A microRNA DNA methylation signature for human cancer metastasis. *Proc Natl Acad Sci* **105:** 13556–13561.

Lund AH. 2010. miR-10 in development and cancer. *Cell Death Differ* **17:** 209–214.

Ma L, Weinberg RA. 2008. MicroRNAs in malignant progression. *Cell Cycle* **7:** 570–572.

Ma L, Teruya-Feldstein J, Weinberg RA. 2007. Tumour invasion and metastasis initiated by microRNA-10b in breast cancer. *Nature* **449:** 682–688.

Marson A, Levine SS, Cole MF, Frampton GM, Brambrink T, Johnstone S, Guenther MG, Johnston WK, Wernig M, Newman J, et al. 2008. Connecting microRNA genes to the core transcriptional regulatory circuitry of embryonic stem cells. *Cell* **134:** 521–533.

Miranda TB, Jones PA. 2007. DNA methylation: the nuts and bolts of repression. *J Cell Physiol* **213:** 384–390.

Novak P, Jensen TJ, Garbe JC, Stampfer MR, Futscher BW. 2009. Stepwise DNA methylation changes are linked to escape from defined proliferation barriers and mammary epithelial cell immortalization. *Cancer Res* **69:** 5251–5258.

Oshiro MM, Watts GS, Wozniak RJ, Junk DJ, Munoz-Rodriguez JL, Domann FE, Futscher BW. 2003. Mutant p53 and aberrant cytosine methylation cooperate to silence gene expression. *Oncogene* **22:** 3624–3634.

Ozsolak F, Poling LL, Wang Z, Liu H, Liu XS, Roeder RG, Zhang X, Song JS, Fisher DE. 2008. Chromatin structure analyses identify miRNA promoters. *Genes Dev* **22:** 3172–3183.

Park SM, Gaur AB, Lengyel E, Peter ME. 2008. The miR-200 family determines the epithelial phenotype of cancer cells by targeting the E-cadherin repressors ZEB1 and ZEB2. *Genes Dev* **22:** 894–907.

Peter ME. 2009. Let-7 and miR-200 microRNAs: guardians against pluripotency and cancer progression. *Cell Cycle* **8:** 843–852.

R_Development_Core_Team. 2011. R: A Language and Environment for Statistical Computing. R Foundation for Statistical Computing, Vienna, Austria.

Rauch T, Wang Z, Zhang X, Zhong X, Wu X, Lau SK, Kernstine KH, Riggs AD, Pfeifer GP. 2007. Homeobox gene methylation in lung cancer studied by genome-wide analysis with a microarray-based methylated CpG island recovery assay. *Proc Natl Acad Sci* **104:** 5527–5532.

Simon JA, Kingston RE. 2009. Mechanisms of polycomb gene silencing: knowns and unknowns. *Nat Rev Mol Cell Biol* **10:** 697–708.

Tachibana M, Sugimoto K, Nozaki M, Ueda J, Ohta T, Ohki M, Fukuda M, Takeda N, Niida H, Kato H, et al. 2002. G9a histone methyltransferase plays a dominant role in euchromatic histone H3 lysine 9 methylation and is essential for early embryogenesis. *Genes Dev* **16:** 1779–1791.

Tellez CS, Juri DE, Do K, Bernauer AM, Thomas CL, Damiani LA, Tessema M, Leng S, Belinsky SA. 2011. EMT and stem cell-like properties associated with miR-205 and miR-200 epigenetic silencing are early manifestations during carcinogen-induced transformation of human lung epithelial cells. *Cancer Res* **71:** 3087–3097.

Tian Y, Luo A, Cai Y, Su Q, Ding F, Chen H, Liu Z. 2010. MicroRNA-10b promotes migration and invasion through KLF4 in human esophageal cancer cell lines. *J Biol Chem* **285:** 7986–7994.

Vrba L, Junk DJ, Novak P, Futscher BW. 2008. p53 induces distinct epigenetic states at its direct target promoters. *BMC Genomics* **9:** 486. doi: 10.1186/1471-2164-9-486.

Vrba L, Jensen TJ, Garbe JC, Heimark RL, Cress AE, Dickinson S, Stampfer MR, Futscher BW. 2010. Role for DNA methylation in the regulation of miR-200c and miR-141 expression in normal and cancer cells. *PLoS ONE* **5:** e8697. doi: 10.1371/journal.pone.0008697.

Weber M, Davies JJ, Wittig D, Oakeley EJ, Haase M, Lam WL, Schubeler D. 2005. Chromosome-wide and promoter-specific analyses identify sites of differential DNA methylation in normal and transformed human cells. *Nat Genet* **37:** 853–862.

Wu H, Coskun V, Tao J, Xie W, Ge W, Yoshikawa K, Li E, Zhang Y, Sun YE. 2010. Dnmt3a-dependent nonpromoter DNA methylation facilitates transcription of neurogenic genes. *Science* **329:** 444–448.

Received March 29, 2011; accepted in revised form August 23, 2011.

VULNERABILITY OF NORMAL HUMAN MAMMARY EPITHELIAL CELLS TO ONCOGENIC TRANSFORMATION

James C. Garbe,1 Mark W. Jackson,2 and Martha Stampfer1
1Lawrence Berkeley National Laboratory and 2Case Western Reserve University

Recent studies have shown that cells derived from breast tumors display great diversity in patterns of gene and protein expression and genomic alterations. Based on gene expression profiling, multiple distinct cancer subtypes have been categorized; importantly, these subtypes show striking differences in clinical parameters. Understanding the pathways of molecular alterations that lead to the different types of breast cancer in vivo could facilitate design of clinical interventions in the carcinogenic progression. One approach to examining human breast carcinogenesis is to model this process in vitro, starting with normal HMEC and using oncogenic agents to transform the normal cells to cancer. However, thus far, almost all in vitro transformed HMEC lines represent a limited subset of the phenotypes observed in breast cancer cells in vivo. We hypothesized that the limited phenotypes of in vitro transformed HMEC could result from culture conditions that restrict proliferation of most normal HMEC. Normal cultured HMEC proliferate for a variable number of population doublings (PD) before encountering a first senescence barrier, stasis, which is stress-associated, mediated by the retinoblastoma (Rb) pathway, correlated with increased levels of p16INK4a, and telomere length independent. HMEC may overcome stasis by inactivation of the Rb pathway and continue growth until encountering a second extremely stringent barrier due to telomere attrition. HMEC grown in a serum-free medium reach stasis quickly and can show spontaneous silencing of p16, giving rise to the p16(-) post-stasis HMEC (called post-selection) that are commercially available. In vitro transformed lines derived from post-selection HMEC have shown a basal phenotype. We now propose to generate HMEC lines more reflective of the in vivo spectrum of breast cancer phenotypes by using improved methods for growing normal pre-stasis HMEC. We have defined low stress culture conditions that allow pre-stasis HMEC to grow for ~60 PD prior to p16 induction and growth arrest at stasis. Pre-stasis HMEC with phenotypes of luminal, basal, and progenitor lineages can be identified, supporting our belief that these cells in these cultures more accurately represent in vivo populations. We hypothesize that these heterogeneous unstressed pre-stasis populations will be more vulnerable to transformation when targeted by oncogenic agents and may yield cell lines with a greater range of transformed phenotypes. Our objectives include addressing the basic research questions—are unstressed pre-stasis HMEC more vulnerable to transformation and is a particular normal cell type more vulnerable or more likely to give a specific transformed phenotype, and producing a practical outcome - generation of useful transformed lines. Our approach will be: (1) Determine whether transduction of unstressed pre-stasis HMEC with oncogenes such as c-myc and Wnt-1, with or without p53 inactivation, will yield transformed lines with phenotypes representative of most human breast cancer cells and if there are correlations of transformed cell phenotypes with the target cell population and/or agents used for in vitro transformation. (2) Experimentally examine whether cultured HMEC that have not encountered stress are more vulnerable to transformation than those exposed to stress. The generation of diverse transformed HMEC lines with defined genetic alterations may aid the identification of potential therapeutic treatments.

DOD BCRP Era of Hope Meeting, June 2008, Baltimore, MD.

A human mammary epithelial cell system to study the reactivation of telomerase activity during carcinogenic progression

James C. Garbe, Andrew F. Wyrobek, Bernard W. Futscher, Martha R. Stampfer

We have developed an extensive human mammary epithelial cell (HMEC) culture system to understand the processes governing normal HMEC growth and senescence, and how these processes are altered during transformation to immortality and malignancy. Our long-term studies have led us to propose a new model for the tumor-suppressive senescence barriers normal HMEC need to overcome to become transformed, and to show that the step in tumor progression involving telomerase reactivation/immortalization is associated with the greatest amount of molecular alterations. We now hypothesize that changes in chromatin structure may be inherent in the transition to immortality and crucial for malignant progression.

Normal HMEC from reduction mammoplasty tissues were exposed to pathologically relevant agents (chemical carcinogen, oncogenes overexpressed in breast cancer, p53 loss, stress) to obtain a large diversity of transformed HMEC lines that exhibited stepwise malignant progression. Depending on the methods used, rare clonal to uniform immortalization was observed. Our model system allows comparison of the finite precursor cultures with the immortalized lines, including the molecular alterations associated with reactivation of telomerase activity.

Normal HMEC first need to bypass or overcome a stress-associated senescence barrier (stasis) mediated by the RB protein. Loss of $p16^{INK4}$ expression due to epigenetic silencing or mutation is the most common alteration seen in the cultured HMEC. However, the different methods used to induce p16 loss resulted in finite post-stasis cultures that differed in gene expression, epigenetic modifications, TRAP activity, and responses to c-myc. Post-stasis HMEC needed to reactivate sufficient telomerase activity to become immortal. The comparison of immortal lines to their finite precursors showed greater amount of alterations in gene expression and promoter methylation than the transition between pre-stasis and post-stasis finite HMEC, or between non-malignant and malignant immortal lines. For example, all the immortalized lines acquired hundreds of promoter methylation changes, regardless of the immortalization agents used. In contrast, 5-191promoter methylation changes were seen during the transition from pre- to post-stasis, depending upon the methods used. Fewer changes also occurred when the non-malignant lines acquired malignancy-associated properties.

Previous studies indicated that HMEC immortalization is a complex process influenced by expression levels of key regulators such as p53, p57, and c-myc. In addition to attaining the potential to express telomerase, newly immortal p53(+) HMEC lines undergo an extended process, termed conversion, to relieve a p53-mediated suppression of telomerase activity; p53(-) HMEC lines appear to undergo a quick conversion. HMEC that have undergone conversion are no longer vulnerable to oncogene-induced senescence (OIS), and overexpression of a single oncogene can render them malignant. HMEC immortalized by ectopic overexpression of hTERT (that do not undergo conversion) remain vulnerable to OIS. We now hypothesize that the transition from a finite to an immortal state entails significant changes in telomere and chromosome structure, and that the thus far poorly understood conversion process may be when these alterations occur. We are currently examining our variety of immortal lines to determine if specific alterations can be associated with specific stages in immortalization, e.g., attaining initial immortal potential or conversion. Our goal is to determine if any observed changes are essential for attaining or maintaining immortalization and could be therapeutic targets in vivo to prevent or reverse immortalization.

AACR conference The Role of Telomeres and Telomerase in Cancer Research, February/March 2010, Ft. Worth TX.

VULNERABILITY OF HUMAN MAMMARY EPITHELIAL CELLS TO ONCOGENIC TRANSFORMATION

James C. Garbe[1], Lukas Vrba[2], Mark W. Jackson[3], Bernard Futscher[2], Mark LaBarge[1], and Martha Stampfer[1]

Lawrence Berkeley National Laboratory[1], University of Arizona, Tucson[2], and Case Western Reserve University[3]

Breast cancers display great phenotypic and molecular diversity. Based on these differences, approximately five breast cancer subtypes have been categorized; importantly, these subtypes show major differences in clinical parameters. Etiology and progression likely differ in subtypes; significant variables may include the type of cell from which the cancer originated and the specific genomic alterations that subverted normal processes to confer malignancy. However, large gaps exist in our knowledge of target-cell identity or molecular events responsible for any breast cancer subtype. Understanding the molecular alterations that lead to the different breast cancer types could facilitate design of clinical interventions in the carcinogenic progression. Our laboratory has addressed this issue with a long-term program to develop an experimentally tractable human mammary epithelial cell (HMEC) culture system for investigating multistep breast carcinogenesis. Normal finite HMECs have been exposed to pathologically relevant oncogenic agents, generating cells at different stages in transformation with properties consistent with what is known about breast cancer progression in vivo. Thus far, however, almost all in vitro transformed HMEC lines represent a limited subset of the phenotypes observed in breast cancer cells in vivo. We hypothesized that this limited phenotype could result from targeting cells in culture conditions that restrict most normal HMEC growth and proposed using HMECs grown in our new media that support growth of cells with luminal, myoepithelial, and progenitor lineage markers. We also hypothesized that unstressed HMECs (without p16INK4a induction) would be more vulnerable to transformation and yield a greater range of transformed phenotypes. Our transformation protocols were based on our model of the tumor-suppressive senescence barriers encountered by cultured HMECs (Garbe et al., *Cancer Res* 2009 Oct 1;69(19):7557–68). To bypass stasis (stress-induced senescence mediated by Rb/p16), we exposed normal HMECs to shRNA to p16. To bypass telomere dysfunction due to telomere attrition, we used cMyc, an hTERT transactivator. Our data show that p16sh, then cMyc, given to unstressed normal HMECs, produced rapid uniform immortalization. cMyc did not immortalize p16(-) post-stasis HMECs that had high stress exposure prior to epigenetic silencing of p16. HMECs that had become p16(-) post-stasis by different means exhibited additional significant differences (i.e., epigenetic alterations and telomerase activity). Unstressed pre-stasis HMECs also were uniformly immortalized by hTERT and showed rare clonal immortalization with cMyc alone. Rare clonal immortalization by p16sh alone occurred during the period of genomic instability at telomere dysfunction. Immortalized lines showed many phenotypic differences, but those derived from young women exhibited mainly basal markers. Our recent work showing age-associated changes in lineage markers could be relevant to the observed age-associated increased luminal breast cancer incidence and to generating luminal lines. Applying our p16sh/cMyc protocol to an older woman's HMECs produced an immortal line with luminal properties. Altogether, we have shown that different pathways to transformation are associated with different molecular properties, opening the possibility of individualized therapy for these distinct means of becoming malignant. Future studies will evaluate the effects of specific oncogenic exposures on different normal HMEC types from young and older women.

DOD Era of Hope Meeting, August 2011, Orlando FL

AN INTEGRATED HUMAN MAMMARY EPITHELIAL CELL (HMEC) SYSTEM FOR THE STUDY OF NORMAL HMEC BIOLOGY AND CARCINOGENESIS

Martha Stampfer, Mark LaBarge, and James Garbe

Lawrence Berkeley National Laboratory

Our long-term program has developed a comprehensive, experimentally tractable human mammary epithelial cell (HMEC) system to study normal HMEC processes and how these processes are altered during transformation. HMEC grown in different culture conditions were exposed to various oncogenic agents associated with breast cancer etiology, generating isogenic cells at different stages of carcinogenesis. The molecular alterations observed during progression in our in vitro model are consistent with multistep carcinogenesis in vivo. This work has led to our molecularly defined model of cultured HMEC senescence barriers (Garbe et al., *Cancer Res.* 2009 Oct 1; 69(19):7557-68) and to studies on how the diverse breast cancer subtypes may be generated by molecularly distinct transformation pathways. Normal cell growth and phenotype is strongly influenced by culture conditions and specimen age. Our recent media can support approximately 60 population doublings and growth of cells with luminal, myoepithelial, and progenitor lineage markers. Large-scale, high-throughput examination of normal HMEC biology is thus possible. Normal HMEC stop growth with high levels of p16INK4a at stasis, a stress-associated telomere, length-independent senescence barrier mediated by the retinoblastoma pathway, and can overcome stasis by errors that inactivate this pathway. We observe significant differences in post-stasis HMEC derived by different oncogenic exposures, as well as between post-stasis and normal HMEC. For example, p16(-) post-stasis post-selection HMEC (aka vHMEC), derived by p16 promoter silencing induced by growth in a high-stress medium, differ from p16(-) post-stasis HMEC derived following exposure to a chemical carcinogen or to p16 shRNA. Many cancer-associated epigenetic alterations, as well as reduced vulnerability to cMyc immortalization, are seen in the post-selection HMEC. These data illustrate how breast cancer progression pathways can diverge early in finite life span HMEC. Finite HMEC need to reactivate sufficient telomerase to overcome the telomere dysfunction barrier due to critically short telomeres. The molecular alterations needed for HMEC immortalization have not been identified; cMyc can produce immortalization under some conditions. We observe large-scale epigenetic alterations in all immortalized lines; however, the specific changes, as well as other phenotypes (e.g., lineage markers and malignant properties), may vary. Immortal lines with endogenous telomerase reactivation are no longer sensitive to oncogene-induced senescence, thus nonmalignant immortal lines, unlike finite HMEC, can be readily transformed to malignancy by many oncogenes. We hypothesize that overcoming stasis correlates with early clonal expansion/atypical hyperplasia while post-stasis HMEC approaching telomere dysfunction show properties similar to ductal carcinoma in situ (short telomeres, genomic instability). Being able to examine the progressive changes that fuel malignancy, starting with normal cells, provides a comprehensive perspective on the origins and consequences of cancer-associated aberrations. Our studies suggest that the most crucial step in progression is obtaining immortality. This integrated culture system also permits investigation of factors that may propel or inhibit molecularly distinct malignant progression pathways (e.g., evaluation of potential therapeutics at different points of early stage breast cancer development). Use of these HMEC cultures is facilitated by our web site (hmec.lbl.gov).

DOD Era of Hope Meeting, August 2011, Orlando FL